QUANTUM LIQUIDS AND QUANTUM CRYSTALS

Carrier transport and localization in a one-dimensional electronic system over liquid helium

S. P. Gladchenko, V. A. Nikolaenko,* Yu. Z. Kovdrya, and S. S. Sokolov

B. Verkin Institute for Low Temperature Physics and Engineering, National Academy of Sciences of Ukraine, pr. Lenina 47, 61164 Kharkov, Ukraine
(Submitted June 30, 2000; revised August 3, 2000)
Fiz. Nizk. Temp. **27**, 3–14 (January 2001)

The carrier mobility in a nearly one-dimensional electronic system over liquid helium is measured. One-dimensional conducting channels are created by using the curvature of the surface of liquid helium covering a profiled dielectric substrate and applying a clamping electric field, which holds the electrons on the bottom of the liquid troughs. Measurements are made in a temperature interval of 0.5–1.6 K at linear densities in the range $(0.5–2.5)\times 10^4$ cm^{-1} at a generator voltage of 2–200 mV. It is shown that for a clean substrate the mobility of the electrons is governed by their interaction with helium atoms in the vapor and with ripplons; the results of the measurements are in satisfactory agreement with a theoretical calculation that assumes no localization. It is found that for substrates carrying a charge or having defects on the surface, the electron mobility decreases in comparison with the value for a clean substrate, and at temperatures $T<1$ K is either practically independent of temperature or decreases slightly as the temperature is lowered. It is observed that the frequency of the plasma waves propagating in the system of conducting channels decreases as the electron mobility decreases. The observed effects can be explained by localization in the one-dimensional electronic system in a random potential and the diffusive motion of the carriers in hops from one localized state to another. [DOI: 10.1063/1.1344136]

INTRODUCTION

Quasi-one-dimensional (Q1D) and one-dimensional (1D) electronic systems have been attracting a great deal of experimental and theoretical research attention recently in connection with progress in lithography and the fabrication of cleaner nanostructures. At the same time, it is known that electrons localized over a liquid helium surface form a very clean and uniform system characterized by high carrier mobility, by strong electron–electron interaction, the presence of which leads to a phase transition in the two-dimensional electronic layer to a crystalline state, and by a number of other features that are no less interesting. It is therefore of great interest to produce Q1D and 1D electronic systems over liquid helium in view of all the advantages enjoyed by surface electrons in comparison with low-dimensional systems in semiconductors.

The characteristic of the transport in 1D and Q1D electronic systems differs strongly from that in systems with higher dimensionality, particularly in that localization effects are more clearly manifested in them. In low-dimensional electronic systems over liquid helium the electron gas obeys Boltzmann statistics, so that the magnitude of the electron wave vector varies from large to very small values. This should lead to peculiar features in the localization effects. For electronic systems over liquid helium the characteristics of the interaction of electrons with the scatterers, which are helium atoms in the vapor and thermal excitations of the surface (ripplons), have been well studied. This makes it possible to separate out the dimensional effects quite reliably, and that is another reason for interest in the study of 1D systems over liquid helium.

A previously proposed method of obtaining 1D electronic systems over liquid helium utilizes narrow dielectric strips[1] or metallic wires[2] lying parallel to the surface of the liquid helium at a shallow depth below it. Under the influence of the electrostatic image force due to the dielectric strips or of a positive potential applied to the metal wires, the electrons are concentrated near them, forming a quasi-one-dimensional or one-dimensional system. However, this method has proved to be technically difficult to implement because of the necessity of precision mounting of the strips or wires at a depth of 10^{-5}–10^{-4} cm beneath the surface of the liquid helium and the uncontrolled disruption of the uniformity of the system by the natural roughness of the strip or wire material. In Ref. 3 another method of creating Q1D and 1D electronic systems was proposed, utilizing the curvature of the surface of liquid helium flowing under the influence of capillary forces into a single groove or system of grooves on a dielectric substrate placed at a certain height above the level of the liquid helium. Here a trough or system of troughs with a certain radius of curvature r is formed on the liquid helium surface. A clamping electric field $E_\perp$ collects the electrons at the bottom of the troughs and form a Q1D or 1D electronic system, depending on the values of r and $E_\perp$. Since the electrons in the troughs lie at a large distance from the substrate, the surface roughness of the substrate has prac-

tically no effect on the behavior of the carriers.

Such systems were realized in Ref. 4 and 5 using substrates in the form high-quality glass optical gratings with parallel grooves of different dimensions and with different spacings between grooves, and in Ref. 6 using two Mylar films coming together at a sharp angle and forming a single channel. The carrier transport in such systems has been studied over a wide interval of temperatures, electron concentrations, and clamping electric fields.[7,8]

Only Q1D systems have been obtained with such substrates. This is because glass has a rather large dielectric constant, and the motion of the carriers found in the troughs above massive helium is strongly influenced by the electrons localized at places where the helium film covering is thin. In this case a high mobility of the carriers could be achieved only for wide channels ($\sim 10^{-4}$ cm), where several electrons are usually found in the transverse direction in the channel, while for narrow channels, where the influence of the electrons localized above the film is large, localization processes appeared and the carrier mobility decreased. In the case of a single channel formed by two Mylar films, it was necessary to accumulate a sufficient number of electrons for signal detection, and again a considerable number of electrons was found in the transverse direction in the channel.

A low-dimensional (close to one-dimensional) electronic system in which only one electron was found in the transverse direction was obtained in Refs. 9 and 10. In those studies the grooves into which the helium leaked were made from a dielectric with a smooth surface and a low dielectric constant. This made it possible to collect charge from the helium film coating the substrate by applying a clamping electric field and to obtain a rather pure one-dimensional system.

In this paper we present the results of a detailed study of the kinetic properties of carriers in a 1D electronic system over liquid helium in the temperature interval 0.5–1.6 K at a frequency of 100 kHz in clamping electric fields up to 450 V/cm at different linear densities of the electrons in the conducting channels.

The structure of this article is as follows. In Sec. 1 we describe the experimental cell and present a calculation by which the electron mobility μ and plasma frequency ω_p in the system of conducting channels can be determined from the experimental data on the conductance of the cell. In Sec. 2 the results of measurements of μ and ω_p for a ''clean'' substrate and a substrate with charge and aging-related defects on its surface. The results are analyzed and various mechanisms of carrier transport and localization are discussed in Sec. 3. The main findings of this study are summarized in the Conclusion.

1. EXPERIMENT

The experimental cell, substrate, and measurement technique in this study are analogous to those described in Ref. 9. The experimental cell is shown in Fig. 1a. A dielectric substrate *1* was placed above the measuring electrodes *A*, *B*, and *C*, the dimensions of which were 15.6×9.2, 2×9.2, and 15.6×9.2 mm, respectively. Electrodes *A*, *B*, and *C* were held at zero potential, and a negative potential $V_\perp$ was applied to electrodes *2* and *3*. A negative potential V_g, obeying

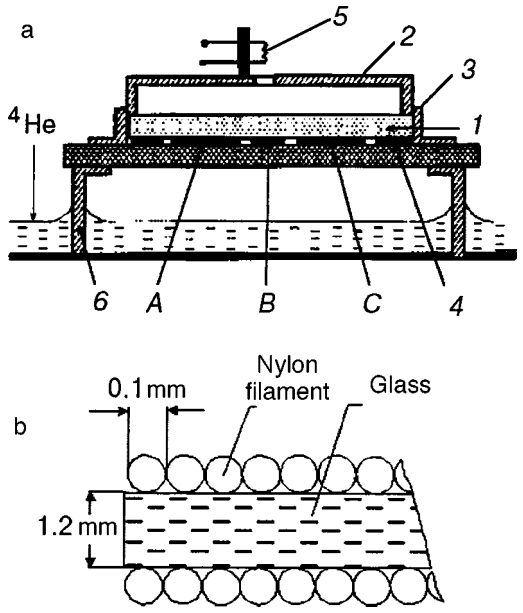

FIG. 1. a: Measurement cell: *1* — substrate; *2,3* — clamping electrodes; *4* — guard electrode; *5* — incandescent filament; *6* — copper core; *A*, *B*, *C* — the measuring electrodes. b: The substrate.

the condition $|V_g|>|V_\perp|$, was applied to the guard electrode *4*. With these provisions an electron spot with rather sharp boundaries could be obtained on the liquid helium surface.

A system of grooves was formed on a dielectric with a low dielectric constant. A nylon filament 0.1 mm in diameter was wound on a glass substrate with dimensions of 24.5×19.1 mm by 1.2 mm thick. Several types of filament were used, and the filament with the smoothest and most defect-free surface was chosen. The substrate was placed in the experimental cell at a certain height H above the liquid helium level. Liquid helium flowed onto the substrate under the influence of capillary and van der Waals forces; the tops of the nylon filaments were covered by a helium film 2.5×10^{-6} cm thick, and troughs of liquid helium formed between filaments (Fig. 1b). The curvature of the liquid helium surface in the troughs depends on H and is given by $r=\alpha/\rho g H$, where α is the surface tension, ρ is the density of the liquid helium, and g is the acceleration due to gravity. The experiments were done for $r=35$ μm. The conducting system consisted of 150 channels.

The dielectric constant of nylon at helium temperatures was determined by extrapolating the values obtained by us at room and nitrogen temperatures and had a value of approximately 1.5.

The calculation done in Ref. 3 shows that electrons collected at the bottom of the liquid channels under the influence of a clamping electric field $E_\perp$ execute oscillatory motion perpendicular to the conducting channels with a frequency determined by $E_\perp$ and r:

$$\omega_0=\left(\frac{eE_\perp}{mr}\right)^{1/2}, \tag{1}$$

where e and m are the charge and mass of an electron. Accordingly, the energy spectrum of the particles is

$$E=(n+1/2)\hbar\omega_0, \tag{2}$$

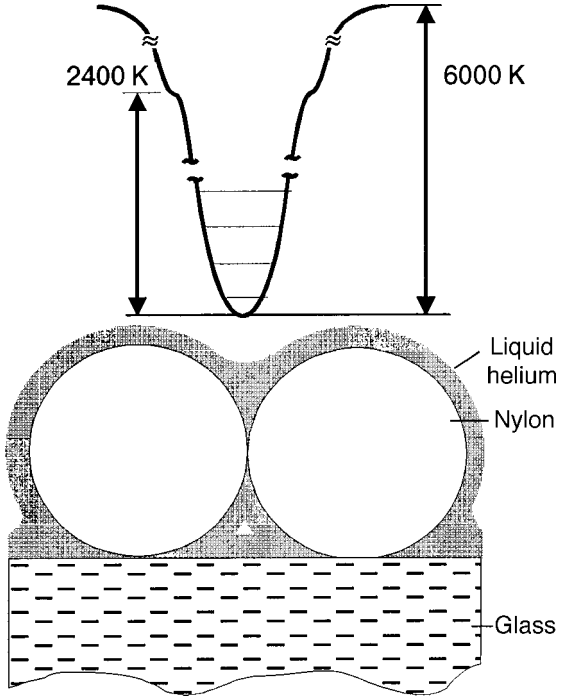

FIG. 2. Schematic illustration of the profile of the potential energy of an electron in a liquid channel at $E_\perp = 450$ V/cm.

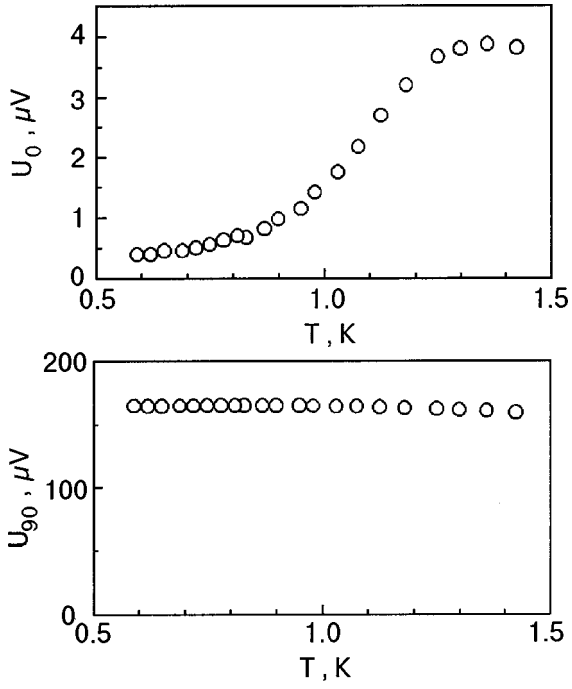

FIG. 3. Temperature dependence of the U_0 and U_{90} components of the signal for a clean substrate.

where $\hbar$ is Planck's constant, and $n = 0, 1, 2, \ldots$.

The form of the potential well in which the electrons are localized and the values of the energy levels for the clamping electric field $E_\perp = 450$ V/cm used in this study are shown in Fig. 2. We see that the potential well in which the electrons are localized is quite deep (~ 6000 K). In the upper part of the well is a discernable feature due to image forces exerted on the electron by the solid substrate at those places where the equilibrium thickness of the film becomes small. We note that there is practically no potential barrier that could confine the electrons above the film. This circumstance makes it possible to remove all of the electrons from the thin layers of the film into the liquid troughs, where the electrons are found above a thick layer of helium and thus to ensure good uniformity of the 1D system in the experiment.

We measured the 0° and 90° components of the electrical signal transmitted through the measuring cell. The generator voltage was applied to electrode *A* and the signal transmitted through the cell was taken from electrode *C*, with the driving electric field $E_\parallel$ directed along the liquid channels. The signal was amplified by a low-noise preamplifier and sent to a synchronous amplifier.

Figure 3 shows the typical temperature dependence of the 0°. (U_0) and 90° (U_{90}) components of the signal transmitted through the electron-charged cell. It is seen that U_0 is rather strongly dependent on the temperature *T*, while U_{90} remains practically constant over the entire temperature interval. The data shown pertain to low linear electron densities n_j in the conducting channels; with increasing n_j and, hence, increasing conductance of the channels, the character of the temperature dependence of U_{90} changes: the value of U_{90} begins to grow as the temperature is lowered.

The values of U_0 and U_{90} obtained can be used to find the real G_r and imaginary G_i parts of the electron-related conductance of the cell. Here we present a calculation of the mobility of the electrons in the conducting channels. The calculation is analogous to that for a two-dimensional electron layer above electrodes of a given configuration.[11] Figure 4 shows schematically the electrodes and the cell (side view) and indicates the notation used in the calculations.

The solution of the electrodynamic problem of the electric field distribution in the experimental cell made it possible to establish the relation between the measured signal and the conductance of the system of parallel channels. It is assumed that an alternating voltage $V_0 \exp(i\omega t)$ is applied to the input electrode. The self-consistent electric field of frequency ω satisfies the equation

$$\operatorname{curl}\operatorname{curl}\mathbf{E} = \frac{\omega^2}{c^2}\mathbf{E}' - \frac{4\pi i\omega}{c^2}\mathbf{J}\delta(z-d), \tag{3}$$

where *c* is the speed of light and **J** is the electron current in the system of conducting channels, located at a distance $z-d$ from the lower electrode. The electron current in the cell can be written in the form

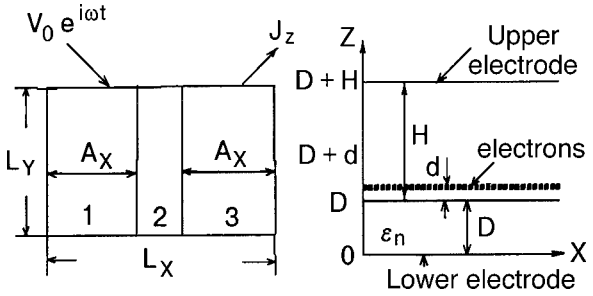

FIG. 4. Schematic illustration of the measuring electrodes.

$$J_x=\sum_{k=1}^{N} j_k f(y-ky_0), \quad j_k=\sigma_k E_x^{d+D}, \quad \sigma_k=n_j e\mu. \tag{4}$$

Here n_j is the one-dimensional density of electrons in the channel: $n_j=N/N_kA_x$, where N is the total number of electrons and N_k is the number of conducting channels in the cell. Using Eq. (3), we obtain an equation for the field E_x along the conducting channels in the cell:

$$\frac{\partial^2 E_x}{\partial x^2}+\frac{\omega^2}{c}E_x=\frac{4\pi i}{\omega}\delta(z-d-D) \times\sum_{k=1}^{N}\left[\frac{\partial^2 j_k}{\partial x^2}+\frac{\omega^2}{c^2}j_i\right]f(y-ky_0). \tag{5}$$

With the boundary conditions on the electric field in the substrate and helium layer, $E_x^{(1)}=E_x^{(2)}|_{z=D+d}$, $E_x^{(2)}=E_x^{(3)}|_{z=D}$, and $E_z^{(2)}|_{z=D}=\varepsilon_n E_z^{(3)}|_{z=D}$, Eq. (5) can be used to find E_x for different values of z and, with the aid of the relation

$$\mathrm{div}\,\mathbf{E}=\frac{\partial E_x}{\partial x}+\frac{\partial E_z}{\partial z}=\frac{4\pi i}{\omega} \times\mathrm{div}\left(\sum_{k=1}^{N} j_k\delta(y-ky_0)\right)\delta(z-d-D) \tag{6}$$

to determine E_z in the cell, including at $z=0$, and, hence, to calculate the current J_z. The expression for the current J_z at the receiving electrode has the form

$$J_z=V_0\exp(i\omega t)(G_r+i\omega G_i). \tag{7}$$

$$G_r=\frac{n_j}{b}e^2\sum_{n,l=1}^{\infty}\Lambda_{nl}\frac{e\omega^2\chi_1\lambda}{(m\omega_p^2-e\omega\chi_2\lambda)^2+(e\omega\chi_1\lambda)^2}; \tag{8}$$

The quantities G_r and G_i can be written as follows:

$$G_i=\frac{n_j}{b}e^2\sum_{n,l=1}^{\infty}\Lambda_{nl}\frac{(m\omega_p^2-e\omega\chi_2\lambda)\omega}{(m\omega_p^2-e\omega\chi_2\lambda)^2+(e\omega\chi_1\lambda)^2}+G_0. \tag{9}$$

Here the quantity G_0 characterizes the impedance of the cell in the absence of electrons; χ_1 and χ_2, which have the meaning of the active and reactive components of the impedance for one electron, are determined by the relation $\mu^{-1}=\chi_1+\chi_2$; b is the distance between channels; ω_p is the frequency of plasma waves propagating in the system of parallel conducting channels. In the calculation it was assumed that the electron density distribution in the direction transverse to the channel is δ-function-like. The parameters Λ_{nl} and λ in expressions (8) and (9) are determined by the geometry of the cell:

$$\Lambda_{nl}=\frac{16\varepsilon_n L_y(-1)^n\sin^2[\pi(A_x/L_x)n]\sinh^2[\pi(H-d)n/L_x]}{\pi^2 L_x(2l-1)^2\Delta_{HD}^2},$$

$$\Delta_{HD}=\varepsilon_n\cosh(q_xD)\sinh(q_xH)+\cosh(q_xH)\sinh(q_xD); \tag{10}$$

$$\lambda=\left[\frac{\pi(2l-1)}{2N_k}\sum_{l,j=1}^{N}\sin\left(j\frac{\pi y_0(2l-1)}{L_y}\right)\right]^{-1}. \tag{11}$$

Here ε_n is the dielectric constant of the substrate, q_x is the wave vector of the plasma waves, and y_0 is the characteristic localization dimension of an electron in the direction transverse to the channel.

In this study we also calculated the frequency ω_p of plasma waves propagating in the system of conducting channels:

$$\omega_p^2(q_x)=\frac{4\pi n_j e^2}{mb}q_x\frac{\Delta_{Dd}}{\Delta_{HD}}\sinh[(q_x(H-d)], \tag{12}$$

$$q_x=\frac{\pi}{L_x}n, \quad n=1,2,3,\ldots$$

$$\Delta_{Dd}=\varepsilon_n\cosh(q_xD)\sinh(q_xd)+\cosh(q_xd)\sinh(q_xD).$$

Estimates show that for the signal frequency used in the experiment, the terms containing χ_2 in expressions (8) and (9) can be neglected. Thus relations (8)–(11) can be used to determine the values of μ and ω_p as adjustable parameters by fitting to the experimental values of G_i and G_r.

The experiment was done as follows. The surface of liquid helium wetting the substrate was charged at a low clamping potential $V_\perp$ (of the order of a few tenths of a volt) by means of a miniature incandescent filament that was briefly turned on. The electrons struck both the surface of the liquid helium between the nylon filaments and the thin helium film at the tops of the filaments. The charging of the liquid helium surface was detected from the change in the measured signal. Then $V_\perp$ was decreased to zero, and the electrons left the massive liquid helium while the electrons above the thin film, which were held by rather strong image forces due to the substrate, remained. The measured signal then recovered to its original value, since the mobility of the electrons localized above the helium film is small and does not contribute to the impedance of the cell.[12] Then, without turning on the incandescent filament, a clamping potential of up to 150 V was applied, causing the electrons found above the helium film to be displaced to the bottom of the liquid troughs. Thereupon the mobility of the electrons sharply increased, and a signal appeared. This procedure made it possible to vary the number of electrons in the conducting channel from a minimum value set by the sensitivity of the apparatus to a very high maximum value set by the instability of the charged helium surface.

This method of charging the liquid channels usually led to high values of the mobility at low temperatures. However, sometimes the electrons in the charging process or upon a too-rapid temperature change reached the substrate. Then the mobility of the electrons at low temperatures turned out to be lower than for the clean substrate, and the decrease in μ was increasingly significant as more charges were found on the substrate. Eventually the substrate itself was damaged, and that also led to a decrease in μ.

To determine the electron mobility it is necessary to know the linear density n_j of electrons in the conducting channel. The technique used to calculate this quantity when the clamping field is compensated by the self-field of the electron layer (saturated case) is described in Ref. 7. In the unsaturated case at relatively high temperatures ($\sim$1.5 K) the value of n_j was determined from the ratio of the resistance of the channels to the resistance in the saturated case.

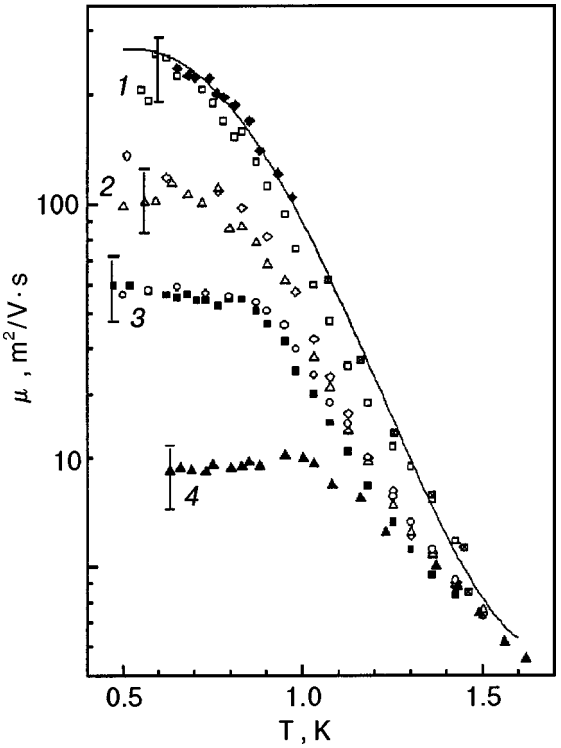

FIG. 5. Temperature dependence of the electron mobility in a 1D system over liquid helium for different states of the substrate: *1* — clean substrate, at the start of a series of measurements for different n_j, 10^3 cm^{-1}: 6.04 (□); 8 (◆); 56 (❖). *2–4* — substrates with charge and defects on the surface for different n_j, 10^3 cm^{-1}: 6.6 (◇); 4.8 (△), 15.04 (■); 6.6 (○); 100 (▲). The solid curve is the theoretical calculation of Ref. 13.

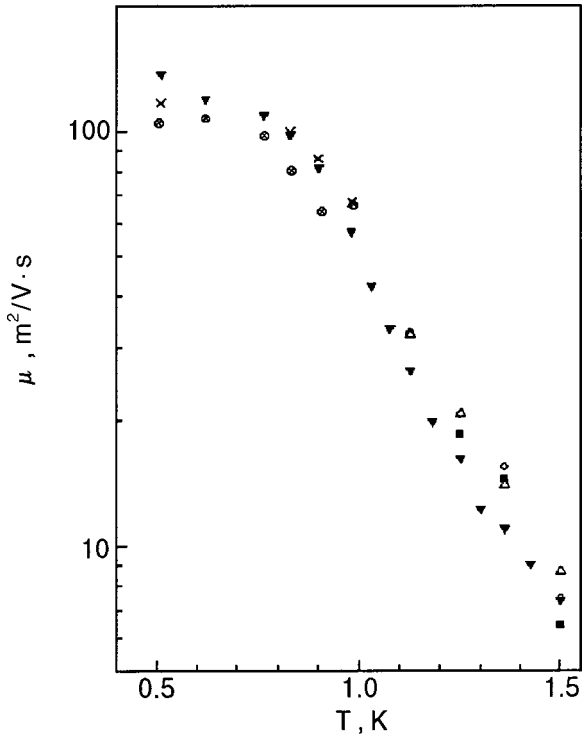

FIG. 6. Frequency of plasma oscillations ω_p as a function of the electron mobility in a 1D system. $T=0.6$ K.

Here the value obtained in Ref. 13 for the electron mobility in a 1D electronic system was used. At $T=1.5$ K the value of μ depends weakly on the clamping field $E_\perp$ and the electron density, so that, by knowing the resistance of the channels, one can determine n_j. The values of n_j determined by these methods agree to an accuracy of 30%. As a rule, in this study we used the second method of determining n_j, which gives substantially more accurate values of this quantity. The values of μ and ω_p were determined to an accuracy of $\sim$20%.

The interval of linear densities in the conducting channels investigated in this study was 5×10^3–2.5×10^4 cm^{-1}, which corresponded to a maximum mean distance between electrons in the channel equal to $a=2\times10^{-4}$ cm.

Thus in this study we realized a system that was close to one-dimensional. The depth of the potential well in which the electrons were localized in the direction perpendicular to the liquid channel was large enough that the electrons could be reliably confined to the bottom of the liquid troughs.

2. EXPERIMENTAL RESULTS

Figure 5 shows the temperature dependence of the electron mobility μ in a 1D electronic system above liquid helium for a clean, uncharged substrate (plot *1*) and for substrates with defects and charge on the surface (plots *2–4*). We see that for all the substrates, μ initially increases quite sharply as the temperature is lowered, and at $T<0.9$ K the mobility for the clean substrate increases more gradually with decreasing T, while that of the charged substrates or substrates containing defects either becomes practically independent of T (plots *2* and *3*) or decreases slightly with decreasing temperature (plot *4*). Interestingly, while at $T\approx1.5$ K the values of the mobility for all the substrates are practically equal, at $T\approx0.5$ K the mobility for the clean substrate is more than an order of magnitude higher than than for the substrate with a large amount of charge (plot *4*). We note that even for $T\approx1.2$ K the mobility for the highly charged substrate is significantly lower than for the clean substrate.

Figure 6 shows the values of the plasma frequency ω_p as a function of the electron mobility, corresponding to the $\mu(T)$ plots in Fig. 5, for substrates of different cleanliness. We see that ω_p is approximately 2.5 times larger for the substrate characterized by the lowest value of μ than for the clean substrate. The values found for ω_p are practically independent of temperature and depend only very weakly on η_j. It was observed experimentally that ω_p increases with increasing numbers of defects and charges on the substrate. It should be noted that the theoretical value of ω_p for $n_j=2.5\times10^3$ cm^{-1}, calculated according to formula (12), is smaller than the experimental value by approximately a factor of three.

Experiments on the measurement of the electron mobility were done in the interval of generator voltages $U_g=2$–200 mV, and no noticeable influence of U_g on the mobility was observed. This circumstance is illustrated in Fig. 7, which shows plots of $\mu(T)$ for different values of U_g. (For $U_g=20$ mV this plot corresponds to the experimental plot *2* in Fig. 5.)

3. DISCUSSION OF THE RESULTS

The electron system investigated in the present study can be used to check the characteristic features of the kinetic properties and localization of the carriers for 1D and Q1D systems.

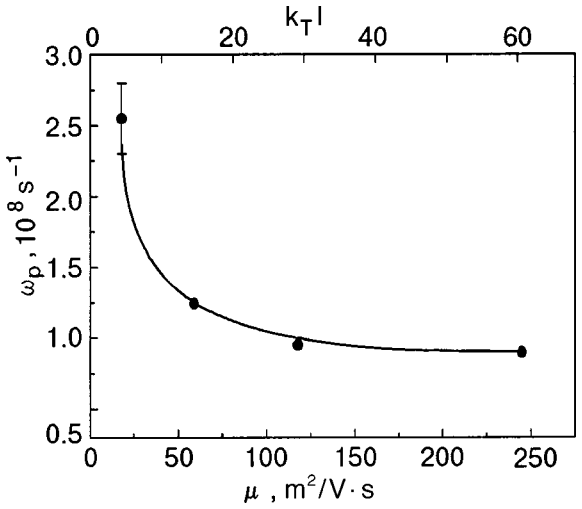

FIG. 7. Temperature dependence of the electron mobility μ for various generator voltages U_g, mV: 2 (×), 20 (▼, ○); 80 (⊗, ■); 200 (△). The carrier concentration $n_j = 4.8\times10^3$ cm^{-1}.

As we have said, in each of the conducting channels the depth U of the potential well typical for the 1D electronic system realized here is 6000 K; at this value the characteristic localization dimension of the electrons in the direction transverse to the channels at the ground-state energy level $y_0=[\hbar/m\omega_0]^{1/2}$ for a clamping electric field $E_\perp = 450$ V/cm is $\sim10^{-5}$ cm; the distance between energy levels is $\Delta E = 0.13$ K. In this case U is much larger than the electron–electron interaction energy U_{ee}. For $a\approx2\times10^{-4}$ cm one has $U_{ee}\approx7$–8 K in the 1D system under study. Thus the ratio $U_{ee}/\Delta E\approx60$; this value is somewhat larger than the analogous value obtained for a two-dimensional electronic system over liquid helium. Unfortunately, the condition $\Delta E > kT$ (where k is Boltzmann's constant) was not satisfied in the experiments, so that the electrons were found not only at the ground-state energy level but also at higher levels. This increased the mean transverse size of the channel. The characteristic localization dimension of electrons found at a level n is $y_n\approx y_0(2n+1)^{1/2}$. Here $y_n\approx3\times10^{-5}$ cm at 0.5 K and $y_n\approx5\times10^{-5}$ cm at $T=1.5$ K.

As we know (see, e.g., Ref. 14), a low-dimensional system is to a good approximation one-dimensional if the distance to which an electron diffuses between inelastic collisions that destroy the coherence of the wave function, $L_{Th} = (v_T\tau_0\tau_{\rm in})^{1/2}$, is much greater than the transverse dimensions of the system (here v_T is the thermal speed of the electron, τ_0 is the relaxation time due to elastic collisions, and $\tau_{\rm in}$ is the relaxation time due to inelastic collisions). We assume that $\tau_{\rm in}$ is of the order of the value of τ determined from the electron mobility data for the clean substrate (Table I), while τ_0 is close to the value of τ determined from the electron mobility data for substrates with surface defects (Table II). As we see from Table II, for plots *3* and *4* in Fig. 5, at $T<1$ K we have $L_{\rm Th}>y_n$, where the quantity on the right characterizes the ''width'' of the conducting channel. We also note that the characteristic localization length ξ, which for 1D systems is taken equal to $3l$ (l is the mean free path),[15] is also greater than y_n, at least for $T<1$ K. Thus one can apparently assume that in its basic properties the investigated system is close to one-dimensional.

TABLE I. Main parameters of a quasi-one-dimensional system above liquid helium in the case of a clean substrate.

	System parameters*		
T, K	μ, m^2/V·s	τ, 10^{-9} s	l, 10^{-4} cm
0.5	250	1.4	3.1
1.0	65	0.37	1.1
1.5	7	0.04	0.15

**Note*: the data are given in Fig. 5 (plot *1*).

We see in Fig. 5 that the electron mobility on a clean substrate at relatively high temperatures increases rapidly as the temperature is lowered. At $T<0.8$ K the change in μ with temperature becomes less steep. This sort of $\mu(T)$ dependence is due to the fact that in the temperature region 0.9–1.5 K the mobility of carriers in a 1D system in the absence of localization, just as in the case of a two-dimensional electronic system over liquid helium, is predominantly determined by scattering on helium atoms in the vapor, the number of which decreases exponentially as the temperature is lowered. At $T<0.8$ K the value of μ is governed by the interaction of the electrons with ripplons.

Theoretically the mobility of carriers in a 1D electronic system in the absence of localization was considered in Refs. 3 and 13. The case in which all the electrons are found at the ground-state energy level was considered in Ref. 3, and in Ref. 13 the influence on the mobility from electrons found at higher energy levels was also taken into account. In Fig. 5 the solid curve gives the results of the calculations of Ref. 13, extrapolated to values of the clamping field $E_\perp = 450$ V/cm. As we see from the figure, the results of the calculation are in good agreement with the experimental data. It should be noted, however, that the calculated curve and experimental data pertain to different values of the radius of curvature r. Nevertheless, it can be supposed that the results of the calculation are not very sensitive to the value of r, since the electrons found at higher energy levels, as in the

TABLE II. The main parameters of a quasi-one-dimensional system over liquid helium for substrates with charge and defects on the surface.

	System parameters									
	Plot *3* in Fig. 5					Plot *4* in Fig. 5				
T, K	μ, m^2/V·s	τ, 10^{-10} s	l, 10^{-5} cm	$L_{\rm Th}$, 10^{-4} cm	k_Tl	μ, m^2/V·s	τ, 10^{-10} s	l, 10^{-5} cm	$L_{\rm Th}$, 10^{-5} cm	k_Tl
0.5	65	3.7	8.1	1.6	15.5	19	1.1	2.4	8.5	4.6
1.0	40	2.3	7.1	0.9	22	20	1.15	3.5	6.3	9.3
1.5	7	0.4	1.5		5	7	0.4	1.5		5

system under consideration, give an appreciable contribution to the total current in the conducting channels. This is indirectly confirmed by the fact that the mobility calculated for a two-dimensional electronic system over liquid helium[16] at the same value of the clamping electric field has approximately the same value.

It was established in Ref. 14 that the carriers in a one-dimensional system must be localized even in a small random potential. In Ref. 17 it was shown that in a sufficiently long 1D system, localization should also occur in the presence of randomly located scattering centers. In our 1D system over liquid helium the electrons are scattered by ripplons and by helium atoms in the vapor. Since the average thermal speed v_T of the electrons is much greater than the velocities of ripplons and helium atoms, one can assume approximately that the electrons are interacting with immobile scatters.

Tables I and II give the mean free paths of electrons in the channels of the 1D system, $l=v_T\tau$, for substrates of different quality (τ is the relaxation time of the electronic system as calculated from the mobility data taken from experimental plots *1–4* in Fig. 5). For plot *1* the mean free path l at temperatures of 0.5 and 1.5 K has the values 3×10^{-4} and 1.5×10^{-5} cm, respectively. Thus localization of the carriers at ripplons and at helium atoms in the vapor must occur at extremely short distances in the system under study. Meanwhile, the data on the mobility and the character of its temperature dependence, which are in good agreement with the theoretical calculation,[13] do not permit the conclusion that the localization of the carriers occurs even in the high-temperature region, where scattering on helium atoms in the vapor is particularly intense.

It can be assumed that the absence of localization is due to the fact that in the given system the scattering of electrons involves transitions from one energy level to another. Such scattering, being in essence inelastic, can destroy the coherence of the wave function and lead to delocalization of electrons moving along the conducting channels. The characteristic times for interlevel transitions of electrons in their interaction with helium atoms in the vapor and with ripplons have not been studied either experimentally or theoretically. However, it can be supposed that those times should be close to the relaxation time of electrons in a 1D system over liquid helium for a clean substrate. This is because the transport characteristics also depend on interlevel transitions.[13]

In order for localization of carriers moving in a random potential to occur, it is necessary that the time for changes in the phase of the wave function of the moving particle, τ_φ, which is determined by the relaxation time due to inelastic processes, τ_{in}, be much longer than the relaxation time due to elastic processes, τ_0: $\tau_\varphi, \tau_{\text{in}} > \tau_0$. In Ref. 18, which investigated the localization of a nondegenerate electron gas over a solid hydrogen substrate in the presence of substrate roughness giving rise to a random potential, it was found that for $\tau_{\text{in}}/\tau_0 < 2$ localization of carriers was largely suppressed. In our study in the case of a clean substrate, we apparently have $\tau_{\text{in}} \approx \tau_0$, a circumstance that probably leads to suppression of localization here, too. It is also possible that if localization does occur, the energy of the localized state is low, and such states are destroyed by temperature fluctuations.

As we have said, in the case when the substrate contains defects or has charges on its surface, the character of the temperature dependence of the mobility changes. While at relatively high temperatures the quality of the substrate has practically no effect on the value of μ, at $T\approx0.5$ K a given decrease in the carrier mobility is observed for substrates with charge or defects (Fig. 5). This effect may be due to either the presence of a comparatively small number of traps, which trap a portion of the electrons and thereby lower the number of carriers contributing to the conductance of the system, or to additional scattering of electrons on the random potential and localization of the carriers directly in the 1D system. We assume that the lowering of the mobility in our case is due to additional scattering and localization of carriers in the liquid channels by the random potential that arises on account of the presence of defects or localized charge on the solid substrate. Here the variations of the potential due to the electrons localized on the substrate are estimated to be small compared to kT.

Unfortunately, we do not know the basic characteristics of the potential that arises on the substrate. Experiments have established that the more highly charged the substrate, the lower the carrier mobility. Furthermore, it has become clear that the substrate quality is degraded over time, probably because of the procedure of vacuum pumping with heating which was done from time to time for cleaning of the cell. At the end of a series of experiments it was no longer possible to obtain high values of the mobility. In an analysis of the substrate quality it was found that the surface of the nylon filaments making up the substrate became rough, and transverse cracks and dents ~1 μm in size appeared on them. Apparently it is these defects and the electrons localized on the substrate that are responsible for the random potential along the conducting channels. The substrate quality can probably be judged from the value of the mobility: the lower the mobility, the poorer the quality of the substrate and the larger the variations of the amplitude of the random potential.

Our experiments made it possible to separate out the influence of the random potential on the carrier mobility in a 1D electronic system. We assume additivity of the contributions to the scattering of electrons on helium atoms in the vapor and on ripplons and also of the processes by which the random potential limits the motion of the carriers. Then the experimental value of the mobility μ for the substrate with charge and defects on the surface is given by the expression $\mu^{-1}=\mu_c^{-1}+\mu_{rp}^{-1}$, where μ_c is the electron mobility for the clean substrate, and μ_{rp} is the mobility limited by the influence of the random potential.

Figure 8 shows the temperature dependence of μ_{rp} calculated with the use of the smoothed experimental plots *1–4* in Fig. 5. Unfortunately, the accuracy with which μ_{rp} is determined, indicated by the error bars, is low, especially for $T\approx1.5$ K, but one can nevertheless see that within the error limits of the calculation for plots *1* and *2* in Fig. 8 there is a slight growth of the mobility as the temperature is lowered, whereas for plot *3* there is a clearly visible decrease in μ_{rp} with decreasing T.

The random potential along each of the conducting channels clearly comprises a system of potential wells and barriers. The 1D system under discussion has the feature that it

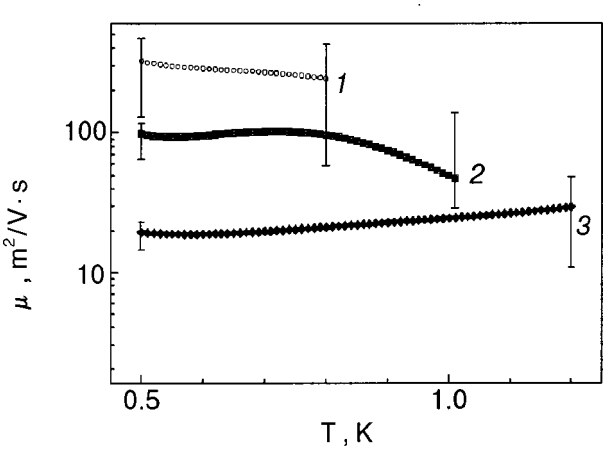

FIG. 8. Temperature dependence of μ_{rp} for the data corresponding to plots *2*, *3*, and *4* in Fig. 5.

permits varying the linear density of the carriers over wide limits, and one can realize the case when n_j is less than the number of potential wells, n_n, and also the condition when $n_j > n_n$.

The characteristic of the carrier motion in a 1D channel should depend strongly on whether a localization of the carriers occurs or if the influence of the random potential reduces merely to the appearance of an additional scattering mechanism. We assume that for the experimental plot *2* in Fig. 5 and, accordingly, for plot *1* in Fig. 8 only an additional scattering on the random potential is observed, while for experimental plots *3* and *4* in Fig. 5 and, accordingly, plots *2* and *3* in Fig. 8, a localization of the carriers occurs.

This assumption is based on an analysis of the behavior of the plasma frequency ω_p for the substrates with charge and defects on the surface. We note that ω_p, determined as an adjustable parameter in a fit of the experimental data, has the meaning of a certain averaged frequency of plasma waves propagating along the channels. We note that for the clean substrate the value of ω_p is greater than its theoretical value calculated according to formula (12). We assume that this is due to the dividing of the conducting channels into shorter segments on account of the imperfection of the substrate; estimates show that in this case the average effective length L_{eff} of the liquid channel for ensuring the necessary increase in the plasmon wave vector q_x is around 2.2 mm. Of course, L_{eff} is actually different for different channels, and the spread in values can be large. Therefore, ω_p for each such channel can also be different, a circumstance that apparently makes it impossible to measure by resonance methods. Nevertheless, we assume that one can speak of a certain average value of ω_p that is determined by the average value of L_{eff} over all of the channels.

As we have shown previously, for two-dimensional[19] and quasi-one-dimensional[7] electronic systems over liquid helium the value of ω_p should increase in the case of localization of the electrons on account of the appearance in the plasma wave spectrum of an optical mode due to vibrations of the localized electrons. In this case the plasmon dispersion relation has the form

$$\omega_p^2 = \omega_\alpha^2 + \omega_p^2(q_x), \tag{13}$$

where ω_α is the frequency of oscillation of the electron in the potential well, $\omega_p(q_x)$ is the plasma frequency given by expression (12). It is seen in Fig. 6 that at large values of μ the value of ω_p is independent of μ. This corresponds to nonlocalized motion of the electrons; when μ is decreased from 100 to 20 $\text{m}^2/\text{V}\cdot\text{s}$ the value of ω_p increases by approximately a factor of 2.5. The value of ω_p is determined to within an error of $\sim 20\%$, as we have said, so that the fact that ω_p increases, which follows from Fig. 6, is apparently quite reliably established. The increase in ω_p together with the substantial decrease in the mobility is probably a consequence of carrier localization. The upper scale in Fig. 6 gives the value of $k_T l$ (k_T is the electron wave vector corresponding to the thermal speed). We see that the increase of ω_p starts at values $k_T l < 20$. This suggests that the carrier localization in the system under study is manifested beginning at values $k_T l \sim 15$–20, which are greater than the value $k_T l \sim 1$ at which carrier localization begins in a two-dimensional nondegenerate electron gas over solid hydrogen.[18] The increase in ω_p, together with the substantial decrease in mobility, is apparently a consequence of carrier localization.

In Ref. 20, which investigated localization of a two-dimensional nondegenerate electron gas, it was assumed that all of the electrons with energies lower than a certain boundary energy E_c are localized, while electrons with energies above E_c are delocalized and contribute to the conductance. According to Ref. 20, the value of E_c is given by the relation $E_c \approx \hbar/2\tau_0 \ln(\tau_{\text{in}}/\tau_0)$. Using this formula, we obtain a value $E_c = 20$ mK for plot *4* in Fig. 5. Since this is much lower than the temperature at which the experiments were done, that model, which was developed for describing localization in two-dimensional systems, is inapplicable for explaining the results in the investigated 1D system.

It was shown in Ref. 21 that the conductance in a 1D electronic system in the case of localization in sufficiently deep potential wells is of a hopping character and at low temperatures can be described as $A\exp(-B/T)$, where A and B are constants. In Figs. 5 and 8 (plots *3*, *4* and *2*, *3*, respectively), however, it is seen that the experimental data reflects the temperature independence or extremely weak temperature dependence of the combination in a 1D system over liquid helium for $T < 1$ K. We assume that because the variations of the random potential in the given system obey $\delta V_{rp} \ll kT$, the particles undergo a diffusive motion stimulated by ripplons, with hops from one localized state to another, with the mobility given by the expression $\mu_l = (e/kT) l^2 \nu_r$, where ν_r is a certain characteristic ripplon frequency for the given temperature. This frequency is analogous to the characteristic phonon frequency that underlies the carrier hopping mechanism in disordered three-dimensional and two-dimensional media. Assuming that ν_r is proportional to T, we find that μ_l should depend on temperature only through the temperature dependence of l, which is relatively weak for $T < 1$ K. Taking $\nu_r \approx 10^{10}$ s^{-1}, we find that the value of μ_l at $T \approx 0.5$ K is equal to 13.5 and 155 $\text{m}^2/\text{V}\cdot\text{s}$, for experimental plots *3* and *4* in Fig. 5 and *2* and *3* in Fig. 8, respectively. Here it is necessary to keep in mind that the electrons localized in the random potential ''poke'' microscopic craters beneath them[12] (an analog of the polaron effect), and this in itself complicates the treatment of the

transport phenomenon. It should also be taken into account that the study under study is characterized by a strong unscreened Coulomb interaction, which can have an appreciable effect on the character of the localization processes. Unfortunately, at present there is no theory describing the transport of localized carriers in a 1D electronic system over liquid helium.

Using (13) and the experimental data on ω_p for a clean substrate and for substrates with charge and defects on the surface, one can determine ω_α and the electron localization length $l_0=[\hbar/m\omega_0]^{1/2}$ corresponding to the given frequency. The value of l_0 for plots *3* and *4* in Fig. 5 is equal to 1×10^{-4} and 8×10^{-5} cm, respectively, which are close to the value of ξ determined from the formula $\xi=3l$.

CONCLUSION

In summary, in this study we have made measurements of the electron mobility in a one-dimensional electronic system over liquid helium. We have shown that for a clean substrate the mobility of the carriers, which is determined by their interaction with helium atoms in the vapor and with ripplons, agrees satisfactorily with the theoretical calculation done on the assumption that localization is not present. It is conjectured that for a clean substrate the inelastic collision time of the electrons and the times for interlevel transitions turn out to be approximately equal to the relaxation time; this leads to suppression of localization. We have shown that the mobility decreases for substrates with charge or defects on the surface, while the frequency of plasma waves propagating in a system of parallel channels increases. The observed effects may be explained by localization in the one-dimensional electronic system in the random potential and by the diffusive motion of carriers with hops from one localized state to another.

The experiments will be continued in magnetic fields and extended to lower temperatures.

The authors thank V. N. Grigor'ev for interest in this study and a discussion of the results.

*E-mail: nikolaenko@ilt.kharkov.ua

[1] V. L. Ginzburg and Yu. P. Monarkha, Fiz. Nizk. Temp. **4**, 1236 (1978) [Sov. J. Low Temp. Phys. **4**, 580 (1978)].
[2] A. V. Chaplik, JETP Lett. **31**, 252 (1980).
[3] Yu. Z. Kovdrya and Yu. P. Monarkha, Fiz. Nizk. Temp. **12**, 1011 (1986) [Sov. J. Low Temp. Phys. **12**, 571 (1986)].
[4] Yu. Z. Kovdrya and V. A. Nikolaenko, Fiz. Nizk. Temp. **18**, 1278 (1992) [Low Temp. Phys. **18**, 894 (1992)].
[5] H. Yayama and A. Tomokiyo, Czech. J. Phys. **46**, 353 (1996).
[6] O. I. Kirichek, Yu. P. Monarkha, Yu. Z. Kovdrya, and V. N. Grigor'ev, Fiz. Nizk. Temp. **19**, 458 (1993) [Low Temp. Phys. **19**, 323 (1993)].
[7] V. A. Nikolaenko, H. Yayama, Yu. Z. Kovdrya, and A. Tomokiyo, Fiz. Nizk. Temp. **23**, 642 (1997) [Low Temp. Phys. **23**, 482 (1997)].
[8] Yu. Z. Kovdrya, V. A. Nikolaenko, H. Yayama, A. Tomokiyo, O. I. Kirichek, and I. B. Berkutov, J. Low Temp. Phys. **110**, 191 (1998).
[9] Yu. Z. Kovdrya, V. A. Nikolaenko, S. P. Gladchenko, and S. S. Sokolov, Fiz. Nizk. Temp. **24**, 1113 (1998) [Low Temp. Phys. **24**, 837 (1998)].
[10] Yu. Z. Kovdrya, V. A. Nikolaenko, S. P. Gladchenko, and S. S. Sokolov, J. Low Temp. Phys. **113**, 1109 (1998).
[11] V. A. Buntar, V. N. Grigorev, Yu. P. Monarkha, Yu. Z. Kovdrya, and S. S. Sokolov, J. Low Temp. Phys. **79**, 323 (1990).
[12] Yu. Z. Kovdrya, F. F. Mende, and V. A. Nikolaenko, Fiz. Nizk. Temp. **10**, 1129 (1984) [Sov. J. Low Temp. Phys. **10**, 589 (1984)].
[13] S. S. Sokolov, Guo-Giang Hai, and N. Studart, Phys. Rev. B **5**, 5977 (1995).
[14] N. F. Mott and E. A. Davis, *Electronic Processes in Non-Crystalline Materials* [Clarendon Press, Oxford (1971); Mir, Moscow (1982)].
[15] P. M. Lee and T. V. Ramakrishna, Rev. Mod. Phys. **57**, 287 (1985).
[16] Yu. P. Monarkha, Fiz. Nizk. Temp. **2**, 1232 (1976) [Sov. J. Low Temp. Phys. **2**, 600 (1976)].
[17] R. E. Borland, Proc. R. Soc. London, Ser. A **274**, 529 (1966).
[18] Ph. Adams and M. Paalanen, Phys. Rev. Lett. **57**, 2106 (1987).
[19] E. Y. Andrey, Phys. Rev. Lett. **52**, 1449 (1984).
[20] M. J. Stephen, Phys. Rev. B **36**, 5663 (1987).
[21] J. Kurkiyarvi, Phys. Rev. B **7**, 922 (1973).

Translated by Steve Torstveit

SUPERCONDUCTIVITY, INCLUDING HIGH-TEMPERATURE SUPERCONDUCTIVITY

Modeling of tunneling spectroscopy in high-T_C superconductors

Yu. M. Shukrinov*

Institute for Advanced Studies in Basic Sciences, Gava Zang, Zanjan 45195-159, Iran
Physical Technical Institute of Tajik Academy of Sciences, 299/1 Aini St., Dushanbe, 734063, Tajikistan, C.I.S.

A. Namiranian and A. Najafi

Institute for Advanced Studies in Basic Sciences, Gava Zang, Zanjan 45195-159, Iran
(Submitted July 11, 2000)
Fiz. Nizk. Temp. **27**, 15–23 (January 2001)

The tunneling density of states of high-T_c superconductors is calculated taking into account the tight-binding band structure, group velocity, and tunneling directionality for *s*-wave and *d*-wave gap symmetry. The characteristic density of states has asymmetry of the quasiparticle peaks, flat *s*-wave and cusplike *d*-wave subgap behavior, and an asymmetric background. It is assumed that the underlying asymmetry of the conductance peaks is primarily due to the features of the quasiparticle energy spectrum and that the *d*-wave symmetry enhances the degree of asymmetry of the peaks. Increasing the lifetime broadening factor changes the degree of asymmetry of the tunneling conductance peaks and leads to confluence of the quasiparticle and van Hove singularity peaks. © *2001 American Institute of Physics.*
[DOI: 10.1063/1.1344137]

INTRODUCTION

Tunneling measurements on high-T_c superconductors (HTSCs) have revealed a rich variety of properties and characteristics.[1–4] They may be classified according to their low- and high-energy features. The low-energy features include: (i) variable subgap shape of the conductance, ranging from a sharp, cusplike to a flat, BCS-like feature;[1] (ii) voltage and temperature dependence of the quasiparticle conductivity;[5,6] (iii) subgap structure;[2] (iv) zero-bias conductance peak (ZBCP).[7] The high-energy features include: (i) asymmetry of the conductance peaks;[1] (ii) van Hove singularity (VHS); (iii) conductance shape outside of the gap region (background (BG)) and its asymmetry;[1] (iv) dip feature;[8] (v) hump feature.[8] These features are collected schematically in Fig. 1. While tunneling spectroscopy on conventional superconductors allows one to find the energy gap of the superconductor directly, the same measurements in HTSCs are not as easily interpreted. Sometimes the same experiments on the same samples show different results:[9] a cusplike or flat subgap feature; symmetric or asymmetric conductance peaks. Usually the sharpest gap features are obtained when the BG is weakly decreasing. A quantitative measure of it is the ratio of the conductance peak height (PH) to the background conductance: PHB=PH/BG. When the BG conductance is decreasing, the PHB$>$2, but when the BG conductance is linearly increasing ($\sim V$), PHB$<$2. Kouznetsov and Coffey[10] and Kirtly and Scalapino[11] suggested that the linearly increasing BG arises from inelastic tunneling. As was mentioned in Ref. 1, the conductance is dominated by quasiparticle tunneling, and the effect of Andreev reflection is not significant. A theoretical model for tunneling spectroscopy employing tight-binding band structure, $d_{x^2-y^2}$ gap symmetry, group velocity, and tunneling directionality was studied by Yusof, Zasadzinski, Coffey, and Miyahawa.[1] An angle-resolved photoemission spectroscopy (ARPES) band structure specific to optimally-doped BSCCO (Bi-2212) was used to calculate the tunneling density of states for a direct comparison to the experimental tunneling conductance. This model produces an asymmetric, decreasing conductance background, asymmetric conductance peaks, and variable subgap shape, ranging from a sharp, cusplike to a flat, BCS-like feature. A standard technique in analyzing the tunneling conductance is to use a smeared BCS function

$$N(E)=N(0)\frac{E-i\Gamma}{\sqrt{(E-i\Gamma)^2-\Delta^2}}, \tag{1}$$

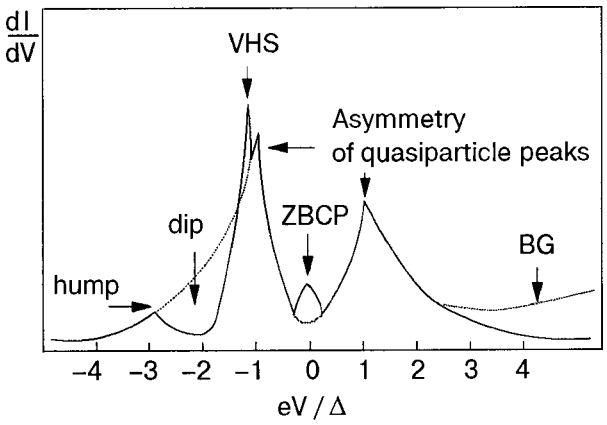

FIG. 1. Schematic dI/dV characteristics of an NIS structure, showing the main features.

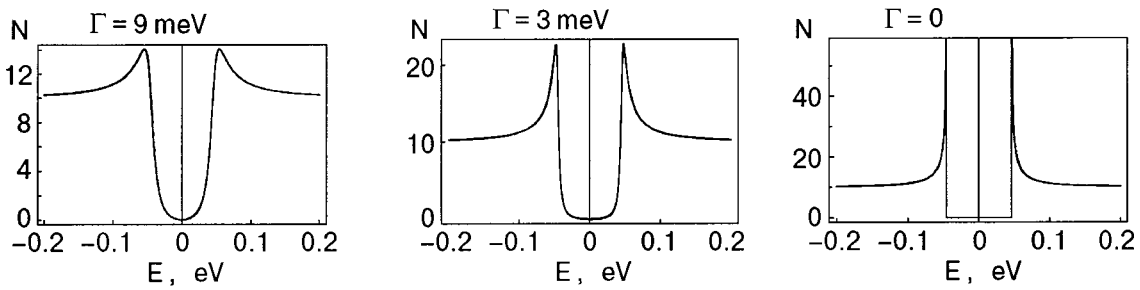

FIG. 2. The *s*-wave DOS calculated by formula (1) for $\Delta = 46$ meV and different values of Γ.

in which a scattering rate parameter (lifetime broadening factor) Γ is used to take into account any broadening of the gap region in the DOS. Figure 2 shows the DOS calculated by formula (1) for $\Delta = 46$ meV and $\Gamma = 9$ meV (a), $\Gamma = 3$ meV (b), and $\Gamma = 0$ (c). A characteristic feature of the DOS is the flat subgap structure for small Γ. This method cannot explain the asymmetry of the conductance peaks observed in the tunneling experiments.

In the case of *d*-wave symmetry we have

$$N(E) = N(0)\mathrm{Re}\int_0^{2\pi} \frac{d\phi}{2\pi} \frac{E - i\Gamma}{[(E - i\Gamma)^2 - \Delta_0^2 \cos^2(2\phi)]^{1/2}}, \tag{2}$$

and the DOS calculated by this formula are presented in Fig. 3. A characteristic feature of the DOS is the cusplike subgap structure. As was mentioned in Ref. 1, this standard technique requires that the comparison be made with normalized tunneling conductance data, and since HTSC tunneling conductance can exhibit a varied and complex background shape, this procedure may ''filter out'' too much information from the conductance data. An alternative is to simply normalize the data by a constant.

In Ref. 8 the tunneling data were first normalized by constructing a ''normal state'' conductance obtained by fitting the high-bias data to a third-degree polynomial. The normalized conductance data were compared to a weighted momentum-averaged *d*-wave DOS:

$$N(E) = \int f(\phi) \frac{E - i\Gamma}{[(E - i\Gamma)^2 - \Delta_0^2 \cos^2(2\phi)]^{1/2}} d\phi. \tag{3}$$

Here $f(\phi)$ is an angular weighting function that allows for a better fit with the experimental data in the gap region. A weighting function $f(\phi) = 1 + 0.4\cos(4\phi)$ was used, which imposes a preferential angular selection of the DOS along the absolute maximum of the *d*-wave gap and tapers off towards the nodes of the gap. This is a rather weak directional function, since the minimum of $f(0)$ along the nodes of the *d*-wave gap is still non-negligible.[8]

Fedro and Koelling[12] have done a modeling of the normal-state and superconducting DOS of HTSCs, using a tight-binding band structure and including the next-nearest neighbors:

$$\xi_k = -2t[\cos(k_x a) + \cos(k_y a)] + 4t' \cos(k_x a)\cos(k_y a) - \mu. \tag{4}$$

The calculation showed two singularities in the DOS: a van Hove singularity at the center of the energy band due to a saddle point near $(\pi, 0)$ for $t' = 0$, and another at the lower edge of the energy band due to extra flattening out at (0,0). Both extended *s*-wave and *d*-wave superconducting DOS were considered in the hole-doped case ($\mu < 0$) for different hole concentrations. The Fermi surface for $t' = 0$ and $t' = 0.45t$ at the same concentration that was used in Ref. 12 corresponding to $\mu/2t = -0.187$, are presented in Fig. 4a. One must move up from the Fermi surface (set as the zero of energy) to reach the point $(\pi, 0)$ in the case $t' = 0$ and move down in the case $t' = 0.45t$. Thus for $t' = 0$ the Fermi energy lies to the left of the van Hove singularity and will move away from it with increased hole doping, while for $t' = 0.45t$ it lies to the right and will move towards it with increased hole doping (see Fig. 4b, where the DOS for $t' = 0$ and $t' = 0.45t$ are presented). For calculation of the superconducting DOS Fedro and Koelling used the formula

$$N(E) = \frac{1}{2}\sum_k \left(1 + \frac{\xi_k}{E_k}\right)\delta(E - E_k) + \left(1 - \frac{\xi_k}{E_k}\right)\delta(E + E_k). \tag{5}$$

This formula is the limit of the expression for the tunneling density of states (6) at $\Gamma = 0$ and $|T_k|^2 = 1$, where T_k is

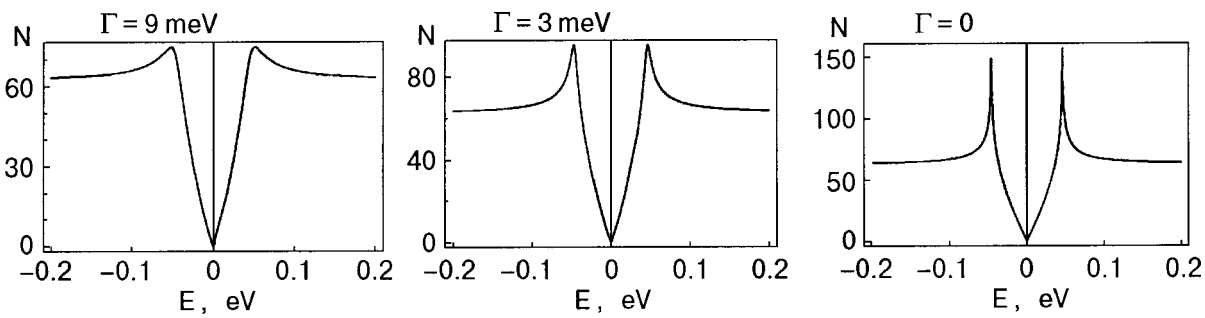

FIG. 3. The *d*-wave DOS calculated by formula (2) for $\Delta = 46$ meV and different values of Γ.

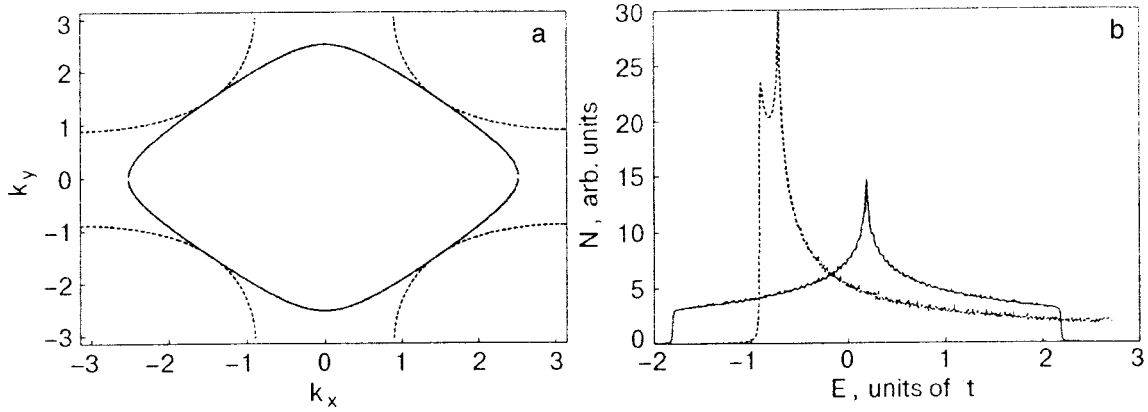

FIG. 4. Fermi surfaces (a) and DOS (b) for $t'=0$ (solid lines) and $t'=0.45t$ (dashed lines) in formula (4) at $\mu/2t=-0.187$, which corresponds to the hole-doped situation.

the tunneling matrix element. Figure 5a shows the results of the calculation of the DOS for $t'=0$ at $\Gamma=0.07$, 0.1, and 0.2 meV for *s*-wave symmetry, reflecting the results of Fedro and Koelling. Figure 5b shows the same DOS for *d*-wave symmetry. In both cases the Fermi energy (set as the zero of energy) lies to the left of the van Hove singularity. There is asymmetry of the peaks, which is more pronounced at large Γ.

MODELS AND METHODS

In the present paper we use the method for calculation of the DOS in Ref. 1. The tunneling DOS of a superconductor is determined by the imaginary part of the retarded single-particle Green's function,

$$N(E)=-\frac{1}{\pi}\mathrm{Im}\sum_k |T_k|^2 G^R(k,E). \tag{6}$$

For the superconducting state

$$G^R(k,E)=\frac{u_k^2}{E-E_k+i\Gamma}+\frac{v_k^2}{E+E_k+i\Gamma}, \tag{7}$$

where u_k^2 and v_k^2 are the usual coherence factors,

$$u_k^2=\frac{1}{2}\left(1+\frac{\xi_k}{E_k}\right), \quad v_k^2=\frac{1}{2}\left(1-\frac{\xi_k}{E_k}\right), \tag{8}$$

and Γ is the quasiparticle lifetime broadening factor. The energy spectrum of quasiparticles in the superconducting state is determined by

$$E_k=\sqrt{|\Delta(k)|^2+\xi_k^2} \tag{9}$$

with the effective band structure extracted from ARPES experiments,[13]

$$\begin{aligned}\xi_k=&C_0+0.5C_1[\cos(k_x a)+\cos(k_y a)]\\&+C_2\cos(k_x a)\cos(k_y a)+0.5C_3[\cos(2k_x a)\\&+\cos(2k_y a)]+0.5C_4[\cos(2k_x a)\cos(k_y a)\\&+\cos(k_x a)\cos(2k_y a)]+C_5\cos(2k_x a)\cos(2k_y a).\end{aligned} \tag{10}$$

Here ξ_k is measured with respect to the Fermi energy ($\xi_k=0$), and the phenomenological parameters are (in units of eV) $C_0=0.1305$, $C_1=-0.5951$, $C_2=0.1636$, $C_3=-0.0519$, $C_4=-0.1117$, and $C_5=0.0510$.

Figure 6 shows the three-dimensional image of function (10). There are a saddle point at $(\pi, 0)$ and a flattening out of the energy band at (0,0), which lead to the van Hove singularities in the DOS. The three-dimensional graph of the coherence factor u_k^2 is shown in Fig. 7.

Since quasiparticles with momentum perpendicular to the barrier interface have the highest probability of tunnel-

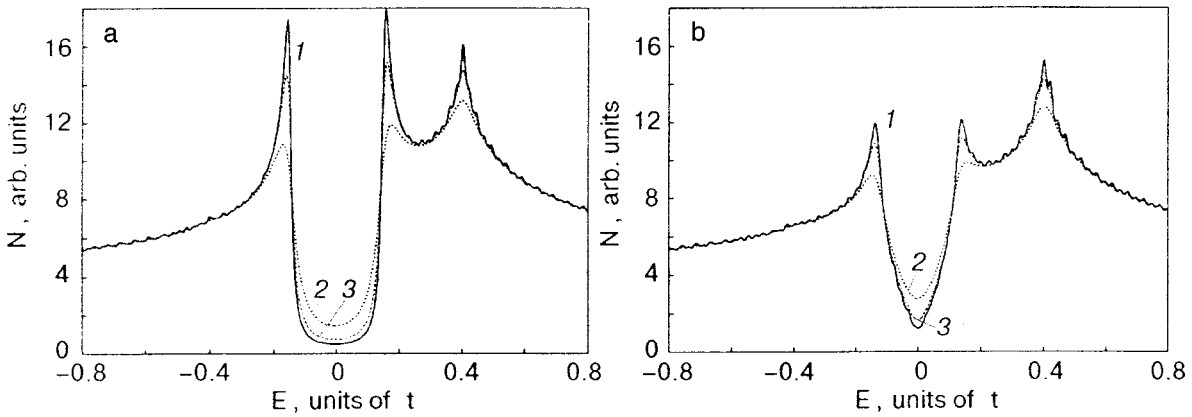

FIG. 5. DOS for $t'=0$ at different Γ for *s*-wave symmetry (a) and *d*-wave symmetry (b), calculated by formula (5). Curves *1, 2, 3* correspond to the Γ equal 0.07, 0.1, and 0.2, respectively.

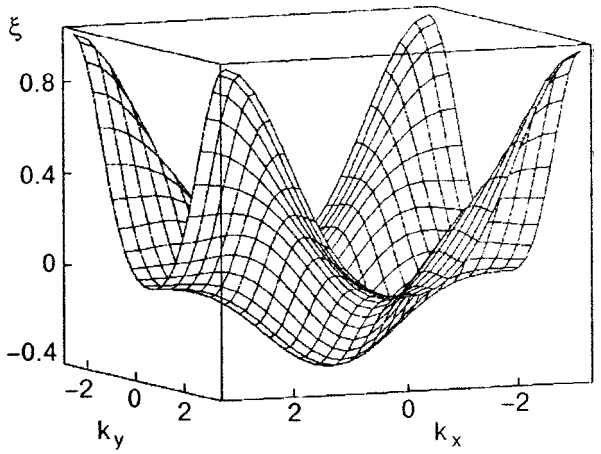

FIG. 6. 3D plot of energy spectrum of the normal state, according to formula (9).

ing, the tunneling matrix element $|T_k|^2$ reveals a need for factors of directionality $D(k)$ and group velocity $v_g(k)$.[1] The group velocity factor is defined by

$$v_g(k)=|\nabla_k \xi_k \cdot \hat{\mathbf{n}}|=\left|\frac{\partial \xi_k}{\partial k_x}\cos\theta+\frac{\partial \xi_k}{\partial k_y}\sin\theta\right|, \tag{11}$$

where the unit vector $\mathbf{n}$ defines the tunneling direction as shown in Fig. 8, which is perpendicular to the plane of the junction.

The directionality function $D(k)$ is defined by

$$D(k)=\exp\left[-\frac{k^2-(\mathbf{k}\cdot\hat{\mathbf{n}})^2}{(\mathbf{k}\cdot\hat{\mathbf{n}})^2\theta_0^2}\right]. \tag{12}$$

Here θ_0 defines the angular spread of the quasiparticle momentum corresponding to non-negligible tunneling probability with respect to $\hat{\mathbf{n}}$. The tunneling matrix element $|T_k|^2$ is written as

$$|T_k|^2=v_g(k)D(k). \tag{13}$$

The three-dimensional graphs of the group velocity $v_g(k)$, directionality $D(k)$, and tunneling matrix element $|T_k|^2$ functions are shown in Fig. 9.

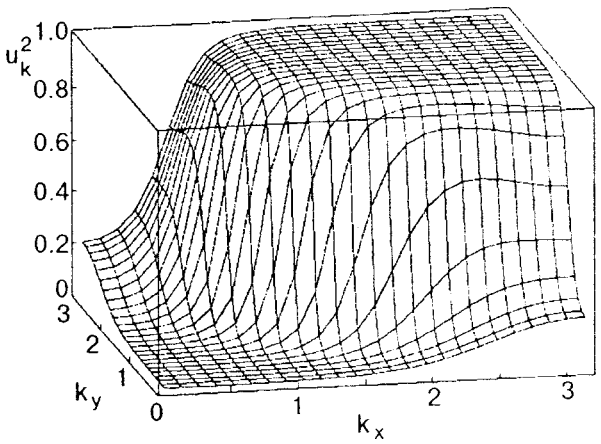

FIG. 7. 3D plot of the coherence factor u_k^2 according to formula (8).

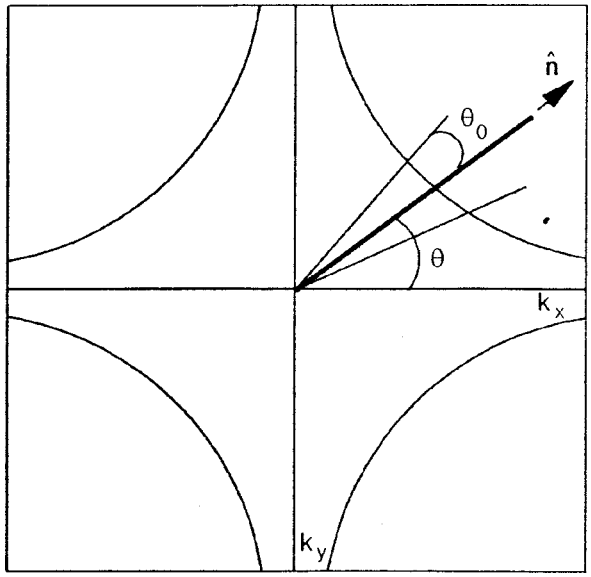

FIG. 8. Fermi surface corresponding to the $\xi_k=0$ in formula (10). The heavy straight line shows the line of directional tunneling, and the lighter lines show the angular spread θ_0.

RESULTS AND DISCUSSIONS

Different factors may lead to the changing of the energy gap Δ_0 in HTSC. In particular, strong effects are caused by nonmagnetic impurities.[14] In superconductors with *d*-wave symmetry the nonmagnetic impurities destroy the superconductivity very efficiently. The possibility of destruction of Cooper pairs by impurities leads to their finite lifetime. If the state with the quasiparticle is not a stationary state, it must attenuate with time due to transitions to other states. The corresponding wave function has the form $\exp(-i\xi(p)t/\hbar - \Gamma t/\hbar)$, where Γ is proportional to the probability of the transitions to the other states. It may be interpreted as an imaginary addition $-i\Gamma$ to the energy of the quasiparticle. The relation between Γ and lifetime of quasiparticle τ_s is $\Gamma = \hbar/\tau_s$. Hence, the impurities lead to a change of Δ_0, and we can model the influence of impurities on the tunneling conductance by numerical calculations of the DOS $N(E)$ considering different values of Δ_0 in formula (6). Here we present the results of a calculation of $N(E)$ at $\Delta_0=\alpha\Delta_{00}$, where $\alpha=0.2$, 0.4, 0.6, 0.8, 1 and $\Delta_{00}=46$ meV.

The peculiarities of the quasiparticle energy spectrum (10) play an essential role in the explanation of the conductance features. Here, based on the numerical calculations of the DOS, we consider that the underlying asymmetry of the conductance peaks is primarily due to the features of the quasiparticle energy spectrum. The *d*-wave gap symmetry simply enhances the degree of the asymmetry of the peaks. This last is also changed by varying the tunneling direction.

Figure 10 shows the results of the numerical calculations of the DOS at $\Gamma_0=3$ meV (a,c) and $\Gamma_0=9$ meV (b,d) without the group velocity and directionality effects for both *s*-wave (a,b) and *d*-wave (c,d) gap symmetry, respectively, for different values of the energy gap Δ_0. We have decreased the energy gap Δ_0, starting from $\Delta_0=46$ meV. For clarity we present only three characteristic curves, which correspond to $\alpha\Delta_0$ with $\alpha=1$, 0.6, and 0.2. We exclude the group velocity and directionality effects to demonstrate that

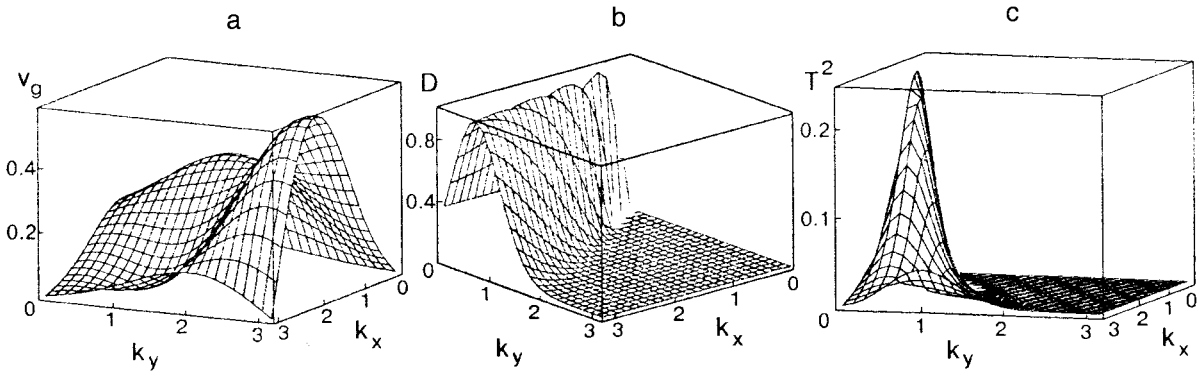

FIG. 9. 3D plot. of the group-velocity function (a), the directionality function (b), and the tunneling matrix element (c) according to formulas (11), (12), and (13), respectively.

they are not responsible for the asymmetry of the peaks.

There is asymmetry of the quasiparticle peak heights for both *s*- and *d*-wave symmetry. Thus the origin of the asymmetry of the peaks is not due to *d*-wave symmetry of the energy gap of the HTSC. There is a flatter subgap behavior of the DOS in the case of *s*-wave symmetry in comparison with the *d*-wave case. Increasing the lifetime broadening factor Γ leads to enhancement of the asymmetry of the peaks. There are van Hove singularities (VHSs) in the DOS at small Γ. Increasing Γ leads to confluence of the quasiparticle and VHS peaks, and this results in enhancement of the asymmetry of the DOS peaks due to the saddle point in the energy spectrum (10) at $(\pi, 0)$. Also note the asymmetry of the background for both *s*- and *d*-wave gap symmetry.

Figure 11 shows the Δ_0 dependence of the DOS, taking into account the group-velocity and directionality effects at $\Gamma = 3$ meV (a,c) and $\Gamma = 9$ meV (b,d) for *s*-wave (a,b) and *d*-wave (c,d) gap symmetry. As in Ref. 1 we have taken $\theta = 0.25$ and $\theta_0 = 0.1$.

There is also asymmetry of the quasiparticle peaks, similar to the *s*- and *d*-wave cases. But in the *d*-wave case the asymmetry is stronger than in the *s*-wave case. The group-velocity and directionality effects lead to disappearance of the VHSs in the DOS. Increasing Γ enhances the asymmetry of the quasiparticle peak. The strongest effect of the energy band structure on the DOS occurs along the k_x axis due to the van Hove singularity at $(\pi, 0)$.

Figure 12 demonstrates this effect. We have presented

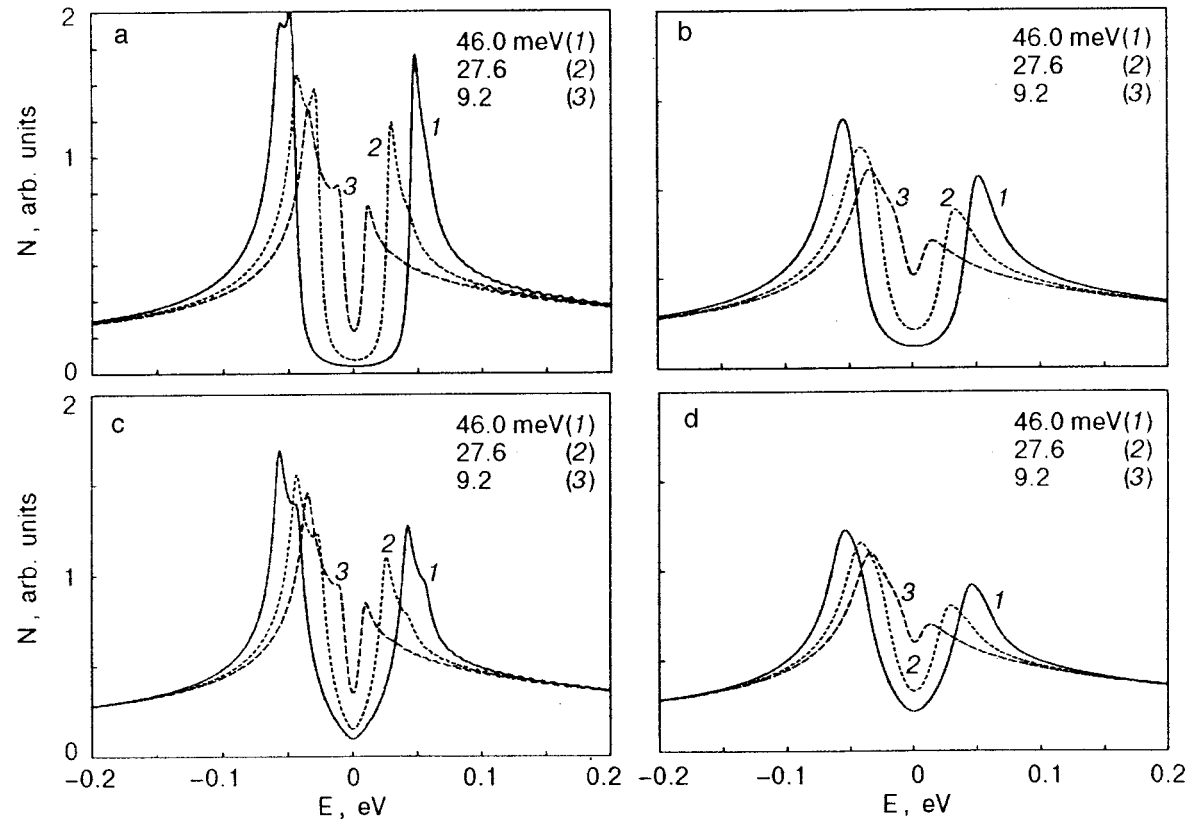

FIG. 10. The changing of the DOS with energy gap Δ_0 for *s*- (a,b) and *d*-wave (c,d) symmetry at $\Gamma = 3$ meV (a,c) and $\Gamma = 9$ meV (b,d) without effects of directionality and group velocity.

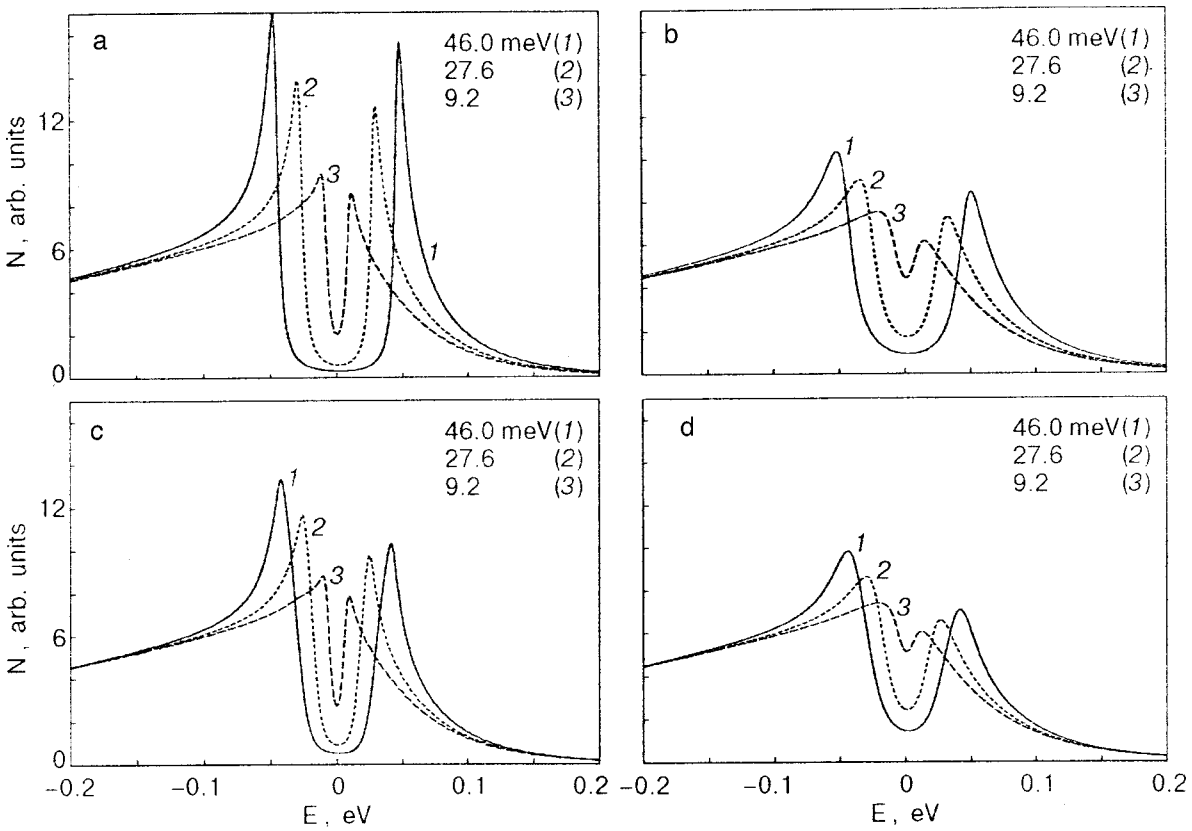

FIG. 11. The change of the DOS with energy gap Δ_0 for *s*- wave (a,b) and *d*-wave (c,d) gap symmetry at $\Gamma = 3$ meV (a,c) and $\Gamma = 9$ meV (b,d) with the effects of directionality and group velocity.

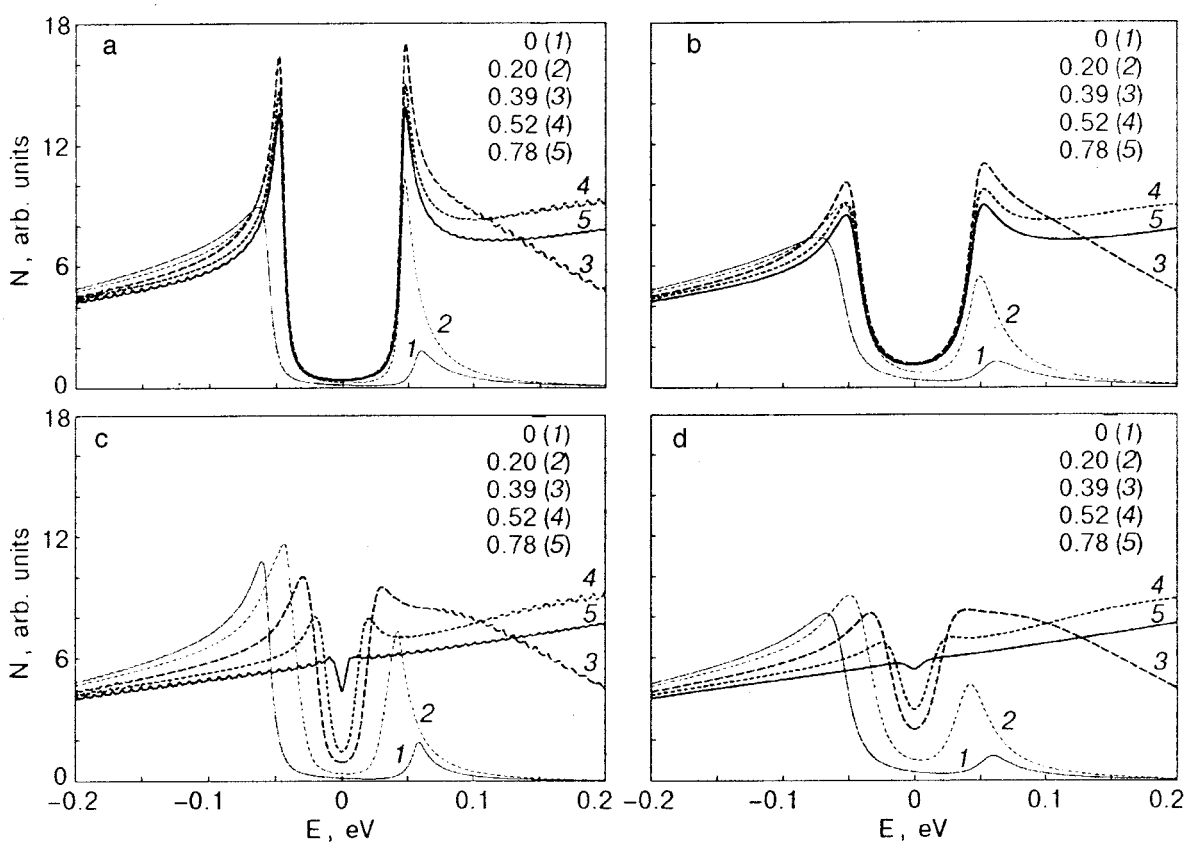

FIG. 12. Effects of directionality on the DOS for *s*-wave (a,b) and *d*-wave gap symmetry at $\Gamma = 3$ meV (a,c) and $\Gamma = 9$ meV (b,d).

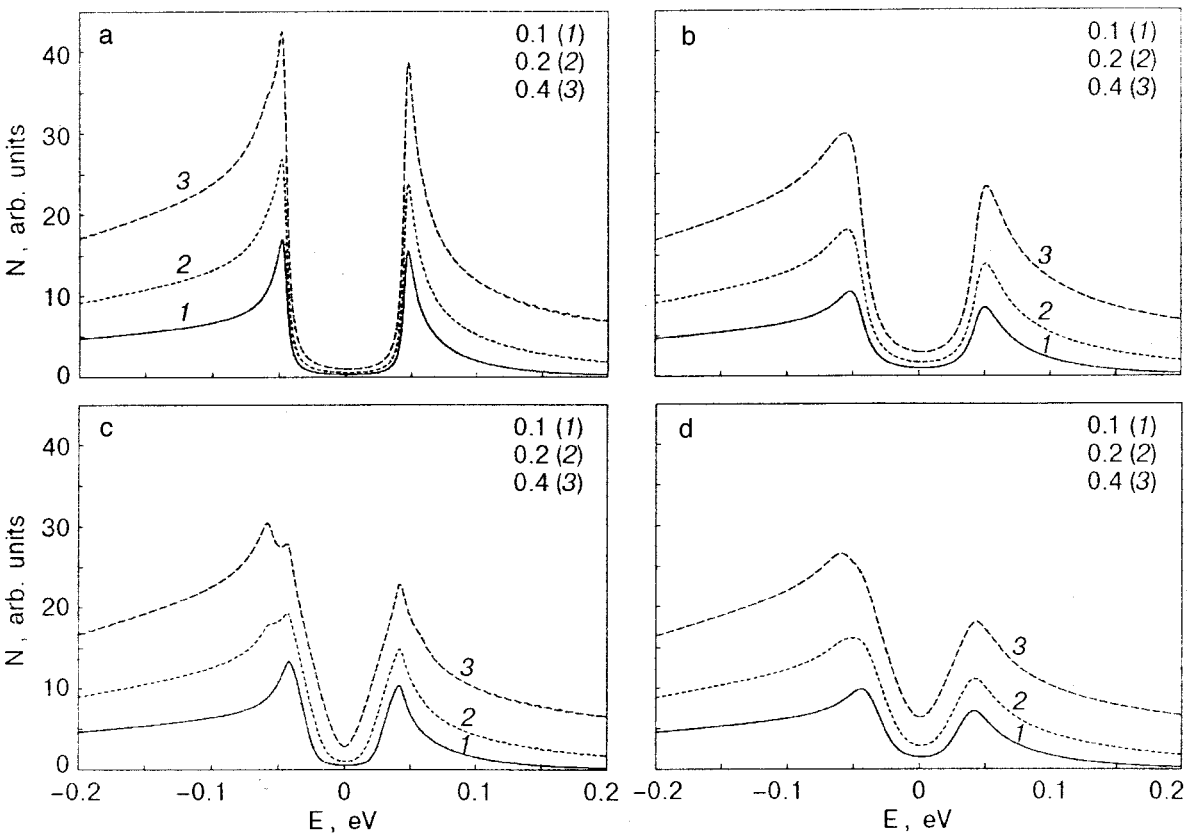

FIG. 13. Numerical calculation of the quasiparticle DOS with *s*-wave (a,b) and *d*-wave (c,d) gap symmetry at $\Gamma=3$ meV (a,c) and $\Gamma=9$ meV (b,d) for different spreads θ_0.

the DOS at different θ at $\Gamma=3$ meV (a,c) and $\Gamma=9$ meV (b,d) for both *s*-wave (a,b) and *d*-wave (c,d) gap symmetry. In the case of *s* symmetry the position of the quasiparticle peaks is constant except in the direction along $k_x(\theta=0)$. Note the strong asymmetry of the peaks in this case.

In the case of *d*-wave symmetry we have practically the same behavior around the k_x direction as for the *s* wave, but the energy gap is changed due to the θ dependence of Δ_0, and, correspondingly, the quasiparticle peaks are shifted to zero energy.

Figure 13 shows the change of the DOS with θ_0 at $\Gamma=3$ meV (a,c) and $\Gamma=9$ meV (b,d) for both *s*-wave (a,b) and *d*-wave (c,d) gap symmetry. Increasing θ_0 brings into play the states close to $(\pi, 0)$. It is reflected as the appearance of a van Hove singularity in both the case of *s*-wave and *d*-wave gap symmetry at small Γ. The VHS is more pronounced in the *d*-wave case in comparison with the *s*-wave symmetry. Increasing Γ leads to confluence of the quasiparticle and VHS peaks.

We consider that the absence of the VHS peak on the experimental dI/dV characteristics is indicative of a rather large lifetime broadening factor Γ in that HTSC material.

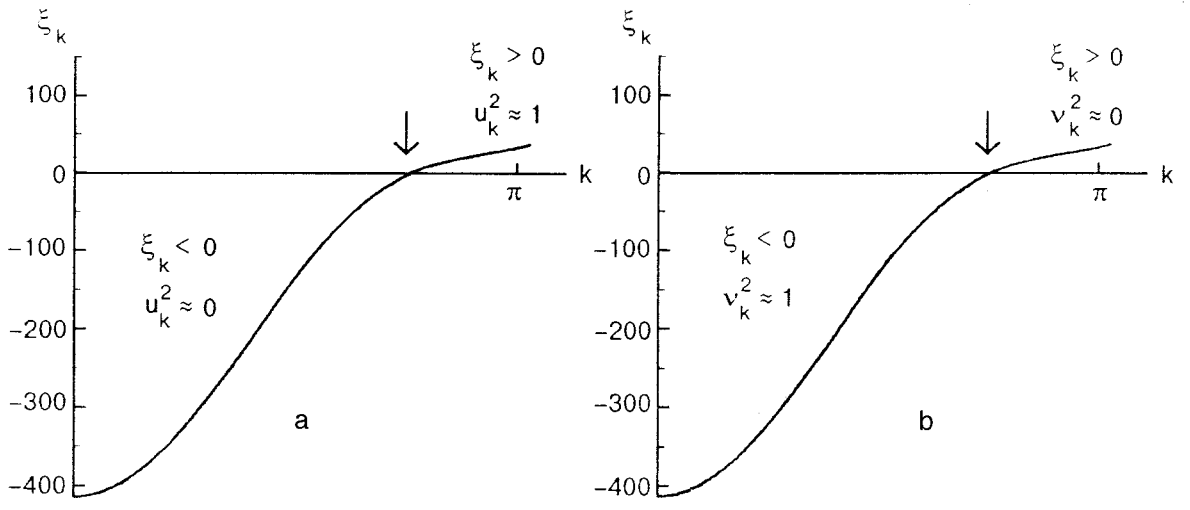

FIG. 14. ARPES energy spectrum along $\theta=0.25$. The values of the coherence factors correspond to $E>0$ (a) and $E<0$ (b).

The origin of the asymmetry of the peaks in the tunneling DOS was studied in Ref. 1 by considering the role of the tunneling matrix element $|T_k|^2$ in the clean limit $\Gamma=0$, where formula (5) was used for the calculation of $N(E)$.

We repeat the explanation of Ref. 1 because we believe that the conclusion as to the origin of the peak asymmetry must be different. At $E>0$ (positive bias voltages) the first term of (5) contributes to $N(E)$ because of $\delta(E_k-E)$. In this case, as one can see from Figs. 7, 9c, and 14a, $|T_k|^2$ selects only a relatively short region of states in k space in which $u_k^2>0$. These are the states with $\xi_k>0$ (above the FS). For the majority of states integrated over at $E<0$ (negative bias voltages; again see Figs. 7 and 9c) the second term of (5) contributes to the DOS because of $\delta(E_k+E)$. In this case, as one can see from Figs. 7, 9c, and 14b $|T_k|^2$ selects out a large region of k states where $v_k^2>0$, in fact, equal to one. These states are below the Fermi surface, where $\xi_k<0$. The overall effect then is to have a large negative bias conductance compared to the positive one. This is true for both *s*- and *d*-wave symmetry. Hence, the underlying asymmetry of the conductance peaks is primarily due to the band structure ξ_k, and *d*-wave symmetry simply enhances the degree of asymmetry of the peaks. Thus, the asymmetry of the peaks, which exists for both *s*-wave and *d*-wave symmetry, is sensitive to the band structure ξ_k.

In summary, by changing the energy gap Δ_0 in HTSC one may model the influence of nonmagnetic impurities on the DOS. We consider that the asymmetry of the quasiparticle peaks is due to the specific features of the energy spectrum of the HTSC and that the *d*-wave gap symmetry only enhances the asymmetry of the peaks.

The absence of the VHS peak on the experimental dI/dV characteristics indicates a rather large lifetime broadening factor Γ in HTSC.

We thank Y. Sobouti, M. R. H. Khajehpour, and Yu. A. Kolesnichenko for helpful discussions.

*E-mail: shukr2@iasbs.ac.ir

[1] Z. Yusof, J. F. Zasadzinski, L. Coffey, and N. Miyakawa, Phys. Rev. B **58**, 514 (1998).
[2] K. Schlenga, R. Kleiner, G. Hechtfischer, M. Moessle, D. Schmitt, P. Mueller, Ch. Helm, Ch. Preis, F. Forsthofer, J. Keller, M. Veith, and E. Steinbess, Phys. Rev. B **57**, 14518 (1998).
[3] Yu. M. Shukrinov, Kh. Nasrulloev, Kh. Mirzoaminov, and I. Sarhadov, Appl. Supercond. **2**, 741 (1994).
[4] Yu. M. Shukrinov, A. Stetsenko, Kh. Nasrulloev, and M. Kohandel, IEEE Trans. Appl. Supercond. **8**, 142 (1998).
[5] Yu. I. Latyshev, T. Yamashita, L. N. Bulaevskii, M. J. Graf, A. V. Balatsky, and M. P. Maley, cond-mat/9903256.
[6] Yu. Shukrinov, P. Seidel, and J. Scherbel, *Quasiparticle current in the intrinsic Josephson junctions in TBCCO* (to be published).
[7] A. M. Cucolo, Physica C **305**, 85 (1998).
[8] L. Ozyuzer, Z. Yusof, J. Zasadzinski, T. Li, T. Hinks, and K. E. Gray, cond-mat/9905370.
[9] Y. DeVilde, N. Migakawa, P. Iavarone, L. Ozyuzer, J. F. Zasadzinski, P. Romano, D. G. Hinks, C. Kendziora, G. W. Grabtree, and K. E. Gray, Phys. Rev. Lett. **80**, 153 (1998).
[10] K. Kouznetsov and L. Coffey, Phys. Rev. B **54**, 3617 (1996).
[11] J. R. Kirtley and D. J. Scalapino, Phys. Rev. Lett. **65**, 798 (1990).
[12] A. J. Fedro and D. D. Koelling, Phys. Rev. B **47**, 14342 (1993).
[13] M. R. Norman, M. Randeria, H. Ding, and J. C. Campuzano, Phys. Rev. B **52**, 615 (1995).
[14] A. A. Abrikosov, Physica C **244**, 243 (1995).

This article was published in English in the original Russian journal. Reproduced here with stylistic changes by AIP.

Features of the temperature dependence of trapped magnetic flux in yttrium high-T_c superconducting ceramics

A. A. Sukhanov and V. I. Omel'chenko

*Institute of Radio Engineering and Electronics, Russian Academy of Sciences, pl. Vvedenskogo d. 1, 141120 Fryazino, Moscow District, Russia**

(Submitted July 14, 2000)
Fiz. Nizk. Temp. **27**, 24–29 (January 2001)

The temperature dependence of the trapped magnetic field (TMF) $H_t(T)$ in yttrium high-T_c superconducting (Y–HTSC) ceramic systems is investigated. For field-cooled trapping the $H_t(T)$ curves are the same as $H_t(T_t)$ (T_t is the trapping temperature): H_t decreases monotonically with increasing temperature, and in weak fields it goes rapidly to saturation as T_t is lowered. In the case of trapping with a magnetic field pulse after zero-field cooling the $H_t(T_t)$ curves have a maximum, and H_t decreases monotonically with increasing T, the rate of this process being faster as the initiating field H is decreased, and the temperature at which the TMF vanishes decreases with decreasing T_t and H. A discussion of the results is presented, and it is shown that the observed features of the temperature dependence of the trapped magnetic flux in Y–HTSCs are not explained in terms of the Bean model but are satisfactorily described by a model in which the magnetic flux is trapped in superconducting loops. [DOI: 10.1063/1.1344138]

1. INTRODUCTION

A study of magnetic hysteresis effects, in particular, of magnetic flux trapping in Josephson high-T_c superconducting (HTSC) media (ceramic materials, polycrystalline films) is of interest from both the fundamental and applied standpoints and can also be an effective way of obtaining information about the distribution function of the weak links with respect to the critical currents, magnetic fields, and temperatures. An important problem in this regard is to choose a model adequate to the description of the magnetic properties of the investigated HTSC system.

The experimental results are most often interpreted in the critical-state (Bean) model[1,2] or in the superconducting-glass model,[3,4] hypervortices model,[5] or superconducting-rings model.[6] Unfortunately, these substantially different models usually predict nearly the same field dependence of the trapped magnetic field (TMF), dependence of the TMF on the trapping temperature, relaxation curves of the magnetic moment, and many other characteristics of the TMFs.

Up till now, however, the falloff of the TMF with increasing temperature after trapping has not been studied in detail, even though it is in such experiments that the predictions of the different models can be considerably different. In fact, in the Bean model the behavior of the system is determined by the temperature dependence of a single critical current density, whereas, for example, for the superconducting-rings model the variance of the weak links with respect to the critical fields and critical temperatures is important.

Below we present results of a study of the temperature dependence of the TMFs as the temperature is raised after trapping, and we compare the results with the predictions of the Bean and superconducting-rings models.

2. SAMPLES AND MEASUREMENT TECHNIQUES

The trapped magnetic fields were measured on samples of (123) yttrium HTSC ceramics obtained as a result of solid-phase reaction in the sintering of powders of Y_2O_3, BaO_2, and CuO. The samples were prepared by a one-time sintering with a comparatively rapid heating over 3–4 h to 950–1050 °C and a slow cooling for 12 h with holds at three temperatures: 950 °C for 1 h, 750–780 °C for 2 h, and 600–650 °C for 3 h. The temperature and width of the resistive transition of the ceramic samples to the superconducting state were $T_c = 92$ K and $\Delta T_c = 2$ K.

The temperature dependence of the TMF was measured on samples $1.5 \times 3 \times 6$ mm in size by a Hall probe with a working area of 0.15×0.45 mm. A 17-Hz alternating current was used in the Hall instrument, with a phase-regulating compensation circuit for improving the sensitivity. The sensitivity and measurement error were 0.05 Oe.

Measurements were made at temperatures of 4.2–100 K at external fields in the interval 1–1000 Oe for two trapping regimes: 1) field cooling (FC), in which the sample is cooled in a magnetic field, and 2) zero-field cooling (ZFC), in which a magnetic field pulse was applied at $T_t < T_c$ after cooling in zero magnetic field.

In the first case the external magnetic field H was applied to the Y–HTSC sample at $T > T_c$, and then the sample was cooled to T_t ($T_t < T_c$), after which the field H was turned off and, after a wait of 300 s, the measurements of the temperature dependence of the trapped magnetic field $H_t(T)$ were started.

In the second case the sample was cooled in zero field to the trapping temperature T_t, at which a magnetic field H was applied in a pulse of duration $t_t > 100$ s, which was long enough that the results did not depend on t_t.

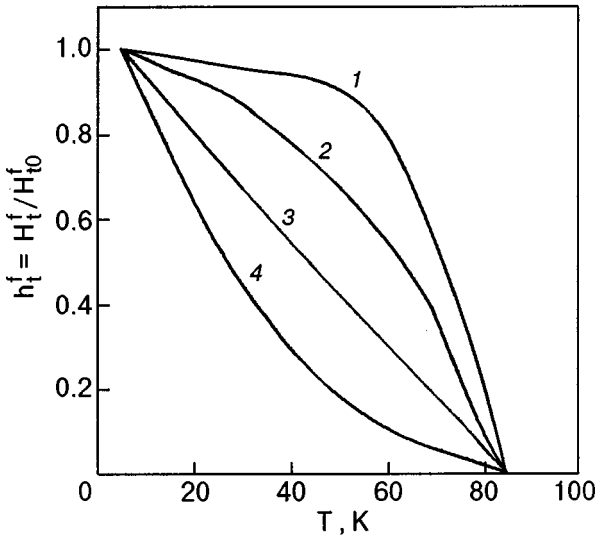

FIG. 1. Normalized temperature dependence of the magnetic field trapped in a 123 ceramic (the FC regime) for different inducing fields H [Oe]: 1.8, $H_{t0}^f = 1.7$ Oe (*1*); 6.7, $H_{t0}^f = 5.7$ Oe (*2*), 16, $H_{t0}^f = 10$ Oe (*3*), 250, $H_{t0}^f = 95$ Oe (*4*).

3. RESULTS OF THE MEASUREMENTS

$H_t^f(T)$ curves for trapping after field cooling

The temperature curves of the TMF obtained as the temperature was increased after trapping are shown in Fig. 1 in a normalized form $h(T)$, where $h = H_t^f/H_{t0}^f$, $H_{t0}^f = H_t^f(T_t = 5$ K).

For each specified value of H the falloff of H_t^f with increasing T occurs monotonically along a single curve that is independent of T_t, and for all fields the $H_t^f(T)$ curves coincide with the curves of the TMF versus trapping temperature, $H_t^f(T_t)$. We note that for small values of the field ($H < 10$ Oe) the TMFs in the low-temperature region depend weakly on T, which agrees with the known data[7] for $H_t^f(T_t)$.

As T is lowered from any point T_0 of the $H_t^f(T)$ curves (such a point is illustrated in Fig. 1) and the temperature is cycled in the region $T < T_0$ the value of H_t^f remains unchanged. When T is increased above T_0, however, H_t^f again falls off along the curve $H_t^f(T) = H_t^f(T_t)$. These results agree with the predictions of both the Bean model and the superconducting-rings model.

$H_t^z(T)$ curves for trapping with a field pulse (ZFC)

The curves of the trapped magnetic fields $H_t^z(T)$ differ substantially from those described for the FC case.

Figure 2 shows the $H_t^z(T)$ curves obtained as the temperature was increased for various values of T_t (Fig. 2a) and for various inducing fields (Fig. 2b).

For weak fields the magnetic fields H_t^z trapped with a field pulse decrease rapidly as the temperature is raised, falling to zero for $T < T_c$, and the lower the inducing field and, accordingly, the trapped field, the more rapid is the falloff of $H_t^z(T)$ (Fig. 2b). The temperature T_d at which the TMF vanishes at low trapping temperatures ($T_t < T_c/2$) falls off approximately linearly with decreasing trapping temperature and with decreasing inducing field H: $T_d = T_t + bH$, $b = 0.5$ K/Oe.

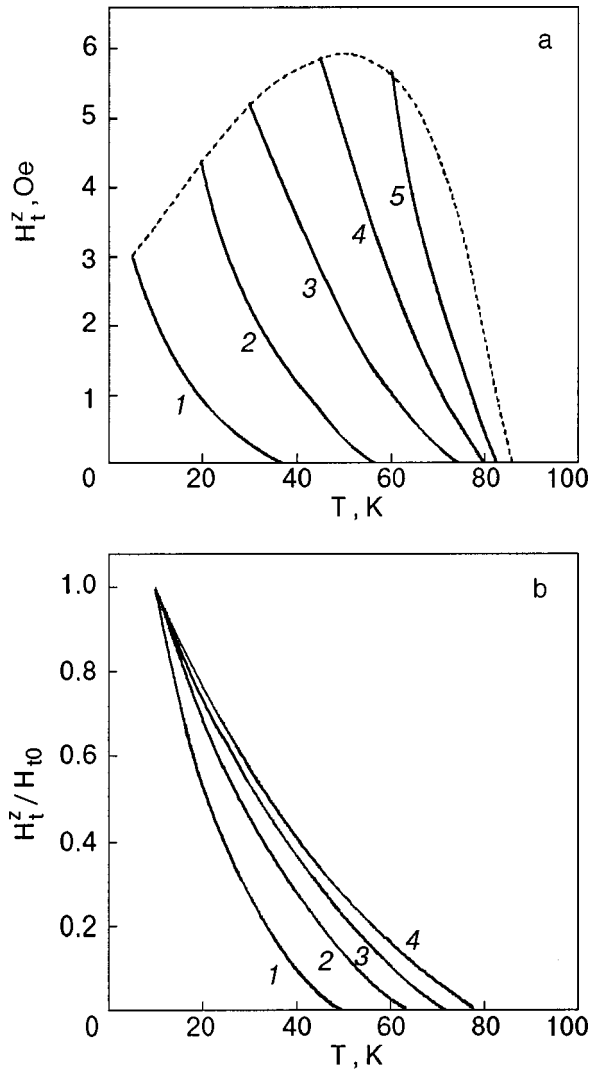

FIG. 2. Temperature dependence of the magnetic fields trapped in the ZFC regime for $H = 60$ Oe and different trapping temperatures T_t [K] ($T > T_t$): 10 (*1*), 19.8 (*2*), 30 (*3*), 45 (*4*), 60 (*5*) (the dotted line shows the curve of $H_t^z(T_t)$ (a) and at $T = 10$ K for different inducing magnetic fields H [Oe]: 60, $H_{t0} = 3.1$ Oe (*1*); 110, $H_{t0} = 8.5$ Oe (*2*); 400, $H_{t0} = 23$ Oe (*3*); 1000, $H_{t0} = 35$ Oe (*4*) (b).

The envelope of the family of $H_t^z(T)$ curves obtained for different T_t (Fig. 2a) is the known curve of the trapped field as a function of trapping temperature, $H_t^z(T_t)$.[7] For weak fields the curves of $H_t^z(T_t)$ have a maximum, which is more pronounced for lower fields and, hence, lower H_t^z. For high inducing magnetic fields the trapped fields H_t^z increase with decreasing trapping temperature T_t. For high fields the curves of $H_t^z(T_t)$ and $H_t^f(T_t)$ approach one another and practically coincide for $H > 500$ Oe.

When the temperature is lowered from any point of the $H_t^z(T_t)$ curve and the temperature is subsequently cycled in the region $T < T_t$, the fields H_t^z, as in the FC case, remain constant.

4. DISCUSSION OF THE RESULTS

In our view, the most interesting feature of the temperature curves considered above is the rapid decrease in the TMF with increasing temperature after trapping in the ZFC regime.

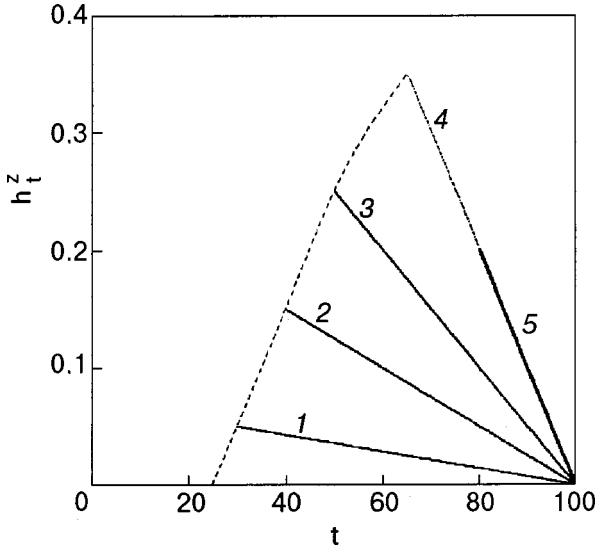

FIG. 3. Normalized temperature dependence of the trapped magnetic fields at the center of the sample for the ZFC regime, $h_t^z = H_t^z/j_c(0)d$, calculated in the Bean model for different trapping temperatures $t=(T/T_c)\times 100$: 30 (*1*), 40 (*2*), 50 (*3*), 65 (*4*), 80 (*5*).

Such a characteristic of the $H_t^z(T)$ curves cannot be explained in the framework of the Bean model, since in that model the trapped fields should vanish as $j_c(T)\to 0$ and, hence, as $T\to T_c$. In fact, a calculation of $H_t(T,T_t,H)$ at the center of a slab of width $2d$ according to the Bean model in the case of trapping with a field pulse gives $(T>T_t)$

$$H_t^z(T,T_t,H)=j_c(T)d\,\theta(L-2d) + j_c(T)(L-d)\,\theta(2d-L)\,\theta(L-d), \qquad (1)$$

where $L=L(H,T_t)=H/j_c(T_t)$.

Figure 3 shows the normalized curves of $H_t^z(T)$ calculated according to Eq. (1) for $H=0.5j_c(0)d$ and for a typical temperature dependence of the critical current for dielectric Josephson junctions:[8]

$$j_c(T)=j_c(0)(1-T/T_c). \qquad (2)$$

It is seen by comparing Figs. 1 and 3 that according to the Bean model, the complete vanishing of the TMF occurs only at the critical temperature T_c, whereas our measured value of the limiting temperature for the falloff of the TMF, as we have said, decreases with decreasing trapping temperature T_t and magnetic field H. The result is basically the same if the Bean model is generalized to the inhomogeneous case.

Thus the predictions of the Bean model do not agree even qualitatively with the experimental data.

The various magnetic hysteresis models involving Abrikosov or Josephson vortices[3,9] are incapable of explaining the magnetic flux trapping in the HTSCs studied here, since upon fractionation, i.e., upon the destruction of the contacts between granules, the TMF rapidly vanished. This is evidence that the contribution to the TMF from Abrikosov vortices pinned in the granules is small. In addition, magnetic flux trapping was not observed at temperatures in the region of the resistive superconducting transition, when Josephson contacts between superconducting granules have already formed and it would seem that Josephson vortices could appear.

The investigated features of the temperature dependence of the TMF can, however, be explained in the superconducting-rings (-loops) model,[6] according to which the trapped magnetic fields in HTSC ceramics and films are determined by the magnetic flux trapping in the system of superconducting rings formed by superconducting granules connected by Josephson weak links. Such a system should be characterized by a rather wide distribution of weak links and, hence, of critical fields H_c and critical temperatures T_c of the superconducting rings.

Let us first consider the TMF in the ZFC regime. When a pulse of external field H is applied after the samples are cooled in zero field to $T_t<T_{c0}$, rings with low critical fields $H_c<H$ and rings with $H_c>H$ behave differently: the magnetic field destroys the superconductivity in the first of these, and a magnetic flux proportional to H_c is trapped in them when the field is removed, while the field does not penetrate rings of the second type, and magnetic flux trapping does not occur in them.

As the temperature is raised after trapping at T_t, the critical fields of the rings decrease, as does the field in each of them, and the maximum trapped field $H_c^*(T)$ is determined by the temperature dependence of the critical fields and the condition $H_c^*(T_t)=H$. Thus for $T>T_t$ we have

$$H_t^z(H,T_t,T)=A\int_0^{H_c^*(T)} H_c f(H_c)\,dH_c, \qquad (3)$$

where the coefficient A takes into account the geometric factors and the demagnetizing factor.

It follows from (3) that the trapped fields vanish at a limiting temperature T_d determined from the conditions $H_c^*(T_d)=0$ and $H_c^*(T_t)=H$, and in the case of a linear temperature dependence of the critical fields this gives, in agreement with the experimental data, $T_d=T_t+\alpha^{-1}H$, where α is the temperature coefficient of the critical fields.

Figure 4a and 4b shows the temperature dependence of the TMFs in the ZFC regime, as calculated with the following model distribution function of the critical fields of the rings, which is both reasonable and convenient for analytical calculations:

$$f(H_c,H_{cc},\Delta H_c)=\frac{[\Delta H_c^2-(H_c-H_{cc})^2]^{1/2}}{1/2\pi\Delta H_c^2}, \qquad (4)$$

where H_{cc} is the mean critical field and ΔH_c is the half-width of the distribution function; for a linear temperature dependence of the critical fields, $H_c(T)=H_c(0)-\alpha T=H_c(0)-H_{cM}(T/T_c)$, $H_{cc}(T)=H_{cc}(0)-\alpha T$, $H_{cM}=H_{cc}(0)+\Delta H_c$, T_c is the maximum temperature of formation of superconducting rings, $H_{cc}(0)=100$ Oe, and $\Delta H_c=50$ Oe.

Comparing Fig. 4a and 4b with 2a and 2b, respectively, we observe good qualitative agreement of the calculated and experimental temperature dependence of the TMF.

The falloff of the $H_t^z(T_t)$ curve with decreasing T_t in the low-temperature region and, hence, the appearance of a maximum on the envelope of the family of $H_t^z(T)$ curves are due to the growth of the critical fields as the temperature is lowered, which, in the case of a distribution function $f(H_c)$

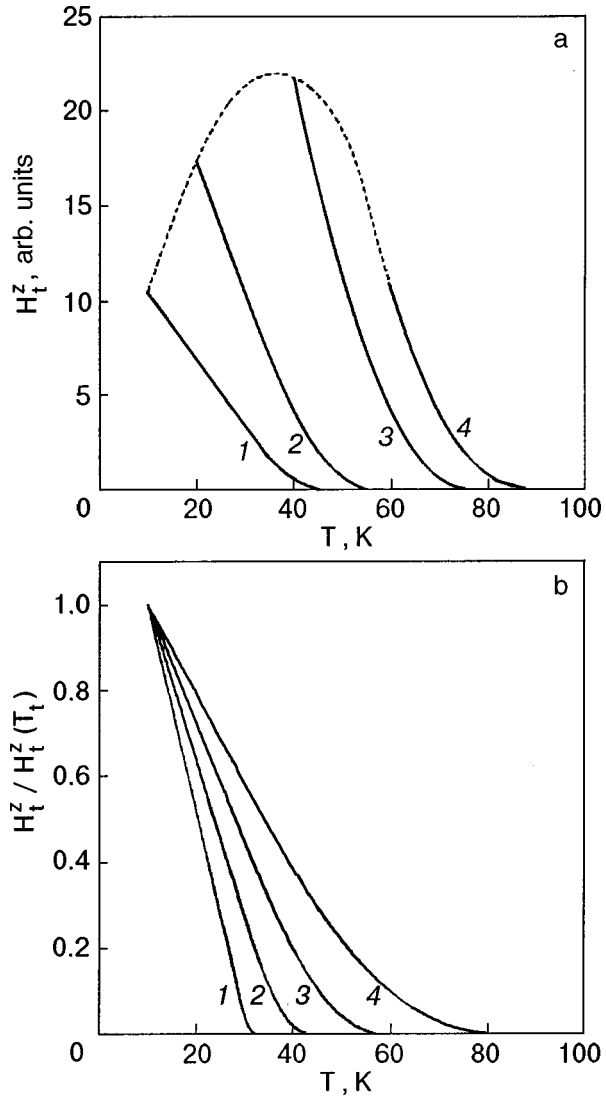

FIG. 4. Temperature dependence of the magnetic field trapped in the ZFC regime, calculated for the superconducting-rings model for $H=60$ Oe and different trapping temperatures T_t [K]: 10 (*1*), 20 (*2*), 40 (*3*), 60 (*4*) (the dotted line shows the curve of $H_t^z(T_t)$ (a) and at $T_t=10$ K for different magnetic fields H [Oe]: 36 (*1*), 55 (*2*), 80 (*3*), 120 (*4*) (b).

having a pronounced maximum at $T=0$, leads to a decrease in the number of rings with $H_c<H$, in which trapping with a field pulse of amplitude H occurs.

The rings model also gives a good description of the TMF in the FC regime. In this case the field H initially exists in both types of rings, and therefore all of the rings trap magnetic flux, although the value of the trapped local fluxes in rings with $H_c<H$ is proportional to H_c, while that trapped in rings with $H_c>H$ is proportional to H.

Thus in the FC regime we have

$$H_t^f(H,T_t,T)=A\left(\int_0^H H_c f(H_c)dH_c+H\int_H^\infty f(H_c)dH_c\right). \tag{5}$$

As the temperature is raised after trapping, the critical fields H_c fall off, and here it is important to note that rings with $H_c(T)>H$ trap fields H, while the maximum field that can be trapped by rings with $H_c(T)<H$ is H_c. Thus expression (5), with allowance for the dependence $H_c(T)$, also describes the temperature dependence of the trapped field for $T>T_t$. It follows from this that the temperature dependence of $H_t(T)$ on heating is the same as $H_t(T_t)$.

It also follows from expressions (3) and (5) that, in agreement with the experimental data:

a) the value of the trapped field in the FC case is always higher than in the ZFC case, $H_t^f>H_t^z$;

b) in weak fields at low temperatures the trapping in the FC regime, according to Eq. (5), occurs in all the rings; the field trapped in the majority of the rings is equal to H, and the TMF depends weakly on temperature;

c) in high fields $H>H_{cM}$ (H_{cM} is the maximum critical field in the system of rings) the trapped fields cease to depend on the value of the inducing field, and $H_t^f=H_t^z$;

d) as the temperature is lowered, the critical field H_c of the loops increases and, hence the fields trapped in the loops cannot change; consequently, $H_t(T)=\text{const}$ for $T<T_t$.

Thus the features of the our measured temperature curves of the TMF and, in particular, the vanishing of the TMF at temperatures much lower than T_c are well explained in a model based on the trapping of magnetic flux in superconducting loops (rings).

*E-mail: vvv195@ire216.msk.su

[1] C. P. Bean, Rev. Mod. Phys. **36**, 31 (1969).
[2] D. M. Ginzburg (Ed.), *Physical Properties of High-Temperature Superconductors* [in Russian], Mir, Moscow (1990).
[3] C. Ebner and D. Stroud, Phys. Rev. B **31**, 165 (1987).
[4] I. Morgenstern, K. A. Muller, and J. G. Bednorz, Physica C **15**, 59 (1988).
[5] É. B. Sonin, JETP Lett. **47**, 496 (1988).
[6] Kh. R. Rostami, A. A. Sukhanov, and V. V. Mantorov, Supercond. Sci. Technol. **9**, 736 (1996).
[7] H. Darhmaoui, J. Jung, J. Talvacchio, M. A.-K. Mohamed, and L. Friedrich, Phys. Rev. B **53**, 12330 (1996).
[8] K. K. Likharev and B. T. Ul'rikh, *Josephson Junction Systems* [in Russian], Izd-vo MGU, Moscow (1978), Ch. 1.
[9] G. Blatter, M. V. Feigel'man, W. B. Geshkenbein, A. I. Larkin, and V. M. Vinokur, Rev. Mod. Phys. **66**, 1125 (1994).

Translated by Steve Torstveit

LOW-TEMPERATURE MAGNETISM

Photoinduced light absorption and dichroism of $Ca_3Mn_2Ge_3O_{12}$ garnet as a probe of electronic processes and intrinsic electric fields

V. V. Eremenko, S. L. Gnatchenko, I. S. Kachur, V. G. Piryatinskaya,* A. M. Ratner, and V. V. Shapiro

B. Verkin Institute for Low Temperature Physics and Engineering, National Academy of Sciences of Ukraine, 47 Lenin Ave., 61164 Kharkov, Ukraine

M. Fally and R. A. Rupp

Institute of Experimental Physics, Vienna University, A-1090 Vienna, Strudlhofgasse 4, Austria
(Submitted July 11, 2000)
Fiz. Nizk. Temp. **27**, 30–45 (January 2001)

Measurements of photoinduced light absorption in $Ca_3Mn_2Ge_3O_{12}$ revealed some unusual features: a saturation with the pumping intensity and a broad straggling of relaxation times with a predominance of very long times. These experimental facts cannot be understood in terms of photoinduced absorption centers associated with impurities or lattice defects, but are naturally explained within the notion of random electric fields of active charges. Active charges are produced by light pumping via the dissociation of coupled pairs of charges (consisting of a Mn-hole coupled with a compensating negative impurity or a negatively charged vacancy) which exist in the ground state. Such active charges create electric fields in a larger volume than coupled pairs, thus enhancing the probability for forbidden optical transitions. On the other hand, the random fields of active charges promote hopping of holes and hence the relaxation of photoinduced effects. A broad distribution of random-field magnitudes gives rise to a very broad range of hole hopping rates. There is also a much faster annihilation process immediately conditioned by light pumping. The simultaneous action of these relaxation channels, depending on the number of active charges, pumping intensity, and temperature, explains the entire experimental picture qualitatively and in part quantitatively. Photoinduced dichroism as well as birefringence, observed under polarized pumping, are caused by an anisotropic distribution of photoproduced holes over polarization directions. [DOI: 10.1063/1.1344139]

INTRODUCTION

There exists a class of related long-lived photoinduced phenomena in magnetic insulators conventionally associated with the transfer of charges caused by photoillumination. Such phenomena are usually observed in ferromagnets or ferrimagnets within the region of magnetic ordering, i.e., the Curie temperature exceeds the upper temperature boundary of the existence region of long-lived photoinduced phenomena. In this temperature region, interrelated photoinduced changes in optical and magnetic properties take place. For instance, in the case of yttrium iron garnet, $Y_3Fe_5O_{12}$, illumination with linearly polarized light induces a change of magnetic anisotropy,[1–3] linear dichroism,[3] and domain structure.[4] Unpolarized light affects the magnetic permeability and susceptibility,[5,6] coercivity and mobility of domain walls,[7,8] magnetostriction,[9] and optical absorption.[10,11] The interconnected variations in optical and magnetic properties make up a complicated physical picture. This has hampered the exploration of the detailed nature of long-lived photoinduced changes.

The purpose of the present work is to elucidate the mechanism of long-lived photoinduced changes in magnetic insulators, in particular, the charge transfer process under photoillumination and the subsequent relaxation in the absence of illumination.

To that end, it is necessary to separate the persistent photoinduced changes of the optical properties from those of the magnetic characteristics related to a magnetically ordered state. Antiferromagnetic garnets with a low Néel temperature T_N offer this possibility because they exhibit a broad temperature range between T_N and the temperature limit for the existence of long-lived photoinduced phenomena. With this in mind, the garnet $Ca_3Mn_2Ge_3O_{12}$, with the Néel temperature $T_N = 13.85$ K, was chosen as a favorable object of investigation.

The elucidation of the mechanism of photoinduced processes is facilitated by the results of the preceding investigation of this crystal carried out by the authors. Recently it was shown[12] that illumination of the garnet $Ca_3Mn_2Ge_3O_{12}$ with visible unpolarized light ($\lambda = 633$ nm) causes a noticeable increase (up to 15%) of the optical absorption coefficient at the same wavelength. Illumination of this crystal with linearly polarized light results in the appearance of linear birefringence which is caused by an anisotropic spatial redistri-

bution of charges.[13–16] Electrons are transferred from Mn^{3+} ions, occupying regular positions in the lattice, to Mn^{4+} ions, which are present in the crystal in a small concentration due to a weak impurity of negative charges. The redistribution of charges between orientationally nonequivalent octahedral positions lowers the crystal symmetry and gives rise to birefringence. As will be shown below, the same mechanism is responsible for linear dichroism.

Thus the photoinduced phenomena in the garnet $Ca_3Mn_2Ge_3O_{12}$ can be divided into two groups: those induced only by linearly polarized light (photoinduced birefringence and linear dichroism) and phenomena induced by light irrespective of its polarization properties (photoinduced absorption).

This paper is organized as follows: we start with the basic assumptions, a statement of the problem, and some general remarks. Then we analyze the problem and draw some general conclusions about photoinduced changes by transfer of charges, which will be helpful in the discussion that follows. The experimental studies of photoinduced absorption, described in Sec. 3, verify these conclusions and reveal the detailed physical picture. In the subsequent Sections, these experimental data are interpreted quantitatively in order to discover the peculiarities of the photoinduced processes and the physically relevant parameters.

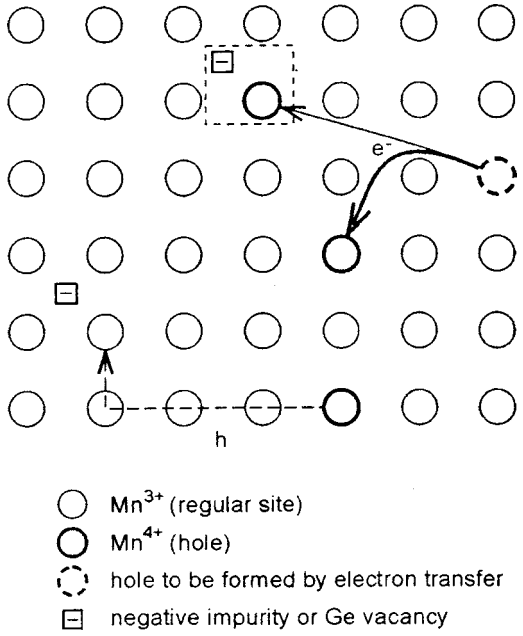

FIG. 1. Scheme of photoproduction and relaxation of active charges. An active charge is generated through the transfer of an electron from a regular Mn^{3+} ion to the Mn^{4+} component of a coupled pair (thin solid arrow). The same electron, being transferred to an existing active charge, annihilates it (bold solid arrow). The dashed arrow shows the relaxation of an active charge through the hopping of a hole and formation of a coupled pair.

1. BASIC ASSUMPTIONS AND STATEMENT OF THE PROBLEM

It is well established that photoinduced changes of the optical properties are conditioned by the transfer of charges (displacement of holes or electrons) between lattice ions.[17,18] In the case of the garnet $Ca_3Mn_2Ge_3O_{12}$, Mn-holes are transferred in the Mn sublattice (between Mn^{4+} and Mn^{3+} ions) by light.[12–16] The concentration of Mn^{4+} is low and corresponds to that of negative impurities or negatively charged Ge vacancies.[19,20] Prior to the description of our experiment, let us outline some basic model assumptions which will be helpful for the analysis of the experimental results (for simplicity, impurity centers with negative unit charge are considered below).

i) Ground state

In the ground state of the crystal, each Mn^{4+} ion is separated from a negatively charged impurity by the minimal possible distance, which does not exceed the lattice period. Thus, in the ground state, the positive effective charges (the Mn^{4+} ions) and the negative impurity charges form coupled pairs. They are inactive in the sense that their electric field acts only on a negligible volume fraction of the crystal as compared with that for separated charges of opposite sign.

ii) Creation of active charges under illumination

The binding of a coupled pair is too strong for the pair to be thermally dissociated. However, it can be dissociated by light. Thereby an electron is taken away from a regular Mn^{3+} ion (positioned far from the coupled pair) and transferred to the Mn^{4+} component of a coupled pair (as shown by the thin arrow in Fig. 1). This results in the creation of active charges: a Mn^{4+} ion and a negative impurity charge that are spatially separated from each other. Note that the free electrons produced can also recombine (and with a greater probability) with any of the existing active charges (separated Mn^{4+} ions). This relaxation channel is indicated by the bold arrow in Fig. 1.

iii) The achievable fraction of dissociated active charges is much less than unity

A photoinduced increase of the number of active charges (the channel designated by the thin arrow in Fig. 1) is possible provided that this channel is not compensated completely by the channel of destruction of existing active charges (shown by the bold arrow). This condition is met only if the number of active charges is much less than the number of coupled pairs, since the cross section for trapping of electrons is much larger for a separate Mn^{4+} ion than for the Mn^{4+} component of a coupled pair.

iv) Existence of two relaxation times for active charges

Photoproduced active charges relax in two different ways: First, through recombination with photoproduced electrons (the process shown by the bold arrow in Fig. 1). The characteristic time τ_p of this process is inversely proportional to the pumping intensity I,

$$\tau_p = C/I \tag{1}$$

and is basically independent of temperature.

Second, an active charge (hole at Mn^{4+}) can disappear by forming an inactive coupled pair with a separate negative impurity ion (or a germanium vacancy). This process is preceded by the diffusive motion of a hole, bringing it into a close vicinity of the negative ion (as shown by the dashed

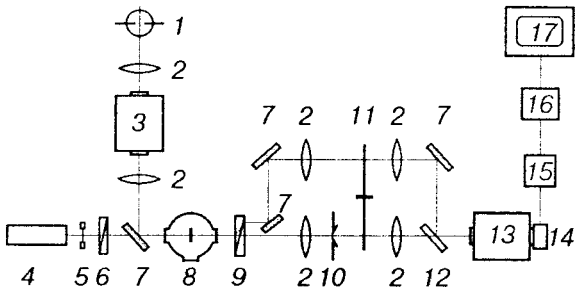

FIG. 2. Diagram of the setup for measuring photoinduced absorption and dichroism. *1*—arc lamp; *2*—lens; *3*—input monochromator; *4*—helium-neon laser; *5*—shutter; *6*—polarizer (Glan prism); *7*—mirror; *8*—cryostat with the sample; *9*—polarizer (Rochon prism); *10*—a variable slit; *11*—rotating disk; *12*—quartz plate; *13*—monochromator; *14*—photomultiplier; *15*—amplifier; *16*—analog-digital converter; *17*—computer.

line in Fig. 1). The characteristic time of such a diffusion process is denoted by $\tau_{\rm dif}$. It generally exceeds τ_p and decreases with rising temperature.

2. EXPERIMENT

2.1. Experimental setup

For the measurements of photoinduced absorption and linear dichroism, the samples were prepared in the form of plane-parallel plates of thickness $d \approx 35\,\mu$m. The samples were cut from a single crystal of calcium–manganese–germanium garnet (CaMnGeG), were polished mechanically and then annealed at the temperature $T \approx 1000\,^\circ$C to eliminate internal stresses caused by polishing.

The measurements of photoinduced absorption were performed with allowance for a twin domain structure of CaMnGeG.[21–23] It arises below the temperature of 520 K due to a Jahn–Teller phase transition from the cubic to the tetragonal phase. A special heat treatment[22] of the samples was carried out to increase the average size of the domains up to about 1 mm. A special sample holder with a diaphragm was used to select a single-domain region of the sample having its tetragonal axis perpendicular to the surface of the plate. Thus the results of the measurements refer to a sample with the tetragonal axis perpendicular to the surface. The sample was placed in a helium cryostat in which the temperature could be continuously varied from 2 K to 300 K. The sample temperature was measured using a copper–Constantan thermocouple.

The effect of illumination on the optical absorption and linear dichroism of CaMnGeG was studied with the use of an optical setup with two light sources. A helium-neon laser with an output power of about 2×10^{-3} W and a wavelength of $\lambda = 633$ nm was used as the pumping source. The laser light had no fixed direction of polarization. The stable wide-band emission of a xenon arc lamp, dispersed by a prism monochromator (with a linear dispersion of 12 nm/mm at $\lambda = 500$ nm), was used as the probe light. The intensity of the probe beam was chosen sufficiently low as not to cause any photoinduced phenomena.

The setup for measuring the time dependence of the linear dichroism is shown schematically in Fig. 2. The salient feature of this setup is the following: after passing through the sample, the intensities of two light beams, linearly polarized in mutually perpendicular directions, are in turn measured by the same channel of the registration system. This method enables us to measure the dichroism of the sample, expressed as the difference in the absorption of perpendicularly polarized rays, with minimal errors.

The arc lamp (*1*) and the monochromator (*3*) form the probe beam, with a wavelength $\lambda = 565$ nm. This beam passes through the sample (*8*) parallel to the tetragonal axis of the crystal. After passing through the polarizer (*9*), the probe beam is split into two mutually perpendicularly polarized beams which are spatially separated from each other. Before irradiating the sample, the intensities of these beams are made exactly equal by using a slit (*10*). The rotating disk (*11*) alternately opens the path for the beams for the same time intervals (30 s). Then the beams pass through the second monochromator (*13*) and are finally registered by the photomultiplier (*14*). The signal of the photomultiplier is enhanced by a direct-current amplifier (*15*), then transformed by an analog-digital converter (*16*) to consecutive codes which are transferred for accumulation to a computer (*17*). The accumulation time of the signal was 1 s (its minimal value being 0.1 s).

The pump beam from the laser (*4*) is slightly deflected from the optical axis in a direction perpendicular to the plane of the figure; it passes through the polarizer (*6*) and the mirror (*7*) and hits the sample. After passing through the cryostat (*8*), the pump beam is blocked by a diaphragm. The scattered pump light is cut off from the photomultiplier (*14*) by the second monochromator (*13*), tuned to the wavelength of the probe light.

The setup was used for measurements in three regimes:

i) Measurement of the absorption spectrum for unpolarized light before or after irradiation of the sample, the laser (*4*) being switched off during measurement. In that configuration, both the polarizers (*6*) and (*9*), as well as the monochromator (*13*), are removed. Using the monochromator (*3*), the wavelength of the probe light was scanned within the examined region and synchronously transferred to the computer. The optical absorption spectrum was obtained from the measurements by the usual processing of the transmission and reflection spectra.

It was established that the transmission of the CaMnGeG sample was noticeably decreased by illumination, whereas no photoinduced variation in the reflection coefficient was registered within the interval $500\text{ nm} < \lambda < 800$ nm. Thus the decrease in transmission observed in this spectral region should be assigned to the light-induced augmentation of the optical absorption coefficient, defined as follows:

$$\Delta K = d^{-1} \ln(j_0/j). \tag{2}$$

Here j_0 and j are the intensities of the transmitted probe beam before and after illumination, respectively.

ii) Measurement of the photoinduced absorption for unpolarized light with a fixed wavelength ($\lambda = 565$ nm) during irradiation of the sample with unpolarized light ($\lambda = 633$ nm). Such measurements were carried out similarly to Item (i) but using both the monochromators (*3*) and (*13*) tuned to the same fixed wavelength $\lambda = 565$ nm.

iii) Measurement of photoinduced dichroism at a fixed wavelength ($\lambda = 565$ nm) during irradiation of the sample

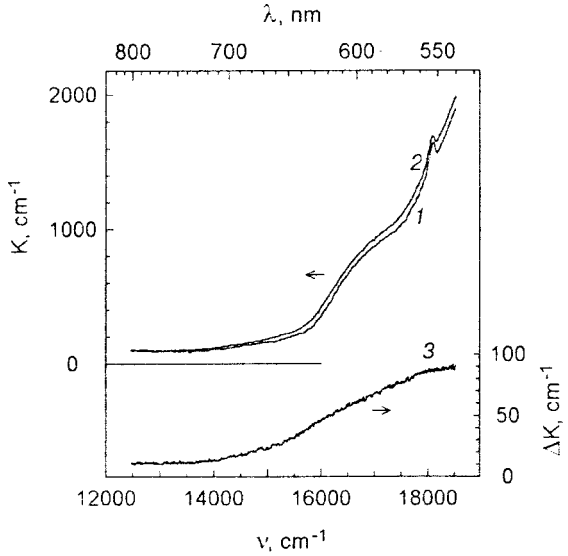

FIG. 3. Spectral dependence of the optical absorption coefficient before illumination (*1*) and after illumination (*2*) measured for the $Ca_3Mn_2Ge_3O_{12}$ garnet in the wavelength interval 540 to 800 nm at the temperature $T=23$ K. Curve *3* shows the photoinduced augmentation of the absorption coefficient, defined as the difference of the curves *2* and *1*.

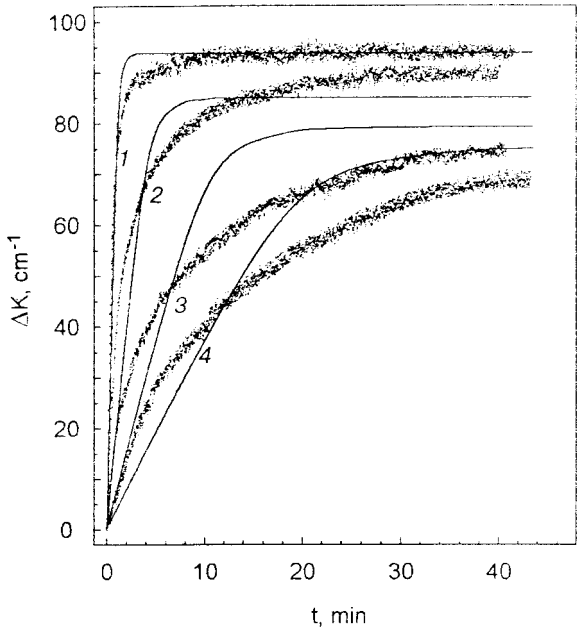

FIG. 4. Time dependences of the photoinduced addition, ΔK, to the optical absorption coefficient of the garnet $Ca_3Mn_2Ge_3O_{12}$ measured at the wavelength 565 nm and $T=23$ K under laser irradiation with different intensities i (given in units of the maximal pumping intensity): 1 (*1*); 0.24 (*2*); 0.085 (*3*); 0.05 (*4*). Experimental data are plotted by dots; the solid lines show the solution of the kinetic Equation (31).

with linearly polarized light ($\lambda=633$ nm). The probe light passes through the sample along its tetragonal axis [001] and is split into two beams polarized in the mutually perpendicular directions [110] and $[\bar{1}10]$ by the polarizer (*9*). Those polarization directions correspond to maximal dichroism. The pump beam passes through the sample parallel to the same axis [001], its polarization being determined by the polarizer (*6*). For definiteness, let the pump light be polarized in the direction [110]. Then the photoinduced augmentations of the absorption coefficient, derived from Eq. (2), are denoted by $\Delta K_{\parallel}$ and $\Delta K_{\perp}$ for the probe beams polarized in the directions [110] and $[\bar{1}10]$, respectively. The photoinduced dichroism ΔK_d is defined as

$$\Delta K_d=\Delta K_{\perp}-\Delta K_{\parallel}. \tag{3}$$

2.2. Experimental results: Photoinduced absorption

Prior to studying photoinduced changes of the absorption, the absorption spectrum of CaMnGeG was measured within the spectral interval $540\text{ nm}<\lambda<800$ nm. The result is shown in Fig. 3 (curve *1*). As can be seen, the garnet is relatively transparent in the interval $650\text{ nm}<\lambda<800$ nm, but its optical absorption strongly increases with decreasing wavelength in the range $\lambda<650$ nm. For $\lambda<540$ nm the transmission of the crystal becomes very low, thus limiting the measurement of the spectrum on the high-frequency side.

Such a spectral dependence of the absorption, strongly increasing with decreasing wavelength below 650 nm, can be attributed to the wide band with a maximum near 500 nm that is usually present in the optical spectra of compounds with Mn^{3+} and is related to the optical transition ${}^5E_g \rightarrow {}^5T_{2g}$ in the Mn^{3+} ion.[24,25] In the case of CaMnGeG, where a Mn^{3+} ion occupies an octahedral position, its orbitally degenerate states ${}^5E_g$ and ${}^5T_{2g}$ are split by the tetragonal distortion of oxygen octahedrons caused by the Jahn–Teller effect.[21] However, the split components of both states retain their g symmetry, so that the optical transition ${}^5E_g \rightarrow {}^5T_{2g}$ is forbidden in the dipole approximation. This reduces the absorption coefficient by four orders of magnitude as compared to an allowed transition.

In Fig. 3 (curve *2*) the spectral dependence of the absorption coefficient after irradiation with unpolarized light is shown, while the lower curve *3* displays the photoinduced change of the absorption coefficient obtained by subtracting curve *1* from curve *2*. It can be seen that the absorption coefficient and its photoinduced part have similar spectral dependences. This allows one to conclude that the initial absorption and its photoinduced augmentation are related to the same optical transition. This is the fundamental inference underlying the proposed model and will be corroborated by the further analysis.

Figure 4 demonstrates the observed time dependence of the photoinduced addition, $\Delta K(t)$, to the absorption coefficient at the wavelength 565 nm under irradiation with different pumping intensities i. It can be seen that the photoinduced absorption saturates with time. The time t_{sat}, during which $\Delta K(t)$ achieves 90% of the saturation level $\Delta K(\infty)$, decreases with an increase of the pumping intensity i approximately as i^{-1}. However, the level of saturation $\Delta K(\infty)$ itself has a much weaker dependence on i and varies only by 25% as i changes by a factor of twenty. This agrees with the statement given in Item (iv) of Sec. 1. Indeed, the saturation time t_{sat} practically coincides with the lifetime of photoproduced active charges (their lifetime is equal to the smaller of the times τ_p and τ_{dif}). The latter, as will be shown below, is very large at low temperatures, so that t_{sat} mainly coincides with the time τ_p, which is proportional to i^{-1}. As to the saturation level $\Delta K(\infty)$, it is mainly determined by the pumping intensity i multiplied by t_{sat}; this product is almost

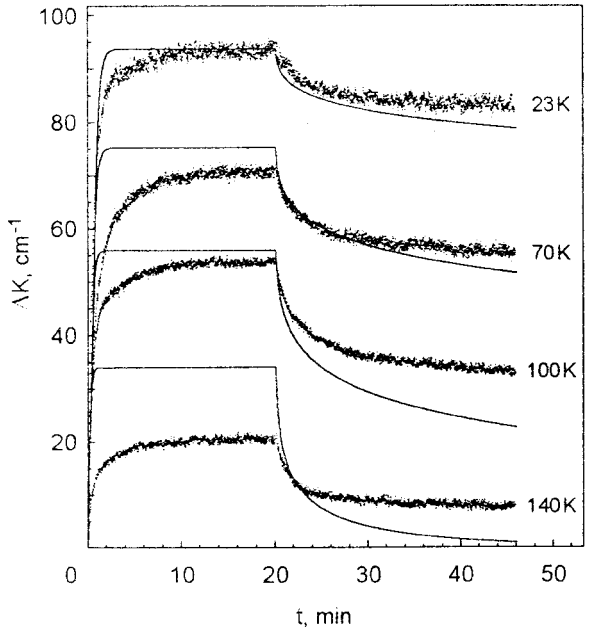

FIG. 5. Time dependences of the photoinduced addition, ΔK, to the absorption coefficient measured at the wavelength 565 nm and different temperatures under the maximal pumping intensity ($i=1$). Pumping was switched off at the time $t=20$ min. Experimental data are plotted by dots; the solid lines show the solution of the kinetic Equation (31).

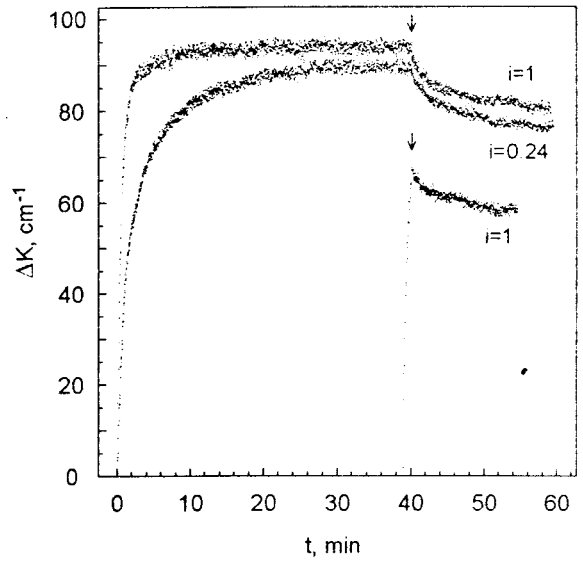

FIG. 6. Comparison of the relaxation curves of the photoinduced absorption after the moment of switching off of the illumination (indicated by an arrow), preceded by various ways of pumping: long pumping until saturation (two upper curves) and short pumping far from saturation (lower curve). The pumping intensity is shown in the figure. The measurements were performed at $\lambda=565$ nm and $T=23$ K (the times of the start of pumping are indicated arbitrarily).

independent of i. This qualitatively explains the observed weak dependence of the saturation level on pumping intensity.

The saturation value of the photoinduced absorption decreases with increasing temperature. This can be seen from Fig. 5, where the time dependences $\Delta K(t)$ at different temperatures are presented. The curves were measured for $\lambda=565$ nm and $i=1$ (maximal pumping in relative units). The decrease of the saturation level with increasing temperature is caused by a decrease of the relaxation time τ_{dif} down to a value comparable with τ_p [see Sec. 1, Item (iv)], so that the resulting relaxation time diminishes. Note that photoinduced absorption in CaMnGeG is no longer observed when the sample temperature exceeds 190 K.

In order to explore the relaxation of photoinduced absorption, the time dependences of ΔK were measured upon switching off the pump light. The corresponding relaxation curves are shown in Fig. 5 for the maximal pumping and different temperatures. Attention should be paid to the fact that each of these curves displays the existence of relaxation components with strongly differing values of the time constant τ. For the fast component, distinctly seen in Fig. 5 just after the switching off of the irradiation, τ does not exceed a few minutes. A very small slope of the relaxation curves, observed 25 min after the switching off of the illumination, proves the existence of a practically stable component with a τ exceeding several hours. As will be shown in Sec. 3, the interval between these limiting values for τ is continuously filled in by intermediate relaxation components. At low temperatures, a predominant part of photoinduced absorption (about 90%) is produced by long-lived centers with lifetime τ exceeding the time τ_p at least by two orders of magnitude.

Note that the shape of the relaxation curve (Fig. 5) cannot be explained by the dependence of the relaxation time on the number of active charges, which decreases in the course of relaxation. Indeed, as is seen from Fig. 6, the shape of the relaxation curve is practically independent of the achieved level of photoinduced absorption, no matter how it is changed: by varying the intensity or duration of the pumping.

Thus there exists a practically stable residual contribution ΔK_{stab} to the photoinduced absorption. At 23 K, ΔK_{stab} amounts to about 90% of the initial ΔK value. As can be seen from Fig. 7, with rising temperature both the quantity ΔK_{stab} and its ratio to the saturation level decrease rapidly and monotonically. This points to a strong thermal acceleration of the relaxation of active charges, related to a decrease of τ_{dif}.

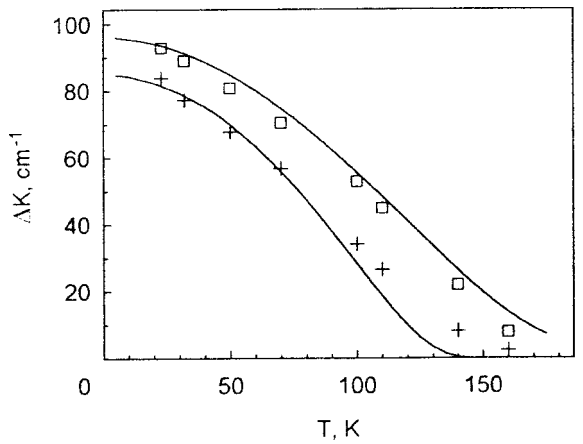

FIG. 7. Temperature dependences of the saturation level of the photoinduced absorption (upper curve) and of its stable part, defined as the ordinate of the corresponding relaxation curve 25 min after the switching off of the irradiation (lower curve). The squares and crosses denote experimental points; the solid lines show the solution of the kinetic Equation (31).

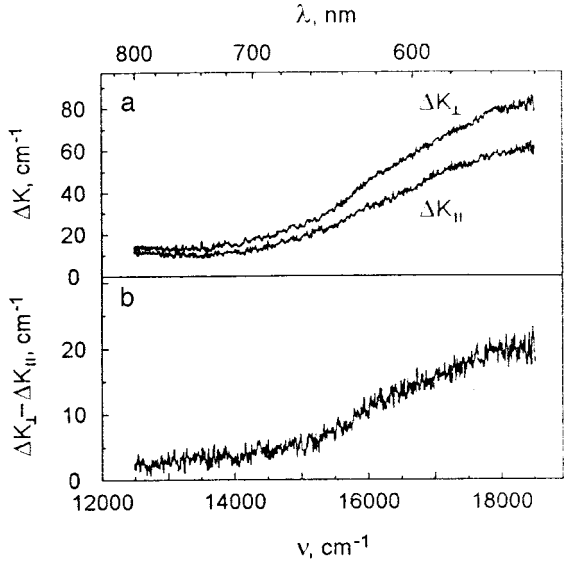

FIG. 8. Spectral dependences of the photoinduced addition to the absorption coefficient for the pumping light polarization [110] and the probe light polarizations [110] and $[\bar{1}10]$ ($\Delta K_{\parallel}$ and $\Delta K_{\perp}$, respectively) (a). Spectral dependence of the linear dichroism, defined as the difference of the above curves $\Delta K_{\perp}-\Delta K_{\parallel}$ (b). The measurements pertain to $T=35$ K and $\lambda=565$ nm.

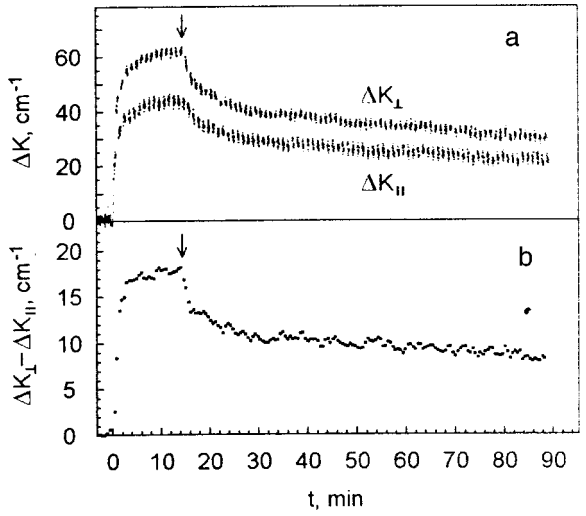

FIG. 9. Time dependences of the photoinduced addition to the absorption coefficient for the pumping light polarization [110] and the probe light polarizations [110] and $[\bar{1}10]$ ($\Delta K_{\parallel}$ and $\Delta K_{\perp}$, respectively) (a). Time dependence of the linear dichroism, defined as the difference of the above curves $\Delta K_{\perp}-\Delta K_{\parallel}$ (b). The measurements are related to $T=90$ K and $\lambda=565$ nm. The moment of the switching off of the illumination is indicated by an arrow.

2.3. Experimental results: Photoinduced dichroism

Figure 8 presents the spectrum of photoinduced dichroism, measured under pumping with linearly polarized light, together with the photoinduced absorption spectra measured with the probe light polarized parallel and perpendicular relative to the pump light. The similarity of all three spectra provides evidence that photoinduced dichroism and absorption are due to the same optical centers and to closely interconnected mechanisms. This conclusion is corroborated by the practical coincidence of the relaxation kinetics measured for dichroism and absorption after the switching off of the irradiation (Figs. 5, 9, and 10).

However, the temperature dependences of the saturation level, measured under pumping for dichroism and absorption, differ somewhat in their character, as can be seen from a comparison of Figs. 7 and 11. The photoinduced dichroism (Fig. 11) depends only very weakly on temperature up to 100 K, whereas the photoinduced absorption (Fig. 7) diminishes in the same temperature interval by 40%. This is an indication of certain differences in the relaxation mechanisms, which will be analyzed below (Sec. 6).

For comparison, the corresponding data on photoinduced birefringence[14,15] are plotted in Figs. 10 and 11. The photoinduced dichroism and birefringence display a complete similarity in their time and temperature behavior.

Similarly to the photoinduced birefringence, the photoinduced dichroism can be eliminated by using unpolarized light (Fig. 12). Note that the time required for the complete elimination of photoinduced dichroism (about 4 min) coincides with the time for achieving the saturation level. If the direction of the pump polarization is changed by $\pi/2$, then the photoinduced dichroism is correspondingly rewritten during the same time interval of 4 min (Fig. 12).

The above-stated complete similarity between photoinduced dichroism and birefringence provides evidence for a common nature of these phenomena, which will be considered in Sec. 6.

3. NATURE OF THE PHOTOINDUCED ABSORPTION

All of the experimental findings will be used for reconstruction of the corresponding electronic processes. This problem will be solved below in two steps. At first, the mechanism of photoinduced absorption will be established on the basis of its experimental dependences on pumping intensity, time, and temperature. Then the experimental data on the dichroism will be used to derive some essential details of this mechanism.

The model of photoinduced absorption, which has to be developed on the basis of the experiments, must explain the broad distribution of photoinduced absorption centers over

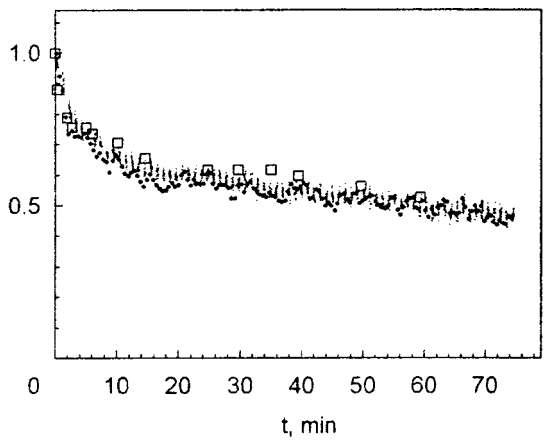

FIG. 10. Time dependence of the photoinduced absorption (dots) and dichroism (full circles) measured at $T=90$ K and $\lambda=565$ nm after the moment of the switching off of the irradiation, $t=0$. For comparison, the time dependence of the photoinduced birefringence[15] is plotted by the squares. All curves are normalized to unity at $t=0$.

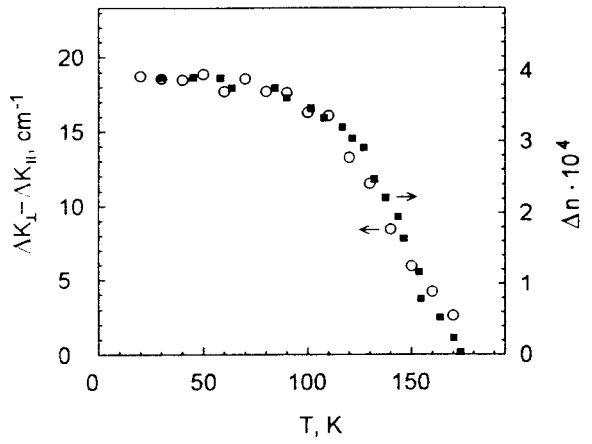

FIG. 11. Saturation values of the photoinduced dichroism (circles, left scale) and birefringence[14] (squares, right scale) measured versus temperature.

relaxation times. To clarify the mechanism of photoinduced absorption, two alternatives could be considered:

a) The photoinduced absorption is caused by some new absorption centers produced by photoillumination of the crystal. They are different from the Mn^{3+} ions responsible for the usual absorption in the absence of illumination and, hence, can be related to some impurities or lattice defects.

b) The photoinduced absorption is associated with the same Mn^{3+} ions that are responsible for absorption in the absence of illumination. Under irradiation, this absorption is enhanced by active charges which partially lift (mainly by their electric fields) the forbiddenness of the ${}^5E_g \rightarrow {}^5T_{2g}$ optical transition in Mn^{3+} ions. On the other hand, the electric fields of the active charges strongly affect their lifetime, resulting in their broad distribution over lifetimes. Such a pattern is suggested by the similarity of the spectral dependences of the initial absorption and its photoinduced augmentation.

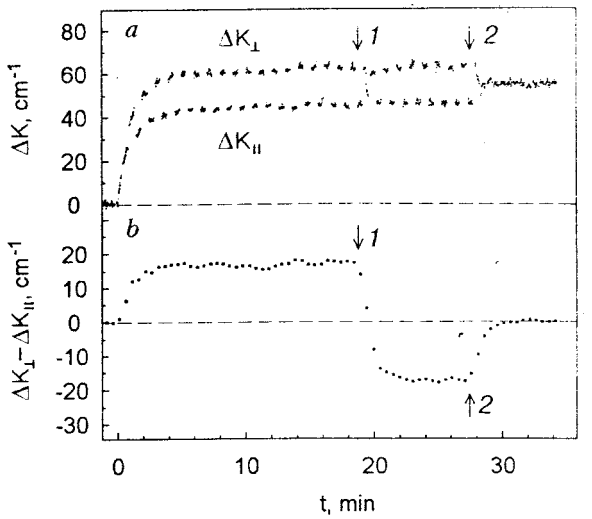

FIG. 12. Time dependence of $\Delta K_\perp$ and $\Delta K_\parallel$ (a) and of the photoinduced dichroism $\Delta K_\perp - \Delta K_\parallel$ (b) measured at $T = 90$ K under varying conditions of pumping. At the moment *1* (indicated by arrow), the direction of the pumping polarization was turned by 90°; at the moment *2*, the polarized pumping was changed to an unpolarized one.

The model (a) should be discarded for the following reason. The photoinduced absorption centers responsible for the observed relaxation scenario (Fig. 5) must have different relaxation times $\tau_1, \tau_2, \ldots$, the shortest of which being less than 2 min and the longest amounting to at least several hours. As the temperature rises, the times τ_j strongly shorten (which follows from the diminution of the photoinduced absorption), whereas the shape of the relaxation curve varies rather weakly, and the stable part of the photoinduced absorption decreases monotonically (Fig. 7). This means that with increasing temperature all of the relaxation components move to the left along the τ axis with nearly the same rates, each of them being replaced by the nearest component with a longer τ. Such a scenario implies the existence of a large number of relaxation components with a regular distribution on the τ axis and with an approximately equal activation energies. For relaxation components associated with impurity or defect centers, this is highly improbable.

The exact meaning of this statement can be expressed in terms of a kinetic equation written under the assumption (a). Taking into account the broad lifetime distribution of photoinduced absorption centers (see Fig. 5), we classify them by their lifetimes τ_j in the excited state. The number $n_j(T,t)$ of excited centers of the jth type is described by the kinetic equation

$$\partial n_j(T,t)/\partial t = I_j(n_{0j} - n_j) - n_j \Gamma_j(T). \tag{4}$$

Here n_{0j} is the total number of centers of the jth type; n_j or $n_{0j} - n_j$ is their number in the excited or ground state, respectively; I_j stands for their pumping rate; $\Gamma_j = 1/\tau_j$ is relaxation rate, and T is the temperature. The excited centers of the jth type make a contribution $\alpha_j n_j$ to the photoinduced absorption. Equation (4) is easily solved in the relaxation regime after the switching off of the irradiation. As the initial condition, we use the stationary solution of Eq. (4) under pumping in the regime of saturation. Finally, the photoinduced augmentation to the absorption coefficient takes on the form

$$\Delta K(T,t) = \sum_j \alpha_j n_j(t) = \sum_j \{\alpha_j n_{0j}/[1+\gamma_j(T)]\} \times \exp\{-t\Gamma_j(T)\} \tag{5}$$

with $\gamma_j = \Gamma_j(T)/I_j$ (the time t is counted from the moment where the illumination is switched off).

Let us separate from the sum (5) a practically stable photoinduced contribution to the absorption, $\Delta K_{\text{stab}}(T)$, related to relaxation components with very low relaxation rates $\Gamma_j < \Gamma_{\text{stab}} \lesssim (300\,\text{min}^{-1})$:

$$\Delta K_{\text{stab}}(T) = \sum{}' \alpha_j n_{0j}. \tag{6}$$

Here the summation goes over indices j for which $\Gamma_j(T) < \Gamma_{\text{stab}}$, the summands $\alpha_j n_{0j}$ not depending on temperature.

With rising temperature the sum (6) diminishes due to a decrease in the number of summands for which $\Gamma_j(T)$ remains less than Γ_{stab}. To fit Eq. (6) with the monotonic temperature dependence $\Delta K_{\text{stab}}(T)$ shown in Fig. 7, it is nec-

essary to assume that each of the sequences $n_{0j}\alpha_j$ and $\Gamma_j(T)$ is of regular character and that the latter retains its character over a broad temperature range in which the quantities $\Gamma_j(T)$ vary considerably. Since it is very improbable that such relaxation components originate from the presence of a variety of impurity centers, it is more plausible to suggest the existence of some identical active centers relaxing under different conditions. Such a mechanism is developed below.

4. PHOTOINDUCED ABSORPTION: MODEL OF FORBIDDEN OPTICAL TRANSITIONS ENHANCED BY RANDOM ELECTRIC FIELDS

4.1. Random fields, their role, and the distribution over magnitudes

The model of random electric fields is based on the well-established fact of the presence of Mn^{4+} ions in the $Ca_3Mn_2Ge_3O_{12}$ garnet.[19,20] An estimation shows that the electric field of these ions, which are contained in a concentration of a few hundredths of an atomic percent, is sufficient to noticeably enhance the probability of the forbidden optical transition ${}^5E_g \rightarrow {}^5T_{2g}$ between even Mn^{3+} states (because the electric field produces an odd addition to an even state). The model of random electric fields consists in the following.

Since the crystal as a whole must be electrically neutral, it contains negative impurity ions or cation vacancies (for brevity we will speak about impurity ions with unit effective charge). The concentration of these impurities coincides with that of Mn^{4+} ions. The electrostatic energy is minimized if the excess positive charges, i.e., Mn-holes, occupy positions adjacent to negative impurity charges in the Mn^{3+} sublattice. Hence, in the ground state all charges form coupled pairs, i.e., dipoles with a length of a few angstroms. Under photoillumination, some electrons are transferred from regular Mn^{3+} ions to Mn^{4+} ions coupled with such negative impurities, thus creating pairs of spatially separated charges of opposite signs (as shown in Fig. 1). These active charges produce electric fields extending into a larger space than for coupled pairs and therefore enhance the probability of the forbidden optical transition. At low concentrations N of active charges, the photoinduced absorption is proportional to N.

On the other hand, the random electric fields of active charges promote hops of holes between Mn ions, which accelerates their recombination with negative impurity charges (for brevity, we use the term recombination as a synonym for the formation of an inactive coupled pair from an active charge and a negative impurity ion). The hopping probability, which determines the lifetime of the active charges, depends on the magnitude of the random electric field. Below we will consider their distribution over magnitudes (Sec. 4.1.), the corresponding lifetime of active charges (Sec. 4.2.), and their kinetics (Secs. 4.3. and 4.4.).

Active charges (numbered by the subscript i) create at a fixed point A random fields $\mathbf{F}_i$ which are assumed to be statistically independent. The squared total field per unit volume at the point A, averaged over random positions of charges, is estimated by

$$\langle \mathbf{F}^2 \rangle \equiv 3\langle F_x^2 \rangle = \sum_i \langle F_i^2 \rangle = \int_{\beta N^{-1/3}}^{\infty} (e/\varepsilon r^2)^2 N 4\pi r^2 dr = 4\pi N^{-4/3}(e^2/\varepsilon^2\beta). \tag{7}$$

Here x,y,z are the equivalent Cartesian axes; N is the number of active charges per unit volume; β is a numerical constant defined below; e stands for the unit charge, and $\varepsilon \approx 3\varepsilon_0/(2+\varepsilon_0) \approx 2$ is the effective permittivity (ε_0 is the static permittivity of the crystal). The integration in (7) is carried out over the distance r of active charges from the point A; the lower limit of the integration is chosen as a characteristic distance between active charges $\beta N^{-1/3}$.

Since the x component of the total field, $F_x = \Sigma F_{ix}$, consists of statistically independent summands, one can write its distribution function in the form of a Gaussian:

$$p_x(F_x) = (2\pi\langle F_x^2 \rangle)^{-1/2} \exp(-F_x^2/2\langle F_x^2 \rangle). \tag{8}$$

Changing to spherical coordinates in $\mathbf{F}$ space, we obtain the magnitude distribution of the random electric fields:

$$P(F) = (3^{3/2}\beta^{3/2}\varepsilon^3/2^{5/2}\pi e^3 N^2)F^2 \times \exp(-3F^2\varepsilon^2\beta/8\pi e^2 N^{4/3}), \quad \beta \cong 0.18. \tag{9}$$

The numerical parameter β was defined by equating the moment $\langle F^4 \rangle$, derived from (9), to its value obtained by summation over active charges as in (7).

4.2. Lifetime of the active charges—hole polarons

Positive active charges, localized on Mn^{3+} ions, form hole polarons. Their hopping within the Mn sublattice results in the disappearance of active charges via formation of coupled pairs with negative impurity ions. Below we will assume that the relaxation rate Γ of active charges via this channel is proportional to the rate of the hole polaron hopping between adjacent Mn^{3+} ions. The rate of hole hopping depends on the electric field and has a large straggle corresponding to the broad distribution (9) of the magnitude of the electric field.

Note that such an approximation can overestimate the relaxation rate of long-lived active charges after the switching off of the irradiation. Indeed, the totality of holes, in the course of their diffusive motion, rearranges to achieve a local minimum of the electrostatic energy. Such a metastable configuration of holes can have a very large lifetime, significantly exceeding the characteristic time of single-hole diffusion.

Now let us consider the probability of hole hopping from the ion A, where it is localized, to another ion B. At first the electric field is put equal to zero. If a hole remains at the ion A, the energy E_e of the electronic subsystem depends on the coordinates x_n of adjacent atoms:

$$E_e = -\sum_n C_n x_n \tag{10}$$

(the energy is linearized in the coordinates x_n, which are counted from their equilibrium position in the absence of

holes). The total energy of the crystal includes the electronic energy (10) and the lattice deformation energy, which is quadric in x_n:

$$E_{\text{tot}} = -\sum_n C_n x_n + \sum_n K_n x_n^2/2$$

$$\equiv \frac{1}{2}\sum_n [-C_n^2/K_n + K_n(x_n - x_{0n})^2]. \quad (11)$$

Here $x_{0n} = C_n/K_n$ is the equilibrium value of the coordinate x_n in the presence of the localized hole. Equation (11) allows one to perform the high-temperature thermodynamic averaging

$$\langle (x_n - x_{0n})^2 \rangle = T/K_n \quad (12)$$

(temperature is expressed in energy units).

To simplify the calculations, they will be carried out using Eq. (12), but the final result will be extended to the case of an arbitrary temperature.

Let a hole hop from the ion *A* to an equivalent ion *B*. At the moment of hopping the surroundings of the ion *A* are in equilibrium with the hole ($x_{nA} \equiv x_{0n}$), but those of the ion *B* are the same as in the ideal lattice ($x_{nB} \cong 0$). Before the hop the electronic energy (10) is

$$-\Delta = -\sum_n C_n x_{0n} = -\sum_n C_n^2/K_n, \quad (13)$$

and just after the hop the electronic energy equals zero. Thus, hopping requires a fluctuation to overcome the energy gap Δ (it is just this gap which conditions the existence of stable active charges). The *A*-to-*B* hopping of the hole is promoted, to the same degree, by fluctuations of the surroundings of both the atoms *A* and *B*. For brevity we will consider only the fluctuation around the atom *A*, but the final result will be written down with allowance for the fluctuations around both atoms.

The *A*-to-*B* hopping of a hole requires a fluctuation of the coordinates $x_n \equiv x_{nA}$ which turns the electronic energy (10) to zero before hopping. (Eq. (10) relates to the lattice being in equilibrium with the electronic subsystem before the hop). This condition can be presented in the form

$$\sum_n y_n = -\Delta, y_n \equiv (x_n - x_{0n})C_n, \quad x_{0n} = C_n/K_n. \quad (14)$$

The sum $y = \Sigma y_n$ of statistically independent coordinates has the distribution function

$$f(y) = \text{const} \exp(-y^2/2\sigma^2). \quad (15)$$

Using Eqs. (14) and (12), we can write the variance σ^2 as

$$\sigma^2 = \sum_n \langle y_n^2 \rangle = T\sum_n C_n^2/K_n. \quad (16)$$

The *A*-to-*B* hop of a hole becomes possible if y attains the gap $\Delta = \Sigma C_n^2/K_n$ between the hole levels after and before the jump. Therefore, the hopping probability is proportional to $f(\Delta)$. In the presence of a field applied in a favorable direction, the gap is reduced by the value *Fea*, where *a* is the distance between the sites *A* and *B*. Finally, the rate of the active charge relaxation, considered to be proportional to the probability of the *A*-to-*B* hopping per unit time, can be written with allowance for (15) and (16) in the form:

$$\Gamma = \Gamma_0 \exp(-\Delta/4T_{\text{eff}} + Fea/2T_{\text{eff}}). \quad (17)$$

Expression (17) is written in the final form, taking into account two essential details which were omitted in the course of the calculations for brevity. First, the temperature T is replaced by an effective temperature T_{eff}, which coincides with T at high temperatures and allows for the zero-point vibrations of the lattice at low temperatures. In the Debye approximation, T_{eff} is defined as $A\langle(\mathbf{r} - \mathbf{r}_0)^2\rangle$, where $\mathbf{r}$ is the radius vector of an atom in the ideal lattice, $\mathbf{r}_0$ is that of the corresponding site, and the choice of the constant A provides the coincidence of T_{eff} with T at high temperatures. This definition can be rewritten in the explicit form

$$T_{\text{eff}} = (2T^2/\hbar\omega_D)\int_0^{\hbar\omega_D/2T} x \coth x\, dx \quad (18)$$

with the Debye frequency ω_D.

Second, Eq. (17) makes allowance not only for the fluctuations in the surroundings of the atom *A* but also for those related to the atom *B* (which results in the additional coefficient 2 multiplying T_{eff}).

4.3. Kinetic equation for active charges in a general form

Within the model of random electric fields developed above, the kinetic equation differs essentially from its simple form (4). The differences will be discussed in what follows.

Active charges are divided into groups, n_j, according to their lifetimes $\tau_j = \Gamma_j^{-1}$. The F axis is divided into M intervals ΔF_j (with centers at the points F_j) in a way providing equal probabilities for an arising active charge to fall in each interval ΔF_j:

$$\int_0^{F_j} P(F)dF = (j - 0.5)/M, \Delta F_j P(F_j) = 1/M, \quad j = 1,...,M \quad (19)$$

where $P(F)$ is the distribution function (9) for the magnitudes of the random fields. For an active charge of the jth group, the recombination rate is

$$\Gamma_j \equiv \Gamma(F_j) = \Gamma_0 \exp(-\Delta/4T_{\text{eff}} + F_j ea/2T_{\text{eff}}). \quad (20)$$

Photoillumination supplies active charges to each of the M groups with the same probability, which should be understood as follows. Light pumping transfers J electrons per unit time from Mn^{3+} ions either to Mn^{4+} ions (with a probability p) or to coupled pairs of charges (with probability $1-p$). The total number of active positive charges is increased through the latter channel by the value $N_+ = J(1-p)$ and decreased through the former channel by $N_- = Jp$. While the number N_+ of generated charges is uniformly distributed among the M groups, the loss N_- of charges is distributed among these groups in proportion to their populations. The probability $p = p(N)$ increases with the total number N of active charges per unit volume.

Thus one can write the kinetic equation for the populations of the M groups of active charges:

$$dn_j/dt = J[1/M - p(N)n_j/N] - \hat{\Gamma} n_j. \quad (21)$$

Here $\hat{\Gamma}$ stands for the recombination operator, which in a rough approximation can be written simply as the recombination rate Γ_j of an active charge at the moment of its generation by pumping. In fact, however, Γ varies as a function of electric field during the active charge lifetime due to random changes in the positions of other active charges (this will be allowed for in Sec. 4.4).

The kinetic Eq. (21) describes the experimentally observed regularities. The lifetime distribution of active charges, given by Eqs. (9) and (17), is continuous and covers a very broad range (about five orders of magnitude at $T=100\,\mathrm{K}$ and an active charge concentration of 0.1%). The kinetic Eq. (21) describes the saturation of the number of active charges with increasing exposition time or pumping intensity, irrespective of the relaxation by hole hopping. Indeed, in the limiting case of zero hopping rate, Eq. (21) after summation over j turns into

$$dN/dt=J[1-p(N)] \quad \text{at} \quad \Gamma_j=0. \tag{22}$$

As N increases, $p(N)$ grows and nears unity, so that dN/dt goes to zero. Let us introduce the characteristic value N_0 of the number of active charges at which the total growth rate is slowed down by a factor of two:

$$p(N_0)=0.5. \tag{23}$$

N_0 defines the scale of the saturation number of active charges under very strong pumping. Note that the characteristic number of active charges N_0 is much less than the number of inactive coupled pairs, N_{coup}:

$$N_0 \ll N_{\mathrm{coup}}. \tag{24}$$

Indeed, at $N=N_0$ the total probability of electron trapping by any active charge is equal to that of electron trapping by any coupled pair. However, in the former case the trapping cross section is much larger than in the latter case due to the stronger field produced by an active charge. Hence, the total number of coupled pairs must correspondingly exceed that of active charges.

4.4. Specific form of the kinetic equation with a model description of generation and recombination of active charges

To carry out a quantitative comparison of the kinetic Eq. (21) with experiment, it is necessary to give concrete definitions of the recombination operator Γ and the probability $p(N)$ appearing in (21). In view of the highly complicated character of the corresponding physical processes, this will be done below in a model way.

At the moment of its generation, an active charge of the jth group has the recombination rate (20) determined by the random field value F_j. After that, the recombination rate of this charge varies due to electric field variations caused by the disappearance and generation of other active charges at random points. The random field F and the corresponding recombination rate of a given active charge are changed substantially when a significant fraction of the other active charges is replaced by new generated charges. The fraction of new active charges, generated during the time dt, is $Jdt/N(t)$. This quantity, integrated over time, can serve as a measure of the corresponding change in the argument of Γ_j. Within the model, this is allowed for through a shift in the argument of the monotonically growing sequence $\Gamma_j (j=1,\ldots,M)$:

$$\hat{\Gamma} n_j = n_j \Gamma_{j+Ms}, s(t)=\int_0^t Jdt/N(t) \tag{25}$$

(the definition of Γ_j in Eq. (20) is periodically extended over the infinite interval j with the period M). The lower limit of integration in (25) does not play any role: a constant addition to $s(t)$ only redefines the numbering of the active charge groups, which has no physical consequences.

Now let us consider the probability p for an electron, removed by pumping from a Mn^{3+} ion, to be captured by one of the positive active charges (the alternative possibility is its capture by one of the inactive coupled pairs). Let us assume that an electron is captured by an active charge under the condition

$$F_{\mathrm{act}} \equiv 1/\varepsilon r^2 > F_{\mathrm{bac}} \tag{26}$$

where F_{act} is the electric field of an active charge at the distance r and F_{bac} is the characteristic magnitude of the background field of coupled pairs (according to (24), their number greatly exceeds the number of active charges). F_{bac}^2 can be estimated as the squared field of the dipole $\mathbf{d}$, $F_0^2 = 2d^2/R^6\varepsilon^2$, averaged over its orientations ($R=N_{\mathrm{coup}}^{-1/3}$ is the mean distance between the dipoles). The quantity F_0^2 should be multiplied by the actual number Z of dipoles with the moment $d=ea$, where a is the lattice constant. (Below we set $Z=12$ as for a close-packed lattice). Thus the condition (26) of electron trapping by an active charge takes the form

$$r < r_0, \quad r_0 \equiv (24)^{-1/4}(aN_{\mathrm{coup}})^{-1/2}. \tag{27}$$

The condition (27) is not met only if *none* of the NV active charges, randomly situated in the crystal volume V, is found inside the spherical volume $V_0=(4/3)\pi r_0^3 \ll V$. The probability for *one* active charge to be found outside the sphere is $1-V_0/V$; for NV charges this quantity should be raised to the power NV, resulting in $\exp(-NV_0)$. Thus, the probability for the condition (27) to be fulfilled is

$$p(N)=1-\exp(-NV_0)=1-\exp[-(4/3)\pi N r_0^3], \tag{28}$$

where r_0 is defined by Eq. (27).

We would like to remark that the probability $p(N)$ could be defined in some other model way; however, the calculations show that this would not exert any noticeable effect on the solution of the kinetic equation.

According to the definition (23), the characteristic number of active charges per unit volume is

$$N_0 = 1.8(aN_{\mathrm{coup}})^{3/2}. \tag{29}$$

Note that this relation meets the inequality (24).

To simplify the form of the kinetic Eq. (21), let us introduce the number v of active charges expressed in units of N_0:

$$v=N/N_0, \quad v_j=n_j/N_0, \quad v=\sum_j v_j. \tag{30}$$

Now the kinetic equation takes the form

$$dv_j/dt = I\left[\frac{1}{M} - (1-2^{-v})v_j/v\right] - v_j\Gamma_{j+Ms(t)},$$
$$s(t) \equiv \int_0^t Idt/v(t) \tag{31}$$

where I is the pumping intensity in some units. (I is proportional to the experimental pumping intensity i).

5. PHOTOINDUCED ABSORPTION. COMPARISON OF THE THEORY WITH EXPERIMENT

The problem under consideration is specified by the following physical parameters:

i) The number a^3N_{coup} of negative impurity ions that form coupled pairs of charges in the ground state, per unit cell. The corresponding number of active charges per unit cell is $1.8v(a^3N_{\text{coup}})^{3/2}$. These parameters specify the distribution function (9) of the electric fields.

ii) The depth Δ of the deformation potential well of a Mn-hole polaron.

iii) The Debye frequency ω_D, which specifies the effective temperature (18) and together with the parameters Δ and Γ_0 determines the recombination rate (17) as a function of temperature.

iv) The proportionality coefficient between N and ΔK and that between I and the experimental pumping intensity i are chosen as fitting parameters.

The solution of the kinetic Eq. (31) is fitted best to the entirety of experimental data for the following set of parameters: $\Delta = 1.08\,\text{eV} = 12500\,\text{K}$; $\hbar\omega_D = 0.035\,\text{eV} = 400\,\text{K}$; $\Gamma_0 = 7\times10^5\,\text{s}^{-1}$. The characteristic number N_0a^3 of active centers per unit cell is equal to 0.2%, and the number of active centers achieved under full pumping ($i=1$), amounts to 0.08%. The corresponding number of coupled pairs of charges per unit cell is 1%.

These values of the parameters seem reasonable for a solid. In particular, active charges of the given concentration create an electric field of about 1.5×10^6 V/cm, which is roughly 300 times less than the intra-atomic field. This leads to an oscillator strength of about 10^{-5} for a forbidden transition. In the visible range this corresponds to an absorption coefficient of the order of 100 cm^{-1}, which is in qualitative agreement with experiment. The rather large depth of the polaronic potential well ($\Delta = 1.08$ eV) is associated with the circumstance that the Jahn–Teller lattice deformation changes during the Mn-hole hopping.

Let us compare the solution of the kinetic Eq. (31), obtained for this set of parameters, with the experimental data. In Figs. 4, 5, 7 the solid lines show the calculated augmentation of the absorption coefficient, ΔK, produced and measured with unpolarized light. The figures demonstrate a qualitative agreement of the theory with the experiment within broad ranges of temperature and pumping intensity, both under irradiation with light and after the pumping is switched off.

In the latter case, the calculated relaxation rate of the total photoinduced absorption (solid lines in Fig. 5) systematically exceeds the experimental one. To all appearance, this discrepancy originates from multiparticle phenomena (mentioned at the beginning of Sec. 4.2.) which have not been taken into account in the above theory.

Attention should be drawn also to another discrepancy between the theory and experiment shown in Fig. 5. In the basic assumptions (Sec. 1, Item 4) and in the theory, the response of the crystal to pumping is described by one characteristic time. Such a description, however, is not quite exact. As can be seen from Fig. 5, the experimental time dependences of photoinduced absorption under pumping, measured at various temperatures, exhibit at least two characteristic times t_1 and $t_2 \gg t_1$. At first, the absorption grows fast during the time $t_1 \cong 2$ min, but this fast growth stops at the level $\Delta K(\infty) - K_1$ near the complete saturation level $\Delta K(\infty)(K_1 \ll \Delta K(\infty))$. After that, the absorption reaches complete saturation much more slowly, with the characteristic time $t_2 \cong 10$ min.

The theory developed above describes the fast process only. The slow process can be associated with deep hole traps (probably Mn^{3+} ions located in the vicinity of some lattice defects). Initially the traps are empty and neutral, but after filling by holes they begin to act as stable active charges with an infinite recombination time τ (a pinned hole cannot recombine with a pinned negative charge). At low temperatures, the contribution of trapped holes to the photoinduced absorption amounts to about 10%; hence, their concentration is ten times less than the total concentration of active charges and amounts to $c_{\text{tr}} \cong 2\times10^{-4}$. Due to their low concentration, the traps are filled slowly, which explains the large characteristic time t_2.

The contribution of filled traps to the absorption, presented in Fig. 5 by the experimental curves, can be satisfactorily described in the exponential form

$$\Delta K_{\text{tr}}(t) = K_1[1 - \exp(-t/t_2)], \tag{32}$$

with parameters that are almost constant in the temperature range $T \leqslant 100$ K: $K_1 \cong 10\,\text{cm}^{-1}$ and $t_2 \cong 7$ min. At $T = T_1 = 130$ K, K_1 diminishes by roughly a factor of two. This allows us to estimate the trap depth as $T_1 \ln(1/c_{\text{tr}}) \cong 1100\,\text{K} = 0.1$ eV.

6. PHOTOINDUCED DICHROISM: ADDITIONAL INFORMATION ON ELECTRONIC PROCESSES

As was already noted, photoinduced dichroism and birefringence are of the same nature: they display quite similar temperature dependences and relaxation curves after the switching off of the irradiation. Earlier,[13] the observed dependence of birefringence on the pumping polarization direction was described with the crystallographic structure of the $Ca_3Mn_2Ge_3O_{12}$ garnet taken into account. Below, this mechanism is generalized somewhat to include birefringence and dichroism simultaneously.

The environment of each Mn^{3+} ion has the symmetry of a distorted octahedron. This distortion eliminates the degeneracy of the angular $3d$ states of the Mn-hole localized at the center of the octahedron. For brevity, the polarization axis of the hole state with the minimal energy will be called the octahedron axis (it may coincide, for example, with the tetragonal axis along which the octahedron is contracted due to the Jahn–Teller deformation of the lattice; note that the en-

ergy scale of the Jahn–Teller effect exceeds that of the temperature within the temperature region examined). At low temperatures, all the occupied hole states are polarized along the octahedron axes. The total set of octahedrons can be divided into chains in such a way that octahedron axes have nearly the same direction within the same chain, but the axis directions differ strongly for chains of different types.

The direction of the pumping light polarization dictates the predominant polarization of generated holes, i.e., the type of chains predominantly occupied by holes. Thus a polarized pumping induces anisotropy of the optical properties, which manifests itself both in birefringence and in dichroism.

It can be seen from Fig. 10 that the relaxation curves of photoinduced dichroism and birefringence practically coincide with the relaxation curve of the photoinduced absorption. This means that after the switching off of the irradiation, the hole polarization and the active charge itself relax in the same way: the initial polarization direction persists until the hole forms a coupled pair with a negative impurity. In other words, a hole retains its polarization direction when hopping between adjacent Mn ions.

Based on this, the relaxation process can be generally described as follows. After the illumination is switched off, a hole hops within the same chain until recombination with a negative impurity charge occurs. The probability for a hole to meet an impurity charge just in the same chain is negligibly small. However, a hole can leave the chain in the strong field of a negative charge lying near the chain, thus changing its polarization and simultaneously disappearing as an active charge (forming an inactive coupled pair).

Now let us call attention to the different temperature dependences of the photoinduced dichroism (Fig. 11) and absorption (Fig. 7, upper curve) measured under pumping after saturation. This difference suggests that pumping modifies the relaxation process somewhat. During relaxation without pumping, as was mentioned in Sec. 4.2., the totality of active charges is rapidly rearranged to minimize their electrostatic energy; because of this the random electric fields are weak and insufficient to force a hole to leave its chain. However, pumping rapidly changes the configuration of active charges and strongly enhances the straggling of their fields. In the course of relaxation *under pumping*, a hole can find itself in a strong random field, which causes it to leave the chain and to change polarization even far from negative impurities. Thus, pumping gives rise to a new relaxation channel which affects only the dichroism. This can explain the observed distinction of its temperature dependence under pumping from that of the photoinduced absorption.

In more detail, this distinction can be understood under the assumption that the two types of hole motion—hopping within the same chain and hopping between different chains in a strong field—are associated with different sets of lattice vibrations. In Sec. 4.2., the relaxation of active charges (i.e., hole hopping within a chain) was satisfactorily described in the Debye approximation, which involves the total set of frequencies. Low-frequency vibrations from this set are responsible for a decrease of photoinduced absorption with increasing temperature, both with and without pumping. To all appearances, hole hopping between different chains is associated with a set of sufficiently high frequencies. The amplitudes of such vibrations begin to increase with temperature only above 100 K, which explains the rather weak temperature dependence of the dichroism measured under pumping (supposing that dichroism relaxes mainly through hopping between chains). In the absence of pumping, this relaxation channel is inactive, and dichroism relaxes only through hopping within the same chain (associated with low-frequency vibrations of the lattice). This explains the noticeable temperature dependence of the relaxation rate in the total interval of temperatures, observed in the absence of pumping for the dichroism and birefringence (as well as for photoinduced absorption).

CONCLUSION

Experiments performed with the garnet $Ca_3Mn_2Ge_3O_{12}$ display unusual features of the photoinduced absorption:

— saturation of the photoinduced absorption with pumping intensity;

— a broad distribution of photoinduced absorption centers over relaxation times, with the predominance of very long times;

— coincidence of the relaxation rates of photoinduced absorption and dichroism and a noticeable difference between their temperature dependences under pumping.

Such experimental results cannot be understood in terms of photoinduced absorption centers associated with impurities or lattice defects. Within the notion of random electric fields, a quite natural explanation can be given: the Mn^{3+} sublattice of the $Ca_3Mn_2Ge_3O_{12}$ garnet contains Mn^{4+} ions (i.e., Mn-holes) in a low concentration.[19,20] Since the crystal as a whole must be electrically neutral, it contains negative impurity ions or cation vacancies in the corresponding concentration. In the ground state, the Mn-holes occupy Mn sites adjacent to negative impurity charges. Such coupled pairs of opposite charges are inactive in the sense that their electric field is very weak in the major part of the crystal volume.

Under photoillumination, a small number of electrons are transferred from regular Mn^{3+} ions to the Mn^{4+} components of coupled pairs, thus creating pairs of spatially separated charges of opposite signs (active charges). Active charges create electric fields in a larger volume than coupled pairs and correspondingly enhance the probability of the forbidden optical transition. At low concentrations of active charges, the photoinduced absorption is proportional to it. Photoinduced dichroism is caused by the predominant generation of holes polarized in a fixed direction. They are responsible for an anisotropic distortion of their surroundings which entails dichroism and birefringence (their time and temperature dependences are quite similar).

The random electric fields of active charges simultaneously manifest themselves in another way: they promote the relaxation of photoinduced changes through hopping of holes. A broad distribution of the magnitudes of the random fields gives rise to a very broad range of hole hopping rates and, hence, of the lifetimes of the photoinduced changes.

Simultaneously, the existing active charges annihilate during the photoproduction of new active charges: electrons, removed from Mn^{3+} ions by pumping, are also transferred to active charges (Mn^{4+} ions). The characteristic time of this

annihilation channel is inversely proportional to the pumping intensity. Under an increase of the pumping intensity this relaxation channel becomes predominant, which results in the saturation of photoinduced changes with pumping.

Photoinduced dichroism and birefringence display the same temperature dependence under pumping and the same time dependence after switching off the irradiation. This provides evidence for a similar nature of photoinduced dichroism and birefringence: they are caused by the anisotropic distribution of Mn-holes, created by polarized pumping, over the polarization directions. The coincidence of the relaxation curves of the photoinduced absorption and dichroism can be seen as a hint that Mn-holes retain their polarization direction when hopping; this can be explained by taking into account some structural features of the $Ca_3Mn_2Ge_3O_{12}$ garnet.

The authors are grateful to Dr. J.-M. Desvigness (CNRS Laboratoire de Physique des Solides, Meudon-Bellevue, France) for providing $Ca_3Mn_2Ge_3O_{12}$ single crystals. This research was partly supported by INTAS Grant No. 96-626 and INTAS Grant No. 97-366.

*E-mail: piryatinskaya@ilt.kharkov.ua

[1] R. W. Teale and D. W. Temple, Phys. Rev. Lett. **19**, 904 (1967).
[2] R. F. Pearson, A. D. Annis, and P. Kompfner, Phys. Rev. Lett. **21**, 1805 (1968).
[3] J. F. Dillon, E. M. Gyorgy, and J. P. Remeika, Phys. Rev. Lett. **23**, 643 (1969).
[4] V. F. Kovalenko, E. S. Kolezhuk, and P. S. Kuts, Zh. Éksp. Teor. Fiz. **81**, 1399 (1981) [Sov. Phys. JETP **54**, 742 (1981)].
[5] K. Hisatake, K. Ohta, N. Ichinose, and H. Yokoyama, Phys. Status Solidi A **26**, K75 (1974).
[6] M. Pardavi-Horvath, P. E. Wigen, and G. Vertesy, J. Appl. Phys. **63**, 3110 (1988).
[7] H. Van der Heide and U. Enz, Solid State Commun. **6**, 347 (1968).
[8] W. Lems, R. Metselaar, P. J. Rijnierse, and U. Enz, J. Appl. Phys. **41**, 1248 (1970).
[9] V. G. Veselago, N. V. Vorob'ev, and R. D. Doroshenko, JETP Lett. **45**, 512 (1987).
[10] E. M. Gyorgy, J. F. Dillon, and J. P. Remeika, J. Appl. Phys. **42**, 1454 (1971).
[11] K. Hisatake, I. Matsubara, K. Maeda, H. Yasuoka, H. Mazaki, and K. Vematsu, J. Magn. Magn. Mater. **140–144**, 2127 (1995).
[12] V. A. Bedarev, S. L. Gnatchenko, R. A. Rupp, and B. Sugg, Fiz. Nizk. Temp. **24**, 281 (1998) [Low Temp. Phys. **24**, 212 (1998)].
[13] S. L. Gnatchenko, V. V. Eremenko, S. V. Sofroneev, and N. F. Kharchenko, JETP Lett. **38**, 233 (1983).
[14] S. L. Gnatchenko, N. F. Kharchenko, V. A. Bedarev, V. V. Eremenko, M. Artinian, J.-M. Desvignes, and H. Le Gall, Fiz. Nizk. Temp. **15**, 627 (1989) [Sov. J. Low Temp. Phys. **15**, 353 (1989)].
[15] V. A. Bedarev and S. L. Gnatchenko, Fiz. Nizk. Temp. **20** 124 (1994) [Low Temp. Phys. **20**, 100 (1994)].
[16] B. Sugg, S. L. Gnatchenko, and R. A. Rupp, J. Opt. Soc. Am. B **13**, 2662 (1996).
[17] R. Alben, E. M. Gyorgy, J. F. Dillon, and J. P. Remeika, Phys. Rev. B **5**, 2560 (1972).
[18] M. Wurlitzer and J. Franke, Phys. Status Solidi A **A64**, 539 (1981).
[19] A. E. Nosenko, B. V. Padlyak, and V. V. Kravchishin, Fiz. Tverd. Tela (Leningrad) **27**, 3455 (1985) [Sov. Phys. Solid State **27**, 2083 (1985)].
[20] B. V. Padlyak and A. E. Nosenko, Fiz. Tverd. Tela (Leningrad) **30**, 1788 (1988) [Sov. Phys. Solid State **30**, 1027 (1988)].
[21] Z. A. Kazei, P. Novak, and V. I. Sokolov, Zh. Éksp. Teor. Fiz. **83**, 1483 (1982) [Sov. Phys. JETP **56**, 854 (1982)].
[22] S. L. Gnatchenko, V. V. Eremenko, S. V. Sofroneev, N. F. Kharchenko, J.-M. Desvignes, P. Feldmann, and H. Le Gall, Zh. Éksp. Teor. Fiz. **90**, 179 (1986) [Sov. Phys. JETP **63**, 102 (1986)].
[23] W. Graeff, J. Kub, and K. Wieteska, Phys. Status Solidi A **A126**, 477 (1991).
[24] L. E. Orgel, J. Chem. Phys. **23**, 1004 (1955).
[25] R. Pappalardo, Philos. Mag. **2**, 1397 (1957).

This article was published in English in the original Russian journal. Reproduced here with stylistic changes by AIP.

Relaxation of Bloch oscillations of a magnetic soliton in a nonuniform magnetic field

I. M. Babich* and A. M. Kosevich

B. Verkin Institute for Low Temperature Physics and Engineering, National Academy of Sciences of Ukraine, pr. Lenina 47, 61164 Kharkov, Ukraine

(Submitted July 12, 2000)
Fiz. Nizk. Temp. **27**, 46–51 (January 2001)

The influence of damping on the Bloch oscillations arising in the motion of a magnetic soliton in an easy-axis one-dimensional ferromagnet in the presence of a small magnetic field gradient is investigated. The most interesting case, that of solitons with low frequencies and low velocities, is considered. In this case there are two soliton damping regimes. When the magnetic field gradient is greater than a critical value set by the damping, the soliton lifetime is considerably greater than the period of the Bloch oscillations. However, together with these oscillations there arises a translational motion of the soliton due to dissipation. If the magnetic field gradient is smaller than the critical value, then the Bloch oscillations vanish, and the soliton undergoes only translational motion.
[DOI: 10.1063/1.1344140]

INTRODUCTION

A characteristic feature of the nonlinear dynamics of the magnetization of ferromagnets and antiferromagnets is the existence of dynamical magnetic solitons. By a dynamical soliton we mean a spatially localized moving disturbance of the magnetization field in which the stability of the disturbance is ensured by the presence of certain integrals of the motion of the dynamical equations of the magnetization field. In the case of one-dimensional ferromagnets in which the long-wavelength dynamics of the magnetization is described by the Landau–Lifshitz equations, there is a complete description of all types of nonlinear excitations and, in particular, there exists an exact analytical solution for dynamical solitons in uniaxial magnets in a uniform magnetic field in the absence of dissipation.[1,2] Such solitons are characterized by two parameters: the velocity of their translation as a whole, and the frequency of precession of the magnetization in them.

In the presence of a small magnetic field gradient a soliton in a uniaxial ferromagnet executes oscillations with a frequency determined by the value of the gradient.[3,4] These are the so-called Bloch oscillations of the magnetic soliton, which are analogous to the oscillations of an electron in a crystal in an electric field. The same type of oscillatory motion is also inherent to solitons in discrete spin chains, the dynamics of which was investigated in Refs. 5 and 6. In discussing oscillations of this kind it is very important to consider the role of dissipative processes, which can lead to the complete vanishing of Bloch oscillations. Relaxation of a two-parameter soliton in an easy-axis ferromagnet was studied in Ref. 7 on the basis of the Landau–Lifshitz equations with dissipation. Here we consider the influence of dissipation on the Bloch oscillations of a soliton in a nonuniform magnetic field. Here, as in Refs. 3, 4, and 7, we restrict discussion to the case of a one-dimensional magnet, for which the problem can be solved analytically.

EQUATIONS

In a phenomenological description of the properties of ferromagnets, inclusion of the simplest types of relaxation leads to the following generalization of the Landau–Lifshitz equations:[7]

$$\frac{\partial \mathbf{M}}{\partial t} = -g[\mathbf{M}\times\mathbf{H}_{\text{eff}}] + gM\{\lambda_r[\mathbf{m}\times[\mathbf{H}_{\text{eff}}\times\mathbf{m}]] - \lambda_e a^2 \Delta \mathbf{H}_{\text{eff}}\}. \tag{1}$$

The magnetization vector $\mathbf{M}(\mathbf{r},t)$ describes the instantaneous state of the ferromagnet; a is the lattice constant, $g = 2\mu_0/\hbar$ is the gyromagnetic ratio (μ_0 is the Bohr magneton), and $\mathbf{m} = \mathbf{M}/M$. The effective magnetic field $\mathbf{H}_{\text{eff}}$ appearing in Eq. (1) is defined by the relation $\mathbf{H}_{\text{eff}} = -\delta E/\delta \mathbf{M}$, where E is the total energy of the magnet. The constants λ_r and λ_e characterize relaxation processes of different natures: λ_r corresponds to the relativistic damping, and λ_e to the exchange damping. Below we consider a one-dimensional ferromagnet in an external field $\mathbf{H}$ directed along the easy axis z. We introduce the polar angles θ and φ, so that $m_z = \cos\theta$, $m_x + i m_y = \sin\theta e^{i\varphi}$. Then the magnetic energy density w can be written as[1]

$$w(\theta,\varphi) = \frac{1}{2}\alpha(\partial \mathbf{M}/\partial x)^2 + \frac{1}{2}\beta M^2 \sin^2\theta + MH(1-\cos\theta), \tag{2}$$

where α is the exchange constant, β is the anisotropy constant, and the coordinate x specifies the position of the point in the one-dimensional magnet.

For a uniaxial ferromagnet the Landau–Lifshitz equation (1) in the absence of dissipation ($\lambda_r = \lambda_e = 0$) always has two integrals of the motion:[1] the total energy of magnetic excitation,

$$E = a^2 \int w(\theta,\varphi)\, dx \tag{3}$$

and the projection of the total magnetic moment on the anisotropy axis,

$$N=(M_0/2\mu_0)a^2\int(1-\cos\theta)dx, \tag{4}$$

where a is the interatomic distance (a^2 is the ''transverse cross-sectional area'' of the 1D magnet), μ_0 is the Bohr magneton, and M_0 is the modulus of the vector **M**. In addition, if the external magnetic field is uniform, then, in addition to E and N, the excitation field momentum **P** is also conserved:[1]

$$P=-(M_0a^2/g)\int(1-\cos\theta)\frac{\partial\varphi}{\partial x}dx. \tag{5}$$

A dynamical magnetic soliton is a spatially localized excitation moving at a constant velocity and corresponding to finite values of the integrals of the motion E, N, and P. For $\lambda_i=0$ the two-parameter solution of equation (1) corresponding to this soliton has the form[1]

$$\varphi=\tilde{\omega}t+\psi(x-Vt);\quad \frac{d\psi}{dx}=-\frac{C}{\cos^2(\theta/2)};$$
$$\tan^2\frac{\theta}{2}=\frac{A+B}{\cosh^2[\kappa(x-Vt)]-B}. \tag{6}$$

Here (and below) we have used dimensionless variables: the coordinate x is measured in units of the magnetic length $l_0=(\alpha/\beta)^{1/2}$ and the frequency ω in units of the homogeneous ferromagnetic resonance frequency $\omega_0=\beta g M_0$. We note that the inclusion of a uniform magnetic field H_0 leads to a frequency shift in $\varphi(t)$: $\tilde{\omega}=\omega+(H_0/\beta M_0)$. The constants A, B, and C are functions of the two parameters ω and V. However, for use below it will be convenient to express them in terms of the conserved quantities N and P:

$$A=\sinh^2\left(\frac{N}{N_1}\right);\quad B=\sin^2\left(\frac{\pi P}{2P_0}\right);\quad C=\frac{\sin(\pi P/P_0)}{\sinh(2N/N_1)}; \tag{7}$$

$$\kappa=\left(1+\frac{B}{A}\right)\tanh(N/N_1); \tag{8}$$

$$\omega=\frac{\cos^2(\pi P/2P_0)}{\cosh^2(N/N_1)}-\frac{\sin^2(\pi P/2P_0)}{\sinh^2(N/N_1)};$$
$$V=2\frac{\sinh(\pi P/P_0)}{\sinh(2N/N_1)}, \tag{9}$$

where $N_1=2a^2l_0M_0/\mu_0$, $P_0=\pi\hbar a^2M_0/\mu_0$.

The soliton energy E in a uniform magnetic field is given by[1,2]

$$E=E_0\kappa+2\mu_0H_0N, \tag{10}$$

where $E_0=4M_0^2a^2(\alpha\beta)^{1/2}$, and κ is given by formula (8). It follows directly from the form of the functions A and B in (7) that the soliton energy is a periodic function of P.

In a nonuniform magnetic field a soliton executes oscillatory motion. In Refs. 3 and 4 the oscillations were investigated in the absence of dissipation for a nonuniform magnetic field of the form $H=H_0+\eta x$ with a small field gradient $\eta=dH/dx$. The soliton momentum P is not conserved in this case, and its time dependence can be found in the adiabatic approximation. It is this time dependence that governs the Bloch oscillations of the magnetic soliton.

In the present paper, on the assumption that the relaxation constants λ_i in Eq. (1) are nonzero but small, we employ adiabatic perturbation theory to describe the evolution of the soliton in a nonuniform magnetic field in the presence of damping.

It follows from Eqs. (7)–(9) that the soliton momentum and the number of magnons appear in all of those relations only in the form of the dimensionless quantities $\pi P/2P_0$ and N/N_1. Continuing the procedure of rendering the equations dimensionless, we shall henceforth use the letters P and N to mean just these ratios. Similarly, the letter E will denote E/E_0. Finally, the dimensionless magnetic field gradient is $\tilde{\eta}=g l_0\eta/\omega_0$.

When the dissipation is taken into account, not only P but also E and N will cease to be integrals of the motion. The time derivatives of these quantities can be found straightforwardly by using Eq. (1) together with (2)–(5). Since the functional form of the soliton is conserved in the adiabatic approximation, the exact soliton solution of the Landau–Lifshitz equations (6) for $\lambda_i=0$ and $\eta=0$ should be substituted into the resulting expressions, with the parameters P, N, and κ assumed to be smooth functions of time. The results in the case when only the dissipation of relativistic origin is taken into account are written

$$\frac{dP}{dt}=-\tilde{\eta}N-2\lambda_r(VQ_{ex}-\tilde{\omega}R), \tag{11}$$

$$\frac{dN}{dt}=-2\lambda_r(\tilde{\omega}Q_{an}-VR), \tag{12}$$

$$\frac{dE}{dt}=-2\lambda_r(V^2Q_{ex}-2V\tilde{\omega}R+\tilde{\omega}^2Q_{an}), \tag{13}$$

where we have introduced the following functions:

$$R=\frac{1}{8}\int\sin^2\theta\frac{\partial\psi}{\partial x}dx, \tag{14}$$

$$Q_{an}=\frac{1}{8}\int\sin^2\theta\,dx, \tag{15}$$

$$Q_{ex}=\frac{1}{8}\int\left[\left(\frac{\partial\theta}{\partial x}\right)^2+\sin^2\theta\left(\frac{\partial\psi}{\partial x}\right)^2\right]dx. \tag{16}$$

Definitions (15) and (16) agree with the expressions for the anisotropy energy and exchange energy

$$E_{an}=\beta M_0^2Q_{an},\quad E_{ex}=\alpha M_0^2Q_{ex}.$$

In the general case, when all of the λ_i are nonzero, explicit expressions for the time derivatives of P, N, and E are analogous to (11)–(13) but are extremely awkward, and we will therefore not give them here. However, in the next Section we present all of the results, including those with the exchange contribution to the relaxation taken into account.

The form in which Eqs. (11)–(16) are presented is extremely convenient for studying the dynamics of solitons with small V and ω, i.e., solitons of large size ($N\gg1$). Assuming that the factors V and ω separated out in (11)–(13) give the main dependence on these parameters, we can evaluate (14)–(16) for $V\to0$ and $\omega\to0$, i.e., essentially in

the static regime. But then, as we know,[1] $\psi=0$ and the function $\theta=\theta(x)$ describes the profile of a wide one-dimensional domain with a magnetization direction opposite to that at infinity ($\theta\approx\pi$ inside the domain, and $\theta=0$ at infinity). The width of the domain is $\Delta x\approx 2N$, and its edges constitute two domain walls, in which

$$\theta(x)=\theta_0(x)\equiv 2\arctan\{\exp[\pm(x\mp x_0)]\}, \tag{17}$$

where $\pm x_0$ are the coordinates of the centers of the two domain walls, and $2x_0=\Delta x$. Since the width of the domain wall l_0 is finite and $l_0\ll\Delta x$, the evaluation of the parameters R, $Q_{\rm an}$, and $Q_{\rm ex}$ in the leading approximation is trivial:

$$R=0;\quad Q_{\rm an}=\frac{1}{4}\int_{-\infty}^{\infty}\sin^2\theta_0(x)dx;$$
$$Q_{\rm ex}=\frac{1}{4}\int_{-\infty}^{\infty}\left(\frac{\partial\theta_0}{\partial x}\right)^2 dx. \tag{18}$$

Substituting (17) into (18), we find that $Q_{\rm ex}=Q_{\rm an}=1/2$.

In the case of small ω and V the form of Eq. (13) corresponds to the usual definition of the change in energy in a dissipative medium,

$$\frac{dE}{dt}=-2F, \tag{19}$$

where the relativistic term of the dissipative function F has the standard form

$$F=\frac{1}{2}\lambda_r(\tilde{\omega}^2+V^2),$$

which agrees with the equations of motion (11), (12):

$$\frac{dP}{dt}=-\frac{\partial E}{\partial X}-\frac{\partial F}{\partial V}, \tag{20}$$

$$\frac{dN}{dt}=-\frac{\partial E}{\partial\tilde{\omega}}. \tag{21}$$

Here E is the expression for the soliton energy in a nonuniform magnetic field,[3,4] generalizing the result (10):

$$E=\kappa+hN+\tilde{\eta}XN, \tag{22}$$

where X is the coordinate of the center of the soliton, and $h=H_0/(\beta M_0)$. Later we shall use (19)–(22) for a detailed analysis of the oscillations of a soliton of large size.

If there are no conditions that V and ω be small, then it will be necessary to use the explicit form of the solution (6) in calculating R, $Q_{\rm ex}$, and $Q_{\rm an}$. After integration we obtain

$$R=-VN/2, \tag{23}$$

$$Q_{\rm an}=\frac{1}{2}\left(\frac{1}{2}\Omega\sinh 2N+N\omega\right), \tag{24}$$

$$Q_{\rm ex}=\frac{1}{2}\left(\frac{1}{2}\Omega\sinh 2N-N\omega\right), \tag{25}$$

where $\Omega^2=\omega^2+V^2$, and ω and V are expressed in terms of the integrals of motion by formulas (9). Equations (11) and (12) describe the smooth changes of the soliton parameters P and N with time, and formula (22) gives an equation for the coordinate $X(t)$ of the center of the soliton.

To find $X(t)$ we differentiate relation (22) with respect to time and use Eqs. (11)–(13). After straightforward manipulations, we find that

$$\frac{1}{N}\frac{d(NX)}{dt}=2\frac{\sin(2P)}{\sinh(2N)}, \tag{26}$$

where the right-hand side is the same as expression (9) for V, only now P and N are functions of time. If we set $\lambda_r=0$ (and hence $N=$ const) in Eqs. (11), (12), and (26), we will arrive at the description obtained in Refs. 3 and 4 for the Bloch oscillations of a magnetic soliton. In the case when $\lambda_r\neq 0$ but $\eta=0$, Eqs. (11)–(13), taken together with (23)–(25), agree with the analogous equations in Ref. 7.

ANALYSIS OF THE EQUATIONS

In the general case of arbitrary values of the parameters ω and V (or N and P) the system of equations (11)–(13) describing the relaxation of the soliton can be studied only numerically. In the absence of a magnetic field gradient the soliton lifetime $t_{\rm life}$ is of the order of $1/\lambda$ (Ref. 7), where $\lambda=\max(\lambda_r,\lambda_c(a/l_0)^2)$. However, for $N\gg 1$ (or, equivalently, for $\omega,V\ll 1$) it increases considerably: $t_{\rm life}\propto N/\lambda$. An especially significant increase in $t_{\rm life}$ occurs for $H_0=0$. Indeed, in that case we have to leading order in $\exp(-2N)$

$$\Omega=4e^{-2N};\quad \omega=4e^{-2N}\cos(2P);$$
$$V=4e^{-2N}\sin(2P);\quad R=0;\quad Q_{\rm an}=Q_{\rm ex}=\frac{1}{2}$$

and λ appears in the equations only in the combination $\lambda\Omega\ll 1$. In other words, the damping of the soliton is determined by the product $(\lambda\Omega)^{-1}$ and becomes very weak. It is this physically interesting case that we analyze below.

For $N\gg 1$ and $H_0=0$ Eqs. (11), (12), and (26) become

$$\frac{dP}{dt}=-\tilde{\eta}N-4\lambda_P e^{-2N}\sin(2P), \tag{27}$$

$$\frac{dN}{dt}=-4\lambda_N e^{-2N}\cos(2P), \tag{28}$$

$$\frac{dX}{dt}=4e^{-2N}\sin(2P)+4\lambda_N\frac{1}{N}e^{-2N}\cos(2P)X, \tag{29}$$

where $\lambda_P=\lambda_r+(1/3)\lambda_e(a/l_0)^2$ and $\lambda_N=\lambda_r+\lambda_e(a/l_0)^2$. We note that here we have taken into account not only the relativistic damping but also the exchange damping, which comes into the equations in different ways ($\lambda_P\neq\lambda_N$).

Let us determine the critical magnetic field gradient $\tilde{\eta}_c$, which divides the values of the nonuniformity of the magnetic field into regions corresponding to different regimes of soliton evolution:

$$\tilde{\eta}_c=\lambda_P\gamma.$$

Here $\gamma=4\exp(-2N_0)/N_0$, where N_0 is the initial value of the parameter N.

Let us consider the two limiting cases. For very small magnetic gradients ($\tilde{\eta}\ll\tilde{\eta}_c$) or, equivalently, strong damping, we can neglect the term $-\tilde{\eta}N$ in Eq. (27), and we arrive

at the results for a uniform magnetic field.[7] In this situation there are no Bloch oscillations of the soliton: it undergoes a gradually damped translational motion.

Let us now turn to the case of weak relaxation ($\tilde{\eta}_c \ll \tilde{\eta}$), where the Bloch oscillations of the magnetic soliton are conserved. The solution of equations (27) and (28) can be found by iteration and can be written in the form of power series in the small parameter ($\tilde{\eta}_c/\tilde{\eta}$). The first terms of these series are

$$N = N_0 - \lambda_N \frac{\gamma}{2\tilde{\eta}} \sin(2\nu_0 t),$$
$$P = -\nu_0 t - \lambda_P \frac{\gamma}{2\tilde{\eta}} \cos(2\nu_0 t), \tag{30}$$

where $\nu_0 = \tilde{\eta} N_0$. The origin of the time coordinate is chosen so as to eliminate from the second equation the constant associated with the initial value of P, and in the second term of the expression for P we have also dropped a contribution proportional to the small parameter $1/N_0$. The terms of higher orders in ($\tilde{\eta}_c/\tilde{\eta}$) are proportional to the higher harmonics of the frequency $2\nu_0$. We note that on average over a period of the Bloch oscillations of the soliton ($T = \pi/\nu_0$) the parameter N remains constant and practically equal to its initial value N_0. Using the results obtained for P and N and Eq. (29), it is also straightforward to find the first two terms of the expansion of $X(t)$ in the parameter ($\tilde{\eta}_c/\tilde{\eta}$):

$$X(t) = 2\frac{1}{\nu_0} e^{-2N_0} \cos(2\nu_0 t) - \frac{\gamma}{2\tilde{\eta}\nu_0}(\lambda_P - \lambda_N) e^{-2N_0} \times \sin(4\nu_0 t) - 2\frac{\gamma}{\tilde{\eta}}(\lambda_P + \lambda_N) e^{-2N_0} t, \tag{31}$$

where in the last term we have again dropped a contribution containing an additional small factor $1/N_0$. The first term in this expression is the same as the result in Refs. 3 and 4 and describes the Bloch oscillations of the magnetic soliton. The inclusion of damping, as we see from formula (31), has two effects. First, the oscillations of the center of the soliton, while remaining periodic with frequency $2\nu_0$, cease to be harmonic: higher harmonics appear in $X(t)$. Second, a drift of the center of the soliton arises, with a constant drift velocity proportional to the damping:

$$V_{\rm dr} = -2\frac{\gamma}{\tilde{\eta}}(\lambda_P + \lambda_N) e^{-2N_0}. \tag{32}$$

This behavior of the soliton is reminiscent of the so-called Shapiro effect in the theory of Josephson junctions.[8]

Since all of the characteristics of the soliton are periodic functions of P, and since N, as we have said, is a periodic function of time, there is no damping of the soliton at all in the case under discussion ($\tilde{\eta} \gg \tilde{\eta}_c$). According to formula (19), the decrease of its energy in this case is proportional to only the square of Ω, and it is exactly equal to the change in energy due to the drift of the center of the soliton into the region of lower magnetic fields. It must be remembered, however, that the value of the field H_0 gradually changes as the soliton drifts. Our approximation $H_0 = 0$ is valid only as long as $h < \Omega$. This leads to the following estimate for the soliton drift time, which agrees in order of magnitude with the soliton lifetime $t_{\rm life}$: $t_{\rm life} \sim N_0/(\lambda\Omega)$. Here the change in h on a scale comparable to the amplitude (Ω/ν_0) of the Bloch oscillations is relatively small: $\Delta h \sim \Omega/N_0 \ll \Omega$, and so formulas (30)–(32) and, hence, the qualitative conclusions as to the character of the Bloch oscillations of the soliton remain valid.

Let us now indicate the conditions under which this weak damping regime is realized. For applicability of the adiabatic perturbation theory it is necessary that the characteristic frequency Ω in the soliton be much greater than the frequency $2\nu_0$ of the Bloch oscillations, i.e., the following inequalities must hold:

$$1 \gg 4e^{-2N_0} \gg 2\nu_0.$$

This gives an upper bound on the magnetic field gradient, since $\nu_0 = \tilde{\eta} N_0$. On the other hand, the condition $\tilde{\eta} \gg \tilde{\eta}_c$ gives

$$2\nu_0 \gg 8\lambda_P e^{-2N_0}.$$

In other words, if $\lambda_P \ll 1$ there is an interval of $\tilde{\eta}$ values in which one should observe weakly damped Bloch oscillations of the soliton. Interestingly, even if $\tilde{\eta} \gtrsim \tilde{\eta}_c$ the soliton can execute many oscillations ($N_0\tilde{\eta}/\tilde{\eta}_c$) before it disappears. Finally, we note that over its lifetime the soliton drifts to a distance of the order of $\exp(-2N_0)/\tilde{\eta} \ll 1$, which is considerably greater than both the soliton size N_0 and the amplitude of its Bloch oscillations $2\exp(-2N_0)/(N_0\tilde{\eta})$.

If $\Omega \ll 1$ but $H_0 \neq 0$ ($h > \Omega$), then all of the qualitative results listed above remain valid. Only certain quantitative characteristics are changed. In particular, the adiabaticity condition becomes weaker: $\tilde{\omega} \sim h \gg \nu_0$, but now $t_{\rm life} \sim N_0/(\lambda h)$, and a soliton can execute only $N_0(\tilde{\eta}/\tilde{\eta}_c) \times (\Omega/h)$ Bloch oscillations before it disappears.

CONCLUSION

We have investigated the influence of damping on the Bloch oscillations of a magnetic soliton in the framework of adiabatic perturbation theory. We have included in the Landau–Lifshitz equations the relaxation terms of both the relativistic and exchange natures. We have called attention to the circumstance that the longest-lived solitons are those with small values of the parameter Ω. For this reason our detailed analysis was done for solitons of that kind.

If the magnetic field gradient exceeds a critical value (but it is small enough for the adiabatic approximation to apply), then the Bloch oscillations of the soliton will exist even in the presence of damping. However, these oscillations will no longer be harmonic and, in addition, the center of the soliton will begin to drift at a constant velocity. Over its lifetime a soliton can execute a large number of Bloch oscillations, and the drift distance is much greater than the amplitude of these oscillations. The critical value of the gradient is proportional to the damping and to the parameter $\Omega/\ln(1/\Omega)$.

If the magnetic field gradient is smaller than the critical value, then the Bloch oscillations will vanish completely, and the soliton undergoes only a gradually damped translational motion.

*E-mail: babich@ilt.kharkov.ua

[1] A. M. Kosevich, B. A. Ivanov, and A. S. Kovalev, *Nonlinear Magnetization Waves. Dynamical and Topological Solitons* [in Russian], Naukova Dumka, Kiev (1983).
[2] A. M. Kosevich, B. A. Ivanov, and A. S. Kovalev, Phys. Rep. **194**, 117 (1990).
[3] A. M. Kosevich, Physica D **119**, 134 (1998).
[4] A. M. Kosevich, V. V. Gann, A. I. Zhukov, and V. P. Voronov, Zh. Éksp. Teor. Fiz. **114**, 735 (1998) [JETP **87**, 401 (1998)].
[5] J. Kyriakidis and D. Loss, Phys. Rev. B **58**, 5568 (1998).
[6] D. Loss, *Dynamical Properties of Unconventional Magnetic Systems*, Kluwer, Dordrecht (1998).
[7] V. G. Bar'yakhtar, B. A. Ivanov, T. K. Soboleva, and A. L. Sukstanskiĭ, Zh. Éksp. Teor. Fiz. **91**, 1454 (1986) [Sov. Phys. JETP **64**, 857 (1986)].
[8] A. A. Abrikosov, *Fundamentals of the Theory of Metals* [North-Holland, Amsterdam (1988); Nauka, Moscow (1987)].

Translated by Steve Torstveit

Anomalies of the magnon spectrum of a bounded antiferromagnet with a center of antisymmetry. I. Zero-exchange approximation

S. V. Tarasenko*

A. A. Galkin Donetsk Physics and Technology Institute, National Academy of Sciences of Ukraine, ul. R. Lyuksemburg 72, 83114 Donetsk, Ukraine

(Submitted July 14, 2000)
Fiz. Nizk. Temp. **27**, 52–59 (January 2001)

It is shown that if the magnetic structure of an infinite antiferromagnet has a center of antisymmetry rather than a center of symmetry, then in a slab of such a crystal the formation of propagating nonexchange bulk spin waves of a previously unknown type can occur. The relationship between the Néel and Debye temperatures of the antiferromagnetic crystal is of fundamental importance for the structure of the spectrum of these magnons. © *2001 American Institute of Physics.* [DOI: 10.1063/1.1344141]

INTRODUCTION

As we know,[1] a magnetoelectric effect can arise in antiferromagnets whose magnetic and crystallographic symmetry admits the existence of a center of antisymmetry. The corresponding contribution to the thermodynamic potential density of such a crystal in the framework of a two-substrate model can be written in terms of the ferromagnetism vector **m** and antiferromagnetism vector **l** as

$$F_{pe}=\gamma_{\alpha\beta\gamma}m_\alpha l_\beta P_\gamma, \tag{1}$$

where $\hat{\gamma}$ is the tensor of magnetoelectric constants, $\mathbf{m}=(\mathbf{M}_1+\mathbf{M}_2)/2M_0$, $\mathbf{l}=(\mathbf{M}_1-\mathbf{M}_2)/2M_0$, $\mathbf{M}_{1,2}$ are the sublattice magnetizations, and $|\mathbf{M}_1|=|\mathbf{M}_2|=M_0$.

The experimental detection of a large value of the magnetoelectric susceptibility in a tetragonal antiferromagnet with a center of antisymmetry[2] was in large measure stimulated by theoretical studies of this class of magnetic materials.[3–7]

However, the construction of a consistent theoretical model of the dynamics of a real magnetic crystal below the magnetic ordering temperature cannot be done without taking into account the interaction of its spin and elastic subsystems; moreover, one of the characteristic features of the dynamics of antiferromagnetic crystals is the possibility of exchange enhancement of magnetoelastic effects. In Refs. 3–5 and 7 it was shown that in the case when the structure of the magnetoelectric interaction is described by relation (1), a number of features arise in both the linear and nonlinear dynamics of a tetragonal antiferromagnet. However, the calculational model chosen in Refs. 3–5 had some substantial limitations, the most important of which, in the opinion of the authors of those papers, were as follows:

1) neglect of the the finite dimensions of a real magnetic sample;

2) the lack of a consistent allowance for the dipole and inhomogeneous exchange mechanisms of nonlocal interactions in the spin system of the magnetically ordered crystal, which shape the dispersion properties of a bounded magnet;

3) analysis of only the low-frequency region of the spectrum of magnetoelastic oscillations,

$$\omega \ll \omega_{AFM}, \tag{2}$$

(ω_{AFM} is the homogeneous antiferromagnetic resonance frequency), as a consequence of which the main effects induced by the magnetoelectric and magnetoelastic interactions were due to oscillations of the elastic subsystem of the crystal. As to the features of the spin dynamics of magnetoelectrics due to the hybridization of the magnetoelastic and magnetoelectric interactions, their influence reduced to the appearance of additive contributions to the activation energy of the normal spin oscillations of the tetragonal magnetoelectric under study, due to the formation of a magnetoelastic and magnetoelectric gap (and also to the magnetoelastic renormalization of the uniaxial magnetic anisotropy constants);

4) the lack of analysis of the magnetoelastic dynamics of the investigated antiferromagnetic magnetoelectric for different relationships between the Debye temperature T_D and the Néel temperature T_N, in spite of the fact that, as was established in Ref. 8, the magnetoelastic dynamics of the high-temperature ($T_N>T_D$) and low-temperature ($T_N<T_D$) antiferromagnets is substantially different even in the model of an infinite crystal. Moreover, it was shown in Refs. 9–11 that in the case of a bounded antiferromagnetic crystal with $T_N<T_D$, consistent allowance for the interaction of the spin and elastic subsystems can give rise to an indirect spin–spin interaction of the magnetic moments through the long-range field of the quasistatic magnetoelastic deformations and the consequent formation of a new type of propagating nonexchange spin-wave excitations — elastostatic spin waves.

In accordance with what we have said, the goal of the present study was to determine the necessary conditions under which the linear magnetoelectric effect will induce the formation of previously uninvestigated anomalies in the spectrum of nonexchange bulk spin-wave excitations of a thin film of a tetragonal antiferromagnet, which are absent in the model of an infinite crystal.

In the general case one must take into account both the magnetic dipole and electric dipole interactions in a magnetoelectric, but in Ref. 6, for the example of a two-sublattice model of a tetragonal antiferromagnet (with $0z$ being the fourfold axis) with a center of antisymmetry, it was found

that in the collinear phase of this crystal ($\mathbf{l}\|0z$) under certain conditions the independent propagation of magnetic polaritons of the TM and TE types can occur. This is because of the fact that if the plane of propagation of the polariton wave passes through the principal axis and the twofold axis of such a crystal, then one of the magnetic modes is magnetic-dipole active, while the second is electric-dipole active.

This paper is arranged in several Sections. In Sec. 1 we describe the model of the investigated tetragonal magnetoelectric crystal. We use this model to analyze the structure of the spectrum of normal oscillations of an antiferromagnetic crystal with a center of antisymmetry. The calculation was based on the simultaneous incorporation of the magnetic dipole, electric dipole, magnetoelastic, and inhomogeneous exchange interactions. In Sec. 1 we also formulate a suitable boundary-value problem for a thin magnetoelectric film and give the structure of the spectrum of normal oscillations of a thin tetragonal antiferromagnet with a center of antisymmetry in the collinear phase for an electric-dipole-active mode. Sections 2 and 3 are devoted to an analysis of the anomalies that arise in the spin dynamics of a magnetoelectric film when the linear magnetoelectric effect is taken into account; in this analysis we neglect both the inhomogeneous exchange interaction (zero-exchange approximation) and the finite propagation velocity of electromagnetic and acoustic oscillations (the electrostatic and elastostatic approximations, respectively). In Sec. 2 we discuss the structure of the spectrum of electric-dipole-active bulk magnons in a slab of a high-temperature antiferromagnet with a center of antisymmetry, and in Sec. 3 we do this for a low-temperature one. We finish with a summary of the main conclusions that follow from the results obtained in this study.

1. BASIC RELATIONS

If we assume that $|\mathbf{m}|\ll|\mathbf{l}|\cong 1$ (the relativistic interactions are small compared to the intersublattice exchange), then, according to Refs. 2 and 3, the energy density of the two-sublattice model of a magnetoelectric antiferromagnet with allowance for the magnetoelastic interaction is expressed in terms of the ferromagnetism vector $\mathbf{m}$ and antiferromagnetism vector $\mathbf{l}$ as

$$
\begin{aligned}
&F=F_m+F_{pe}+F_{me}+F_e+F_p;\\
&F_m=M_0^2\left\{\frac{\delta}{2}\mathbf{m}^2+\frac{\alpha}{2}(\nabla\mathbf{l})^2-\frac{\beta}{2}l_z^2-\mathbf{m}H\right\};\\
&F_p=\frac{1}{2\kappa}P_z^2+\frac{1}{2\kappa_\perp}(P_x^2+P_y^2)-\mathbf{PE};\\
&F_{me}=B_{11}(l_x^2u_{xx}+l_y^2u_{yy})+B_{12}(l_x^2u_{yy}+l_y^2u_{xx})\\
&\quad+B_{13}(u_{xx}+u_{yy})l_z^2+B_{31}u_{zz}(l_x^2+l_y^2)+B_{33}u_{zz}l_z^2\\
&\quad+2B_{44}l_z(l_xu_{zx}+l_yu_{zy})+2B_{66}l_xl_yu_{xy};\\
&F_e=\frac{1}{2}c_{11}(u_{xx}^2+u_{yy}^2)+c_{12}u_{yy}u_{xx}+c_{33}(u_{xx}+u_{yy})u_{zz}\\
&\quad+\frac{1}{2}c_{33}u_{zz}^2+2c_{44}(u_{zx}^2+u_{zy}^2)+2c_{66}u_{xy}^2;
\end{aligned}
\tag{3}
$$

where δ, α, and β are the homogeneous and inhomogeneous intersublattice exchange constants and the anisotropy constant, respectively, $\mathbf{E}$ and $\mathbf{H}$ are the electric and magnetic fields, $\mathbf{P}$ is the electric polarization vector, $\kappa_\perp$ and κ are the inverse dielectric susceptibilities, u_{ik} is the magnetoelastic strain tensor, and $\hat{B}$ and $\hat{c}$ are the magnetoelastic and elastic interaction coefficients, respectively. [Note: Throughout this paper the vector product of two vectors is denoted by enclosure in square brackets, and the scalar product is written with or without enclosing parentheses.]

In the particular case of a tetragonal antiferromagnet with the $4_z^{\pm}2_x^-1^-$ or $4_z^{\pm}2_x^+1^-$ structure, the expression for the magnetoelastic interaction energy can be written as[2–6]

$$
\begin{aligned}
F_{pe}=&-\gamma_1m_z(l_xP_y\pm l_yP_x)-\gamma_2P_z(m_xl_y\pm m_yl_x)\\
&-\gamma_3l_z(m_xP_y\pm m_yP_x)(4_z^{\pm}2_x^+1^-),\\
F_{me}=&-\gamma_1m_z(l_xP_x\pm l_yP_y)-\gamma_2P_z(m_xl_x\pm m_yl_y)\\
&-\gamma_3l_z(m_xP_x\pm m_yP_y)-\gamma_4l_zm_zP_z(4_z^{\pm}2_x^-1^-),
\end{aligned}
\tag{4}
$$

($\hat{\gamma}_{1-4}$ are the magnetoelectric interaction coefficients).

The dynamical properties of the system under study are described in the framework of the phenomenological theory by the following system of coupled vector equations:

$$
\begin{aligned}
&(2/gM_0)\mathbf{m}_t=[\mathbf{m}H_{\mathbf{m}}]+[\mathbf{l}H_{\mathbf{l}}];\\
&(2/gM_0)\mathbf{l}_t=[\mathbf{l}H_{\mathbf{m}}]+[\mathbf{m}H_{\mathbf{l}}];\\
&\mathbf{P}_{tt}=fH_{\mathbf{p}};\quad \operatorname{curl}\mathbf{H}=\frac{1}{c}\frac{\partial\mathbf{D}}{\partial t};\quad \operatorname{curl}\mathbf{E}=-\frac{1}{c}\frac{\partial\mathbf{B}}{\partial t};\\
&\operatorname{div}\mathbf{D}=0;\quad \operatorname{div}\mathbf{B}=0;\quad \rho\frac{\partial^2u_i}{\partial t^2}=\frac{\partial^2W}{\partial x_i\partial u_{ik}},
\end{aligned}
\tag{5}
$$

where $H_j\equiv\delta H/\delta j$ $(j=m,l,P)$, g is the gyromagnetic ratio, and ρ is the density.

In the case when the oscillation frequency of the system satisfies the condition

$$
\omega\ll\min\{g\delta M_0,(f/\kappa_\perp)^{1/2},(f/\kappa)^{1/2}\},
\tag{6}
$$

one can exclude the vectors $\mathbf{m}$ and $\mathbf{P}$ from consideration. As a result, the equations describing the dynamics of a magnetoelectric in the approximation (6) can be written (on the condition that $H_p=0$) in the form

$$
\begin{aligned}
&\alpha\left[\mathbf{l}\left(\Delta\mathbf{l}-\frac{1}{s^2}\mathbf{l}_{tt}-\frac{\partial W_a}{\partial\mathbf{l}}-\frac{\partial W_{me}}{\partial\mathbf{l}}\right)\right]-\frac{8}{\delta\omega_s}(\mathbf{l}H)\mathbf{l}_t-\frac{4}{8}(\mathbf{l}\mathbf{H})[\mathbf{l}\mathbf{H}]\\
&\quad+\frac{2}{\delta\omega_s}\{\hat{\varepsilon}\mathbf{l}\hat{\gamma}\mathbf{P}\hat{\varepsilon}\mathbf{l}\mathbf{l}_t+2(\Gamma\mathbf{P})\mathbf{l}_t+\mathbf{l}\hat{\gamma}\mathbf{P}\mathbf{l}\mathbf{l}_t-\hat{\gamma}\mathbf{P}\mathbf{l}\mathbf{l}_t\}\\
&\quad+\frac{2}{\delta}\hat{\varepsilon}\mathbf{l}\{(\mathbf{l}\mathbf{H})(\hat{\gamma}\mathbf{P}\mathbf{l})+\mathbf{H}(\Gamma\mathbf{P})-\hat{\gamma}\mathbf{P}\mathbf{H}\}=0;\\
&\operatorname{curl}\mathbf{H}=\frac{1}{c}\frac{\partial\mathbf{D}}{\partial t};\quad \operatorname{curl}\mathbf{E}=-\frac{1}{c}\frac{\partial\mathbf{B}}{\partial t};\quad \operatorname{div}\mathbf{D}=0;\\
&\operatorname{div}\mathbf{B}=0;\quad \rho\frac{\partial^2u_i}{\partial t^2}=\frac{\partial^2W}{\partial x_i\partial u_{ik}}.
\end{aligned}
\tag{7}
$$

Here $\Gamma_\alpha \equiv \gamma_{\alpha\beta\gamma} l_\beta l_\gamma$, $\omega_s = gM_0$, and $\hat{\varepsilon}$ is the antisymmetric unit tensor. In the approximation (6), the vectors **m** and **P** that appear in Maxwell's equations are related to the components of the antiferromagnetism vector **l** as

$$\mathbf{m} = \left\{ \frac{2}{\delta\omega_s}[\mathbf{l}_t\dot{\mathbf{l}}] + \frac{2}{\delta}(\mathbf{H} - \mathbf{l}(\mathbf{lH})) \right\} + \frac{2}{\delta\omega_s}\{\mathbf{l}(\Gamma\mathbf{P}) - \hat{\gamma}\mathbf{P}\};$$
$$P = \hat{\kappa}(\mathbf{E} - \hat{\gamma} lm). \tag{8}$$

The tensor $\hat{\kappa}$ has the following nonzero components: $\kappa_{xx} = \kappa_{yy} = \kappa_\perp$, $\kappa_{zz} = \kappa$.

Thus in the low-frequency limit (6) the system of dynamical equations (7), (8), which intercouple only the components of the vectors **l**, **H**, **E**, and **u**, govern the magnetoelastic dynamics of a magnetoelectric. This reduced system is valid for arbitrary values of the deviation of the antiferromagnetism vector **l** from its equilibrium orientation.

A calculation shows that one of two equilibrium magnetic configurations can be realized in the model antiferromagnet under study: easy-axis ($\mathbf{l} \| 0z$) and easy-plane ($\mathbf{l} \perp 0z$).[2–5] We consider the same geometry of propagation of the electromagnetic wave and the same equilibrium magnetic configuration that were studied previously in Ref. 6 in neglect of the homogeneous exchange interaction — the easy-axis phase ($\mathbf{l} \| 0z$, $|\mathbf{M}| = |\mathbf{P}| = 0$) of a tetragonal antiferromagnet $4_z^+ 2_x^+ 1^{-1}$, and we adopt the xz plane as the plane of propagation of the electromagnetic wave.

Using Eqs. (7) and (8), we can that in this case the corresponding dispersion relation describing the spectrum of normal oscillations of the given antiferromagnet, with the magnetic dipole, electric dipole, magnetoelastic, and inhomogeneous exchange interactions simultaneously taken into account, factorizes. This is a consequence of the fact that in the given model the intercoupled oscillations of the magnetic polaritons of the TE type and the elastic shear SH wave ($H_{x,z}, E_y, l_y, m_{x,z}, u_y \neq 0$) propagate independently, as do the magnetic TM polaritons and the elastic oscillations with lattice displacement vector **u** lying in the plane of propagation ($H_y, E_{x,z}, l_{x,z}, m_y, u_{x,z} \neq 0$). Thus both of these types of normal oscillations of the magnetic crystal can be be classed as phonon–magnon polaritons, which form as a result of hybridization of the acoustical phonons and electric-dipole-active acoustical magnons ($H_y, E_{x,z}, l_{x,z}, m_y, u_{x,z} \neq 0$) or magnetic-dipole-active acoustical magnons ($H_{x,z}, E_y, l_y, m_{x,z}, u_y \neq 0$). In the approximation (6) the corresponding dispersion relation for the spectrum of normal oscillations of an infinite antiferromagnetic magnetoelectric with the involvement of magnetic-dipole-active ($l_y, m_x \neq 0$) or electric-dipole-active magnon modes ($l_x, m_y \neq 0$) can be written for $H_y, E_{x,z}, l_{x,z}, m_y, u_{x,z} \neq 0$ in the form

$$\frac{\omega^2}{c^2}\varepsilon_{xx}\varepsilon_{zz}\mu_{yy} - \varepsilon_{zz}\left(k_z + \frac{\omega}{c}\lambda\right)^2 = \varepsilon_{xx}k_x^2, \tag{9}$$

and for $u_y, E_y, H_{x,z}, l_y, m_x \neq 0$ in the form

$$\chi_{xx} = \chi_0 \frac{R(\omega,k)}{\Delta_R(\omega,k)}; \quad \alpha_{xx} = \alpha_{yy} = \kappa_\perp \frac{R(\omega,k) - \omega^2}{\Delta_R(\omega,k)};$$

$$\frac{\omega^2}{c^2}\mu_{xx}\mu_{zz}\varepsilon_{yy} - \mu_{zz}\left(k_z - \frac{\omega}{c}\lambda\right)^2 = \mu_{xx}k_x^2; \tag{10}$$

$$\lambda = (\kappa_\perp \chi_0 \xi)^{1/2} \frac{R(\omega,k)}{\Delta_R(\omega,k)}; \quad \chi_0 = 1/\delta; \quad \xi^2 = \frac{\gamma_3^2 \kappa_\perp}{\delta};$$

$$\Delta_R(\omega,k) \equiv R(\omega,k)(1-\xi^2) - \omega^2;$$

$$R(\omega,k) \equiv \omega_0^2 + s^2(k_x^2 + k_z^2)$$

$$+ \omega_{me}^2\left(1 - \frac{c_{44}[k_x^2(\Lambda_{11} - \omega^2) + k_z^2(\Lambda_{33} - \omega^2) - 2\Lambda_{13}k_x k_z]}{\rho[(\Lambda_{11} - \omega^2)(\Lambda_{33} - \omega^2) - \Lambda_{13}^2]}\right);$$

$$s^2 \equiv \frac{\alpha\delta\omega_s^2}{4}; \quad \omega_0^2 \equiv s^2\beta/\alpha; \quad \omega_s \equiv gM_0;$$

$$\chi_{yy} = \chi_0 \frac{F(\omega,k)}{\Delta_F(\omega,k)}; \quad \chi_{zz} = \alpha_{zz} = 0;$$

$$\Delta_F(\omega,k) \equiv F(\omega,k)(1-\xi^2) - \omega^2;$$

$$F(\omega,k) \equiv \omega_0^2 + s^2(k_x^2 + k_z^2) - \omega_{me}^2\left[1 - \frac{c_{44}k_z^2}{\rho[\Lambda_{22} - \omega^2]}\right];$$

$$\mu_{ik}(\omega,\mathbf{k}) \equiv \delta_{ik} + 4\pi\chi_{ik}(\omega,\mathbf{k});$$

$$\varepsilon_{ik}(\omega,\mathbf{k}) \equiv \delta_{ik} + 4\pi\alpha_{ik}(\omega,\mathbf{k}); \quad \mathbf{k} \in xz;$$

where Λ_{ik} are the components of the Christoffel tensor, $i,k = 1-3$.

Thus it follows already from Eqs. (9) and (10) that in the general case the linear magnetoelectric effect leads to nonreciprocity not only of the polariton but also of the magnetoelastic spectrum $\omega(k_z) \neq \omega(-k_z)$, but this effect is rather small, since even when electromagnetic retardation effects are neglected ($\omega/c \to 0$, i.e., in the electro- and magnetostatic limit), it follows from Eqs. (9) and (10) that $\omega(k_z) = \omega \times (-k_z)$.

Since in this study we are interested in the dynamics of a bounded magnetoelectric, the system of dynamical equations (7) presented above must be supplemented with appropriate boundary conditions.

In the case when the magnetic moments on the surface of the film are completely pinned (Kittel boundary conditions) the exchange boundary conditions can be written in the form[12]

$$m = l = 0; \quad \zeta = \pm d, \tag{11}$$

where ζ is the coordinate along the direction of n, and $2d$ is the thickness of the film.

As to the elastic part of the boundary-value problem under consideration, up till now only two boundary conditions have been considered[13,14] in the theory for the solution of magnetoacoustic boundary-value problems: a mechanically free surface of the crystal,

$$\sigma_{ik} n_k = 0, \quad \zeta = \pm d, \tag{12}$$

(σ_{ik} is the elastic stress tensor), or a completely clamped sample,

$$u_i = 0, \quad \zeta = \pm d. \tag{13}$$

Meanwhile, as we know, besides the two types of elastic boundary conditions indicated above, a third type of boundary condition is also used in physical acoustics, corresponding to a boundary that admits slip:[15]

$$(\tilde{\mathbf{u}}\mathbf{n})=0, \quad [\mathbf{ns}]=0, \quad s=\sigma_{ik}n_k, \quad \zeta=\pm d. \tag{14}$$

Physically this relation corresponds to satisfaction of the conditions of completely incoherent mating[16] at the interface between two media, one of which is absolutely rigid. Analysis shows that the use of elastic boundary conditions of the type (12) and (13) leads to the situation that if the elastic lattice displacement vector **u** lies in the sagittal plane, then for any type of exchange boundary conditions the solution of the corresponding magnetoelastic boundary-value problem for the relation between the frequency ω of the magnetoelastic excitations and their wave vectors $\mathbf{k}_\perp$ in the developed plane of the crystal will be a transcendental equation[14,17] that must be studied by some approximate method. In Ref. 18, for the example of a slab of a two-sublattice antiferromagnet, it was shown for the first time that even for the collinear phase of the easy-axis antiferromagnet with $\mathbf{l}\|\mathbf{n}$ the joint use of boundary conditions (11) and (14) permits one to represent the dispersion relation for the spectrum of bulk magnetoelastic waves of a thin magnetic film in the form of a polynomial in ω^2 for any direction of the wave vector in the plane of the magnetic film, $\mathbf{k}_\perp$. The coefficients of this polynomial are known functions of the components of the wave vector $\mathbf{k}_\perp$.

As to the electrodynamic boundary conditions, we shall assume that, depending on the relative orientation of the normal to the surface of the film, **n**, and the direction of the equilibrium orientation of the antiferromagnetism vector **l** (Ref. 19), we will have

$$\begin{aligned} &\mathbf{E}_\tau=\mathbf{H}_\tau=0; \quad \zeta=\pm d \quad \text{for } \mathbf{n}\|\mathbf{l}, \\ &\mathbf{Dn}=\mathbf{Bn}=0; \quad \xi=\pm d \quad \text{for } \mathbf{n}\perp\mathbf{l}\|\mathbf{k}_\perp, \end{aligned} \tag{15}$$

where $\boldsymbol{\tau}$ is a unit vector in the plane of the film.

A calculation shows that if the exchange (11), elastic (14), and electrodynamic (15) boundary conditions are simultaneously satisfied on both surfaces of the magnetoelectric film under study, then for $\mathbf{k}\in xz$, $\mathbf{n}\perp\mathbf{l}\|\mathbf{k}_\perp$ the structure of the spectrum of normal oscillations of the bounded antiferromagnet under study, with the magnetic-dipole, electric-dipole, magnetoelastic, and inhomogeneous exchange interactions taken into account, also has the form not of a transcendental equation, but of a polynomial in ω^2 ($\varepsilon \equiv 4\pi\alpha_0$; $\kappa_\nu=\pi\nu/2d$, $\nu=1,2,\ldots$):

$$\frac{\omega^2}{c^2}\varepsilon_{xx}\varepsilon_{zz}\mu_{yy}-\varepsilon_{zz}\left(k_\perp+\frac{\omega}{c}\lambda\right)^2=\varepsilon_{xx}\kappa_\nu^2, \tag{16}$$

$$H_y, E_{x,z}, l_x, m_y, u_{x,z}\neq 0,$$

$$\frac{\omega^2}{c^2}\mu_{xx}\mu_{zz}\varepsilon_{yy}-\mu_{zz}\left(k_\perp-\frac{\omega}{c}\lambda\right)^2=\mu_{xx}\kappa_\nu^2, \tag{17}$$

$$u_y, E_y, H_{x,z}, l_y, m_x\neq 0,$$

$$\chi_{xx}=\chi_0\frac{R_*}{\Delta_{R_*}}; \quad \alpha_{xx}=\kappa_\perp\frac{R_*^2-\omega^2}{\Delta_{R_*}};$$

$$\lambda=(\kappa_\perp\chi_0\xi)^{1/2}\frac{R_*}{\Delta R_*}; \quad \chi_{yy}=\chi_0\frac{F_*}{\Delta_{F_*}};$$

$$\Delta_{R_*}\equiv R_*(1-\xi^2)-\omega^2; \quad \Delta_{F_*}\equiv F_*(1-\xi^2)-\omega^2;$$

$$R_*\equiv R(\omega, k_z\equiv k_\perp; k_x\equiv\kappa_\nu);$$

$$F_*\equiv F(\omega, k_z\equiv k_\perp; k_x\equiv\kappa_\nu).$$

It follows from an analysis of (16) and (17) that for $\mathbf{n}\perp 0z$ ($\mathbf{k}\in xz$) and $\omega/c\neq 0$ the linear magnetoelectric interaction, both for magnetic-dipole-active and electric-dipole-active types of spin oscillations, leads to nonreciprocity of the spectrum of bulk magnetoelastic oscillations, $\omega(k_\perp)\neq\omega(-k_\perp)$ propagating along a thin film of a magnetoelectric antiferromagnet.

A calculation shows that the linear magnetoelectric effect does not give rise to features in the spectrum of normal oscillations involving magnetic-dipole-active modes of the magnon spectrum of a tetragonal antiferromagnet with a center of antisymmetry in the approximation of an infinite propagation velocity of electromagnetic oscillations ($\omega/c\to 0$). Therefore, in what follows we shall consider normal oscillations of a thin film of a tetragonal antiferromagnet in the collinear phase ($\mathbf{l}\|0z$) with the participation of only the electric-dipole-active mode of the spectrum of this magnet, assuming that the condition of the electrostatic approximation is satisfied ($\omega/c\to 0$).

To analyze in detail the role of the different mechanisms of spin–spin interaction in the formation of the structure of the spectrum of normal spin oscillations, let us consider the corresponding general expression (16) in individual particular cases: $\omega/c_{\rm ph}k_\perp\to 0$; $\omega/c_{\rm ph}k_\perp\to\infty$, and $\alpha\to 0$ ($c_{\rm ph}$ is the minimum phase velocity of elastic waves in an infinite magnet). The first of these approximations is valid if one can neglect the finiteness of the propagation velocity of elastic waves in comparison with the characteristic times of spin-wave oscillations in the spin subsystem of the magnet, i.e., in order for the elastostatic approximation to be valid, the condition $c_{\rm ph}>s$ must hold. The second case corresponds to the frozen lattice approximation, and it can be realized not only for $c_{\rm ph}<s$ but also for $c_{\rm ph}>s$ in the region of sufficiently small wave numbers $k_\perp<\omega/c_{\rm ph}$. The last limiting case ($\alpha\to 0$) corresponds to the zero-exchange approximation (neglect of effects due to the inhomogeneous exchange interaction).

2. SPIN DYNAMICS OF A MAGNETOELECTRIC FILM IN THE ZERO-EXCHANGE APPROXIMATION (HIGH-TEMPERATURE ANTIFERROMAGNET)

It follows from (16) that under conditions such that $\alpha\to 0$, $\omega/c_{\rm ph}k_\perp\to\infty$ for $T_N>T_D$ and $\alpha\to 0$, $\omega/c_{\rm ph}k_\perp\to 0$ for $T_N<T_D$, the structure of the spectrum of electric-dipole-active bulk magnons of a thin magnetoelectric film as a function of the relationship between the Néel temperature (T_N) and Debye temperature (T_D) can be written for $T_N>T_D$ in the form

$$\Omega_\nu^2(k_\perp)=R\left(1-\xi^2+\frac{\xi^2\varepsilon_\perp k_\perp^2}{\kappa_\nu^2\varepsilon+k_\perp^2(1+\varepsilon_\perp)}\right), \quad \mathbf{n}\|0z, \tag{18}$$

$$\Omega_\nu^2(k_\perp)=R\left(1-\xi^2+\frac{\xi^2\varepsilon_\perp\kappa_\nu^2}{k_\perp^2\varepsilon+\kappa_\nu^2(1+\varepsilon_\perp)}\right),\quad \mathbf{n}\|0x \qquad (19)$$

and for $T_N<T_D$ in the form

$$\Omega_\nu^2(k_\perp)=R_\nu(k_\perp)\left(1-\xi^2+\frac{\xi^2\varepsilon_\perp k_\perp^2}{\kappa_\nu^2\varepsilon+k_\perp^2(1+\varepsilon_\perp)}\right),\quad \mathbf{n}\|0z, \qquad (20)$$

$$\Omega_\nu^2(k_\perp)=R_\nu(k_\perp)\left(1-\xi^2+\frac{\xi^2\varepsilon_\perp\kappa_\nu^2}{k_\perp^2\varepsilon>+\kappa_\nu^2(1+\varepsilon_\perp)}\right),\quad \mathbf{n}\|0x \qquad (21)$$

$$R_\nu(k_\perp)\equiv\omega_0^2+\omega_{me}^2\left(1-\frac{c_{44}[(k_x^2\Lambda_{11}^*+k_z^2\Lambda_{33}^*-2\Lambda_{13}^*k_xk_z)]}{[\Lambda_{11}^*\Lambda_{33}^*-\Lambda_{13}^{*2}]\rho}\right)$$

$$\varepsilon_\perp\equiv4\pi\kappa_\perp;\quad \varepsilon\equiv4\pi\kappa;\quad R\equiv\omega_0^2+\omega_{me}^2.$$

In (18)–(21) $\Lambda_{ik}^*\equiv\Lambda_{ik}$ under the condition $k_z=\kappa_\nu$, $k_z=k_\perp$ for $\mathbf{n}\|\mathbf{l}$ or $k_z=k_\perp$, $k_x=\kappa_\nu$ for $\mathbf{n}\perp\mathbf{l}\|\mathbf{k}_\perp$ ($\mathbf{k}\in xz$).

Analysis of relations (18)–(21) shows that the corresponding spectra of nonexchange spin-wave excitations has a bunching point both for $k_\perp\to0$ and for $k_\perp\to\infty$, i.e., for two fixed mode indices ν and ρ the condition $|\Omega_\nu(k_\perp)-\Omega_\rho(k_\perp)|\to0$ holds. In the case of a high-temperature antiferromagnet with a center of antisymmetry [Eqs. (18) and (19)] in the zero-exchange limit, independently of the mode index ν the dispersion curves of the spectrum of electric-dipole-active magnons with $\mathbf{n}\|\mathbf{l}$ is a wave of the forward type ($\partial\Omega_\nu/\partial k_\perp>0$), while for $\mathbf{n}\perp\mathbf{l}$ it is a backward wave ($\partial\Omega_\nu/\partial k_\perp<0$). For a fixed value of the wave number $k_\perp$ and a fixed mode index $\nu<\rho$ in the case $\mathbf{n}\|\mathbf{l}$ (18) the inequality $\Omega_\nu(k_\perp)>\Omega_\rho(k_\perp)$ holds, whereas for $\mathbf{n}\perp\mathbf{l}\perp\mathbf{k}_\perp$ (19) the condition $\Omega_\nu(k_\perp)<\Omega_\rho(k_\perp)$ holds. For both types of waves, independently of the mode index ν the corresponding dispersion curves (18) and (19) have an inflection point ($\partial^2\Omega_\nu/\partial k_\perp^2=0$) for $k_\perp\neq0$. In this case the dispersion properties of the magnons, the dispersion relation of which for $T_N>T_D$ is given by relations (18) and (19), are formed as a result of the magnetoelectric interaction $\Omega_\nu(k_\perp)\neq$ const for $\gamma_3\neq0$ (electrostatic spin waves), whereas the magnetoelastic interaction governs only the value of the magnetoelastic gap ω_{me} and the renormalization of the magnetic anisotropy constants, which are independent of the value of the wave number $k_\perp$ and the direction. If we introduce the characteristic frequencies $\omega_A^2\equiv R^2(1-\xi^2)$ and $\omega_B^2\equiv R[1-\xi^2/(1+\varepsilon_\perp)]$ ($\omega_A<\omega_B$), then independently of the mode index ν one has $\Omega_\nu(k_\perp\to0)\to\omega_A$ and $\Omega_\nu(k_\perp\to\infty)\to\omega_B$ for $\mathbf{n}\|\mathbf{l}$, while for $\mathbf{n}\perp\mathbf{l}\|\mathbf{k}_\perp$ one has $\Omega_\nu(k_\perp\to0)\to\omega_B$ and $\Omega_\nu(k_\perp\to\infty)\to\omega_A$.

3. SPIN DYNAMICS OF A MAGNETOELECTRIC FILM IN THE ZERO-EXCHANGE APPROXIMATION (LOW-TEMPERATURE ANTIFERROMAGNET)

It follows from relations (18), (19) and (20), (21) that the additional [in comparison to (18), (19)] anomalies in the spectrum of nonexchange spin oscillations of a thin film of a low-temperature magnetoelectric antiferromagnet are due to the fact that for $T_N<T_D$, in addition to the electric-dipole mechanism of formation of the magnon dispersion there is also an indirect spin–spin interaction through the long-range field of the quasistatic magnetoelastic deformations. This makes it possible to form the dispersion properties of the spin-wave oscillations of a thin antiferromagnetic film in the zero-exchange approximation even in the case when $\gamma=0$. The corresponding class of nonexchange magnons is called elastostatic spin waves.[10,11] It follows from (20) and (21) that in the geometry under study this mechanism of indirect spin–spin interaction leads to the situation that for a specified mode index ν the investigated type of nonexchange spin oscillations, both for $\mathbf{n}\|\mathbf{l}$ and for $\mathbf{n}\perp\mathbf{l}\|\mathbf{k}_\perp$, are waves of the forward type ($\partial\Omega_\nu/\partial k_\perp>0$) for $k_\perp<k_{*\nu}$, for $k_\perp>k_{*\nu}$ they are backward waves ($\partial\Omega_\nu/\partial k_\perp<0$), and for $k_\perp=k_{*\nu}\neq0$ ($\partial\Omega_\nu/\partial k_\perp=0$) the dispersion curve of the given mode of magnetic oscillations has a maximum independently of its mode index ν. Here for $k_\perp<k_{*\nu}$ the condition $\Omega_\nu(k_\perp)>\Omega_\rho(k_\perp)$ holds, whereas for $k_\perp>k_{*\nu}$ the relation $\Omega_\nu(k_\perp)<\Omega_\rho(k_\perp)$ ($\nu<\rho$) is valid. Furthermore, unlike the case of a high-temperature antiferromagnet (18) and (19), the elastostatic mechanism of formation of the dispersion of nonexchange magnons leads to the circumstance that even in the limit $\hat\gamma\to0$ in a thin film of a low-temperature antiferromagnet with a center of antisymmetry it becomes possible for a crossing point of the dispersion curves of the modes (20) and (21) to occur at $k_\perp=k_{\nu\rho}$ for specified indices ν and ρ ($\Omega_\nu(k_{\nu\rho})=\Omega_\rho(k_{\nu\rho})$). If $\nu<\rho$, then $k_{*\nu}<k_{\nu\rho}<k_{*\rho}$. In the crossover region $k_\perp\cong k_{\nu\rho}$ the mode with index ν is a wave of the backward type, while the mode with index ρ is opposite to it. The bunching points of the spectrum of the investigated type of nonexchange bulk elastostatic magnons are $\Omega_\nu(k_\perp)=\omega_0$ (both for $k_\perp\to0$ and for $k_\perp\to\infty$).

Let us now take into account that in the low-temperature antiferromagnetic magnetoelectric film under study the indirect spin–spin exchange is due not only to the long-range quasistatic magnetoelastic strain field but also to the electric-dipole field ($\hat\gamma\neq0$). As a result, as follows from (20) and (21), in a thin film of a low-temperature antiferromagnet with a center of antisymmetry it is possible even in the zero-exchange approximation ($\alpha\to0$) for the dispersion curve of a mode of nonexchange bulk spin oscillations with a specified index ν to have not only a maximum but also a minimum for $k_\perp\neq0$. The corresponding wave numbers $k_{\nu\pm}^2$ ($k_{\nu-}<k_{\nu+}$) are the positive real roots of the equation $\partial\Omega_\nu(k_\perp)/\partial k_\perp=0$. Such a form of the dispersion curve for the bulk mode of the magnon mode of index ν is possible, in particular, under the following conditions:

$\mathbf{n}\|\mathbf{l}$,

$$\frac{c_{11}c_{33}+c_{44}^2-(c_{13}+c_{44})^2}{c_{11}c_{44}},\quad \left(\frac{c_{33}}{c_{11}}\right)^{1/2}\ll\frac{\varepsilon}{1+\varepsilon_\perp};$$

$\mathbf{n}\perp\mathbf{l}\|\mathbf{k}_\perp$,

$$\frac{c_{11}c_{33}+c_{44}^2-(c_{13}+c_{44})^2}{c_{33}c_{44}},\quad \left(\frac{c_{11}}{c_{33}}\right)^{1/2}\gg\frac{1+\varepsilon_\perp}{\varepsilon}. \qquad (22)$$

Analysis of the relations for $k_{\nu\pm}^2$ shows that for $\hat\gamma\to0$ one has $k_{\nu+}\to\infty$, $k_{\nu-}\to k_{\nu*}$ in the case $\mathbf{n}\|\mathbf{l}$, whereas $k_{\nu-}\to0$,

$k_{\nu+} \to k_{\nu *}$ for $\mathbf{n} \perp \mathbf{k} \| \mathbf{k}_\perp$. If we introduce the characteristic frequencies $\omega_A^{*2} \equiv \omega_0^2(1-\xi^2)$ and $\omega_B^{*2} \equiv \omega_0^2[1-\xi^2/(1+\varepsilon_\perp)]$, then, as for a high-temperature antiferromagnet, independently of the mode index ν, one has $\Omega_\nu(k_\perp \to 0) \to \omega_A^*$ and $\Omega_\nu(k_\perp \to \infty) \to \omega_B^*$ for $\mathbf{n} \| \mathbf{l}$, while if $\mathbf{n} \perp \mathbf{l} \| \mathbf{k}_\perp$ then $\Omega_\nu(k_\perp \to 0) \to \omega_B^*$ and $\Omega_\nu(k_\perp \to \infty) \to \omega_A^*$.

In addition, it follows from (20) and (21) that when both mechanisms of dispersion formation (electric-dipole and elastostatic) for nonexchange magnons in a thin film of a low-temperature antiferromagnet with a center of antisymmetry are simultaneously taken into account, two crossover points of the modes can exist at $k_\perp \neq 0$ for fixed mode indices ν and ρ of the spectrum of nonexchange bulk spin oscillations (20) and (21) (in particular, when conditions (22) hold). The corresponding wave numbers $k_\pm$ ($k_- < k_+$) are determined from (20) and (21):

$$\Omega_\nu(k_\pm) = \Omega_\rho(k_\pm). \tag{23}$$

Formally taking the limit $\hat{\gamma} \to 0$ (neglecting the magnetoelectric interaction), we have $k_- \to k_{\nu\rho}$, $k_+ \to \infty$ for $\mathbf{n} \| \mathbf{l}$, whereas $k_+ \to k_{\nu\rho}$, $k_- \to 0$ for $\mathbf{n} \perp \mathbf{l} \| \mathbf{k}_\perp$.

If the opposite condition to (22) holds, then (both for $\mathbf{n} \| \mathbf{l}$ and for $\mathbf{n} \perp \mathbf{l} \| \mathbf{k}_\perp$) the dispersion curve (20) and (21) will have only one extremum (a maximum) for $k_\perp \neq 0$, and for modes with specified indices ν and ρ there will be only one crossover point.

CONCLUSION

In summary, in this paper, for the example of a film of an antiferromagnet with a center of antisymmetry, we have determined the necessary conditions under which the presence of a linear magnetoelectric effect will lead, even in the zero-exchange approximation, to the formation of previously unknown anomalies in the spectrum of exchange magnons; these anomalies are not only absent in the model of an infinite magnet but also in the case of a film of an antiferromagnet having a center of symmetry. For the existence of these magnons it is of fundamental importance that both the finite size of the real sample and the relationship between the Néel and Debye temperatures be simultaneously taken into account. We have found the following features of the exchange magnon spectrum that are induced by the magnetoelectric interaction:

1) A thin film of an antiferromagnet with a center of antisymmetry can support propagating nonexchange electric-dipole-active bulk spin oscillations whose spectral structure $\Omega_\nu(k_\perp)$ depends substantially on the relationship between the Néel and Debye temperatures and has a nonmonotonic character as a function of the magnitude of the wave number $k_\perp$, having bunching points of the spectrum for $k_\perp \to 0$ and $k_\perp \to \infty$.

2) For this type of bulk magnons there can be parts of the dispersion curve $\Omega_\nu(k_\perp)$ with $\partial\Omega_\nu/\partial k_\perp = 0$ for $k_\perp \neq 0$. The indicated points can correspond to a local maximum or a local minimum of the dispersion curve.

3) For $k_\perp \neq 0$ there can exist crossover points of the dispersion curves corresponding to modes with indices ν and ρ in the spectrum of nonexchange bulk magnons $\Omega_\nu(k_\perp)$ of a thin magnetoelectric film (on account of hybridization of the elastostatic and electrostatic mechanisms of spin–spin interaction).

*E-mail: tarasen@host.dipt.donetsk.ua

[1] R. V. Pisarev, Ferroelectrics **162**, 191 (1994).
[2] S. Bluck and H. G. Kahle, J. Phys. C **21**, 5193 (1988).
[3] E. A. Turov, V. V. Men'shenin, and V. V. Nikolaev, Zh. Éksp. Teor. Fiz. **104**, 2061 (1993) [JETP **77**, 1014 (1993)].
[4] E. A. Turov, Zh. Éksp. Teor. Fiz. **104**, 3886 (1993) [JETP **77**, 868 (1993)].
[5] E. A. Turov, Ferroelectrics **162**, 191 (1994).
[6] V. D. Buchel'nikov and V. G. Shavrov, Zh. Éksp. Teor. Fiz. **109**, 706 (1996) [JETP **82**, 380 (1996)].
[7] E. A. Turov and V. V. Men'shenin, Zh. Éksp. Teor. Fiz. **108**, 2061 (1995) [JETP **81**, 1124 (1995)].
[8] V. I. Ozhogin and V. L. Preobrazhenskiĭ, Usp. Fiz. Nauk **155**, 593 (1988) [Sov. Phys. Usp. **31**, 713 (1988)].
[9] S. V. Tarasenko, Pis'ma Zh. Tekh. Fiz. **14**, 2041 (1988) [Sov. Tech. Phys. Lett. **14**, 858 (1988)].
[10] A. L. Sukstanskiĭ and S. V. Tarasenko, Zh. Éksp. Teor. Fiz. **105**, 928 (1994) [JETP **78**, 498 (1994)].
[11] S. V. Tarasenko, Zh. Éksp. Teor. Fiz. **110**, 1411 (1996) [JETP **83**, 520 (1996)].
[12] A. G. Gurevich and G. A. Melkov, *Magnetic Oscillations and Waves* [in Russian], Nauka, Moscow (1994).
[13] Yu. V. Gulyaev and P. E. Zil'berman, Izv. Vyssh. Uchebn. Zaved. Fiz. **31**, 6 (1988).
[14] Yu. V. Gulyaev, I. E. Dikshteĭn, and V. G. Shavrov, Usp. Fiz. Nauk **167**, 735 (1997).
[15] V. A. Krasil'nikov and V. V. Krylov, *Introduction to Physical Acoustics* [in Russian], Nauka, Moscow (1984).
[16] A. G. Khachaturyan, *Theory of Phase Transformations and the Structure of Solid Solutions* [in Russian], Nauka, Moscow (1974).
[17] B. N. Filippov, ''Surface spin and magnetoelastic waves in ferromagnets'' [in Russian], IFM UNTs AN SSSR Preprint No. 80-1, Institute of Metal Physics, Ural Scientific Center of the Academy of Sciences of the USSR, Sverdlovsk (1980).
[18] S. V. Tarasenko, Akust. Zh. **44**, 260 (1998).
[19] V. I. Alshits, A. N. Darinskii, and J. Lothe, Wave Motion **16**, 265 (1992).

Translated by Steve Torstveit

ELECTRONIC PROPERTIES OF METALS AND ALLOYS

Magnetodynamic nonlinearity of the electrical properties of uncompensated metals

V. R. Sobol* and O. N. Mazurenko

Institute of Solid State and Semiconductor Physics, National Academy of Sciences of Belarus, ul. P. Brovki 17, 220072 Minsk, Belarus

(Submitted June 23, 2000; revised August 14, 2000)
Fiz. Nizk. Temp. **27**, 60–67 (January 2001)

The magnetodynamic nonlinearity of the electrical properties of uncompensated metals, wherein the drift of charge carriers at a high density in crossed electric and magnetic fields leads to generation of a self-field of the current, is investigated experimentally and analytically. The experiment is done on cylindrical conductors made from high-purity polycrystalline aluminum, in an arrangement in which the radial current is acted on by an external magnetic field coaxial to the sample. The electric potential and the nonlinear correction to it are determined over a wide range of values of the energy dissipation, all the way up to levels corresponding to the boiling crisis of liquid helium. In the approximation that the contributions to the resistive effect of the external field and self-field are additive, the results of a calculation based on the macroscopic field equations are found to be in good agreement with experiment. Questions pertaining to the concentration of magnetic field energy of the current for a cylindrical geometry of the conductor are discussed in the approximations of long and short solenoids. [DOI: 10.1063/1.1344142]

INTRODUCTION

A magnetic field gives rise to nonlocal effects in charge transport when, in addition to the usual coupling between the current density and the electric and magnetic fields, there are also gradient terms resulting from the nonlinearity due to the self-field of the current. In metals there are known dynamic effects stimulated by a static external magnetic field and which lead to a redistribution of the current density over the cross section of a film conductor on account of the substantial nonuniformity of the self-magnetic field under conditions of the static skin effect at a high degree of compensation of the electronic and hole volumes.[1–3] Similar effects are encountered in massive samples. In particular, in polycrystalline conductors with a complex type of constant-energy surface, e.g., in randomly inhomogeneous media, because of the spatial fluctuations of the conductivity in differently oriented crystallites in the presence of a uniform external magnetic field the asymptotic effective conductivity, which relates the volume-averaged values of the current density and electric field, differs appreciably from the local values of the conductivity.[4] In addition to the nonlinear dynamics of the charge carriers considered here, in a dc electromagnetic field there exists an extremely wide class of nonlinear electrical properties of metals under conditions such that the motion of the charges is efficiently influenced by the magnetic component of the field of an rf wave. Much of the experimental and theoretical work on this class of phenomena is reflected in the review article by Makarov and Yampol'skiĭ.[5] An external gradient magnetic field also has an additional effect on the charge transport in a polycrystalline conductor, and the current density at each point depends on the degree of spatial variation of the components of the conductivity tensor.[6,7] Magnetic nonlinearity in massive conductors can also be observed in the transport of a high charge density, when the character and intensity of the carrier motion give rise to an additional field as a factor affecting the carrier dynamics and the kinetic properties of the medium.[8,9] The intrinsic motion of the carriers and the magnetic field due to it are especially efficient under conditions such that an additional azimuthal drift occurs under the influence of the Lorentz force. Additional drift of the carriers causes the conductivity at each point to be determined not only by the external magnetic field but also by the character of the collective motion of the carriers in the bulk, stimulating a macroscopic nonlinearity of the properties.

The goal of this study was to investigate experimentally the magnetodynamic nonlinearity of the low-temperature conducting properties of normal uncompensated metals (for the particular case of aluminum) under conditions of steady charge flow. Such research is topical in view of the necessity of exploring further the questions of the electromagnetic interaction in anisotropic nonlinear conducting media. We consider the problem in which the properties are determined by the intrinsic internal parameters (dispersion relation, physical purity, mean free path of the carriers, etc.) in conjunction with the conditions of the external influences (the strength of the external magnetic field, the charge flux density, and the character of the motion of the charge, which is set by the shape of the sample and the boundary conditions, the nature of its thermal coupling to the surrounding medium, etc.). In addition, it remains important to look for ways of expediting the application of existing materials. Knowing the behavior of the nonlinearity of the properties of conductors, one can determine ways of improving the efficiency for materials

used in the cores and windings of electric motors and other devices, where it is necessary to produce a magnetic field, accumulate field energy, and concentrate this energy in local regions of space.

EXPERIMENT

Methods of investigation, choice of materials, and experimental procedures

The scale of the magnetodynamic nonlinearity can be estimated by recording the material characteristics that are sensitive to magnetic field. For normal uncompensated metals under certain conditions the coefficient of proportionality between the electric field E and current density j will be a strong function of the magnetic field B. Such a situation occurs in a cylindrical conductor in which a radial current is flowing and a coaxial external magnetic field causes additional drift of the particles through the Lorentz force. In such a geometry the magnitude of the electric field in the radial direction is proportional to the reciprocal of the diagonal component of the conductivity tensor and the radial current density. This is because the drift of the carriers is due not to the Hall field but to its radial component. The azimuthal drift current density can be written as

$$j_\theta = -\frac{(\rho_{\theta r} j_r + \rho_{\theta z} j_z)}{\rho_{\theta\theta}}, \tag{1}$$

where ρ_{ij} are the components of the resistivity tensor and j_k the components of the current density vector in a cylindrical coordinate system. We neglect the motion of the carriers along the magnetic field. The intensity of the azimuthal drift of the carriers is determined by the parameter $\rho_{\theta r}/\rho_{\theta\theta}$, which depends on the band structure and the structural state of the material. It follows from what we have said that the most preferable from the standpoint of efficient generation of a self-magnetic field and the onset of nonlinearity of the properties are materials whose dispersion relations provide for the maximum possible conversion of the radial motion of the carriers into azimuthal motion, i.e., dispersion relations close to that for a free electron gas. In the approximation of a free electron gas one has $\rho_{\theta r}/\rho_{\theta\theta} = \omega\tau$ (ω is the cyclotron frequency and τ the relaxation time), and large effective magnetic fields are required for realization of the effect. Real conducting materials have complicated dispersion relations, and, in addition, the requirement that the crystalline symmetry of the metal be compatible with the cylindrical symmetry of the conductor makes it necessary to use a conductor material in the polycrystalline state. The polycrystalline nature of the conducting medium in a certain sense ''generalizes'' the features of the dispersion relation. In view of what we have said, we chose pure polycrystalline aluminum as the conducting material for our investigations, as aluminum is the material most often used in cryogenic power systems, whether in the form of a pure metal, a solid solution, or as a component of various alloys and composites.

The sample conductors were made of fine-grained aluminum in the form of cylinders of height $h = 0.4$ cm. They were connected to inner and outer concentric current electrodes to provide for the passage of a radial current through the sample. The inner and outer radii of the samples were $r_1 = 0.25$ and $r_2 = 1.5$ cm, respectively. Potential contacts were mounted on the surface of samples along the radius r at distances of 0.5, 0.7, and 1.0 cm from the axis so as to permit determining the spatial dependence of the potential φ during the measurements by recording the potential difference $\Delta\varphi$ between two pairs of contacts. The external coaxial magnetic field B_0 led to an additional Hall drift of the carriers under the influence of the Lorentz force, and the self-magnetic drift field B_s was either collinear or anticollinear with the external field. The self-magnetic field was recorded by means of Hall sensors mounted on the surface of the disks by subtracting the component provided by the solenoid from the total measured value of the magnetic field B_t. Measurements were made at magnetic fields of up to 8 T, generated by the superconducting solenoid of a UIS-1 helium cryostat. The samples were immersed in liquid helium, and the thermal regime was determined by the relationship between the level of Joule power dissipation and the intensity of the boiling of the cryogenic liquid. In the course of the experiment the potential difference between pairs of contacts and the value of the self-magnetic drift field were recorded for various values of the external field as a function of the value of the radial current and its direction. Measurements were made in the current-generator regime, making it possible to create different thermal heads.

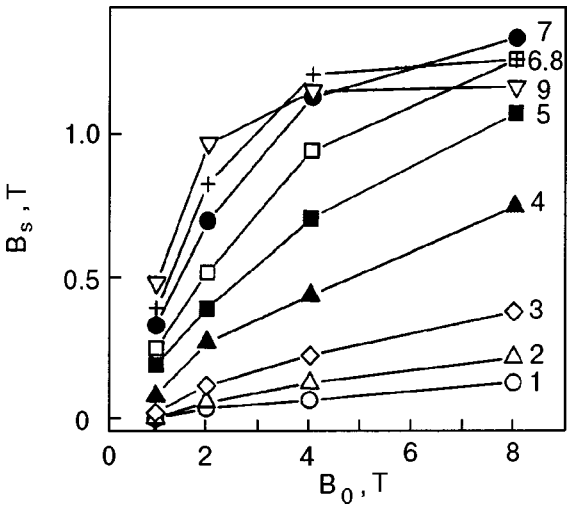

FIG. 1. Self-magnetic field as a function of the external magnetic field for different values of the mean current density j [A/cm^2]: 25 (*1*), 50 (*2*), 100 (*3*), 200 (*4*), 300 (*5*), 400 (*6*), 500 (*7*), 600 (*8*), 700 (*9*).

Experimental results and their interpretation

The intrinsic motion of the carriers under the influence of the Lorentz force affects the resistive properties of the medium, since during the time that a particle moves from the inner diameter to the outer diameter the path traversed in the azimuthal direction will be a factor of $\omega\tau$ larger than in the radial direction, i.e., each electron forms effective current loops that contribute to the total magnetic field. The character of the spatial distribution of the self-magnetic field is illustrated in Fig. 1. We see that the self-magnetic field increases as the external field increases, the rate of growth being determined by the radial current density. On the whole, the curves characteristically have a slower-than-linear depen-

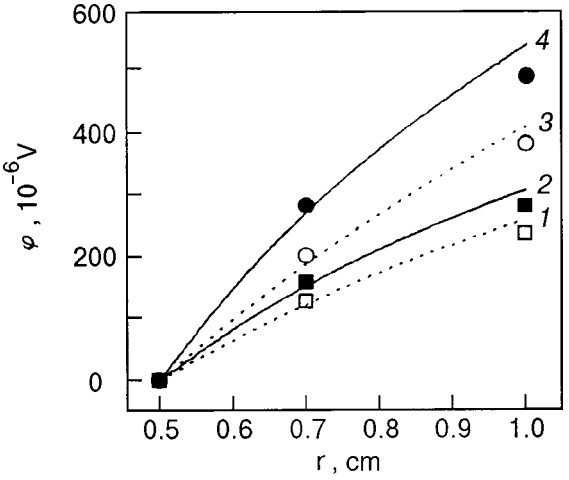

FIG. 2. Distribution of the electric potential along the radius of the sample under conditions of electrical nonlinearity, with the self-magnetic field collinear to the external field (*2,4*, ———) or anticollinear (*1,3*, – – –) for different current densities j [A/cm^2]: 150 (*1,2*), 250 (*3,4*). The symbols are experimental, the curves are theoretical.

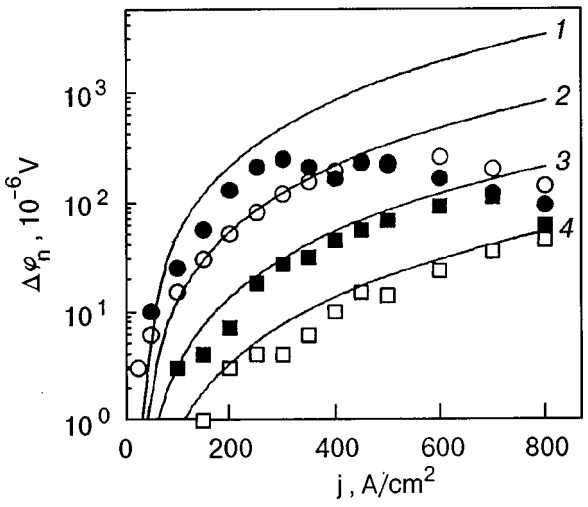

FIG. 3. Nonlinear correction to the electric potential as a function of the radial current density for various values of the external magnetic field B [T]: 8 (*1*, ●); 4 (*2*, ○), 2 (*3*, ■), 1 (*4*, □). The symbols are experimental, the curves are theoretical.

dence. In addition, at high current densities, corresponding to the upper family of curves, the curves cross, indicating that new factors that limit the intensity of the azimuthal drift of the particles have come into play. This leads to saturation of the self-field at current densities of 400–750 A/cm^2. These factors, their nature, and also their influence on the dynamic nonlinearity will be discussed in the analysis Section below.

The typical character of the spatial distribution of the potential is shown in Fig. 2. The scale of the potential difference in the case of the collinear and anticollinear geometries increases with increasing magnetic field and increasing radial current density. Starting from the measured potential differences on pairs of contacts in the collinear ($\Delta\varphi_c$) and anticollinear ($\Delta\varphi_a$) geometries of the flow of charge, we determined the increment of potential difference that is odd in the current: this is defined below as the nonlinear correction to the potential, $\Delta\varphi_n$. In calculating $\Delta\varphi_n$ it was assumed that the change in the potential difference in the collinear and anticollinear geometries is symmetric with respect to a certain average value of the potential difference, $\Delta\varphi_0$, corresponding to the zero level of the nonlinearity. On this basis the nonlinear correction was found from the relation $\Delta\varphi_n = 1/2(\Delta\varphi_c - \Delta\varphi_a)$. Figure 3 shows the indicated increment of the potential difference $\Delta\varphi_n$ for the inner pair of contacts as a function of the radial current density. It should be noted that the inner pair of contacts to the sample are more subject to the influence of the self-magnetic field of the Hall drift, since it is localized mainly in the inner region of the disk-shaped sample, by analogy with the magnetic field of any solenoid.

To estimate the level of the magnetodynamic nonlinearity we use the relative nonlinear correction to the potential, $\Delta\varphi_n/\Delta\varphi_0 = (\Delta\varphi_c - \Delta\varphi_a)/(\Delta\varphi_c + \Delta\varphi_a)$, which we call the magnetodynamic parameter. This characteristic is shown in Fig. 4 as a function of the current density. It is important to note that in the range of radial current densities below 300 A/cm^2 the magnetodynamic parameter exhibits approximately the same scale of values for different external magnetic fields. At high levels of the radial current density the behavior of the magnetodynamic parameter becomes nonmonotonic, except for the data obtained in a field of 1 T. We see that the efficiency of the magnetic self-effect of the system in the range of current densities used is highest for external fields below 4 T. This has definite practical value from the standpoint of realizing this effect in cryogenic machines and other devices, which ordinarily have working fields of the order of 4 T or lower. The ''dips'' observed on the characteristic are naturally attributed to the vanishing of the additional Hall drift magnetic field under the influence of factors that cause a decrease of the efficiency parameter $\omega\tau$ of the magnetic field.

Let us analyze the character of the electric field distribution and electric potential under conditions of magnetodynamic nonlinearity on the basis of the relation

$$E_r = \rho_{rr} j_r + \rho_{r\theta} j_\theta, \tag{2}$$

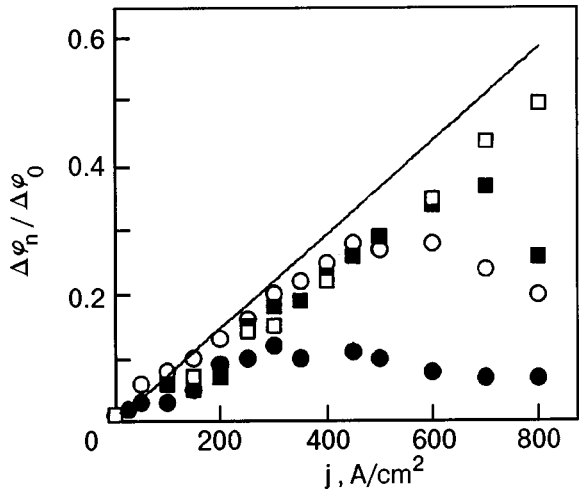

FIG. 4. Behavior of the magnetodynamic parameter as a function of the radial current density for various values of the external magnetic field B [T]: 1 (□), 2 (■), 4 (○), 8 (●). The symbols are experimental, the curves are theoretical.

where E_r is the radial component of the electric field vector. Then for an electric potential $\varphi(r)$ we obtain the following integral relation:

$$\varphi(r)=\int\left(\rho_{rr}-\rho_{r\theta}\frac{\rho_{\theta r}}{\rho_{\theta\theta}}\right)j_r dr;\quad j_r=\frac{I}{2\pi rh},\tag{3}$$

where I is the generator current.

The character of the spatial dependence of the potential is determined by local values of the kinetic coefficients and radial current density vector. The spatial topology of the kinetic coefficients of a cylindrical conductor whose height is independent of the radius is largely determined by the type of distribution of the Lorentzian drift magnetic field $B_s(r)$, which, as is readily seen after integration over the length of the cylinder, has the form

$$B_s(r)=\frac{\mu_0\mu}{4\pi}h \times\int\int\frac{j_s(r')r'(r'-r\cos\theta)d\theta dr'}{(r^2+r'^2-2rr'\cos\theta)(r^2+r'^2+h^2-2rr'\cos\theta)^{1/2}}.\tag{4}$$

Here μ_0 and μ are the magnetic permeability of free space and the relative permeability of the material. We now linearize this relationship, apply the residue theorem in the summation over the azimuthal variable in the approximation that the thickness of the sample is small compared to the mean radius, and integrate from the point in question over all of its volume domain to get

$$B_s(r)=\mu_0\mu\frac{I}{4\pi}\frac{RB_0}{\rho}\frac{1}{r}\ln\frac{(1+\sqrt{2})r_2}{r+(r^2+r_2^2)^{1/2}},\tag{5}$$

where ρ is the diagonal component of the resistivity tensor.

For a quasi-closed type of constant-energy surface we choose the diagonal components $\rho_{\theta\theta}$ and ρ_{rr} of the resistivity tensor as quantities of the order of the resistivity in zero magnetic field, ρ_0, while the component $\rho_{\theta r}$ is written as RB_0, where R is the Hall constant. In a high magnetic field we may neglect the contribution of the diagonal component of the resistivity and write the potential as a function of the external field B_0, which implicitly includes the self-field B_s:

$$\varphi(r)=\frac{I}{2\pi h}\frac{(RB_0)^2}{\rho_0}\ln\left(\frac{r}{r_1}\right)\left\{1+\frac{\mu_0\mu R}{2\pi\rho\ln(r/r_1)}\right. \times\left[\frac{1}{r}\ln\left(\frac{r+(r^2+r_2^2)^{1/2}}{r_2}\right)-\frac{1}{r_1}\ln\left(\frac{r_1+(r_1^2+r_2^2)^{1/2}}{r_2}\right)\right. +\frac{1}{r_2}\ln\left(\frac{r_1}{r}\frac{r_2+(r^2+r_2^2)^{1/2}}{r_2+(r_1^2+r_2^2)^{1/2}}\right) \left.\left.+\left(\frac{1}{r_1}-\frac{1}{r}\right)\ln(1+\sqrt{2})\right]\right\}+\varphi_0.\tag{6}$$

The first term describes the potential distribution in the presence of a uniform magnetic field, while the remaining terms constitute the magnetodynamic correction to the potential. Using this expression for the potential, we did an estimatory calculation of the dependence of the potential on the radial current density and the scale of the nonlinearity. The results are presented for comparison with the experimental data in Figs. 2, 3, and 4. It follows from a comparison that the above expression on the whole gives a correct description of the nonlinearity under discussion in the region of low levels of Joule power dissipation.

For describing the nonmonotonicity of the behavior of the magnetodynamic parameter we turn to an analysis of the thermal state of the sample. We consider the steady-state problem of the thermal regime of the sample, taking into account the balance condition between the Joule power dissipated in the volume and the heat removed through the surface of the sample on boiling of the cryogenic liquid. The smallest thermal heads are observed for nucleate boiling, when the temperature of the surface exceeds the temperature of the cryogenic liquid by a few tenths of a degree. It should be noted that the transition from nucleate to film boiling occurs in a rather narrow temperature interval, amounting to a fraction of a degree. At first glance the transition region and the adjacent film-boiling region should have a weak influence on the resistive properties. However, there is actually a sharp decrease in the magnetodynamic parameters in this region. This is due to the behavior of the magnetoresistance of the sample in the given geometry. The temperature dependence of the effective relaxation time, which is the main factor shaping the behavior of the resistivity and which consists of an impurity component and a phonon component, retains the same form as for the conventional geometry. Specifically, the phonon component of the relaxation time, which is considerably longer than the impurity component, begins to grow shorter as the temperature is raised. Since here the resistivity is equal to the reciprocal of the diagonal component of the conductivity tensor, the resistance of the sample is proportional to the square of the cyclotron frequency and of the relaxation time. The temperature derivative of the resistance increases sharply in absolute magnitude, and the resistance falls off much more strongly with changing temperature than in the conventional situation in which the resistance is inversely proportional to the relaxation time. As a result, the conditions of high magnetic field cease to hold because of the heating of the surface and of the entire volume of the conductor. The balance conditions can be used to write the heat flux density q through the surface as a function of the current, wherein the magnetoresistive properties of the conductor are given by the algebraic sum of the external and self-magnetic field:

$$q(I)=I^2\frac{R^2(B_0+B_s)^2}{\rho_0[1+\lambda(B_0+B_s)]}\frac{1}{2\pi^2h}\ln\left(\frac{r_2}{r_1}\right)\frac{1}{[(r_2^2-r_1^2)+r_2h]}.\tag{7}$$

This expression takes into account the weak linear dependence of the diagonal component of the resistivity tensor on the magnetic field, and the parameter λ, on the basis of the experimental data, is 0.1 T^{-1}.

On the basis of the relation obtained we calculate the heat flux density through the surface of the sample as a function of the averaged radial current density. Figure 5 shows a family of such curves for the collinear geometry of the charge flow. Taking into account that in the case of nucleate

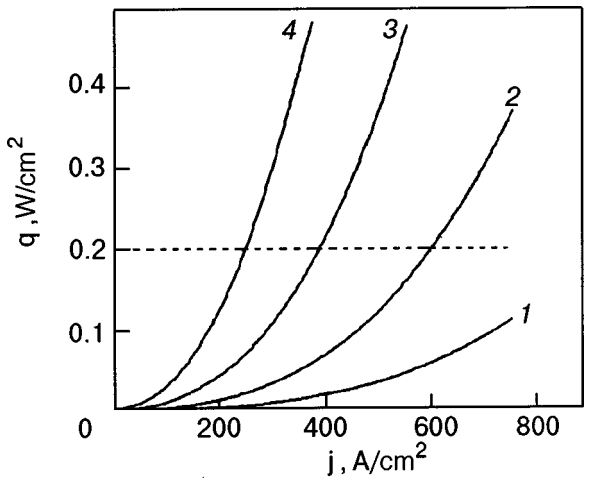

FIG. 5. Thermal flux density as a function of the mean current density in the collinear direction of the external magnetic field for various values of B [T]: 1 (*1*), 2 (*2*), 4 (*3*), 8 (*4*).

boiling of helium in large volumes on the surface of nonferrous metals the boiling crisis begins under conditions corresponding to a heat flux dissipation of the order of 0.20–0.30 W/cm^2, one can state that the transition to film boiling as the efficiency parameter of the magnetic field decreases occurs in an interval of values of the current density that decreases sharply with increasing external magnetic field.[10] The scales of current density at which the heat flux density reaches critical values (see Fig. 5) are in agreement with the plots in Figs. 3 and 4, where the start of the boiling crisis corresponds to the appearance of some sort of maximum on the experimental curves.

It follows from the experiment and a calculation that the magnetodynamic nonlinearity effect in high-purity aluminum under favorable conditions can reach fifty percent in terms of the resistance. These effects are especially efficient in low external fields, when the thermal heating processes due to the Joule power dissipation cannot be manifested. Control of the resistive properties of cylindrical conductors via such parameters as the value and direction of the current can be implemented for processes based on the unipolar conductivity. For example, in the voltage-generator regime the value of the current through the active element is varied on account of the difference of the resistivities for the collinear and anticollinear geometries. Such a process can be realized for circuits with a quasisteady flow of charge.

The enhancement of the resistivity in the collinear geometry is accompanied by an increase in the magnetic energy of the circulating current. A cylindrical conductor, like a solenoid, has circular current lines, the magnetic field of which is proportional to the azimuthal current and, in the bulk of the sample, judging from the results of this study, can reach fifty percent of the value of the external field. As a consequence, there is a likelihood for the magnetic field energy of the whole system, the solenoid plus the cylindrical conductor, to be doubled, and for systems having large volumes, this nonlinearity should serve as an additional source of accumulation and concentration of field energy. It should be noted that for a cylindrical core with a height greater than the mean radius, the concentrating of magnetic field energy will be more pronounced, as in the case of a long wire solenoid, in which the field is concentrated mainly in the interior volume. The concentration of energy and the enhancement of the self-field are important for increasing the magnetic self-effect, which in a long cylindrical conductor should lead to a power-law variation of the field strength inside the volume, rather than the logarithmic dependence obtained in this study. This follows from the basic Maxwell equations if the magnetic field pattern is considered self-consistently. However, this assertion does not mean that the same current passed through a short and a long cylinder of the same diameter will produce a stronger field at the center of the long conductor. A calculation shows that the field strength in a conductor having a height of 4 cm and the previously indicated radial dimensions will be smaller than in the experimental case. This is because the linear current density for the long conductor is smaller, and the self-effect is insufficient to wind up the electrons to such a degree that the concentration of magnetic field lines in the large volume would exceed the corresponding concentration in the small volume of the short cylinder. The integrated energy of the azimuthal drift magnetic field for the long cylindrical conductor is larger, since the degree of the magnetic self-effect is higher for it. It is clear that the problem of heat removal for a long cylindrical conductor is more complicated than for a short one, since the surface increases in proportion to the square of the linear dimension as the volume increases.

CONCLUSION

An experimental study has shown that nonlinearity of the electrical properties of a magnetodynamic nature can arise in normal metals having uncompensated electronic and hole volumes.

The scale of the nonlinearity is determined by the intensity of the circulation of the Hall current in conductors of circular cylindrical geometry in an external magnetic field.

The basic parameters of the magnetic self-effect of metals have been established experimentally for the particular case of aluminum over a wide range charge flux densities, all the way up to levels of dissipation corresponding to the boiling crisis of helium.

The considerable scale of the azimuthal drift magnetic field and its gradient nature make it important to address the question of its influence on the charge transport and the character of the electrical nonlinearity under conditions of a nonlocal heat-transfer function.

*E-mail: sobol@ifttp.bas-net.by

[1] M. I. Kaganov and V. G. Peschanskiĭ, Zh. Éksp. Teor. Fiz. **33**, 1957 (1961) [*sic*].
[2] V. G. Peschanskiĭ and M. Ya. Azbel', Zh. Éksp. Teor. Fiz. **55**, 1980 (1968) [Sov. Phys. JETP **28**, 1045 (1969)].
[3] V. G. Peschanskiĭ, K. Oyamada, and D. I. Stepanenko, Fiz. Nizk. Temp. **17**, 328 (1991) [Sov. J. Low Temp. Phys. **17**, 170 (1991)].
[4] Yu. A. Dreĭzin and A. M. Dykhne, Zh. Éksp. Teor. Fiz. **63**, 242 (1972) [Sov. Phys. JETP **36**, 127 (1973)].
[5] N. M. Makarov and V. A. Yampol'skiĭ, Fiz. Nizk. Temp. **17**, 547 (1991) [Sov. J. Low Temp. Phys. **17**, 285 (1991)].

[6] O. N. Mazurenko, V. R. Sobol, and A. A. Drozd, Fiz. Nizk. Temp. **21**, 78 (1995) [Low Temp. Phys. **21**, 59 (1995)].
[7] V. R. Sobol', O. N. Mazurenko, and A. A. Drozd, Fiz. Nizk. Temp. **25**, 1212 (1999) [Low Temp. Phys. **25**, 907 (1999)].
[8] B. B. Boĭko, V. I. Gostishchev, A. A. Drozd, V. S. Kuz'min, and O. N. Mazurenko, Fiz. Met. Metalloved. **63**, 1133 (1987).
[9] B. B. Boiko, V. R. Sobol, and O. N. Mazugenko *et al.*, Adv. Cryog. Eng. (Mater.) **42**, 1063 (1996).
[10] M. Jergel and R. Stevenson, Cryogenics **14**, 431 (1974).

Translated by Steve Torstveit

LOW-DIMENSIONAL AND DISORDERED SYSTEMS

Mechanisms for the generation of thermopower carbon–graphite materials with different crystal structures

L. Yu. Matsuĭ, I. V. Ovsienko,* and L. L. Vovchenko

Taras Shevchenko Kiev University, ul. Vladimirskaya 64, 01017 Kiev, Ukraine
(Submitted May 22, 2000; revised July 3, 2000)
Fiz. Nizk. Temp. **27**, 68–72 (January 2001)

The results of experimental and theoretical studies of the temperature dependence of the thermopower of carbon–graphite materials with different crystal structures are presented. It is shown that the mechanisms giving rise to the thermopower in these materials are different. In coarse-grained graphites the main contribution to the total thermopower at low temperatures derives from the phonon-drag effect on the charge carriers, while the contribution of the diffusion component of the thermopower at these temperatures is insignificant. In a fine-grained graphite the main contribution to the total thermopower in the entire temperature interval is from the diffusion component of the thermopower, while the contribution of the phonon component is small even at low temperatures.
[DOI: 10.1063/1.1344143]

The thermopower is particularly sensitive to changes in the parameters of the electronic structure of a material. As we know, carbon–graphite (CG) materials synthesized by different methods (pyrolysis, coking) and at different temperatures have different parameters of the crystal structure and, hence, of the electronic structure. However, all CG materials to some degree have the structural characteristics inherent to the graphite crystal: a layered structure, the arrangement of the atoms in the layer, etc. Therefore, CG materials make an ideal model material for studying how the mechanisms that give rise to the thermopower depend on the electronic structure of a material.

For our studies of the thermopower we chose samples of CG materials having different parameters of the crystal structure: a sample obtained by the coking of coarse-grained macroscopically isotropic graphite (type V–1), a sample of thermally expanded graphite (TEG) obtained by the preliminary intercalation of highly oriented pyrolytic graphite (HOPG) by sulfuric acid, followed by its thermal expansion at 400 °C, and a sample obtained by pyrolysis of fine-grained anisotropic graphite (type UPV). The parameters of the crystal structure of the of the CG samples studied are given in Table I, where the following notation is used: d_{002} is the distance between adjacent graphite layers, L is the size of the crystallites, γ is the graphitation parameter, defined as

$$\gamma = \frac{d_{002\max} - d_{002}}{d_{002\max} - d_{002\min}}, \tag{1}$$

where $d_{002\max} = 3.446 \times 10^{-10}$ m corresponds to the interlayer distance in a completely disordered CG material, and $d_{002\min} = 3.35 \times 10^{-10}$ m corresponds to the interlayer distance in natural single-crystal graphite; m is the predominant orientation parameter, which is defined as the ratio of the intensities of the 002 lines of graphite on the diffraction patterns obtained in the directions perpendicular to and parallel to the graphite layers. As we see from the table, TEG is a coarse-grained material with a pronounced anisotropy, i.e., its electrophysical, mechanical, and thermal properties differ along different crystallographic directions. In the type V–1 graphite each crystallite also has anisotropy, but the larger crystallites of that material are randomly arranged with respect to one another, and the V–1 material on the whole is therefore isotropic. The type UPV graphite consists of small crystallites, but because of their identical mutual orientation this fine-grained material on the whole is anisotropic.

TABLE I. Parameters of the crystal structure of carbon–graphite materials.

Type of CG material	$d_{002}, 10^{-10}$ m	L, m	γ	m
TEG	3.352	4×10^{-6}	0.97	$\sim 10^4$
V–1	3.390	1×10^{-7}	0.60	~ 1
UPV	3.400	3×10^{-8}	0.30	$\sim 10^3$

In the samples described we measured the temperature dependence of the thermopower (Seebeck coefficient) S in the temperature interval 4.2–300 K by the method described in Ref. 1. The $S(T)$ curves obtained are shown in Fig. 1.

As we see from the figure, for coarse-grained graphites of the types V–1 and TEG the $S(T)$ curve is similar to that in HOPG:[2] at 30–35 K the thermopower has a deep minimum approximately equal to -52 μV/K for V–1 graphite and around -18 μV/K for TEG. For $T > 120$ K the thermopower depends weakly on temperature, and that of V–1 graphite remains negative throughout the entire temperature interval, while the thermopower of TEG changes sign at $T = 100$ K and then remains positive as the temperature is increased further. A completely different form is obtained for $S(T)$ in the fine-grained UPV graphite: the thermopower is

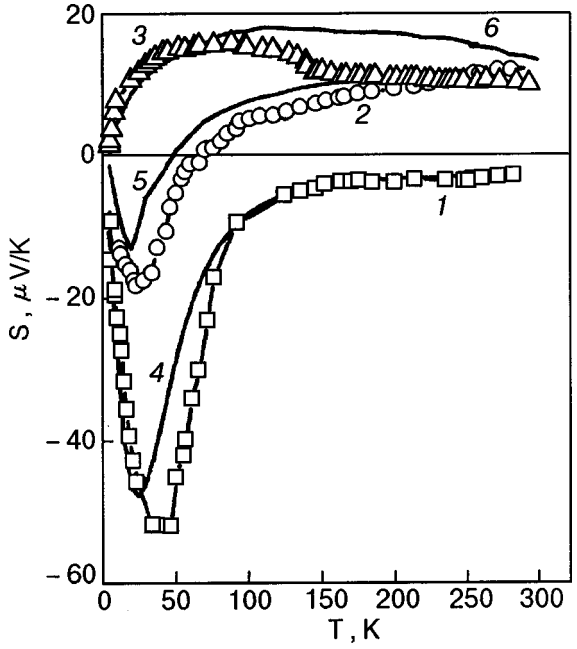

FIG. 1. Temperature dependence of the thermopower in structurally different carbon–graphite materials: type V–1 graphite (*1,4*), TEG (*2,5*), type UPV graphite (*3,6*). Experiment (*1,2,3*), calculated total thermopower S_{calc} (*4,5,6*).

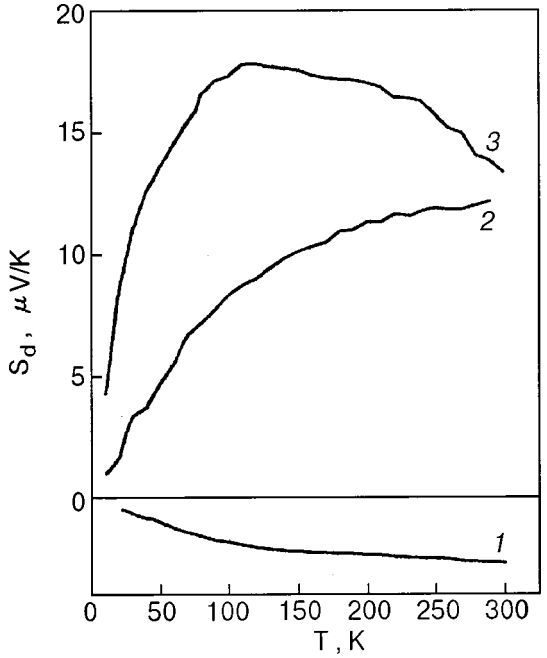

FIG. 2. Calculated temperature dependence of the diffusion component of the thermopower, S_d: type V–1 graphite (*1*), TEG (*2*), type UPV graphite (*3*).

positive throughout the entire temperature interval, has a broad maximum at 60–120 K, and for $T>160$ K is weakly dependent on temperature.

As we know, the thermopower S of graphite is the sum of two components: the diffusion thermopower S_d, and the thermopower due to the phonon-drag effect S_{ph}:

$$S=S_d+S_{\text{ph}}. \tag{2}$$

The contribution of the phonon component of the thermopower is important at low temperatures, when the phonon–phonon scattering is small. With increasing temperature the role of the phonon–phonon interaction increases, and S_{ph} goes to zero. Thus at room temperature the total thermopower is mainly due to the contribution of the diffusion component of the thermopower.

For graphites having two types of carriers, including TEG and V–1 graphite, the thermopower in the framework of the cylindrical model of the band structure is given by the expression[3]

$$S_d=\frac{k_B}{e}\,\frac{a-b}{a+b}\left[\frac{2F_1(E_0/k_BT)}{F_0(E_0/k_BT)}-\frac{E_0}{k_BT}\right], \tag{3}$$

where k_B is Boltzmann's constant, e is the electron charge, a is the ratio of the hole concentration p to the electron concentration n, b is the ratio of the electron mobility μ_n to the hole mobility μ_p, F_1 and F_0 are the Fermi integrals, and E_0 is the overlap of the valence and conduction bands. To calculate the diffusion component of the thermopower it is necessary to know the value of the overlap E_0 and the temperature dependence of the concentrations and mobilities of the charge carriers. For materials with two types of carriers the conductivity σ, Hall coefficient R_H, and magnetoresistance $\Delta\rho/\rho$ are related to the concentrations and mobilities of the electrons and holes as[4]

$$\sigma=(en\mu_n+ep\mu_p);$$

$$R_H=\frac{1}{en}\left[\frac{p/n-(\mu_n/\mu_p)^2}{(p/n+\mu_n/\mu_p)^2}\right]; \tag{4}$$

$$\frac{\Delta\rho}{\rho}=\frac{p}{n}\mu_n\mu_pH^2,$$

where H is the magnetic field strength.

Using the experimental curves of $\sigma(T)$, $R_H(T)$, and $\Delta\rho/\rho(T)$ for V–1 graphite obtained previously[5,6] in the interval interval 77–300 K and taking into account the facts that at room temperature the thermopower is essentially due solely to the contribution S_d and that the electron and hole concentrations in V–1 graphite can be assumed equal ($a=1$), as was shown in Refs. 5 and 6, we calculated the value of the overlap E_0 ($E_0=0.02$ eV), the temperature dependence of the electron and hole concentrations and mobility and, as a result, the temperature dependence of the diffusion component S_d in the temperature interval 77–300 K. For calculating S_d below 77 K we made use of the fact that the parameter b is very weakly temperature dependent for coarse-grained graphites with a structure that differs significantly from the crystal structure of perfect natural single-crystal graphite.[7] The calculated $S_d(T)$ curve in the temperature interval 10–300 K is shown by curve *1* in Fig. 2. Analogous calculations were done for TEG graphite, which has crystal structure parameters (interlayer distance, size of the crystallites) close to those of the HOPG structure. However, the incomplete removal of the acceptor-type intercalant in the thermal expansion causes TEG to have an excess hole concentration, which can amount to as much as 20%. For calculating E_0 and S_d in TEG we used the values of $\sigma(T)$, $R_H(T)$, and $\Delta\rho/\rho(T)$ given in Ref. 8 for TEG synthesized by a method analogous to our method of obtaining TEG; the

value of a was chosen equal to 1.1. Since in Ref. 8 the dependence of $\sigma(T)$ was determined below 77 K, while R_H and $\Delta\rho/\rho$ were given only at room temperature, it was assumed that at lower temperatures the parameter b varies with temperature in the same way as for HOPG.[7] For TEG the calculated value of E_0 is 0.038 eV. The temperature dependence of the calculated S_d for TEG is presented in Fig. 2 (curve *2*). As we see in the figure, in TEG the component S_d is positive over the entire temperature interval, while in V–1 graphite S_d is negative. In both materials the absolute values of S_d decrease monotonically with decreasing temperature.

UPV graphite is a disordered fine-grained graphite in which, as was shown in Ref. 8, the hole concentration exceeds the electron concentration on account of the precipitation of electrons on ''traps'' — grain boundaries, point defects, etc. In other words, $a \neq 1$ for UPV graphite, and E_0 becomes small compared to k_BT or vanishes altogether. For such materials formula (3) takes the form[7]

$$S_d = \frac{k_B}{e}\left[\frac{a}{a+b}\left(\delta^+ - \frac{\Delta}{k_BT}\right) - \frac{b}{a+b}\left(\delta^- + \frac{\Delta}{k_BT}\right)\right],$$
$$\delta^{\pm} = \frac{2F_1(\pm\Delta/k_BT)}{F_0(\pm\Delta/k_BT)}, \tag{5}$$

where Δ is the shift of the Fermi level into the valence band. The parameter a is related to the shifted Fermi level as

$$a = \frac{\ln[1+\exp(\Delta/k_BT)]}{\ln[1+\exp(-\Delta/k_BT)]}. \tag{6}$$

For calculating $S_d(T)$ in UPV graphite we used the values given in Ref. 9 for the electron and hole concentrations and mobilities in UPV graphite. As was shown in Ref. 9, the hole concentration is 3.5–5 times larger than the electron concentration, and when the temperature is raised from 180 K to 300 K the concentration ratio a decreases by a factor of 1.5, while the mobility ratio b remains constant and equal to 2.5. The shift of the Fermi level into the interior of the valence band is calculated according to formula (6) to be $\Delta \approx 0.002$ eV. The calculated $S_d(T)$ curve for UPV graphite is presented in Fig. 2 (curve *3*). As we see in the figure, $S_d(T)$ for UPV graphite differs substantially from $S_d(T)$ for coarse-grained graphites: in UPV $S_d(T)$ has an indistinct broad maximum at a temperature $\sim$100–120 K.

It follows from our calculations of the diffusion component of the thermopower that in the coarse-grained graphites at low temperatures the calculated curve $S_d(T)$ differs from the experimentally measured curve $S(T)$, while at the same time for UPV graphite the form of the $S_d(T)$ curve is in practically complete agreement with that of the experimentally measured curve $S(T)$. These differences in the temperature dependence of the thermopower indicate that at low temperatures the main mechanism giving rise to the thermopower in the coarse-grained graphites (V–1, TEG, and HOPG) is not the diffusion but the phonon mechanism. In the fine-grained graphite UPV, for which the calculated curve $S_d(T)$ agrees with the measured thermopower, the contribution of the phonon thermopower at low temperatures can only be insignificant.

For a more detailed analysis of the mechanisms giving rise to the thermopower at low temperatures we calculated the phonon component of the thermopower in the investigated CG materials. To calculate $S_{\rm ph}$ we used the equations proposed in Ref. 10 for analysis of the phonon component of the thermopower in HOPG:

$$S_{\rm ph}^{(i)} = \pm\frac{k_B}{e}\frac{[k^{(i)}]^2}{\pi^2 N}\left(\frac{k_BT}{\hbar v_S}\right)F_{(i)}T,$$
$$F_i(T) = \int_0^{\hbar v_s q_s^{(i)}/k_BT} dZ Z^2 \frac{\exp(Z)}{[\exp(Z)-1]^2} R_i, \quad Z = \frac{\hbar v_s q_s}{k_BT}, \tag{7}$$
$$R_i = \frac{a_i q_s}{v_s/L + a_i q_s + B q_s T^3} (<1),$$

where the plus sign and the index $i \equiv h$ correspond to the holes, and the minus sign and $i \equiv e$ correspond to electrons; $k^{(i)}$ is the wave vector of the electrons or holes, q_s is the phonon wave vector, v_s is the sound velocity, L is the dimension of a crystallite, N is the total concentration of electrons and holes, and a_i and B are adjustable parameters. We calculated the phonon component $S_{\rm ph}$ according to formula (7) for the coarse-grained V–1 and TEG graphites and the fine-grained UPV graphite. In the calculations we also used the following values of the parameters:

— total carrier concentration $N = n + p$. For V–1 and TEG graphite the experimental curves[5,6,8] of $\sigma(T)$, $R_H(T)$, and $\Delta\rho/\rho(T)$ yielded the values $N_{\rm V-1} \approx 1.2\times10^{24}$ m^{-1} and $N_{\rm TEG} \approx 5\times10^{-24}$ m^{-1}, while for UPV graphite the value was taken from Ref. 9;

— the values of the wave vectors $k^{(i)}$ for V–1 and TEG graphite are the same as in Ref. 10, for UPV the value of $k^{(e)}$ are the same as in Ref. 10, and the relative sizes of $k^{(e)}$ and $k^{(h)}$ were chosen equal to the ratio of the electron and hole concentrations in this material;

— the maximum value $q_{\rm max}$ was determined from the condition that the effective interaction of the charge carriers and phonons be maximum, $q_{\rm max}^{(i)} = 2k^{(i)}$;

— for V–1 and TEG graphite, v_s is determined in Ref. 10, while for UPV graphite it is determined in Ref. 1;

— the parameter a_i was chosen the same as in Ref. 10, while the parameter B, which is an adjustable parameter in Ref. 10, was chosen by fitting here, too (the value of B used in our calculations differs slightly from the value of B in Ref. 10).

The calculated curves of $S_{\rm ph}(T)$ are shown in Fig. 3. One can see from this figure that graphites with different parameters of the crystal structure exhibit different forms of the phonon component of the thermopower. For the coarse-grained graphites $S_{\rm ph}(T)$ is negative and has a deep minimum at $T \sim 35$ K. The absolute values of $S_{\rm ph}$ at low temperatures in these graphites is substantially larger than S_d at these same temperatures. The largest absolute values at the minimum are those for $S_{\rm ph}$ for V–1 graphite. The absolute value of $S_{\rm ph}$ at the minimum for the TEG is somewhat lower. This is because of the excess hole concentration in TEG. The excess hole concentration in TEG does not alter the sign of $S_{\rm ph}$ but only decreases the value of $S_{\rm ph}$ at the minimum, since the phonons interact more efficiently with electrons than with holes. The values of $S_{\rm ph}$ in UPV graphite even at low temperatures are small, and at the maximum at $T = 30$ K

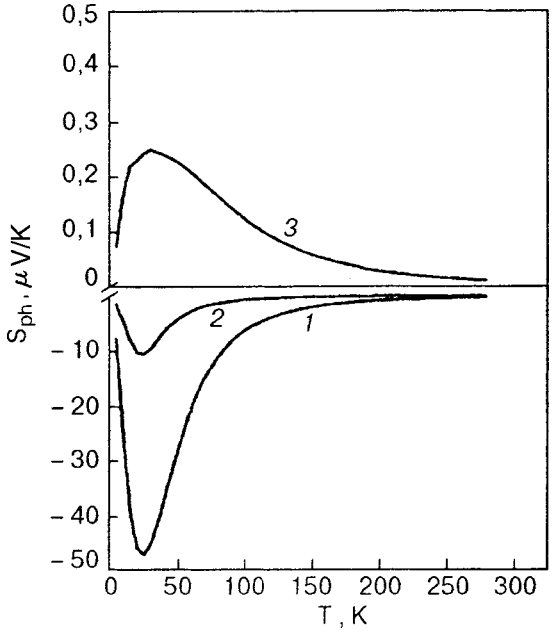

FIG. 3. Calculated temperature dependence of the phonon component of the thermopower, S_{ph}: type V–1 graphite (*1*), TEG (*2*), type UPV graphite (*3*).

amount to $\sim 0.25\ \mu$V/K. It should be noted that in spite of the fact that the calculations of S_d and S_{ph} in the investigated materials employed a number of parameters that had been determined for HOPG, the total calculated thermopower $S_{calc}=S_d+S_{ph}$ for type V–1 graphite and TEG gives a fair description of the experimentally measured $S(T)$ curve for these materials (curves *4* and *5* in Fig. 1). For UPV graphite the experimentally measured $S(T)$ curve is almost completely described by the calculated $S_d(T)$ curve over the entire temperature interval (curve *6* in Fig. 1).

Thus our experimental and theoretical studies of the thermopower in CG materials with different crystal structures has shown that the mechanisms giving rise to the thermopower in these materials are different. In the coarse-grained graphites the main contribution to the total thermopower at low temperatures is from that due to the phonon-drag effect of the charge carriers, and the contribution of the diffusion component of the thermopower at these temperatures is insignificant. As the temperature is raised the phonon component of the thermopower goes to zero. Then the macroscopic isotropicity of the material does not affect the form of the functions $S_d(T)$ and $S_{ph}(T)$. Degradation of the graphite crystal structure, a decrease in the size of the crystallites, and an increase in the interplane distance lead to a change in the form of the functions $S_d(T)$ and $S_{ph}(T)$. In the fine-grained graphite the main contribution to the total thermopower is given by the diffusion component over the entire temperature interval, and the contribution of the phonon component of the thermopower is small even at low temperatures.

This study was supported by the UNTTs as part of Project 1089.

*E-mail: ovsienko@mail.univ.kiev.ua

[1] L. L. Vovchenko, I. V. Dvorkina, and L. Yu. Matzui, Fiz. Nizk. Temp. **20**, 463 (1994) [Low Temp. Phys. **20**, 368 (1994)].
[2] K. Sugihara, J. Phys. Soc. Jpn. **29**, 1465 (1977).
[3] C. Ayache and L. Spain, Carbon **17**, 277 (1979).
[4] I. L. Bonch-Bruevich and S. T. Kalashnikov, *Physics of Semiconductors* [in Russian], Nauka, Moscow (1977).
[5] Yu. I. Sementsov, E. I. Kharkov, and L. Yu. Vavilina, Ukr. Fiz. Zh. **23**, 616 (1978).
[6] E. I. Kharkov and L. Yu. Matsuĭ, Ukr. Fiz. Zh. **26**, 1371 (1981).
[7] L. S. Semko, I. G. Chernysh, L. L. Vovchenko, and L. Yu. Matsuĭ, Plasticheskie Massy, No. 8, 20 (1991).
[8] Yu. I. Sementsov, Author's Abstract of Candidate's Dissertation [in Russian], L'vov (1983).
[9] C. A. Klein, J. Appl. Phys. **35**, 2947 (1964).
[10] K. Kobayashi, K. Sugihara, H. Oshima, and T. Tsuzuku, J. Phys. Soc. Jpn. **62**, 4393 (1993).

Translated by Steve Torstveit

Spectroscopy of the electron–phonon interaction in the layered two-dimensional dichalcogenide $1T$–VSe_2

G. V. Kamarchuk,* A. V. Khotkevich, and V. M. Bagatskiĭ

B. Verkin Institute for Low Temperature Physics and Engineering, National Academy of Sciences of Ukraine, pr. Lenina 47, 61164 Kharkov, Ukraine

P. Molinie, A. Leblanc, and E. Faulques

Institute des Materiaux Jean Rouxel, 2 rue de la Houssiniere, BP32229, F-44322 Nantes, France
(Submitted July 11, 2000)
Fiz. Nizk. Temp. **27**, 73–79 (January 2001)

The vibrational spectra of the layered two-dimensional transition-metal dichalcogenide $1T$–VSe_2 are investigated by the methods of point-contact and Raman spectroscopy. The measured point-contact spectra and the Raman scattering spectra contain features that coincide in position and relative intensity. Various regimes of current passage (ballistic, diffusive, and thermal) in $1T$–VSe_2/Cu point contacts are investigated. Both direct and inverse point-contact spectra are recorded, the former demonstrating the effect of the electron–phonon interaction in $1T$–VSe_2 and the latter reflecting the destruction of localization of the electronic states in the region near the contact, which leads to growth of the contact conductance. A study of the point contacts in the regime of small energy and momentum mean free paths of the electrons reveals nonlinearities caused by a phase transition of the material to a state with a charge density wave. The point-contact electron–phonon interaction function, previously unknown for this compound, is recovered from the data, and the values of the mean and rms phonon frequencies in $1T$–VSe_2 are calculated. An estimate of the Debye temperature is made. © *2001 American Institute of Physics.* [DOI: 10.1063/1.1344144]

INTRODUCTION

The creation of new materials having a set of optimal properties for technological application is one of the most active topics in solid-state physics. It is therefore necessary to make a detailed study of the characteristics of both newly created compounds and the materials used for their synthesis. It was recently reported[1] that a new class of superconductors and ferromagnets has been created on the basis of metallic dichalcogenides and superconductors of the A15 family. One compound of this class is GaV_5Se_9, which is obtained by the dissolution of V_3Ga in $1T$–VSe_2 and exhibits ferromagnetic and metallic properties. Before embarking on a study of the magnetic and spectral properties of this compound, we have made a detailed spectral study of the vanadium dichalcogenide $1T$–VSe_2 by the method of point-contact and Raman spectroscopy; here we present the results of that study.

The compound $1T$–VSe_2 belongs to the class of quasi-two-dimensional layered structures. Its crystals consist of a set of planar sandwich structures stacked on top of one another. Each of these elements is made up of three layers: upper and lower layers of selenium atoms separated by an interlayer of vanadium atoms, forming a Se–V–Se sandwich. The metal and chalcogen layers in $1T$–VSe_2 are displaced relative to each other in such a way that the vanadium atoms inside the sandwich are found in an octahedral environment of selenium atoms.[2] The distance between the chalcogen and metal layers is almost a factor of two smaller than the distance between sandwiches. This, together with the strong covalent bonding within the sandwich, the weak van der Waals forces acting between sandwiches, and the small overlap of the electronic wave functions of the metallic layers make for quasi-two-dimensionality and anisotropy of the physical properties of $1T$–VSe_2.

As the temperature is lowered, VSe_2, like other transition-metal dichalcogenides, undergoes a phase transition to a state with a charge density wave, accompanied by the formation of a crystalline superstructure with a period incommensurate with the period of the initial lattice. The transition temperature is 112 K.[3] Further decrease in temperature leads to a change in the period of the superstructure, which at 62 K becomes commensurate with the basic lattice parameter. VSe_2 crystals have a metallic type of temperature dependence of the resistivity and possess paramagnetic properties (see, e.g., Refs. 4–6).

Although VSe_2 is a compound that has been studied intensively and for quite some time, the information about the quasiparticle spectra in it is rather narrow in scope. In particular, quite a few studies have been done on the electronic structure of this material. As a result, the electronic band structure and Fermi surface are well determined (see, e.g., Refs. 7–11). At the same time, the phonon subsystem and its properties have not be adequately studied. We have been unable to find any published data on the phonon dispersion curve, the density of phonon states, the electron–phonon interaction (EPI) function, the Debye temperature, etc., which are among the important parameters influencing the electrophysical properties. This is not really surprising, since VSe_2 is an extremely complex material for investigation by the methods traditionally employed for obtaining the character-

istics mentioned. For example, optical measurements in this compound are complicated by the low value of the useful signal in view of the high reflectivity; in particular, the Raman scattering intensity in it is small, at least an order of magnitude smaller than in $2H$-$TaSe_2$ (Ref. 12). In view of what we have said, we set out in this study to investigate the phonon subsystem and the interactions of the quasiparticle excitations with the current carriers in $1T$–VSe_2.

To accomplish this task we used point-contact spectroscopy, since it is advantageous in cases when analogous studies by other methods are difficult. As a result, we were able to determine the EPI function and a number of other characteristics of the vibrational spectrum of VSe_2. In addition to the point-contact studies, we made precision Raman scattering measurements. The relations obtained are well correlated with each other and demonstrate the reproducibility of the observed features.

RESULTS AND DISCUSSION

The Raman spectra were excited at the frequency $\hbar\omega = 2.41$ eV of the argon laser line and were collected in a microscope with a $50\times$ magnification with the aid of a triple monochromator equipped with a liquid-nitrogen-cooled detector. The point-contact studies we done on $1T$–VSe_2/Cu heterocontacts on a specially built point-contact spectroscope designed by the authors at the B. Verkin Institute for Low Temperature Physics and Engineering, Kharkov, Ukraine. The contacts were created by means of the apparatus and techniques that have proven themselves in research on organic conductors, which, like VSe_2, have a lamellar layered structure.[13] The displacement technique[14] of obtaining contact between a copper electrode in the form of a prism and the lateral surface of a $1T$–VSe_2 slab ensured the predominant creation of contacts with the axis oriented parallel to the layers of the dichalcogenide crystal. These contacts made it possible to study the properties of the crystals in the regime of current flow in the plane of the sandwich. This is important, since the electrical characteristics of transition-metal dichalcogenides are highly anisotropic in the directions along and perpendicular to the layers.

It is known that vanadium is extremely complicated material for point-contact studies, since it has a high chemical activity and forms a number of conducting oxides on the surface; this circumstance can lead to shunting of the contacts along the conducting oxide films.[15] These formations are hard to clean off the vanadium surface by chemical means. Point-contact studies of selenium have not been done, and we do not have any specific information about obtaining point contacts in this material. In working with VSe_2 it was necessary to allow for the possibility that selective etching of the atoms of this compound would take place during chemical treatment, which would alter the composition of the surface layer of the treated crystal. We therefore had to avoid the use of chemical treatment of the $1T$–VSe_2 samples, and the contacts were made by touching a copper electrode either against the untreated surface or against a fresh cleavage surface obtained under liquid helium. In the latter case it was most often possible to create point contacts that permitted achieving spectral regimes of current flow and the recording of spectra having the highest intensity and quality. The copper electrode was treated by chemical polishing in HNO_3.

In investigating the point contacts the main source of spectral information is the current–voltage (I–V) characteristic, which contains nonlinearities numbers arising as a result of the scattering of electrons on phonons and other quasiparticle excitations during the passage of current through the contact.[16,17] Upon differentiation these nonlinearities transform into maxima on the second derivative of the I–V characteristic, which correspond to maxima of the phonon density of states and the electron–phonon interaction function in the material under study. The recording of the I–V characteristics and their second derivatives was done at voltages of 0–120 mV. At higher biases the contact resistance became unstable or the contact was damaged, apparently because of heating of the material near the contact. The investigation of the point-contact characteristics was done at a temperature of 4.2 K. More than 50 contacts were studied. Among them, 32 corresponded to spectral regimes of current flow and had spectra of good quality.

Depending on the purity and structural perfection of the material forming the contact and, accordingly, the regime of current flow in the contact region of the electrodes when a potential difference is applied to them, different types of I–V second-derivative curves (point-contact spectra) were observed. When the ballistic or diffusive regimes of current flow were realized, we observed point-contact spectra with pronounced structure, which was well reproduced on the second-derivative curves for different contacts. Some typical curves of the second derivative of the I–V characteristic are shown in Fig. 1 (curves *1* and *2*) for a group of the most intense EPI spectra.

As we know,[18] the point-contact spectrum of a heterocontact is a sum of partial contributions from the spectra of the electrode materials in contact. In the case of $1T$–VSe_2/Cu heterocontacts the contribution of the copper to the point-contact spectrum does not appear at all. This result is in qualitative agreement with the data for contacts of copper with niobium dichalcogenide, $2H$–$NbSe_2$/Cu,[19] and with the results of Refs. 20 and 21 obtained for heterocontacts of Nb and Ta, which are electronic analogs of vanadium in the subgroup VA.

As we see from the curves of the second derivatives of the I–V characteristic in Fig. 1, the compound $1T$–VSe_2 has a rather broad EPI spectrum, the boundary of which lies at 88–90 meV. This result can be compared qualitatively with the data obtained from measurements of the point-contact spectra in pure vanadium.[15,16] According to Ref. 16, the highest-frequency phonons in the point-contact spectra of vanadium correspond to energies of the order of 60 meV. Thus the maximum phonon frequency ω_{max} increases quite considerably in going from V to VSe_2. Taking into account that the boundary of the EPI spectrum in the analogous niobium compound is shifted to higher energies by approximately 30 meV in going from pure niobium to the dichalcogenide $NbSe_2$ (see, e.g., Refs. 16 and 19), the value of ω_{max} obtained for VSe_2 seems entirely reasonable.

The most intense peak in the point-contact spectra of the EPI lies in the low-frequency region, at energies of 5–7

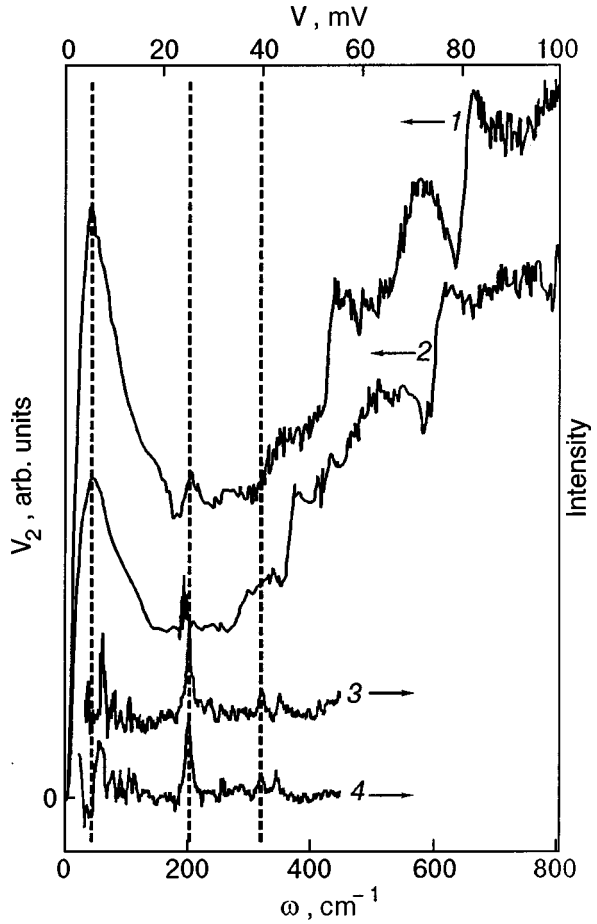

FIG. 1. Vibrational spectra of the compound $1T-VSe_2$: *1,2* — second derivatives of the I–V characteristics of $1T-VSe_2$/Cu contacts, $R_0=84\ \Omega$ (*1*), $R_0=78\ \Omega$ (*2*), $T=4.2$ K; *3,4* — Raman spectra at $T=180$ K (*3*) and $T=10$ K (*4*).

meV. Its position is in good agreement with the Raman scattering data obtained for $1T-VSe_2$ (curves *3* and *4* in Fig. 1) in the temperature interval 10–180 K. One also observes a correlation in the positions of the features at energies of 26 and 40 meV, as can be seen by comparing the curves in Fig. 1. It follows from the data of Refs. 12 and 19, which agree with our results, that as the temperature is lowered and $1T-VSe_2$ undergoes a transition to a state with a charge density wave and a superstructure commensurate with the initial crystal lattice parameters, there is a softening of the phonon spectrum of this compound and an increase in the intensity of the low-frequency vibrational modes. In addition to this there is a shift of the ''center of gravity'' in the point-contact spectra and an enhancement of the low-energy peaks due to a decrease in the relative intensity of the high-frequency features on account of the influence of the point-contact form factor. This form factor emphasizes large-angle scattering and the role of umklapp processes in the back-scattering of electrons, as is manifested with particular clarity in metals with a complex Fermi surface.[22,23] For this reason the high-energy features of the EPI in the point-contact spectra of $1T-VSe_2$ have a much lower intensity relative to the low-frequency features than is the case in optical experiments (for example, compare the peaks at 48 and 203 cm^{-1} on curves *3* and *4* of Fig. 1 and in Ref. 12 with the corresponding features on the point-contact curves).

An examination of the published data on the conductivity of $1T-VSe_2$ in conjunction with the point-contact studies suggests that in contacts of this compound a current regime can arise in which the localization of the electronic states is destroyed, as is typical of semimetal contacts. This is suggested by the fact that the parameters of the conductivity for these objects are close in value. In particular, the conductivity of the compound $1T-VSe_2$ at low temperatures is even lower than in antimony. At $T=20$ K the resistivity of $1T-VSe_2$ has a value $\rho\sim10^{-4}\ \Omega\cdot$cm,[6] which is two orders of magnitude larger than that of antimony.[24] Thus there are clear grounds for suggesting that such a current regime, which has been investigated previously in antimony[25] and in organic conductors,[26] is observed in $1T-VSe_2$ contacts as well. The essence of the delocalization effect is as follows. In point contacts of semimetals in the case of a low momentum mean free path of the electrons, localization of the electronic states will arise in the neck region.[27] Here the electron–phonon interaction, by destroying the localization of the electrons, will lead to an increase in the contact conductance. Thus the contact resistance decreases, contrary to the increase that is observed in contacts of pure metals in the ballistic regime of electron passage, which occurs in the case of large momentum mean free paths l_i satisfying the condition $l_i \gg d$ (d is the contact diameter). As a result, the curves of the second derivative of the I–V characteristic will have minima near the characteristic energies of the EPI, in contrast to the maxima observed in the case of increasing contact resistance. A clear example is the inverse point-contact spectrum of a $1T-VSe_2$/Cu heterocontact, shown by curve *1* in Fig. 2. We see that this curve is a mirror reflection of curves *1* and *2* in Fig. 1. The accumulation of phonons in the neck region as the voltage is increased can also lead to a decrease in the mean free path in the contact region. Then the regime of electron passage through the contact changes from ballistic to diffusive, in which an important role is played by weak localization effects. This is reflected in the behavior of the features on the point-contact spectrum: an intermediate type of point-contact spectrum appears (with the inverted features at high voltages). An example of such a characteristic is shown by curve *2* in Fig. 1, the maxima and minima of which are mirror reflections of the corresponding nonlinearities on curve *1* of Fig. 1 at voltages above 60 mV.

In a number of point contacts the spectra at high energies exhibited nonlinearities of the type representing the derivative of a maximum, which are hard to interpret as being the result of the EPI. Similar features have been observed previously in the spectra of superconducting contacts[28] and contacts of magnetic materials.[29,30] In Refs. 28–30 the appearance of these sharp nonlinearities was attributed to the destruction of the superconductive or magnetic ordering, specifically, to a phase transition of the contact material from the superconducting to the normal or from the ferromagnetic (antiferromagnetic) to the paramagnetic state as the region near the contact is heated by the transport current to the corresponding temperatures, or to an orientational phase transition of a spin density wave.[30] In the compound $1T-VSe_2$ at $T=62$ K a change in the period of the superstructure occurs, which is manifested as a change in the slope of the temperature dependence of the resistivity ρ.[5,6] There-

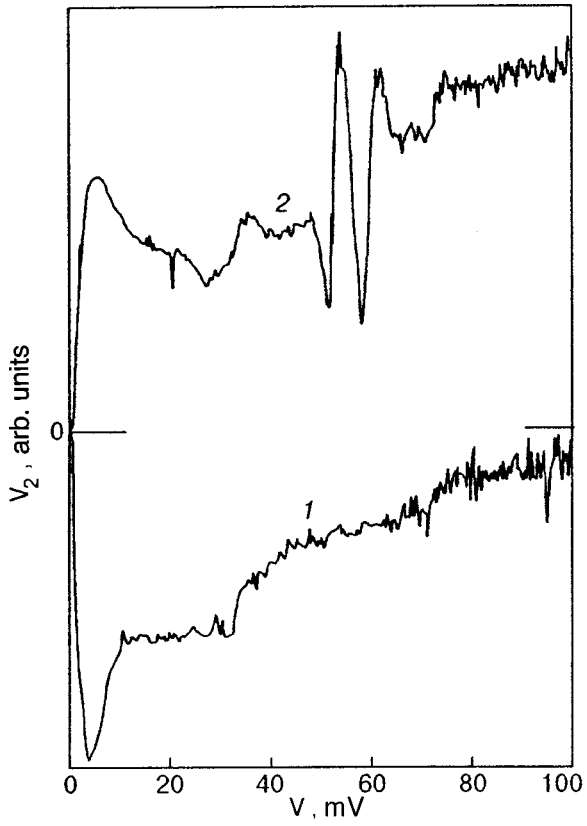

FIG. 2. Point-contact spectra of $1T-VSe_2$/Cu contacts, corresponding to different regimes of current passage: inverse spectrum, $R_0=163\ \Omega$ (*1*); second derivative of the I–V characteristic, containing nonlinearities due to a structural phase transition, $R_0=82\ \Omega$ (*2*).

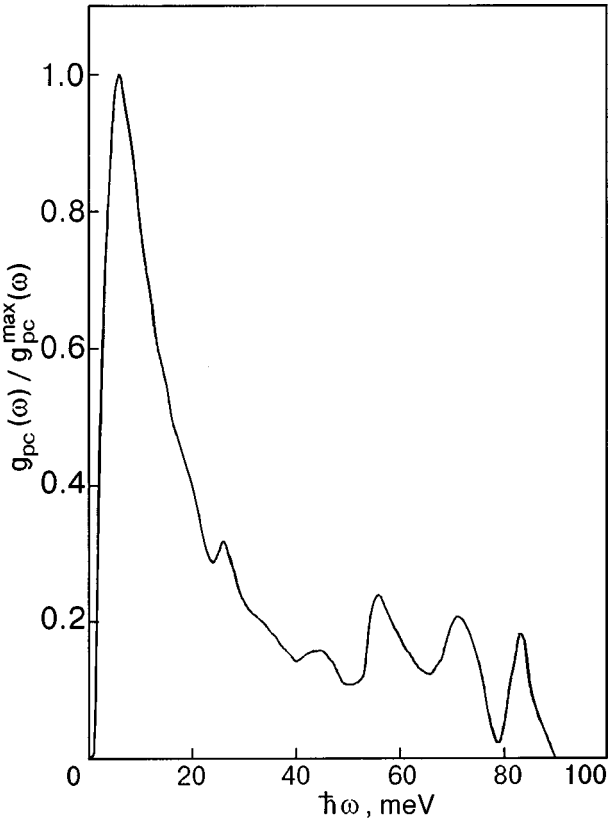

FIG. 3. Point-contact EPI function $g_{pc}(\omega)$ recovered from curve *1* in Fig. 1.

fore a heating of the $1T-VSe_2$ contact region to 62 K will also lead to a structural transition in the contact region, which should be manifested directly in the form a maximum on the temperature dependence of the differential resistance of the contact or as a nonlinearity of the type corresponding the derivative of a maximum on the second derivative of the I–V characteristic. According to the data of Ref. 3, the change of the period of the superstructure from being commensurate with the period of the initial lattice to incommensurate occurs as the temperature is changed in the interval 62–112 K. At the resolution of the method of measuring the temperature dependence of the resistivity of massive samples, this nonlinearity is detected only as a smooth change in $\rho(T)$ in this temperature interval.[5,6] At the same time, the point-contact method can reveal much more clearly even the tiniest variations of the resistivity of the material upon a change in the external conditions, thanks to the technique of differentiating the I–V characteristic in the regime of thermal modulation spectroscopy.[29] The heating of the contact region by the transport current allows one to vary the temperature of the contact region by changing the voltage applied to the contact. Thus, if a temperature of 62 K is reached at the contact, then when the applied voltage and, accordingly, the temperature in the contact region is increased, one can observe the singularities due to the changes in the structure and resistivity of the material in the temperature interval 62–112 K. At higher voltages and, hence, at temperatures above 112 K one observes a smooth segment of the $\rho(T)$ curve, and the second derivative of the I–V characteristic of the contact should be monotonic. If it is assumed that the features of the type representing the derivative of a maximum arise on the point-contact spectra of $1T-VSe_2$/Cu contacts at voltages corresponding to the conditions of the thermal limit, then, in accordance with the relation governing the change in temperature at the contact as a function of the applied voltage in the thermal limit, namely $eV=3.63kT$ (Ref. 29), the temperature interval 62–112 K corresponds to a voltage interval $\cong 16$ mV wide. It is in this interval that one should observe sharp nonlinearities of the second derivative of the I–V characteristic of the contact, as is demonstrated by curve *2* in Fig. 2: the features in question start at $\cong 50$ meV and end at $\cong 65$ meV, and at higher energy the second derivative of the I–V characteristic does not exhibit nonlinearities. It should be noted that the onset of the nonlinearities in question on the point-contact spectra of different contacts can vary (this is natural in view of the different initial conditions at $V=0$), but the width of the interval in which they exist is approximately the same for all such curves.

The point-contact spectra of the $1T-VSe_2$ heterocontacts were used to calculate the point-contact EPI function $g_{pc}(\omega)$. Figure 3 shows a plot of $g_{pc}(\omega)$ obtained from curve *1* in Fig. 1. The calculation was done by the software package of Ref. 31 with the use of a linear point-contact background function.[16] The value of the EPI parameter λ_{pc} for curve *1* is 0.27. Since it cannot be stated with certainty that the current regime in the heterocontacts under study is definitely ballistic, this value of λ_{pc} should be regarded as an estimated lower bound on the EPI parameter in VSe_2. The values of the mean $\langle\omega\rangle$ and rms $\langle\omega^2\rangle^{1/2}$ phonon frequencies are 10.14 and 15.99 meV. From the data obtained one can

determine the Debye frequency of the phonons and the Debye temperature θ_D in the compound $1T-VSe_2$ from the relation proposed in Ref. 32:

$$\theta_D = \frac{\hbar}{k}\left(\frac{3\langle\omega^2\rangle}{2}\right)^{1/2}.$$

The values of the Debye temperature calculated with the use of the data for the point-contact spectra *1* and *2* in Fig. 1 and *1* in Fig. 2 came out to be 215 K, 228 K, and 220 K, respectively. The average for the 5 spectra is 220 ± 5 K. It should be noted that the values of θ_D obtained from the point-contact spectra of different metals are generally somewhat smaller than the values obtained from temperature measurements of the specific heat.[33] This is because of the decrease in the relative intensity of the high-frequency features of the point-contact EPI function $g_{pc}(\omega)$ in comparison with the phonon density of states function on account of the influence of the point-contact form factor.

In summary, the results obtained in this study contain new information about the electrophysical properties of the dichalcogenide $1T-VSe_2$, making it possible to determine a number of previously unknown parameters of the electron–phonon interaction and Debye temperature.

The authors are grateful to A. V. Eremenko and A. R. Kazachkov for collaboration and helpful discussions, to Yu. A. Kolesnichenko for a discussion of the results, and to V. V. Khotkevich for assistance in the calculations of the EPI function.

This study was supported by NATO Grant CRG-CRGP 972846.

*E-mail: kamarchuk@ilt.kharkov.ua

[1] P. Molinie, A. Leblanc, E. Faulques, Z. Ouili, J-C. Jumas, and C. Ayache, in *Spectroscopy of Superconducting Materials*, edited by E. Faulques, ACS Symp. Ser. 730, American Chemical Society, Oxford University Press, Washington, D.C. (1999), Ch. 2, p. 21.
[2] L. N. Bulaevskiĭ, Usp. Fiz. Nauk **116**, 449 (1975) [Sov. Phys. Usp. **19**, 836 (1976)].
[3] R. H. Friend, D. Jerome, D. M. Schleich, and P. Molinie, Solid State Commun. **27**, 169 (1978).
[4] C. F. van Bruggen, C. Haas, and G. A. Wiegers, J. Solid State Chem. **27**, 9 (1979).
[5] A. H. Thompson and B. G. Silbernagel, Phys. Rev. B **19**, 3420 (1979).
[6] H. Mutka and P. Molinie, J. Phys. C **15**, 6305 (1982).
[7] J. A. Wilson and A. D. Yoffe, Adv. Phys. **18**, 193 (1969).
[8] A. Zunger and A. J. Freeman, Phys. Rev. B **19**, 6001 (1979).
[9] H. P. Hughes, C. Webb, and P. M. Williams, J. Phys. C **13**, 1125 (1980).
[10] R. Claessen, I. Schafer, and M. Skibovski, J. Phys.: Condens. Matter **2**, 10045 (1990).
[11] H. E. Brauer, H. I. Starnberg, L. J. Holleboom, V. N. Strokov, and H. P. Hughes, Phys. Rev. B **58**, 10031 (1998).
[12] S. Sugai, K. Murase, S. Uchida, and S. Tanaka, J. Phys. (Paris) **42**, C6-740 (1981).
[13] G. V. Kamarchuk, A. V. Khotkevich, V. M. Bagatsky, and A. V. Kravchenko, in *Spectroscopy of Superconducting Materials*, edited by E. Faulques, ACS Symp. Ser. 730, American Chemical Society, Oxford University Press, Washington, D.C. (1999), Ch. 14, p. 196.
[14] P. N. Chubov, I. K. Yanson, and A. I. Akimenko, Fiz. Nizk. Temp. **8**, 64 (1982) [Sov. J. Low Temp. Phys. **8**, 32 (1982)].
[15] L. F. Rybal'chenko, I. K. Yanson, and V. V. Fisun, Fiz. Tverd. Tela (Leningrad) **22**, 2028 (1980) [Sov. Phys. Solid State **22**, 1182 (1980)].
[16] A. V. Khotkevich and I. K. Yanson, *Atlas of Point Contact Spectra of Electron-Phonon Interaction in Metals*, Kluver Academic Publishers, Boston/Dordrecht/London (1995).
[17] Yu. A. Kolesnichenko, I. G. Tuluzov, and A. V. Khotkevich, Fiz. Nizk. Temp. **19**, 402 (1993) [Low Temp. Phys. **19**, 282 (1993)].
[18] R. I. Shekhter and I. O. Kulik, Fiz. Nizk. Temp. **9**, 46 (1983) [Sov. J. Low Temp. Phys. **9**, 22 (1983)].
[19] R. L. Bobrov, L. F. Rybal'chenko, M. A. Obolenskiĭ, and V. V. Fisun, Fiz. Nizk. Temp. **11**, 925 (1985) [Sov. J. Low Temp. Phys. **11**, 510 (1985)].
[20] I. K. Yanson, R. L. Bobrov, L. F. Rybal'chenko, and V. V. Fisun, Fiz. Nizk. Temp. **9**, 1155 (1983) [Sov. J. Low Temp. Phys. **9**, 596 (1983)].
[21] R. L. Bobrov, L. F. Rybal'chenko, V. V. Fisun, and I. K. Yanson, Fiz. Nizk. Temp. **13**, 611 (1987) [Sov. J. Low Temp. Phys. **13**, 344 (1987)].
[22] I. O. Kulik, A. N. Omel'yanchuk, and R. I. Shekhter, Fiz. Nizk. Temp. **3**, 1543 (1977) [Sov. J. Low Temp. Phys. **3**, 740 (1977)].
[23] I. K. Yanson, Fiz. Nizk. Temp. **9**, 676 (1983) [Sov. J. Low Temp. Phys. **9**, 343 (1983)].
[24] M. P. Malkov (Ed.), *Handbook on the Physical and Engineering Principles of Cryogenics*, Énergiya, Moscow (1973).
[25] I. K. Yanson, N. N. Gribov, and O. I. Shklyarevskiĭ, JETP Lett. **42**, 159 (1985).
[26] G. V. Kamarchuk, A. V. Khotkevich, V. M. Bagatskiĭ, and A. V. Kravchenko, Fiz. Nizk. Temp. **24**, 53 (1998) [Low Temp. Phys. **24**, 40 (1998)].
[27] I. F. Itskovich, I. O. Kulik, and R. I. Shekhter, Fiz. Nizk. Temp. **13**, 1166 (1987) [Sov. J. Low Temp. Phys. **13**, 659 (1987)].
[28] G. V. Kamarchuk and A. V. Khotkevich, Fiz. Nizk. Temp. **13**, 1275 (1987) [Sov. J. Low Temp. Phys. **13**, 717 (1987)].
[29] B. I. Verkin, I. K. Yanson, I. O. Kulik, O. I. Shklyarevskiĭ, A. A. Lysykh, and Yu. G. Naĭdyuk, Izv. Akad. Nauk SSSR, Ser. Fiz. **44**, 1330 (1980).
[30] A. V. Khotkevich and S. N. Kraĭnyukov, Fiz. Nizk. Temp. **17**, 335 (1991) [Sov. J. Low Temp. Phys. **17**, 173 (1991)].
[31] V. V. Khotkevich and A. V. Khotkevich, ''Recovery of the electron–phonon interaction function from experimental data in the method of point-contact spectroscopy'' [Deposited ms, in Russian], Dep. VINITI 07.01.86, No. 164–V86, All-Union Institute of Scientific and Technical Information, Moscow (1986).
[32] F. J. Pinski, P. B. Allen, and W. H. Butler, Phys. Rev. B **23**, 5080 (1981).
[33] A. V. Khotkevich, Author's Abstract of Doctoral Dissertation [in Russian], Kharkov (1990).

Translated by Steve Torstveit

LATTICE DYNAMICS

Raman studies of the temperature dependence of the internal vibrations of the ammonium ions in the mixed crystals $K_{1-x}A_xDP$ and $R_{1-x}A_xDP$

A. V. Van'kevich,* Yu. A. Popkov, and I. A. Taranova

V. N. Karazin Kharkov National University, pl. Svobody 4, 61077 Kharkov, Ukraine
(Submitted June 30, 2000)
Fiz. Nizk. Temp. **27**, 80–89 (January 2001)

The Raman spectra in the frequency region corresponding to the internal vibrations of the ammonium ions are investigated in the temperature range 4.2–300 K for the mixed crystals $K_{1-x}(NH_4)_xH_2PO_4$ with different ammonium concentrations ($x=0.22$, 0.32, 0.53, 0.74, and 0.82). Analysis of the temperature dependence of the frequencies and half-widths of the internal vibration lines of the ammonium ions confirms that in the paraelectric phase the position of the ammonium ions in the crystal lattice is not fixed: they execute hops with a change in the position of the center of mass. The activation energies of these reorientation processes are determined. It is found that at temperatures of the order of 110–120 K for the $K_{1-x}(NH_4)_xH_2PO_4$ crystals of all concentrations a correlated fixing of the ammonium ion in the lattice occurs, leading to the formation of an antiferroelectric cluster structure. For the crystals with concentrations $x=0.22$, 0.32, and 0.53 this structure is preserved in the structural glass phase down to liquid helium temperatures, while for the crystals with $x=0.74$ and 0.82 it is preserved to the temperatures of the antiferroelectric phase transition T_N (68.5 and 80.5 K, respectively). Analogous processes are also observed in the isostructural crystal $Rb_{0.20}(NH_4)_{0.80}H_2PO_4$. [DOI: 10.1063/1.1344145]

The low-temperature phase transition in crystals of the KDP family is usually treated as a transition of the order–disorder type, involving an ordering of the proton subsystem in the O–H...O bonds of the PO_4 (AsO_4) tetrahedra.[1–3] This phase transition mechanism is generally assumed to operate in all the crystals of this family, regardless of the character of the low-temperature phase. Thus, while the position of the protons along the bond in the paraelectric (PE) phase is not fixed, i.e., the protons tunnel between two equilibrium positions, in the low-temperature phase the position of the protons becomes ordered: now only two protons are found near each PO_4 (AsO_4) tetrahedron. However, whereas in KH_2PO_4 (KDP), RbH_2PO_4 (RDP), KH_2AsO_4 (KDA), etc., both protons are found near the ''upper'' or near the ''lower'' corners of a PO_4 (AsO_4) tetrahedron, in the $NH_4H_2PO_4$ (ADP) and $NH_4H_2AsO_4$ (ADA) crystals, one proton is found near an ''upper'' and the other near a ''lower'' corner of the tetrahedron. In the first case a ferroelectric (FE) phase is formed, and in the second case an antiferroelectric (AFE) phase.

In mixed FE–AFE crystals, however, frustration of the proton subsystem arises as the temperature is lowered, on account of the competition between the different types of low-temperature ordering of the protons in the different constituents of the mixture, and this leads to the formation of a new disordered state, which has been given the name structural (proton, dipole) glass (SG).[4–6]

Recently in a number of experimental papers reporting Raman scattering studies it has been conjectured that the ferroelectric phase transition in KDP crystals involves the ordering of local distortions of the PO_4 tetrahedra.[7–9] On the other hand, studies of the different phase states existing in the mixed crystals $Rb_{1-x}(NH_4)_xH_2PO_4$ ($R_{1-x}A_xDP$) and $K_{1-x}(NH_4)_xH_2PO_4$ ($K_{1-x}A_xDP$) at low temperatures have established that the ammonium ions play an important role in the mechanism of the phase transition to the ordered AFE phase and the disordered SG phase.[10–16]

On the basis of an analysis of the temperature dependence of the line shape, frequency position, and half-width of a Raman spectral line corresponding to a librational vibration of the ammonium ions, we have proposed[14] a phase transition mechanism according to which the position of the ammonium ions in the crystal lattice of the PE phase is not fixed: these ions execute disordered ''hops'' involving a change in the position of the center of mass among four equally probable positions; this is consistent with the x-ray structural data reported in Refs. 17 and 18 for the ADP crystal in the PE phase. As a result of these hops the ammonium ions acquire the shape of nearly regular tetrahedra with an intantaneous symmetry close to T_d. As the temperature is lowered, the frequency of these hops decreases and they become increasing correlated. At a temperature T_N the whole network of ammonium ions becomes fixed in one of the possible positions, and this leads to an AFE phase transition.

In this paper we report a Raman-scattering investigation of the behavior of the internal vibrations of the ammonium ions in the mixed crystals $K_{1-x}A_xDP$ ($x=0.22$, 0.32, 0.53, 0.74, 0.82, 1.00) in the temperature interval 4.2–300 K for the purpose of obtaining additional information about the role of the ammonium ions in the mechanism of the phase

transition to the various low-temperature phases.

EXPERIMENTAL TECHNIQUES

The techniques used to grow the $K_{1-x}A_xDP$ single crystals and to determine the percent content of the constituents in the solid solutions are set forth in detail in Ref. 12.

The grown single crystals were cut into parallelepipeds with dimensions of $3\times3\times4$ mm. The laboratory coordinate system was chosen in relation to the crystallographic axes as follows: $X\|a$, $Y\|b$, $Z\|c$. We note that in the PE phase all of the investigated crystals have tetragonal symmetry. In the SG phase ($x=0.22$, 0.32, and 0.53) the overall symmetry of the crystals remains tetragonal, but in the AFE phase ($x=0.74$, 0.82) it is lowered to orthorhombic.[12–16] Since the X and Y axes are equivalent in the PE phase, either of them can become an antipolarization axis in the AFE phase. Therefore, in making the polarization measurements the X and Y axes for each sample were arbitrarily fixed, and the coordinate system thus chosen was kept unchanged.

Measurements were made on an automated spectroscope based on a DFS-24 double monochromator. A 90° scattering geometry was used for all the polarization measurements. The excitation source was an argon laser ($\lambda=488.0$ nm, $P_{out}=100$ mW). The signal was detected in a photon-counting scheme. The measurements were made in the temperature interval 4.2–300 K, with the temperature measured and stabilized to a precision of 0.1 K.

EXPERIMENTAL RESULTS AND DISCUSSION

In the PE phase all of the mixed crystals $K_{1-x}A_xDP$ (as in the pure components KDP and ADP) have a space symmetry D_{2d}^{12} with two formula units per unit cell. The local symmetry of the NH_4 ions, according to published data,[19] is C_2.

According to a group-theoretical analysis, the vibrational representation for the internal modes of the ammonium ions in the PE phase has the form[10]

$$\Gamma_{in}=2A_1+2A_2+3B_1+3B_2+4E.$$

Here the vibrational mode ν_1 is manifested in the A_1 and A_2 symmetries, the mode ν_2 in the A_1, A_2, B_1, and B_2 symmetries, and the ν_3 and ν_4 modes in the B_1, B_2, and E symmetries. Here the classification of the internal vibrations of the NH_4 ion is given in the notation customarily used for the free molecule.[20]

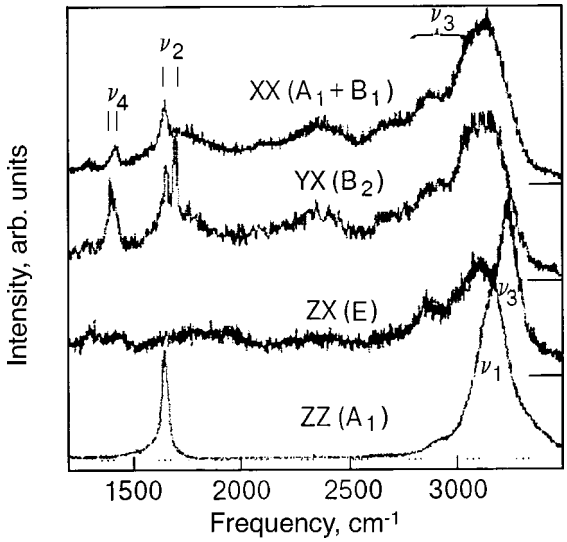

FIG. 1. Raman spectra of different symmetries in the paraelectric phase ($T=296$ K) of the $K_{0.26}A_{0.74}DP$ crystal at frequencies corresponding to the internal vibrations of the ammonium ions. The spectral resolution is 2 cm^{-1}.

According to the selection rules, for the D_{2d} group the modes of A_1, B_1, B_2, and E symmetry are active in the first-order Raman spectra. As an example, Fig. 1 shows the Raman spectra for the $K_{0.26}A_{0.74}DP$ crystal at room temperature in the frequency range of the internal vibrations of the ammonium ions. It is seen that the spectra are clearly polarized. There is good agreement with the results of the group-theoretical analysis and with published data.[19,21,22] Changing the concentration of the constituents of the mixed crystals does not qualitatively alter the Raman spectra, i.e., the number and polarization of the lines remain unchanged. On the other hand, the intensity of the lines corresponding to the internal vibrations of the ammonium ions falls off in proportion to the decreasing ammonium concentration in the mixed crystals. Table I gives the values of the frequencies and half-widths of the lines of the internal vibrations of the ammonium ions in $K_{1-x}A_xDP$ crystals for the different concentrations. From the values given there we see that the

TABLE I. Frequencies and half-widths of the internal vibrations of ammonium ions in mixed crystals $K_{1-x}A_xDP$ with different concentrations. $T=296$ K.

Concentration, x	$A_1(\nu_1)$		$A_1(\nu_2)$		$B_2(\nu_2)$		$E(\nu_3)$		$E(\nu_3)$		$B_2(\nu_4)$		$B_1(\nu_4)$	
	ν	$\Delta\nu$	ν	$\Delta\nu$	ν	$\Delta\nu$	ν	$\Delta\nu$	ν	$\Delta\nu$	ν	$\Delta\nu$	ν	$\Delta\nu$
1.00	3162	165	1656	27	1702	17	2862	169	3237	90	1406	24	1437	17
0.82	3165	173	1656	28	1703	17	2864	172	3239	93	1407	26	1435	17
0.74	3166	177	1657	28	1706	17	2865	173	3241	99	1406	27	1434	18
0.53	3168	179	1661	30	1707	20	2865	175	3241	99	1411	32	1434	20
0.32	3170	183	1664	35	1711	22					1411	35	1428	21
0.22	3170	185	1665	32										

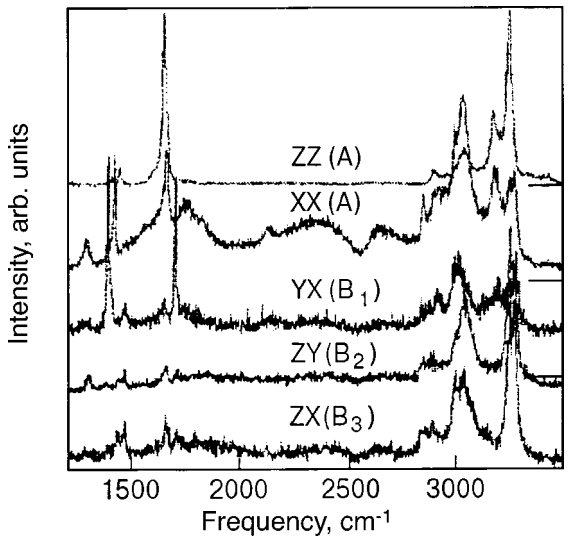

FIG. 2. Raman spectra of different symmetries in the antiferroelectric phase ($T=4.2$ K) of the $K_{0.26}A_{0.74}DP$ crystal at frequencies corresponding to the internal vibrations of the ammonium ions. The spectral resolution is 2 cm^{-1}.

frequencies of all the lines of the internal vibrations in the mixed crystals have a nearly linear dependence on the ammonium ion concentration. As the concentration decreases, the lines of all the internal vibrations broaden, an effect that can be explained by a change in the local environment of the ammonium ions in the lattice of the mixed crystals. For crystals with a low ammonium concentration it is hard to determine the positions of the lines on account of their low intensity.

Analysis of the temperature dependence of the internal vibrations of the ammonium ions

In the the mixed crystals of $K_{1-x}A_xDP$ with concentrations $x=1.00$, 0.82, and 0.74 an AFE phase transition occurs at the temperatures $T_N=148$, 80.5, and 68.5 K, respectively.[12–16,19] At the phase transition the symmetry of the crystal is lowered from tetragonal (space group D_{2d}^{12}) to orthorhombic (space group D_2^4), the unit cell is doubled, and the local symmetry of the ammonium ions is lowered to C_1 (Ref. 19). The lowering of the local symmetry of the ammonium ions should lead to a total lifting of the degeneracy of the internal vibrations.

Figure 2 shows the Raman spectra of the $K_{0.26}A_{0.74}DP$ crystal in the AFE phase ($T_N=68.5$ K) at liquid helium temperature in the frequency region corresponding to the internal vibrations of the ammonium ions.

In comparing the spectra in the PE and AFE phases (Figs. 1 and 2), we clearly see that the spectra undergo a substantial transformation at the phase transition. The appearance of additional lines and the appearance of lines in spectra of different symmetry is due to the doubling of the unit cell at the AFE phase transition and the lowering of the local symmetry of the ammonium ions in the crystal lattices to C_1. The frequency positions of the lines are in good agreement with published data.[10,11,19]

Although the transition to the SG state in the mixed crystals of $K_{1-x}A_xDP$ with concentrations $x=0.22$, 0.32, and 0.53 is not accompanied by a change in the overall symmetry of the crystals,[12,14–16] the Raman spectra in the frequency region corresponding to the internal vibrations of ammonium are also transformed somewhat, as will be seen below.

Let us analyze the temperature dependence of the Raman lines of the internal vibrations ν_2 and ν_4 of the ammonium ion in the mixed crystals $K_{1-x}A_xDP$. The corresponding analysis for lines of the types ν_1 and ν_3 is complicated by the presence of a large number of broad overlapping lines in the frequency region ~ 3000 cm^{-1} (see Fig. 2).

The lines of the internal vibrations ν_2 and ν_4 of the ammonium ions appear in the Raman spectra of $K_{1-x}A_xDP$ crystals of all concentrations and throughout the entire temperature interval as narrow symmetric single lines. A fitting of the experimental spectra in this frequency region was done using a single line of the Lorentzian type. Figures 3–5 show the temperature dependence of the frequencies and half-widths of the ν_2 and ν_4 lines of the internal vibrations of the ammonium ions in the mixed crystals $K_{0.26}A_{0.74}DP$ and $K_{0.68}A_{0.32}DP$ for the different components of the scattering tensor in the temperature interval 4.2–300 K.

As we see from these figures, the character of the tem-

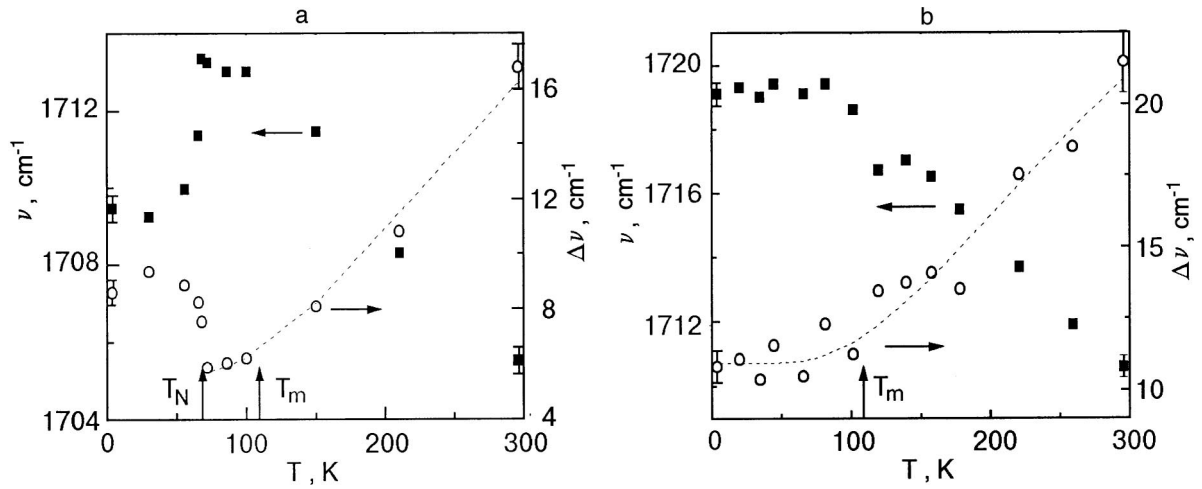

FIG. 3. Temperature dependence of the frequency (■) and the half-width (○) of the ν_2 line of the internal vibrations of the ammonium ions (XY component of the scattering tensor) in the crystals $K_{0.26}A_{0.74}DP$ (a) and $K_{0.68}A_{0.32}DP$ (b).

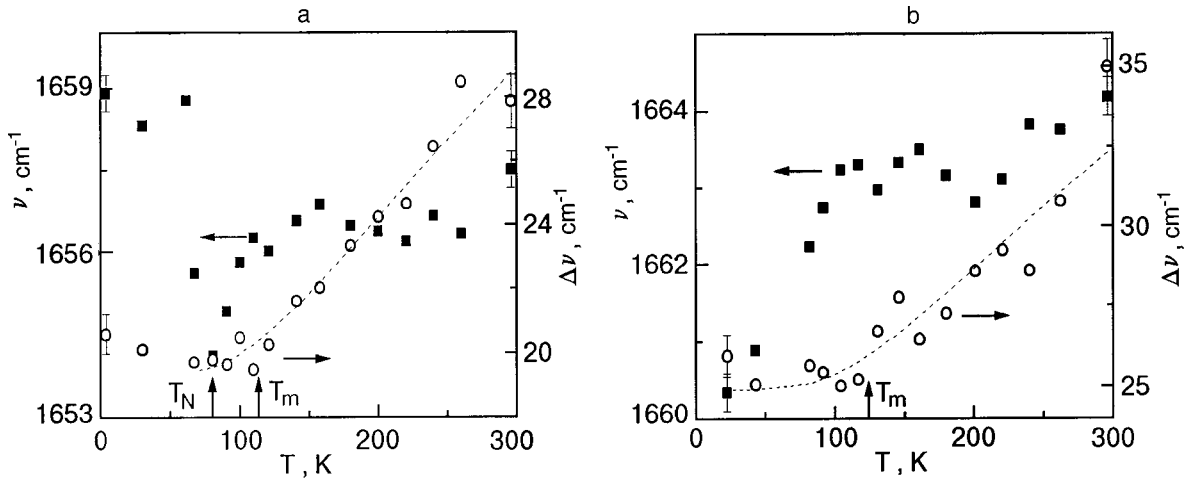

FIG. 4. Temperature dependence of the frequency (■) and the half-width (○) of the ν_2 line of the internal vibrations of the ammonium ions (ZZ component of the scattering tensor) in the crystals $K_{0.26}A_{0.74}DP$ (a) and $K_{0.68}A_{0.32}DP$ (b).

perature dependence of the frequencies and half-widths of all the Raman lines corresponding to internal vibrations of the ammonium ions is identical for the two crystals. A substantial difference is observed only near the phase transition temperature.

In both crystals the frequencies of the lines of the internal vibrations $\nu_2(B)$ increase linearly as the temperature is lowered (Fig. 3); this linear growth stops at temperatures of the order of 110–120 K. In the temperature interval 300–110 K the frequency of the line increases substantially (≈ 8 cm^{-1}). On further lowering of the temperature the frequency of the line remains practically unchanged all the way down to helium temperatures for the $K_{0.68}A_{0.32}DP$ crystal, while for the $K_{0.26}A_{0.74}DP$ crystal it remains constant only down to the temperature T_N, below which the frequency of the line exhibits a jumplike decrease that is characteristic of a first-order phase transition.

The frequency of the $\nu_2(A)$ line of the internal vibrations of the ammonium ions in $K_{0.26}A_{0.74}DP$ and $K_{0.68}A_{0.32}DP$ crystals (Fig. 4) are practically unchanged as the temperature is lowered to 110–120 K. On further lowering of the temperature the frequency of this vibrational line decreases monotonically in the $K_{0.68}A_{0.32}DP$ crystal in the temperature interval 110–4.2 K, while in the $K_{0.26}A_{0.74}DP$ crystal this decrease stops at the temperature T_N, below which the frequency of the line exhibits a jumplike increase.

The frequency of the ν_4 line of the internal vibrations of the ammonium ion in the crystals $K_{0.26}A_{0.74}DP$ and $K_{0.68}A_{0.32}DP$ (Fig. 5) decreases linearly as the saample is cooled from room temperature. At temperatures of the order of 110–120 K the frequency position of the ν_4 line, like that of the $\nu_2(B)$ line, stabilizes. On further lowering of the temperature the frequency of the line remains practically constant, down to liquid helium temperatures for the $K_{0.68}A_{0.32}DP$ crystal and to the temperature T_N for the $K_{0.26}A_{0.74}DP$ crystal, and below that temperature, as in the previous cases, the frequency exhibits a jumplike change due to the AFE phase transition.

There is a noteworthy difference in the temperature dependence of the frequency position of the Raman lines corresponding to different types of internal vibrations of the ammonium ions. For both crystals referred to in Figs. 3, 4, and 5, in the interval interval 300–120 K the frequency of the $\nu_2(B)$ line increases by 8 cm^{-1}, the frequency of the ν_4

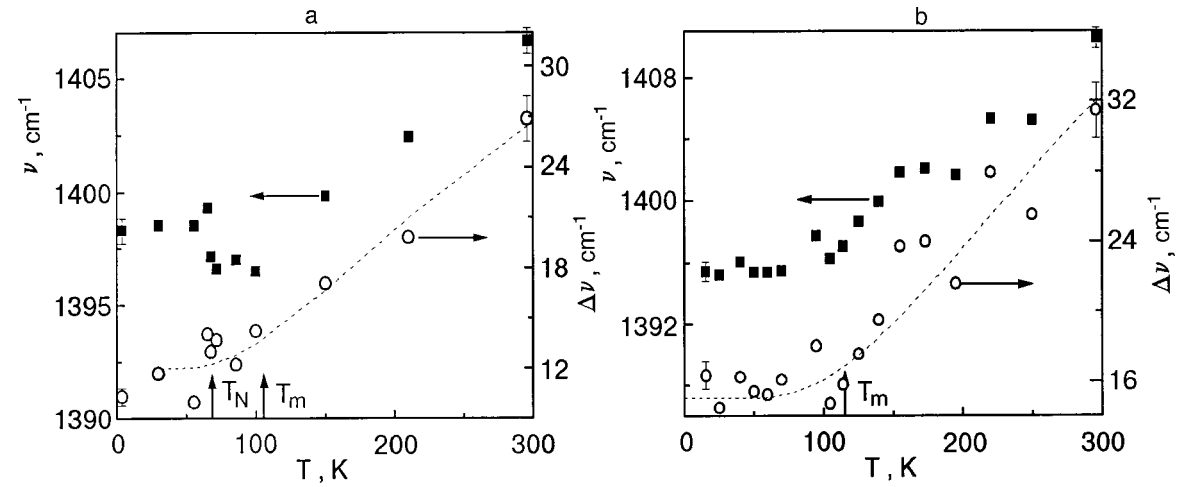

FIG. 5. Temperature dependence of the frequency (■) and the half-width (○) of the ν_4 line of the internal vibrations of the ammonium ions (XY component of the scattering tensor) in the crystals $K_{0.26}A_{0.74}DP$ (a) and $K_{0.68}A_{0.32}DP$ (b).

TABLE II. Values of the activation energy obtained by fitting the temperature dependence of the half-width of the Raman lines of various types of vibrations of the ammonium ions in $K_{1-x}A_xDP$ crystals.

Concentration, x	Activation energy U, meV			
	lib	$\nu_2(A)$	$\nu_2(B)$	ν_4
0.82	54±2		48±2	32±2
0.74	29±2	33±2	36±2	29±2
0.53	41±2	32±2	33±2	
0.32	36±2	36±2	35±2	30±2
0.22	39±2	32±2		

Note: U(lib) data are from Ref. 14.

line decreases by about 8 cm^{-1}, and the frequency of the $\nu_2(A)$ line remains practically unchanged. This difference can be explained in the framework of a model according to which in the PE phase the center of gravity of the ammonium ions in the crystal lattice is not fixed. As the temperature is lowered, the frequency of the hopping processes decreases. This increases the influence of the environment of the ammonium ion in the lattice and, hence, increases the distortion of the NH_4 tetrahedra.

Figures 3, 4, and 5 also show the temperature dependence of the half-widths of the ν_2 and ν_4 line of internal vibrations of the ammonium ions in the crystals $K_{0.26}A_{0.74}DP$ and $K_{0.68}A_{0.32}DP$. It should be noted that as the temperature decreases from room temperature to a value of the order of 110–120 K, the half-widths of the lines of all the internal vibrations decrease monotonically. On further decrease in temperature the half-widths of the lines, like their frequencies, remain practically constant to helium temperatures for $K_{0.68}A_{0.32}DP$ and to the temperature T_N for $K_{0.26}A_{0.74}DP$.

A fitting of the temperature dependence of the half-widths of the lines corresponding to the internal vibrations of the ammonium ions for all the $K_{1-x}A_xDP$ crystals was carried out in the framework of a model in which the half-width of a line is given by the sum of anharmonic and reorientational terms:

$$\delta = \delta_{\text{anh}} + \delta_{\text{reor}} = AT + B\exp\left(-\frac{U}{kT}\right),$$

where A and B are some constants and U is the activation energy of the reorientation processes.[27] As we showed in Ref. 14, the main contribution to the temperature broadening of the lines of the internal vibrations of the ammonium ions comes from ''hopping'' processes involving a change in the position of the center of mass of the ions in the crystal lattice. The rotational motion of the ammonium ions gives a much smaller contribution to the line broadening and was not taken into account in the fitting. We note that for the $K_{1-x}A_xDP$ crystals with $x=0.82$ and 0.74 the half-widths of the lines in the temperature interval from 296 K to T_N were used for an approximation.

Table II gives the values of the activation energy U obtained as a result of the fitting. Also given for comparison are the values of the activation energy obtained from an analysis of the temperature dependence of the half-widths of the line of the librational vibration of the ammonium ions in mixed $K_{1-x}A_xDP$ crystals of the same concentrations, according to the data of Ref. 14. One notices the close agreement of the values of the activation energy obtained from analysis of the different types of vibrations of the ammonium ions.

According to the phase transition mechanism proposed in Ref. 14, the low-frequency ''hopping'' processes involving a change in the position of the center of mass of the ammonium ions modulate all of the internal vibrations of the ion, and that should equalize the values of the activation energy.

Phase composition of the mixed crystals $K_{1-x}A_xDP$ as a function of temperature

Analysis of the $x-T$ phase diagram constructed for the mixed crystals $K_{1-x}A_xDP$ from the data of different experiments (see, e.g., Ref. 14) indicates that the structural changes in the crystals of all concentrations begin at temperatures of the order of 110–120 K. This is confirmed by the above analysis of the temperature dependence of the frequencies and half-widths of the Raman lines corresponding to the internal vibrations of the ammonium ions.

Let us analyze the states that are realized in the mixed system $K_{1-x}A_xDP$ as the temperature is lowered. As we see from a comparative analysis of the Raman spectra of the PE (Fig. 1) and AFE (Fig. 2) phases, the most important changes in the spectra are observed at frequencies near the totally symmetric internal vibration ν_1. Figure 6a shows the Raman spectra of the $K_{0.26}A_{0.74}DP$ crystal in the frequency interval 2800–3500 cm^{-1} at several temperatures for the ZZ component of the scattering tensor. At room temperature (the PE phase) a broad, intense, single line is observed in this frequency range, corresponding to the totally symmetric internal vibration ν_1 of the ammonium ions.

In the AFE phase at $T<T_N=68.5$ K one observes three lines in the Raman spectra for the ZZ component of the scattering tensor in this frequency interval: these are two lines of the vibration ν_1 (3030 and 3165 cm^{-1}) and one line of the vibration ν_3 (3239 cm^{-1}). However, as we see from Fig. 6, the change in the spectrum has already begun to appear at temperatures much higher than T_N. In this frequency interval the Raman spectra at room temperature were approximated by a single line of the Lorentzian type. At temperatures of the order of 120 K we observed anomalous growth of the half-width of this line. Therefore the Raman spectra at $T<120$ K were approximated by three Lorentzian lines. Figure 7a shows the temperature dependence of the frequencies of the Raman lines for the $K_{0.26}A_{0.74}DP$ crystal as obtained using such an approximation. An analogous temperature evolution of the Raman spectra is also observed for the $K_{0.18}A_{0.82}DP$ crystal. The results are evidence that AFE clusters begin to form in $K_{1-x}A_xDP$ crystals with $x=0.82$ and 0.74 at temperatures of the order of 110–120 K, i.e., a short-range AFE order is established in them. At the temperatures T_N an AFE phase transition occurs, and long-range order is established throughout the entire volume of the crystal.

Analogous changes in the Raman spectra with decreasing temperature are also observed in $K_{1-x}A_xDP$ crystals with $x=0.22$, 0.32, and 0.53. Figure 6b shows the Raman spectra of a $K_{0.47}A_{0.53}DP$ crystal at several temperatures for the ZZ component of the scattering tensor. Figure 7b shows the temperature dependence of the frequencies of the Raman

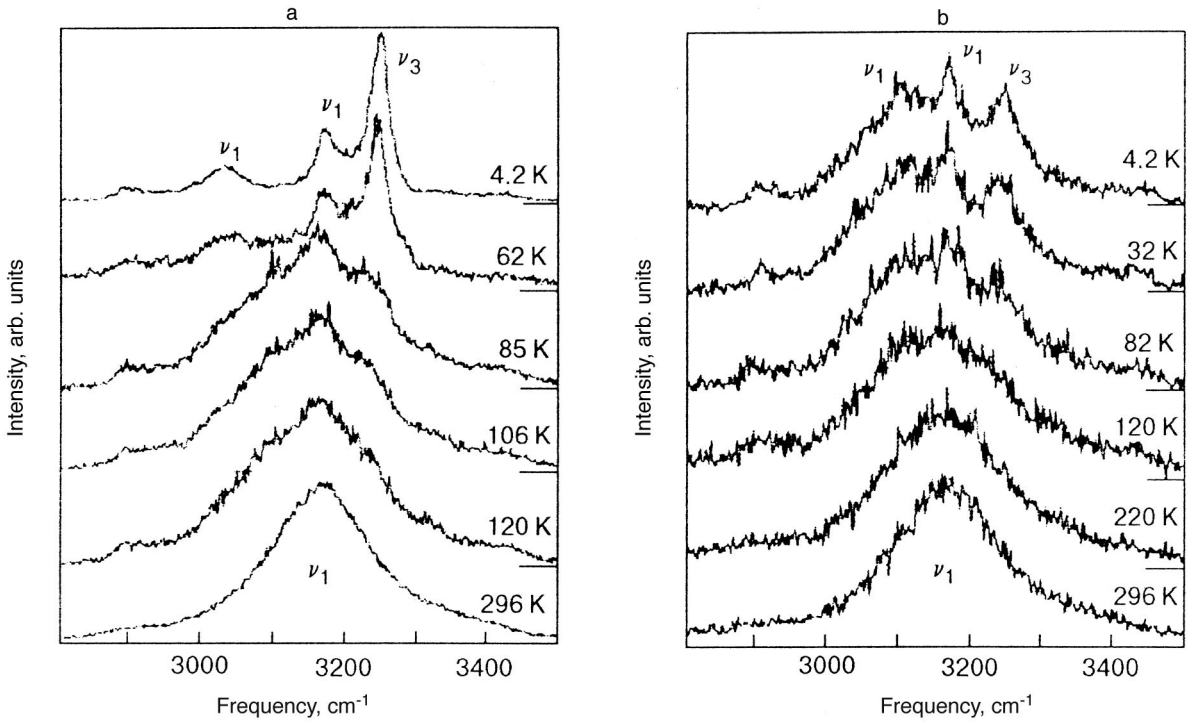

FIG. 6. Raman spectra of $K_{0.26}A_{0.74}DP$ (a) and $K_{0.47}A_{0.53}DP$ (b) crystals for the *ZZ* component of the scattering tensor at several temperatures. The spectral resolution is 2 cm^{-1}. The classification of the spectral lines is according to the data of Ref. 10.

lines for the $K_{0.68}A_{0.32}DP$ crystal, obtained by approximating the experimental spectra by a method similar to that described above.

A comparative analysis of the data presented in Figs. 4–7 suggests that the $K_{0.47}A_{0.53}DP$ crystal suffers structural changes analogous to those observed in $K_{0.26}A_{0.74}DP$ as the temperature is lowered: in the temperature interval 110–120 K a correlated fixing of the ammonium ions in the crystal lattices begins, leading to the formation of AFE clusters. The corresponding temperature can regarded as the temperature at which freezing begins, T_m. However, unlike the $K_{1-x}A_xDP$ crystals with $x=0.82$ and 0.74, in which long-range order is established at T_N and an AFE phase transition occurs, in the crystals with $x=0.22$, 0.32, and 0.53 the AFE cluster structure persists down to liquid helium temperatures. The establishment of long-range AFE order and the transition of the crystal to the AFE phase are prevented by the large concentration of potassium ions, which can be regarded as ''rigid'' defects that do not break the symmetry of the crystals.[23]

The formation of AFE clusters is also observed in other isomorphic mixed crystals of the KDP family.[24–26] We note that similar processes involving structural changes have also been observed by the authors in the mixed crystal $Rb_{0.20}(NH_4)_{0.80}H_2PO_4$, which undergoes a transition to the glass phase. Figure 8 shows the temperature dependence of the frequency and half-width of the librational and internal vibrations ν_2 of the ammonium ions in

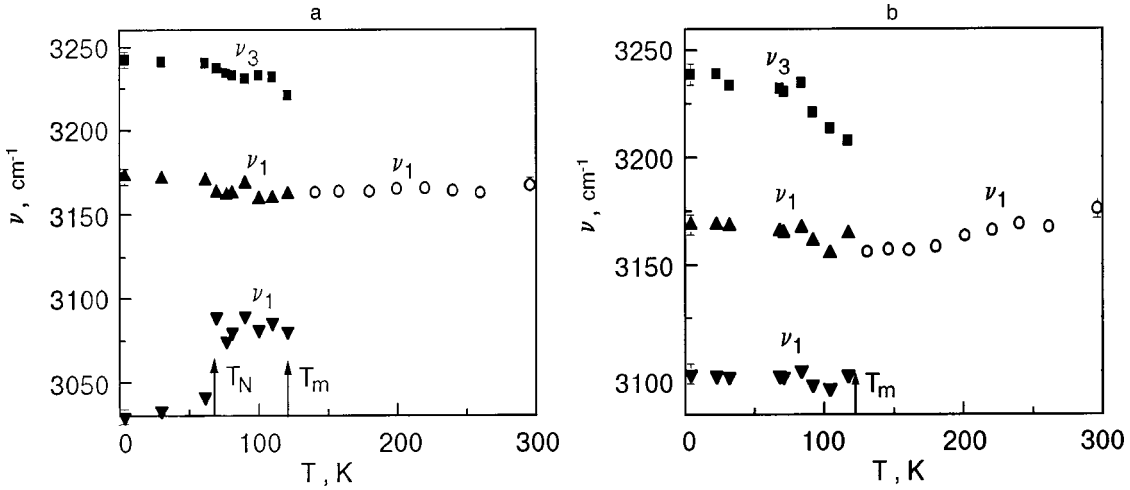

FIG. 7. Temperature dependence of the frequencies of the lines for the *ZZ* component of the scattering tensor in the crystals $K_{0.26}A_{0.74}DP$ (a) and $K_{0.68}A_{0.32}DP$ (b).

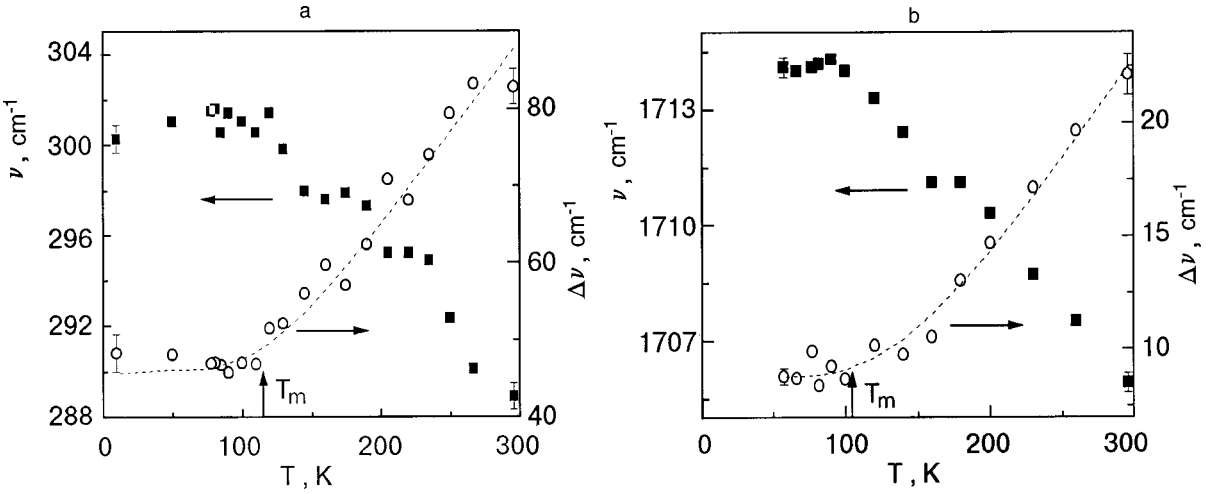

FIG. 8. Temperature dependence of the frequency (■) and the half-width (○) of a librational vibration (a) and of the internal vibration ν_2 (XY component of the scattering tensor) (b) of the ammonium ions in the $Rb_{0.20}A_{0.80}DP$ crystal.

$Rb_{0.20}(NH_4)_{0.80}H_2PO_4$. We see that the character of the temperature dependence of these quantities is practically identical to that of the analogous curves given above for the $K_{1-x}A_xDP$ crystals.

All of the temperature curves of the frequencies and half-widths of the investigated lines at temperatures of the order of 120 K exhibit the characteristic anomalies due to the fixing of the ammonium ions in the crystal lattices. At this temperature, as in the $K_{1-x}A_xDP$ crystals, AFE clusters begin to form; this is confirmed by the temperature evolution of the Raman spectra shown in Fig. 9. Furthermore, the activation energies obtained as a result of approximating the temperature dependence of the half-widths of the lines of the librational and internal vibrations in the framework of the model set forth above are practically equal, having values of 34 and 32 meV, respectively.

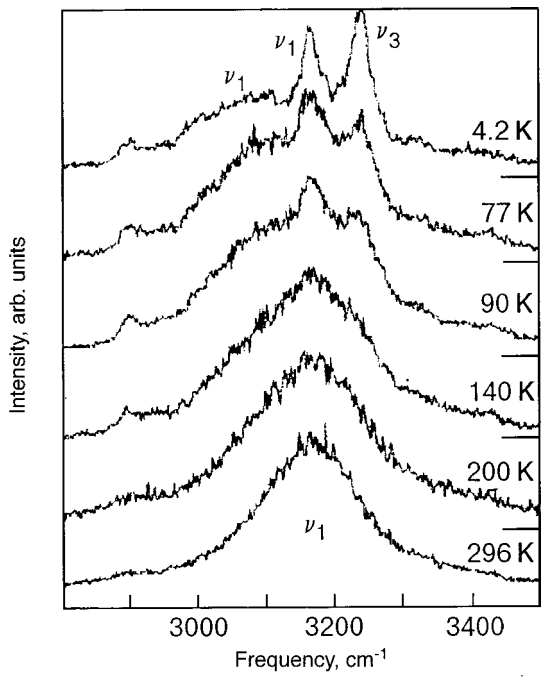

FIG. 9. Raman spectra of the crystal $Rb_{0.20}A_{0.80}DP$ for the ZZ component of the scattering tensor at several temperatures. The spectral resolution is 2 cm^{-1}.

CONCLUSION

We have carried out polarization Raman measurements and spectrum analysis in the temperature interval 4.2–300 K for the mixed crystals $K_{1-x}A_xDP$ with concentrations $x = 0.82$, 0.74, 0.53, 0.32, and 0.22 and $R_{1-x}A_xDP$ with $x = 0.80$ in the frequency region corresponding to the internal vibrations of the ammonium ions.

The results of the polarization measurements confirm the lowering of the local symmetry of the ammonium ions from C_2 to C_1 at the phase transition from the PE to the AFE phase.

The results obtained in this study confirm the AFE transition mechanism proposed in Ref. 14, according to which the position of the ammonium ions in the crystal lattice of the PE phase is not fixed, i.e., the ions execute ''hops'' involving a change in the position of the center of mass. As the temperature is lowered the hopping processes slow down, and a correlated fixing of the ammonium ions in the crystal lattices occurs, leading to an AFE phase transition.

Based on an analysis of the temperature dependence of the frequencies and half-widths of the lines corresponding to the internal vibrations of the ammonium ions, we have established that the fixing of the ammonium ions in the lattices of the mixed crystals $K_{1-x}A_xDP$ begins at temperatures of the order of 110–120 K, independently of the character of the low-temperature phase.

We have determined the activation energies of the reorientation processes involving the ammonium ions. We found that the fixing of the ammonium ions leads to the establishment of a short-range order and to the formation of AFE clusters. The formation of the AFE cluster structure in the mixed crystals involves correlated ''freezing'' of the ammonium ions in the crystal lattice, as is indicated by the set of data obtained in this study: the close values of the activation energy obtained from analysis of different type of vibrations, the stabilizing of the frequency position of the lines of the internal vibrations of the ammonium ions at roughly the

same temperature (of the order of 110–120 K), and the appearance of lines characteristic for the AFE phase in the Raman spectra at these temperatures. The corresponding temperature can be regarded as the temperature T_m at which ''freezing'' begins. In $K_{1-x}A_xDP$ crystals with concentrations $x=0.82$ and 0.74, at the temperatures $T_N=80.5$ and 68.5 K, respectively, long-range order is established throughout the volume of the crystal, and an AFE phase transition occurs. In $K_{1-x}A_xDP$ crystals with concentrations $x=0.53$, 0.32, and 0.22 the AFE cluster structure persists down to liquid helium temperatures.

Based on an analysis of the temperature dependence of the Raman spectra of the crystal $Rb_{0.20}(NH_4)_{0.80}H_2PO_4$, which is isomorphic to the KADP system, and of the temperature dependence of the frequencies and half-widths of the lines of the internal vibrations of the ammonium ions, we have established that with decreasing temperature this mixed system undergoes structural changes analogous to those observed in the $K_{1-x}A_xDP$ crystals.

*E-mail: Alexander.V.Vankevich@univer.kharkov.ua

[1] G. A. Smolenskiĭ, V. A. Bokov, V. A. Isupov, N. N. Kraĭnik, R. E. Pasynkov, A. I. Sokolov, and N. K. Yushin, *Physics of Ferroelectric Phenomena* [in Russian], Nauka, Leningrad (1985).
[2] M. E. Lines and A. M. Glass, *Principles and Applications of Ferroelectrics and Related Materials* [Clarendon Press, Oxford (1977); Mir, Moscow (1981)].
[3] R. Blinc and B. Žekš, *Soft Modes in Ferroelectrics and Antiferroelectrics* [North-Holland, Amsterdam (1974); Mir, Moscow (1975)].
[4] U. T. Hochli, K. Knorr, and A. Loide, Adv. Phys. **39**, 405 (1990).
[5] E. Courtens, Ferroelectrics **72**, 229 (1987).
[6] V. H. Schmidt, Ferroelectrics **72**, 157 (1987).
[7] Y. Tominaga, M. Tokunaga, and I. Tatsuzaki, in *Proceedings of the 6th International Meeting on Ferroelectricity*, Kobe, 1985; Jpn. J. Appl. Phys. **24**, Suppl. 24-2, 917 (1985).
[8] M. Tokunaga, Y. Tominaga, and I. Tatsuzaki, Ferroelectrics **63**, 171 (1985).
[9] A. Sakai and T. Yagi, Ferroelectrics **72**, 51 (1987).
[10] E. Courtens and H. Vogt, J. Chim. Phys. (Paris) **82**, 317 (1985).
[11] J. L. Martinez, F. Agullo-Rueda, and V. H. Schmidt, Ferroelectrics **76**, 23 (1987).
[12] Yu. A. Popkov, A. V. Van'kevich, L. A. Shuvalov, and R. M. Fedosyuk, Fiz. Nizk. Temp. **19**, 195 (1993) [Low Temp. Phys. **19**, 138 (1993)].
[13] Yu. A. Popkov and A. V. Van'kevich, Fiz. Nizk. Temp. **21**, 1217 (1995) [Low Temp. Phys. **21**, 930 (1995)].
[14] A. V. Van'kevich, Yu. A. Popkov, E. M. Savchenko, and I. A. Taranova, Fiz. Nizk. Temp. **22**, 1216 (1996) [Low Temp. Phys. **22**, 930 (1996)].
[15] Yu. A. Popkov, I. A. Taranova, A. V. Vankevich, and E. M. Savchenko, J. Korean Phys. Soc. **32**, S613 (1998).
[16] Yu. A. Popkov, A. V. Van'kevich, I. A. Taranova, E. M. Savchenko, and L. A. Shuvalov, Fiz. Nizk. Temp. **25**, 861 (1999) [Low Temp. Phys. **25**, 645 (1999)].
[17] T. Fukami, S. Akahoshi, K. Hukuda, and T. Yagi, J. Phys. Soc. Jpn. **56**, 4388 (1987).
[18] T. Fukami, J. Phys. Soc. Jpn. **57**, 2211 (1988).
[19] M. Kasahara, M. Tokunaga, and I. Tatsuzaki, J. Phys. Soc. Jpn. **55**, 367 (1986).
[20] M. V. Vol'kenshteĭn, M. A. El'yashkevich, and B. I. Stepanov, *Vibrations of Molecules* [in Russian], Vol. 2, Izd. Teor. Lit., Moscow–Leningrad (1949).
[21] H. Hammer, in *Proceedings of the Second International Conference on Light Scattering in Solids*, Paris, 1971; publ. Flammarion Sciences, Paris (1971), p. 425.
[22] D. K. Agrawal and C. H. Perry, in *Proceedings of the Second International Conference on Light Scattering in Solids*, Paris, 1971; publ. Flammarion Sciences, Paris (1971), p. 429.
[23] A. D. Bruce and R. A. Cowley, *Structural Phase Transitions* [Taylor and Francis, Philadelphia (1981); Mir, Moscow (1984)].
[24] T. Hattori, H. Araki, S.-J. Nakashima, A. Mitsuishi, and H. Terauchi, J. Phys. Soc. Jpn. **57**, 1127 (1988).
[25] C.-S. Tu, S.-S. Gao, R.-J. Jaw, L.-G. Hwa, V. H. Schmidt, D. Brandt, and R.-M. Chien, J. Korean Phys. Soc. **32**, S490, (1998).
[26] J.-J. Kim, H.-K. Shin, and O.-J. Kwon, Ferroelectrics **151**, 247 (1994).
[27] M. M. Sushchinskiĭ, *Raman Scattering Spectra of Molecules and Crystals*, Nauka, Moscow (1969).

Translated by Steve Torstveit

Relaxation dynamics in the high-frequency crystal-field spectroscopy of $PrNi_5$ point contacts

O. P. Balkashin*

B. Verkin Institute for Low Temperature Physics and Engineering, National Academy of Science of Ukraine, 47 Lenin Ave., 310164 Kharkov, Ukraine;
Grenoble High Magnetic Field Laboratory, Max-Planck-Institute für Festkörperforschung and Centre National de la Recherche Scientifique, B.P. 166, F-38042 Grenoble Cedex 09, France

T. M. Brill, A. G. M. Jansen, and P. Wyder

Grenoble High Magnetic Field Laboratory, Max-Planck-Institute für Festkörperforschung and Centre National de la Recherche Scientifique, B.P. 166, F-38042 Grenoble Cedex 09, France

G. L. Sukhodub and I. K. Yanson

B. Verkin Institute of Low Temperature Physics and Engineering, National Academy of Science of Ukraine, 47 Lenin Ave., 310164 Kharkov, Ukraine
(Submitted July 7, 2000)
Fiz. Nizk. Temp. **27**, 90–95 (January 2001)

High-frequency point-contact (PC) spectroscopy is used to investigate the kinetics of relaxation processes in the intermetallic rare-earth compound $PrNi_5$. A difference is observed in the spectral response between the conventional low-frequency PC data and the response signal to microwave and far-infrared radiation of $PrNi_5$–Cu point contacts. This difference is connected with the *f*-shell electronic levels (CEF levels) and phonon temporal dynamics. The phonon reabsorption contribution to the spectra above the Debye energy *decreases* for microwave and far-infrared frequencies. However, the crystal-field contribution to the spectra at 4.2 meV is *enhanced* for high frequencies, reflecting the relaxation processes specific for these Fermi-statistics electronic excitations. The characteristic frequency for CEF-level relaxation is evaluated as ~200 GHz. © *2001 American Institute of Physics.* [DOI: 10.1063/1.1344146]

INTRODUCTION

The crystal-electric-field (CEF) level excitations determine the magnetic, thermodynamic, and transport properties of the intermetallic rare-earth compound $PrNi_5$ (Refs. 1 and 2). The temperature dependences of these characteristics show a Schottky-like anomaly at $T \sim 15$ K. It arises from the ground state splitting of the $4f$ electrons of the Pr^{3+} ions in the CEF of hexagonal symmetry. A crystal-field eigenstate scheme of $PrNi_5$ has been estimated both from neutron diffraction experiments[3] and point-contact-spectroscopy measurements.[4,5]

Point-contact spectroscopy deals with the nonlinear correction to the current–voltage ($I-V$) characteristics of a PC. This method has been successfully employed for estimating the energy relaxation spectra of quasiparticle excitations in many metals and compounds under steady-state conditions.[6–8] Recently, high-frequency PC spectroscopy has been developed and applied to investigating the relaxation kinetics of the electron–phonon system and the temperature in metallic contacts.[9–11] The PC spectra measurements over a wide frequency range make it possible to separate different transient phenomena in PCs and evaluate the appropriate relaxation times.

In accordance with the theory,[12] the second-order derivative of the $I-V$ curve (PC spectrum) for a contact formed by rare-earth metals with two-level splitting Δ of the *f*-shell states consists of three nonlinear contributions to the conductivity:[1)]

$$-\frac{d^2I}{dV^2}(eV) \sim g_f(eV) + \left[\frac{1}{2}g_f(eV) - 4\Delta^2 \int_0^{eV} \frac{g_f(\varepsilon)}{(\varepsilon + eV)^3} d\varepsilon\right], \tag{1}$$

where the first term $g_f(eV)$, the PC spectral function of the CEF-level excitations, is due to inelastic *f*-shell excitations by conduction electrons. The other term, in brackets, describes the background signal and is determined by two different mechanisms. The first one is the reverse CEF-excitation transitions from the excited to the ground state, which enhance the probability of direct transitions. The second is the increasing of the excited-state population and the decreasing of the ground-state population with voltage gain that decreases the probability of the inelastic scattering processes.

It should be noted that the CEF-level spectral function $g_f(eV)$ depends on the CEF-level population because of the Fermi statistics of the excitations,[12]

$$g_f(eV) = N(0) n_f (N_k - N_i) \langle\langle |W^{ik}_{\mathbf{pp}'}|^2 K(\mathbf{p},\mathbf{p}')\rangle\rangle \delta(eV - \Delta), \tag{2}$$

where $N(0)$ is the density of states at the Fermi level; n_f is the rare-earth ion concentration; N_k and N_i are the population numbers for the ground and excited CEF states; $W^{ik}_{\mathbf{pp}'}$ is the matrix element for the electron–CEF-level interaction for

the rare-earth ion transition between an initial and a final state, and $K(\mathbf{p},\mathbf{p}')$ is the point-contact weight factor. Therefore, $g_f(eV)$ depends on temperature and voltage. At zero temperature one has $N_i=(eV-\Delta)\Theta(eV-\Delta)/2(eV+\Delta)$ and $N_k=1-N_i$. The background in Eq. (1) has a contribution with *negative* sign. It reflects the diminution of probability of the inelastic electron scattering by the CEF levels at $eV>\Delta$, because the level population changes with voltage.

In addition to the CEF-level scattering processes, the electron–phonon interaction must be taken into account,[13]

$$-\frac{d^2I}{dV^2}(eV)\sim g_{\rm ph}(eV) + \left[\frac{\gamma}{2}\frac{eV}{eV+\hbar\omega_0}g_{\rm ph}(eV)+\gamma\int_0^{eV}\frac{g_{\rm ph}(\varepsilon)}{\varepsilon+\hbar\omega_0}d\varepsilon\right], \tag{3}$$

where $g_{\rm ph}(eV)$ is electron–phonon spectral function, $\gamma=0.58$, and ω_0 is the phonon escape frequency, $\omega_0=\omega_D(l_{\rm ph}l_r)/d^2$, determined by the relation between the inelastic $l_{\rm ph}$ and elastic l_r phonon path lengths and the contact diameter d, and ω_D is the Debye phonon frequency. In contrast to $g_f(eV)$, the spectral function $g_{\rm ph}(eV)$ is temperature and voltage independent. The two last terms in Eq. (3) correspond to the background signal caused by the stimulated phonon emission and reabsorption of nonequilibrium phonons by conduction electrons.

The PC response to high-frequency irradiation depends on the relation between the external field frequency ν and the inverse relaxation times τ_i of the intrinsic electron scattering processes, which are responsible for the nonlinearity of the $I-V$ curve. Frequency dispersion of the response occurs when $2\pi\nu\tau_i\sim 1$. For instance, the electron–phonon or electron–CEF-level relaxation are very fast processes, with characteristic frequencies $\nu_{e-{\rm ph}},\nu_{e-f}\sim 10^{13}$ Hz. The reabsorption of nonequilibrium phonons having the Debye energy by conduction electrons takes place more slowly, with $\nu_{{\rm ph}-e}\sim 10^9-10^{10}$ Hz.[10] The CEF-level relaxation on electrons, as was estimated in Ref. 12, has a frequency $\nu_{f-e}\sim\nu_{e-f}n\Delta/n_f\varepsilon_F\sim 10^{11}$ Hz (n_f is the concentration of rare-earth atoms, and ε_F is the Fermi energy). For irradiation frequencies $\nu\gg\nu_{f-e},\nu_{{\rm ph}-e}$ the background signal in the PC spectrum [Eqs. (1), (2)] drops like $[1+(\nu/\nu_i)^2]^{-1}$ with increasing frequency[12,13] (ν_i denotes the CEF level-electron or phonon-electron collision frequency).

In this paper we report experiments combining the low-frequency PC spectroscopy of $PrNi_5$–Cu contacts with measurements of the response to microwave and FIR irradiation up to 525 GHz for the same contacts. These frequencies are comparable with ν_{f-e} but are not large enough to cause considerable smearing the features of the CEF levels on the $I-V$ curve upon transition to the quantum regime of radiation detection.[14,15] Small broadening of the spectral lines takes place only for the highest frequency we have used and was taken into account as follows below.

EXPERIMENT

The PCs were formed between a copper tip and the polished surface of the $PrNi_5$ single crystal, with the contact axis parallel to the C axis. The choice of the ''needle–plane'' configuration was aimed at obtaining the best electrodynamic coupling of the contact with the high-frequency field. The contacts were produced in liquid helium by bringing two electrodes together with a precise differential screw mechanism. The contact resistances ranged from a few ohms to about twenty ohms. All measurements were done at temperature 1.5–1.7 K in superfluid helium to avoid the bubble boiling causing unstabilities of the rf power in the contact area. The electromagnetic radiation was generated by reflex klystron oscillators in the microwave range. A methyl alcohol submillimeter-wavelengths laser, optically pumped by a cw carbon dioxide laser, was used as a source of FIR radiation. The radiation was delivered to the PC by a standard *x*-band waveguide with a smooth transition to a 2×23 mm cross section[9,16] or through a lightpipe with a focusing cone.[17] For monitoring the power level a small part of the radiation was reflected to a semiconductor detector by a beam splitter.

In a measuring cycle both the second-harmonic amplitude of the low-frequency (1.873 kHz) modulating current and the response signal—the difference of the $I-V$ curve under and without rf irradiation (chopped by 2.433 kHz), were registered versus the bias voltage using a conventional lock-in technique for the same contact. In the small-signal limit ($V(t)=V_0+v_1\cos(2\pi\nu t), v_1\ll V_0$) both these quantities are proportional to the second derivative of the $I-V$ curve $d^2V/dI^2=-(d^2I/dV^2)(dV/dI)^3$ (Refs. 14 and 16). To avoid the modulation broadening of the PC spectra the intensity of rf irradiation and low frequency ac current were adjusted to the minimal levels providing an output signal amplitude about 1 μV.

RESULTS AND DISCUSSION

The experimental data obtained for the $PrNi_5$–Cu contacts are plotted in Fig. 1. Both the low-frequency and high-frequency PC spectra show the spectral features[2)] that have been well established in previous studies[4,5] for these materials. The pronounced sharp peak at $eV\sim 4.2$ meV is connected with the Pr^{3+} ion transitions ($\Gamma_4\rightarrow\Gamma_{5,A}$) from the ground state Γ_4. Additional singularities at 13 and 30 meV, corresponding to the CEF excitations ($\Gamma_4\rightarrow\Gamma_3$) and ($\Gamma_4\rightarrow\Gamma_{5B}$), are rather weak. The peak at 9 meV and the wide maximum at 17 meV are usually ascribed to the characteristic phonon frequencies in $PrNi_5$ and Cu.[4,5]

Unfortunately, in contrast to low-frequency measurements, the high-frequency current amplitude in point contacts is unknown. Therefore, in order to make a comparison between the spectral line heights in different frequency ranges the high-frequency data were multiplied by scaling factors. All the measurements were done in the small-signal limit, where the spectral line amplitudes were proportional to the power level of the high-frequency field and therefore the scaling procedure did not modify the shape of singularities. The normalization was carried out in an energy range where the external field frequency is much smaller than the intrinsic characteristic frequency of the scattering events determining the PC spectral singularities. For instance, the external frequency $\nu_1=0.61$ GHz for the PC spectrum in Fig. 1a is much smaller than the characteristic frequencies of electron–CEF-level and CEF-level–electron relaxation processes ($\nu_1\ll\nu_{e-f},\nu_{f-e}$) which are responsible for the main peak at

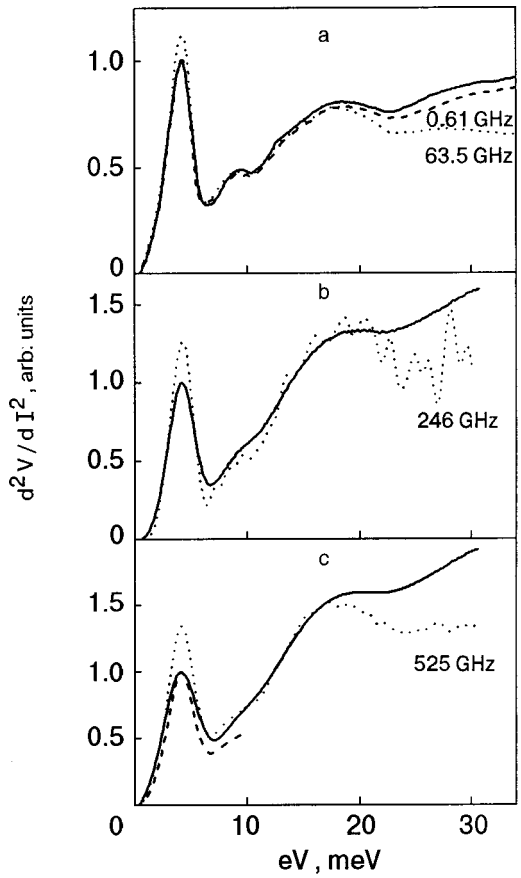

FIG. 1. Point-contact spectra (solid lines) and response signals at different frequencies (dashed and dotted lines). The dashed line in (c)—response signal fitted to audio-frequency data at $V=4.2$ meV. The contact resistances are: $R_0=2.8\Omega$ for (a) and $R_0=7.4\Omega$ for (b, c).

$eV=4.2$ meV. The data at $\nu_1=0.61$ GHz were therefore fitted to the low-frequency peak at that energy. The frequency ν_1 is approximately equal to the thermal relaxation frequency, estimated as 0.5 GHz (see also Refs. 11 and 18). The difference between these curves in Fig. 1a increases slightly with energy but is quite small, showing the weak influence of heating effects in the contact. At $eV=4.2$ meV the heating is negligible, so the normalization we have used is correct. The other rf spectra for $\nu_2=63.5$, $\nu_3=246$, and $\nu_4=525$ GHz were normalized to the audio-frequency data in the energy range 7–17 meV, where the contact resistance is mainly determined by an electron–phonon scattering processes ($\nu_2,\nu_3,\nu_4 \ll \nu_{e-\mathrm{ph}}$). The phonon reabsorption background still has a rather low level in this energy interval. The large noise on the $\nu_3=246$ GHz curve is due to the smaller signal amplitude, because the laser power is about ten times smaller for this frequency compared to ν_4. Therefore a larger value of the scaling factor has to be used for the fitting of the ν_3 data to audio-frequency spectrum.

It should be remarked that there is an additional problem in comparing the low-frequency PC spectra with the FIR data. The photon energy of $\nu_3=246$ GHz radiation ($h\nu_3=1$ meV) is equal to the amplitude of the low-frequency modulation ($ev_1=1$ meV), and these two spectra can be directly compared (Fig. 1b). But for $\nu_4=525$ GHz the photon energy ($h\nu_4=2.2$ meV) is larger than ev_1 and is comparable with the CEF linewidth at 4.2 meV. Therefore, the spectral line is smeared in energy range $eV=h\nu_4$ because the quantum regime of radiation detection[14,15] occurs for this frequency even in the low-power limit used in our experiments. That is why the low-frequency spectra in Fig. 1c were calculated by the standard smearing procedure[6] with $ev_1=2.2$ meV for the curve in Fig. 1b (experiments at ν_3 and ν_4 were performed with the same contact) to permit a correct comparison of the low-frequency and FIR data. Thus, each set of curves in Fig. 1 are characterized by an equal instrumental broadening.

For additional confirmation of the scaling procedure we have used the CEF peak for $\nu_4=525$ GHz, normalized to the audio-frequency data at $eV=4.2$ meV and shown by the dashed curve in Fig. 1c. In that case the CEF linewidth turns out to be abnormally narrow, confirming the validity of the fitting procedure previously described.

The difference between the audio- and high-frequency spectra in Fig. 1 appears in the CEF peak position (4.2 meV) and in the high-energy range. It is well known[7,8,13] that the background signal in the PC spectra at high energy $eV \geqslant \hbar\omega_D$ is determined by the phonon–electron reabsorption processes. At high frequencies $\nu > \nu_{\mathrm{ph}-e}$ the number of nonequilibrium phonons does not follow the high-frequency voltage induced in the contact. The higher the frequency, the smaller the fraction of these phonons that relaxes to the equilibrium state synchronously with the voltage, thus *decreasing* the contribution to the second-derivative signal. The background frequency dispersion has been studied in detail[9,19] and the characteristic relaxation frequencies $\nu_{\mathrm{ph}-e}$ have been determined for several simple metals. Our data in Fig. 1 are in good agreement with those of previous measurements.

The characteristic frequency of phonon–electron scattering $\nu_{\mathrm{ph}-e}$ for the compound $PrNi_5$ is estimated as about 3–5 GHz, and therefore the condition $\nu \gg \nu_{\mathrm{ph}-e}$ is fulfilled for the three frequencies ν_2,ν_3,ν_4 in our experiments, and the phonon background damping has to be independent of frequency for these spectra. Indeed, as is shown in Fig. 1b, 1c, the rf background is decreased to an identical value for the same contact. A slightly different background is observed in Fig. 1a for another contact because of the different conditions of phonon escape (the larger diameter, different concentration of crystal lattice defects, etc.). But different phonon transport conditions do not create an obstacle for the correct comparison of the CEF-peak amplitude because the *f*-shell excitation rate are dependent on the transport of conduction electrons and these excitations are localized on the $PrNi_5$ ions.

In the low-energy region the high-frequency signal *increases*, showing growth of the CEF-peak amplitude, opposite to the behavior in the high-energy region (Fig. 1). In accordance with Eq. (1) the background part of the PC spectrum for CEF-level excitations has a *negative* contribution, in contrast to the phonon part of spectrum [Eq. (3)]. At high frequencies $\nu > \nu_{f-e}$ the population numbers N do not follow the high-frequency voltage, the background part of the PC spectrum decreases, similarly to the phonon reabsorption processes discussed above, and the high-frequency second-harmonic amplitude becomes exactly equal to $g_f(eV)$, as was shown in the theory.[12] In our experiments the difference between the $I-V$ curves under and without irradiation was

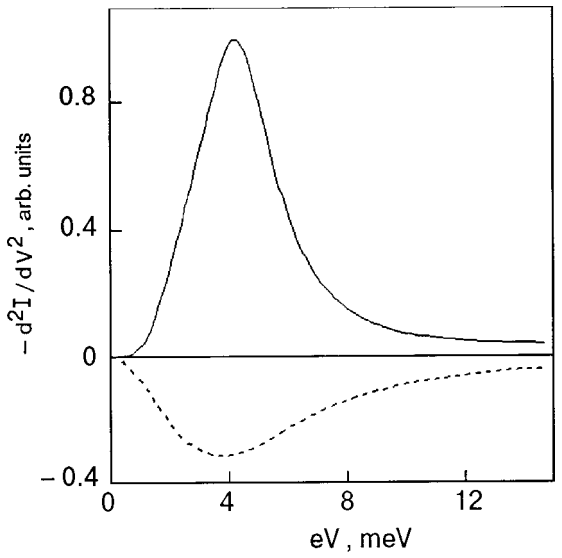

FIG. 2. Components of PC spectrum for CEF-level excitations: spectral part $g_f(eV)$ (solid line), negative background signal (dashed line).

determined. In such a method the steady-state population of excited f levels is increased under high-frequency irradiation (similarly to the bolometric effect in the phonon reabsorption study),[9] increasing the probability of reverse transition to the ground state. This brings about an additional contribution to the measured signal (renormalizing term $1/2g_f(eV)$ in Eq. (1), and the output signal amplitude becomes equal to $1.5\,g_f(eV)$ (see Eq. (34) in Ref. 12).

For qualitative analysis we calculated the negative background components of the CEF spectrum from Eq. (1). The spectral line $g_f(eV)$ was represented by a Lorentzian curve with a small exponential part in the low-energy range and a linewidth equal to the experimental peak width for $\nu_4 = 525$ GHz. The result is shown in Fig. 2 by the dashed line.

The frequency dispersion of the absolute value of the negative background signal for the CEF-level–electron scattering processes is shown in Fig. 3, where $B_\nu = (S_\infty - S_\nu)/(S_\infty - S_0)$; S_0 is the CEF-peak height at audio frequency, and S_ν is the height at high frequency ν. The experimental

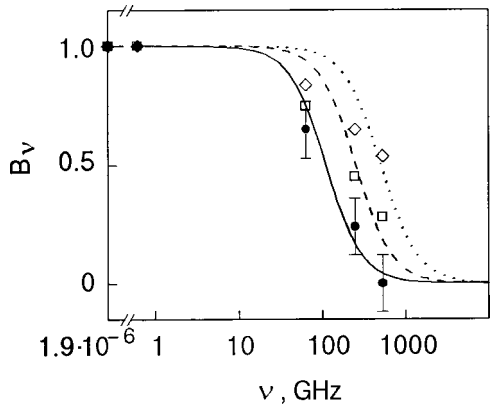

FIG. 3. Frequency dispersion of background signal. The sets of points were obtained from the experimental data normalized by different S_∞ equal to: $S_\infty = S(\nu_4 = 525\,\text{GHz})$ (solid circles), $S_\infty = 1.1S(\nu_4)$ (squares), and $S_\infty = 1.3S(\nu_4)$ (diamonds). The lines represent the background amplitude calculated for different ν_{f-e} values: 110 GHz (solid), 250 GHz (dashed), and 500 GHz (dotted line).

data are represented as three sets of points for three different values of S_∞: $S_\infty = S(\nu_4 = 525\,\text{GHz})$ (solid circles), $S_\infty = 1.1S(\nu_4)$ (squares), and $S_\infty = 1.3S(\nu_4)$ (diamonds). The last two series are shown for the case when signal saturation was not reached in our experiments, i.e., $2\pi\nu_4\tau_{f-e} < 1$. The three curves in Fig. 3 show plots of $[1+(\nu/\nu_i)^2]^{-1}$ for three values of the characteristic frequencies ν_{f-e}: 110 GHz (solid), 250 GHz (dashed), and 500 GHz (dotted line). The best coincidence between the experimental points and the calculated curves occurs in the range 110–250 GHz. Thus we can evaluate the CEF-level–electron relaxation frequency ν_{f-e} as ~200 GHz.

It should be emphasized that the results in Fig. 3 are essentially dependent on the fitting procedure in Fig. 1. But, as was mentioned above, the phonon background damping is independent of frequency at $\nu \gg \nu_{\text{ph}-e}$, and any deviations in the scaling procedure have to be the same for all S_ν values. These deviations do not significantly influence the estimation of ν_{f-e} because the ratio of the measured signals is used in the calculations. Thus, for instance, if the differences between the rf and audio-frequency spectra were decreased by two or three times, the B_ν values would coincide with the points shown in Fig. 3.

It should be noted that in our experiments the absolute value of the background signal B is about $0.4g_f$ (Fig. 1c) at the CEF-peak position, but the calculated $B \sim 0.3$ in Fig. 2. This distinction is possibly caused by the large renormalizing coefficient 1/2 connected with reverse CEF-level transitions, which was considered in the theory,[12] where a strong localization of f-shell excitations on Pr^{3+} ions was assumed. Moreover, the ion–ion and f-level–phonon interaction were neglected. This results in a very narrow spectral line in the PC spectrum (δ-function shape at $T=0$, which is smeared to 0.74 meV at 1.6 K). In special experiments the half-width of the CEF peak at $eV = 4.2$ meV has been measured for different audio-frequency current modulation amplitudes. Extrapolating this data to $v_1 \to 0$, we estimated the linewidth as ~1.93 meV at $T = 1.6$ K. This means that additional dissipation mechanisms should be taken into account compared to Ref. 12. There are various possible causes of the CEF-line broadening: bilinear and quadrupolar exchange interaction between rare-earth ions, a quadrupolar contribution to the spin-disorder resistivity, and f-shell-excitation–phonon coupling, as have been well established for $PrNi_5$ crystals by magnetoelastic, resistivity, and neutron diffraction experiments.[1,2,20] These interactions destroy the strong localization of f-shell excitations and therefore result in a decreasing of the second term amplitude in Eq. (1). Moreover, the inelastic neutron scattering study[21] shows the drop and disappearance of the f-spectral line in the energy range ~4.2 meV during the crystal-to-amorphous-state transition. Hence, some crystal lattice irregularities at contact forming assist the further broadening of the f-shell excitation line in the PC spectrum. We believe that in the general case all these phenomena are responsible for the discrepancies between our experimental data and the theory.[12]

CONCLUSION

The PC spectra measurements over a wide frequency range give an excellent opportunity to distinguish between

the different electron scattering mechanisms causing the nonlinear contact conductivity when the electromagnetic field frequency satisfies the condition $2\pi v\tau_i \sim 1$. Similar experiments allow one to study the kinetics of relaxation phenomena in metals. In this paper we have demonstrated the applicability of this method to the investigation of $PrNi_5$–Cu point contacts. It was found that the rf response signal amplitude *decreases* for thermal and phonon reabsorption processes while it *increases* for the CEF-level relaxation in the limit $2\pi v\tau_{f-e} > 1$. The CEF-level relaxation was studied in detail, and a characteristic frequency $\nu_{f-e} \sim 200$ GHz was estimated. It should be noted that the experimental data show the presence of *f*-level excitation damping, which smears the corresponding peak in the PC spectrum.

We would like to thank A. N. Omelyanchouk for helpful discussions. Part of this work was supported by International Science Foundation Grant No. U9V000.

*E-mail: balkashin@ilt.kharkov.ua

[1)]The small term connected with elastic scattering processes is neglected in Eq. (1).

[2)]We neglected the small negative thermoelectric contribution (~5%) to the signal at $V \to 0$.

[1] V. M. T. S. Barthem, D. Gignoux, A. Naït-Saada, and D. Schmitt, Phys. Rev. B **37**, 1733 (1988).
[2] J. A. Blanco, M. Reiffers, D. Gignoux, D. Schmitt, and A. G. M. Jansen, Phys. Rev. B **44**, 9325 (1991).
[3] P. A. Alekseev, A. Andreeff, H. Griesmann, L. P. Kaun, B. Lipplod, W. Matz, I. P. Sadikov, O. D. Christyakov, I. A. Markova, and E. M. Savitskii, Phys. Status Solidi B **97**, 87 (1980).
[4] A. I. Akimenko, N. M. Ponomerenko, I. K. Yanson, S. Janos, and M. Reiffers, Fiz. Tverd. Tela (Leningrad) **26**, 2264 (1984) [Sov. Phys. Solid State **26**, 1374 (1984)].
[5] M. Reiffers, Yu. G. Naidyuk, A. G. M. Jansen, P. Wyder, I. K. Yanson, D. Gignoux, and D. Schmitt, Phys. Rev. Lett. **62**, 1560 (1989).
[6] A. V. Khotkevich and I. K. Yanson, *Atlas of Point Contact Spectra of Electron-Phonon Interaction in Metals*, Kluwer Academic Publishers, Boston (1995).
[7] A. G. M. Jansen, A. P. van Gelder, and P. Wyder, J. Phys. C **13**, 6073 (1980).
[8] I. K. Yanson and O. I. Shklyarevskii, Fiz. Nizk. Temp. **12**, 899 (1986) [Sov. J. Low Temp. Phys. **12**, 509 (1986)].
[9] O. P. Balkashin, I. K. Yanson, and Yu. A. Pilipenko, Fiz. Nizk. Temp. **13**, 389 (1987) [Sov. J. Low Temp. Phys. **13**, 222 (1987)].
[10] O. P. Balkashin, Fiz. Nizk. Temp. **18**, 659 (1992) [Sov. J. Low Temp. Phys. **18**, 470 (1992)].
[11] O. P. Balkashin and I. I. Kulik, Physica B **218**, 50 (1996).
[12] I. O. Kulik, A. M. Omelyanchouk, and I. G. Tuluzov, Fiz. Nizk. Temp. **14**, 149 (1988) [Sov. J. Low Temp. Phys. **14**, 89 (1988)].
[13] I. O. Kulik, Fiz. Nizk. Temp. **11**, 937 (1985) [Sov. J. Low Temp. Phys. **11**, 516 (1985)].
[14] J. R. Tucker, IEEE J. Quantum Electron. **15**, 1234 (1979).
[15] A. I. Omelyanchouk, and I. G. Tuluzov, Fiz. Nizk. Temp. **9**, 284 (1983) [Sov. J. Low Temp. Phys. **9**, 142 (1983)].
[16] O. P. Balkashin, R. J. P. Keijsers, H. van Kempen, Yu. A. Kolesnichenko, and O. I. Shklyarevskii, Phys. Rev. B **58**, 1294 (1998).
[17] R. V. van der Heijden, Ph.D. Thesis, University of Nijmegen (1982).
[18] O. P. Balkashin, I. K. Yanson, V. S. Solov'ev, and A. Yu. Krasnogorov, Zh. Tekh. Fiz. **52**, 811 (1982) [Sov. Phys. Tech. Phys. **27**, 522 (1982)].
[19] O. P. Balkashin, I. K. Yanson, and Yu. A. Pilipenko, Fiz. Nizk. Temp. **17**, 221 (1991) [Sov. J. Low Temp. Phys. **17**, 114 (1991)].
[20] V. L. Aksenov, E. A. Goremychkin, E. Muhle, Th. Frauenheim, and W. Buhrer, Physica B **120**, 310 (1983).
[21] P. A. Alekseev, V. N. Lazukov, V. G. Orlov, I. P. Sadikov, and J. B. Suck, Physica B **180–181**, 167 (1992).

This article was published in English in the original Russian journal. Reproduced here with stylistic changes by AIP.

LOW-TEMPERATURE PHYSICS OF PLASTICITY AND STRENGTH

Dependence of the shear modulus of a Bi ceramic on external influences in the temperature interval 65–130 K

L. A. Chirkina, G. G. Sergeeva,* Ya. D. Starodubov, M. B. Lazareva, and V. S. Okovit

National Science Center, Kharkov Physicotechnical Institute, ul. Akademicheskaya 1, 61108 Kharkov, Ukraine

(Submitted June 2, 2000; revised August 29, 2000)
Fiz. Nizk. Temp. **27**, 96–102 (January 2001)

The dynamic shear modulus of a two-phase bismuth ceramic (Bi-2212 and Bi-2223) is measured as a function of temperature, magnetic field, and deformation. The results attest to the multistage penetration of magnetic field into the sample. It is found that the level of the shear modulus is sensitive to the magnetic and defect structure of the ceramic. The conjecture that the observed defects of the shear modulus are due to phase separation in the CuO_2 planes of the 2212 phase is discussed. © *2001 American Institute of Physics.* [DOI: 10.1063/1.1344147]

INTRODUCTION

There is now a considerable amount of published data on the elastic characteristics of high-T_c superconducting (HTSC) materials and their relation to features of the lattice, electronic, and magnetic structures.[1–7] The elastic properties of the crystal lattice of HTSC compounds are determined by the chemical and phase state and their homogeneity, the layered character of their structure, their specific density, the spectrum and concentration of structural defects (including microcracks, grain and phase boundaries, pores and individual vacancies, dislocations, and twins), the presence of local internal stresses and nonstoichiometric oxygen, the structure of the cuprate planes, the features of the electron–phonon interaction in them, the type of cations, etc.[1,7]

Perovskite and perovskitelike structures are characterized by the presence of phase transitions of the displacive type, which can be initiated by small changes in the external conditions as a result of local distortions of the crystal lattice.[8] In addition, there are data indicating the possibility of phase transitions of the antiferromagnetic, ferroelectric, and insulator–metal types.[9,10] A particularly crucial matter in Bi-containing superconductors may be the magnetic state of the CuO_2 planes.[6,11]

It follows from what we have said that even small deviations from the optimum technology of preparation of the ceramic or a change in its chemical homogeneity or of its phase and defect structure during the study of an object under the influence of temperature, especially during multiple cooling and heating cycles (77–300–77 K), deformation (even small), or fields (magnetic and electric) can give rise to internal peak stresses and local distortions of the crystal lattice. In previous studies of the temperature dependence of the absorption of low-frequency sound in Bi ceramic samples it was found that the influence of magnetic field leads to irreversible changes in the state of the samples and to a stable magnetization of them, which indicates the presence of ''trapped'' magnetic flux.[12] The present paper is devoted to a further study of the behavior of Bi ceramics under various external influences. The changes of the dynamic shear modulus (DSM) are measured as a function of temperature, magnetic field, and deformation, and the results of the measurements are analyzed.

SAMPLES AND MEASUREMENT TECHNIQUE

We investigated samples of the two-phase (65% in the 2223 phase and 30% in the 2212 phase) Bi–Pb–Sr–Ca–Cu–O ceramic, with $T_c = 104$ K for the 2223 phase and 85 K for the 2212 phase. The remaining 5% of the material was in nonsuperconducting phases, e.g., $CaPbO_4$. The powder for pressing of the ceramic consisted of the compounds Bi_2O_3, PbO, $SrCo_3$, $CaCo_3$, and CuO. The phase state of the powder was determined on a DRON-2 diffractometer in CuK_α radiation. Samples of dimensions $2\times2\times24$ mm were pressed at 300 MPa and then mechanically processed into a cylindrical shape with a diameter of 2 mm. The resulting cylinders were annealed in air at 1093 for 24 h and then cooled to room temperature at a rate of 150 deg/h. The samples chosen for study were closely matched in terms of T_c, ΔT_c, and grain size and had the same texture (80% of the grains had the C axis oriented in the direction of pressing, and so the CuO_2 planes were oriented along the axis of the sample).

The temperature dependence of the DSM was measured on samples in five structural states: A — the initial sample; B — after the imposition and removal of a longitudinal static magnetic field (235 Oe) at 77 K, leading to a residual magnetization of the ceramic; C — after annealing of the sample at 380 K for 10 h for the purpose of demagnetizing it; D — after a macroelastic deformation to $\gamma = 7.1\times10^{-4}$ at 65 K; E — after heating of the deformed sample to 300 K.

The DSM was studied on an apparatus of the inverted torsion pendulum type[13] in the temperature interval 65–130 K at a frequency of 0.8 Hz with heating at a rate of 0.5–0.6 deg/min. The amplitude of the strain at the surface of the sample in the measurement of the shear modulus did not exceed 1×10^{-5}. The frequency of the free torsional oscillations used in calculating the values of the DSM was deter-

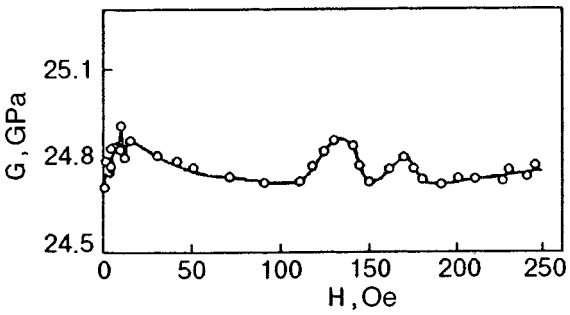

FIG. 1. Field dependence of the dynamic shear modulus of a Bi ceramic in the initial state at 77 K.

mined on the basis of 100–120 vibrations of the sample with the aid of a frequency meter. The error in the calculation did not exceed 0.1%. Selection of the samples and a mandatory three or four temperature cycles (65–300–65 K) made it possible to achieve good reproducibility in the measurements of the DSM. A hold of the sample at 300 K (for up to 6 months) did not reveal any instability of the DSM. Conclusions were drawn on the basis of a comparison of the results of the measurements of the DSM on five identical samples. For each of these samples a series of curves was obtained for the whole sequence of states produced (A, B, C, D, E). A comparison of five series of curves showed that the character of the change in the temperature dependence of the dynamic shear modulus $G(T)$ under the influence of the various external factors was the same in all of them. For this reason the series of curves for only one of the samples is given in this paper.

The straining of the samples was carried out at 65 K directly in the apparatus used to measure the internal friction. An alternating torsion was applied at a strain rate of 10^{-3} s^{-1} to a relative strain of $\gamma = 7.1 \times 10^{-4}$, which exceeds the working amplitude in the measurement of the internal friction by two orders of magnitude. The temperature at which the straining was done, 65 K, which was achieved by pumping the nitrogen vapor, was chosen so as to ensure the stability of the structural–phase state of the initial samples (below the NS transitions of both phases). An optical method was used to monitor the return of the oscillatory system to its initial position after the pendulum had stopped; it showed that there was no residual deformation. For the samples with the dimensions indicated above, the length of the rocker arm (540 mm) and the optical system (with a 50× magnification) used to record the amplitude of the oscillations of the rocker arm made it possible to determination the strain of the sample to an error of 1×10^{-4}%. The DSM was measured not later than 5 min after the straining was completed, without demounting or heating the sample.

The magnetic field dependence of the DSM of the Bi ceramic in the initial state was investigated at 77 K in a static longitudinal field, parallel to the CuO_2 planes, over the interval 1.5–235 Oe. The magnetic field was imposed after the sample was cooled to 77 K.

RESULTS OF THE MEASUREMENTS

1. The field dependence of the DSM of the Bi ceramic in the initial state A is shown in Fig. 1. Measurements of $G(H)$ in the interval 1.5 Oe$\leqslant H \leqslant$235 Oe showed that, against the background of a practically constant DSM as a function of the external magnetic field there are two field regions in which the DSM deviates noticeably (up to 0.6%) from the background. The first region in which the DSM deviates from the background lies in the interval 1.5–15 Oe, and the second at 110–180 Oe. The data presented for the two-phase samples agrees with the previously discovered multistage character of the penetration of magnetic field into the ceramic.[12,14–16]

In the region 1.5 Oe$< H_1 <$10 Oe the $G(H)$ dependence observed in this study can be attributed to the penetration of the magnetic field into the ceramic along microstructural inhomogeneities of the weak-links type; this agrees with the results of Ref. 17, according to which the critical fields of the intergranular Josephson links are $H_{c1J} = 2$ Oe and $H_{c2J} = 5$ Oe.

At 77 K the range of values of the magnetic fields that penetrate into the interior of the Bi ceramic, according to Refs. 18 and 19, is very wide (2.5 Oe$< H_{c1} <$80 Oe). This disagreement in the data on the value of H_{c1} is due to a number of causes, among which are the difference in the penetration fields for the 2212 and 2223 phases[20] and the strong anisotropy of the superconducting parameters.[18,19]

2. The temperature dependence of the shear modulus of the Bi ceramic in the states A, B, C, D, and E is presented in Fig. 2. As we see from Fig. 2a, the DSM of the Bi ceramic in the initial state decreases sharply (by 0.8%) in the region 80–87 K, which corresponds to the region of the superconducting transition of the 2212 phase. Upon further increase in the temperature to 130 K no change in the DSM is observed, i.e., in the region of the superconducting transition of the 2223 phase for the two-phase Bi ceramic sample did not exhibit any anomalies on the $G(T)$ curve.

The ''trapped'' magnetic flux in the sample (state B) (Fig. 2b) leads to an increase in the DSM in both the mixed and normal states (by 2.5% and 1.6%, respectively) and to a pronounced modulus defect with a softening effect (by 1%) as the temperature is increased from 93 to 102 K. The value of the ''trapped'' magnetic flux (1.5 Oe) was determined by comparing the $G(T)$ curves in various fields with the DSM in the B state. It was found that these curves are identical both in terms of absolute value (the value of the DSM in a field of 1.5 Oe at 77 K is 25.14 GPa) and in the character of the temperature dependence.

After the sample was annealed at 380 K (state C) (Fig. 2c) a partial recovery of the DSM had occurred: the level of the $G(T)$ curve is lowered over the entire interval of temperatures studied; the value of the modulus defect is decreased while the temperature at which it starts remains the same. Here the demagnetization procedure did not completely restore the $G(T)$ curve to the level of its initial state (see Fig. 2a,c), i.e., there is a residual value of the magnetization B_{res}. Measurements of B_{res} at 300 K with shielding of the Earth's magnetic field gave a value $\sim$0.024 G (see Ref. 12). In addition, the samples in the state C exhibit characteristic temperature oscillations of the DSM in the interval 73–95 K, i.e., in the region of the superconducting transition of the 2212 phase ($T_c = 85$ K). The amplitude of the oscilla-

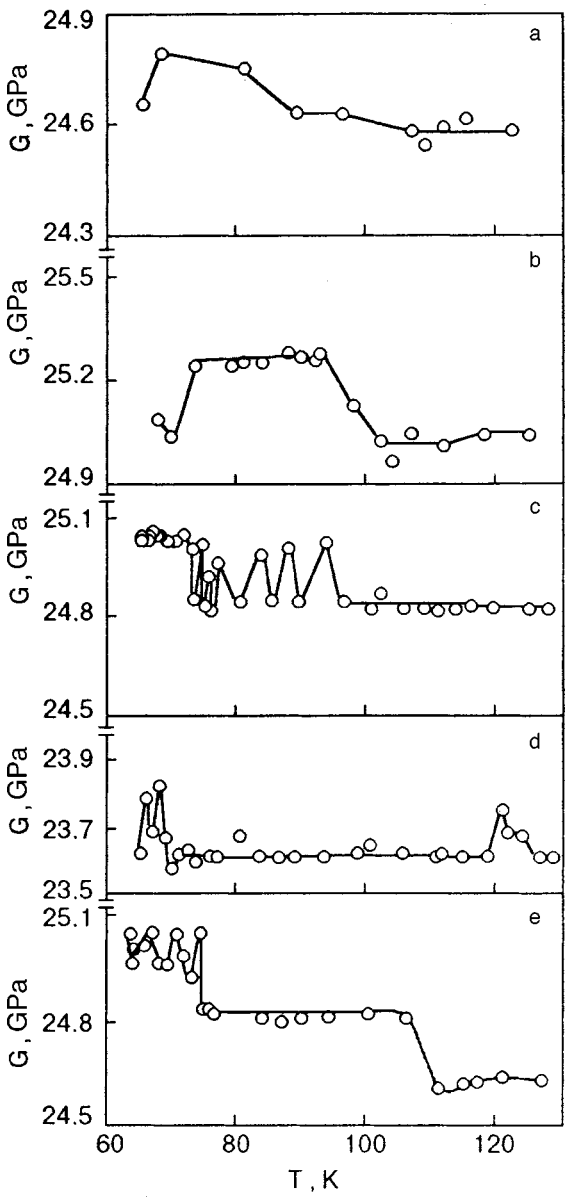

FIG. 2. Temperature dependence of the dynamic shear modulus of a Bi ceramic after various procedures have been performed on it: initial state (a), in the presence of a ''trapped'' magnetic field (b), after annealing to 380 K (c), after deformation by an alternating torsion to $\gamma_{max}=7.1\times10^{-4}$ at 65 K (d), after heating of the deformed sample to 300 K (e).

tions of the DSM is 0.4–0.6%, which is greater than the measurement error.

Deforming the sample (state D) (Fig. 2d) substantially (by 5%) decreased the value of the shear modulus over the entire temperature interval, eliminated the shear modulus defect observed in the B and C states, and shifted the region of $G(T)$ oscillations to 65–72 K.

Heating the deformed sample to 300 K (state E) (Fig. 2e) almost completely restored the elastic properties of the ceramic to the pre-deformation level at temperatures below T_c (compare with the curve in Fig. 2c), while for $T>T_c$ the curve in Fig. 2e approaches the level of the curve in Fig. 2a, i.e., to the level of the modulus in the initial state. At the same time, the curve in Fig. 2e exhibits shear modulus defects in the regions 75–77 K and 106–112 K, and oscillations of $G(T)$ are observed at $T<75$ K.

DISCUSSION OF THE RESULTS

Let us consider the possible reasons for the appearance of ''trapped'' magnetic flux and the residual magnetic field and for the influence of temperature and external influences on the structural state of the Bi ceramic, which is responsible for the observed changes in the DSM.

Level of the DSM. Analysis of the experimental data obtained in this study shows that the ''trapped'' magnetic flux (1.5 Oe) increases the level of the DSM, that lowering of the residual magnetic field to $B_{res}=0.024$ Oe leads to a decrease in the degree of rise of the DSM, and that macroelastic deformation lowers the DSM substantially. According to published data,[4] one reason for the increase of the DSM in weak magnetic fields is the change in shape of the unit cell of the vortex lattice. Another possible cause of the observed effect is a structural rearrangement due either to the establishment of short-range antiferromagnetic order in the CuO_2 planes[6] or to separation of the 2212 phase in the CuO_2 planes into insulating and metallic stripes with different structures.[20,21] Such a restructuring, by analogy with the change in oxygen concentration in the Cu1–O1 chains in the yttrium ceramic, leads to a change of all the force constants.[7] Then the interaction of any strain-carriers with the different types of boundaries (e.g., the boundaries between the 2223 and 2212 phases, the presence of stripe structures in the copper–oxygen planes) should promote growth of the dynamic characteristics.[22]

It is known that a localization of the magnetic field in ceramics occurs at the intergranular links.[5,23,24] We therefore assume that, as in the yttrium ceramic,[9] the localization of the ''trapped'' magnetic flux will be limited to systems of weak links and the regions adjacent to them. This would make the observed increase in the DSM a 2.5% effect.

The more significant (5% and of the opposite sign) change in the DSM level after macroelastic deformation of the ceramic (state D) can be attributed to the circumstance that the deformation involves not only the intergranular contact regions but also microregions in the interior of the grains. At the degree of deformation investigated in the present study the DSM level of the Bi ceramic is probably due both to accumulation of defects in the region of the Josephson contacts[9] and to changes in the defect structure in the grains. Any change in the dislocation structure resulting from the deformation investigated here, which was limited to the region of macroelasticity, could only occur through an increase in the number of long-loop dislocations on account of the breaking away of dislocation segments from pinning points under the influence of the alternating external force field, but multiplication of dislocations does not take place. This is also confirmed by the absence of residual deformation and by the recovery of the $G(T)$ curve to the pre-deformation level (Fig. 2c) after heating of the deformed sample to 300 K (Fig. 2e).

The observed character of the recovery of $G(T)$ after heating to 300 K suggests that during the deformation at 65 K to $\gamma=7.1\times10^{-4}$, unstable low-energy structural formations arise for which the thermal activation on heating of the ceramic to 300 K turns out to be sufficient for the practically total recovery of these structural defects. The probability of formation of such structural defects will increase on account

of the two-phase nature of the ceramic under study, the instability of which on thermocyling 300–77–300 K has been noted previously.[12] Such unstable structural defects of deformational origin can be either point defects with a low energy of migration, i.e., interstitial atoms and isolated vacancies, or metastable phases. A high concentration of point defects can result both from the appearance of interstitial atoms and vacancies during the motion of dislocation loops with steps under the influence of an external alternating load and from displacement of the oxygen atoms in the CuO_2 planes from their equilibrium positions to interstitial sites.[25]

Metastable phases arise in perovskite structures, according to Ref. 8, through the initiation of phase transitions of the displacive type, which occurs during local distortions of the crystal lattice even for very small deformations of the ceramic. Apparently the macroelastic deformation, by displacing the oxygen atoms, can destroy the structure that arises under the influence of the ''trapped'' magnetic flux, much as this structure is destroyed in magnetic fields because of spin polarization,[6] i.e., deformation ''nullifies'' the influence of the residual magnetic moment on the DSM level, and the dynamic shear modulus of the Bi ceramic is lower after deformation. Upon heating the elastic deformation is partially relieved, the defect and phase structures recover, and the influence of the residual magnetic field at $T<T_c$ is restored.

DSM defects. The data on the character of the anomalies of the temperature dependence of the elastic moduli of one- and two-phase bismuth compounds in the superconducting transition regions (70–120 K) and their interpretation are extremely contradictory.[1,26–31]

In a number of papers the acoustic anomalies are directly linked to the development of the superconducting transition.[1,30] In the majority of cases the anomalies of the acoustical parameters near T_c are judged to be the result of structural and phase instability and the development of phase transitions of the shear type with a multicomponent order parameter.[1,27,29,31] In an analysis of phase transitions of the shear type, which coincide in temperature with the superconducting transitions of the phases 2212 and 2223, much attention is paid to the state of the CuO_2 planes and the possibility of local correlated anharmonic displacements of the oxygen atoms relative to the copper atoms by 0.2–0.3 Å along the C axis.[29]

In this study we did not observe anomalies of the temperature dependence of $G(T)$ near T_c in the initial sample (Fig. 2a), but upon the appearance of the ''trapped'' magnetic flux (Fig. 2b) a substantial defect of the DSM, of the softening type (on heating), is observed at $T<T_c$. If this modulus defect were due to a superconducting transition, then its sign and magnitude would be different from what they are.[27] We therefore assume that the appearance of the DSM defect when ''trapped'' magnetic flux appears in the sample is a consequence of a transformation stimulated by the field. One of these transformations in Bi ceramics in the presence of a residual magnetization is probably the establishment of short-range antiferromagnetic order in the insulating stripes in the CuO_2 planes.[6] In the present study the start of the DSM defect in the presence of a ''trapped'' magnetic flux (Fig. 2b) or residual magnetic field (Fig. 2c) and in the absence of other influences, just as in Ref. 6, is fixed in temperature, but the value of the defect depends on the level of these fields.

It can be supposed that the macroelastic deformation (state D), by introducing an excess number of deformation defects, destroys the magnetic ordering of the insulating stripes in the CuO_2 plane of the 2212 phase, and that leads to vanishing of the DSM defects (Fig. 2d). For the heated sample (Fig. 2e) two modulus defects appear, very likely attesting to the partial restoration of magnetic ordering of the insulating stripes in the superconducting state.

Oscillations on the G(T) curve. The oscillatory dependence of the elastic characteristics for $H<200$ Oe has been observed previously on yttrium ceramics[5,32,33] and has been linked to lattice deformations in the superconducting transition region, to the appearance of structural regions with close values of the sound velocities, and to the onset of interference due to the penetration of the magnetic flux into the intergranular contacts and into closed granule clusters.

We have observed oscillations on the $G(T)$ curve at a small residual magnetic field at temperatures below the superconducting transition of the 2212 phase, which agree with the results of measurements of the temperature dependence of the low-frequency internal friction in the same samples.[12] A possible cause of the oscillations is phase separation in the CuO_2 planes of the 2212 phase into metallic and insulating stripes with different elastic properties.[34]

CONCLUSIONS

Analysis of the results of the measurements of the field dependence ($0\leqslant H\leqslant 250$ Oe) and temperature dependence (65 K$\leqslant T\leqslant$130 K) of the DSM both for the initial state and after magnetization, annealing, and deformation of the samples of a two-phase bismuth ceramic leads to the following conclusions.

1. The field dependence of the DSM has two magnetic field regions (1.5–15 Oe and 110–180 Oe) in which changes in the DSM are observed; these changes may be due to the multistage character of the penetration of magnetic field into HTSC ceramics having substantially inhomogeneous micro- and macrostructure.

2. The temperature dependence of the DSM level is very sensitive to the magnetic and defect structures of the ceramic. The ''trapped'' magnetic flux (1.5 Oe) increases the DSM level by 2.5% in the mixed state and by 1.6% in the normal state). Demagnetizing the sample (by annealing at 380 K) to the level of the residual magnetization roughly halves the degree of increase of the DSM. Macroelastic deformation ($\gamma=7.1\times10^{-4}$) at 65 K lowers the DSM level substantially (by 5%). It is conjectured that the influence of the ''trapped'' magnetic flux or the residual magnetic field on the DSM level is due to the correlated displacement of atoms and point defects and to the establishment of short-range antiferromagnetic ordering of the copper atoms in the CuO_2 planes of the 2212 phase within the insulating stripes. Deformation, by creating a high concentration of unstable low-energy structural defects (such as interstitial atoms, isolated vacancies, and metastable phases), destroys the short-range antiferromagnetic order in the insulating stripes and thus lowers the DSM level.

3. At $T<T_c$ the structural states A, B, and C are characterized by the presence of one DSM defect of the softening type (in measurements during heating), while the states arising after heating of the deformed sample (E) have two such DSM defects, which are not rigidly tied to the temperatures of the superconducting transitions of the 2212 and 2223 phases. The temperature position of the modulus defects depends on the presence of residual magnetization and the number and spectrum of the defects, particularly of point defects. It is assumed that the observed DSM defects are due to phase separation in the CuO_2 planes of the 2212 phase.

4. In the presence of a small residual magnetization the $G(T)$ curves exhibit oscillations in the region of the superconducting state of the 2212 phase. These oscillations probably arise as a result of phase separation in the CuO_2 planes of the 2212 phase into metallic and insulating stripes with different elastic characteristics.

Additional comprehensive studies will be needed in order to reach a definite conclusion as to the influence of small residual magnetic fields, deformation, and temperature on the elastic characteristics and their anomalies in Bi ceramics.

*E-mail: gsergeeva@kipt.kharkov.ua

[1] S. V. Lubenets, V. D. Natsik, and L. S. Fomenko, Fiz. Nizk. Temp. **21**, 475 (1995) [Low Temp. Phys. **21**, 367 (1995)].
[2] N. K. Zhuchenko and R. Z. Yaguz, Sverkhprovod. (KIAE) **6**, 1801 (1993).
[3] V. P. Seminozhenko, V. F. Khirnyĭ, Yu. A. Grinchenko, and A. A. Kozlovskiĭ, Sverkhprovod. (KIAE) **6**, 2010 (1993).
[4] D. A. Kuptsov, Sverkhprovod. (KIAE) **4**, 1846 (1991) [Superconductivity **4**, 1751 (1991)].
[5] M. M. Gaĭdukov, E. F. Gatsura, E. K. Gol'dman, L. Kovalevich, A. B. Kozyrev, A. Yu. Popov, and T. B. Samoĭlov, Sverkhprovod. (KIAE) **3**, 2194 (1990) [Superconductivity **3**, 1628 (1990)].
[6] A. L. Gaĭduk, V. D. Fil', N. G. Burma, V. I. Dotsenko, M. N. Sorin, N. M Chaĭkovskaya, A. M. Gurevich, V. N. Eropkin, and A. I. Smirnov, in *Proceedings of the Third All-Union Conference on High-Temperature Superconductivity* [in Russian], Kharkov (1991), Vol. 3, p. 122.
[7] I. Natkanets, A. V. Belushkin, E. A. Goremychkin, Ya. Maĭer, I. L. Sashin, V. K. Fedotov, R. K. Nikolaev, E. G. Ponyatovskiĭ, and N. S. Sidorov, JETP Lett. **48**, 181 (1988).
[8] E. G. Fesenko, *The Perovskite Family and Ferroelectricity* [in Russian], Atomizdat, Moscow (1972).
[9] A. M. Dolgin, V. D. Natsik, and S. N. Smirnov, Fiz. Nizk. Temp. **16**, 1326 (1990) [Sov. J. Low Temp. Phys. **16**, 759 (1990)].
[10] N. V. Anushukova, A. I. Golovashkin, L. I. Ivanova, O. T. Malyuchkov, and A. P. Rusakov, Fiz. Nizk. Temp. **22**, 485 (1996) [Low Temp. Phys. **22**, 372 (1996)].
[11] B. I. Ivlev, Yu. N. Ovchinnikov, and V. Z. Pokrovsky, Europhys. Lett. **13**, 187 (1991).
[12] B. G. Lazarev, Ya. D. Starodubov, G. G. Sergeeva, M. B. Lazareva, L. A. Chirkina, V. S. Okovit, A. V. Chechkin, V. T. Petrenko, and M. A. Tikhonovskiĭ, Fiz. Nizk. Temp. **22**, 819 (1996) [Low Temp. Phys. **22**, 629 (1996)].
[13] I. A. Gindin, V. I. Kovalenko, V. S. Okovit, Ya. D. Starodubov, and L. A. Chirkina, Zavod. Lab. **11**, 1397 (1970).
[14] É. B. Sonin and A. K. Tagantsev, Zh. Éksp. Teor. Fiz. **95**, 994 (1989) [Sov. Phys. JETP **68**, 572 (1989)].
[15] M. A. Zelikman, Sverkhprovod. (KIAE) **5**, 1819 (1992) [Superconductivity **5**, 1738 (1992)].
[16] S. G. Ovchinnikov, Usp. Fiz. Nauk **167**, 1042 (1997).
[17] Yu. N. Myasoedov, I. I. Gabriel', and V. N. Davydov, in *Proceedings of the Second International Conference on Materials Science of High-Temperature Superconductors* [in Russian] Kharkov, (1995), p. 20.
[18] N. V. Zavaritskiĭ and V. N. Zavaritskiĭ, JETP Lett. **53**, 226 (1991).
[19] K. Tagaya, K. Senda, T. Yosida, N. Fukuoka, and H. Sasakura, Jpn. J. Appl. Phys. **31**, part 2, L1170 (1992).
[20] G. G. Sergeeva, Yu. P. Stepanovskiĭ, and A. V. Chechkin, Fiz. Nizk. Temp. **24**, 1029 (1998) [Low Temp. Phys. **24**, 771 (1998)].
[21] K. A. Muller (Ed.), *Phase Separation in Cuprate Superconductors*, World Scientific Pub., Singapore (1992); A. Bianconi and M. Missori, J. Phys. (Paris) **4**, 361 (1994).
[22] V. S. Postnikov (Ed.), *Internal Friction and Defects in Metals* [in Russian], Metallurgiya, Moscow (1965).
[23] G. V. Golubnichaya, A. Ya. Kirichenko, I. G. Maksimchuk, and N. T. Cherpak, Fiz. Nizk. Temp. **23**, 167 (1997) [Low Temp. Phys. **23**, 122 (1997)].
[24] P. K. Mishra, G. Ravikumar, and P. Chaddan, Jpn. J. Appl. Phys. **29**, L1612 (1990).
[25] A. V. Soldatov and T. S. Ivanchenko, Sverkhprovod. (KIAE) **6**, 1997 (1993).
[26] P. P. Pal-Val, L. N. Pal-Val, V. D. Natsik, I. F. Kislyak, and V. I. Dotsenko, Fiz. Nizk. Temp. **22**, 1452 (1996) [Low Temp. Phys. **22**, 1103 (1996)].
[27] M. Saint-Paul, I. Z. Tholence, H. Noel, J. C. Zevet, M. Potel, and P. Gongeon, Physica B **165–166**, 1279 (1990).
[28] M. B. Lazareva, V. S. Okovit, V. T. Petrenko, G. G. Sergeeva, Ya. D. Starodubov, M. A. Tikhonovskiĭ, and L. A. Chirkina, Fiz. Nizk. Temp. **20**, 840 (1994) [Low Temp. Phys. **20**, 660 (1994)].
[29] J. Wu, Y. Wang, P. Guo, H. Shen, Y. Yan, and Z. Zhao, Phys. Rev. B **47**, 2806 (1993).
[30] G. d'Anna, W. Benoit, and H. Berger, Phys. Status Solidi A **125**, **2**, 589 (1991).
[31] Y. N. Wang, J. Wu, H. M. Shen, J. S. Zhu, X. H. Chen, Y. F. Van, and Z. X. Zhao, Phys. Rev. B **41**, 8981 (1990).
[32] A. I. Golovashkin, O. M. Ivanenko, A. V. Mitsek, V. A. Danilov, I. I. Perepechko, G. M. Leĭtus, O. G. Karpinskiĭ, and V. F. Shamraĭ, in *Proceedings of the Conference on Problems in High-Temperature Superconductivity* [in Russian], Sverdlovsk (1987), part 3, p. 180.
[33] L. Ya. Kobelev, L. L. Nugaeva, Yu. F. Gorin, Yu. A. Lobanov, and V. B. Zlokazov, in *Proceedings of the Conference on Problems in High-Temperature Superconductivity* [in Russian], Sverdlovsk (1987), part 2, p. 180.
[34] M. B. Lazareva, B. G. Lazarev, Ya. D. Starodubov, G. G. Sergeeva, L. A. Chirkina, and V. S. Okovit, LT-22, Finland (to be publ. in Physica B, 2000).

Translated by Steve Torstveit

NEW METHODS OF LOW-TEMPERATURE EXPERIMENT

Noncontact method for measurement of the critical current densities and diagnostics of superconductors

Kh. R. Rostami*

Institute of Radio Engineering and Electronics, Russian Academy of Sciences, pl. Vvedenskogo 1, 141120 Fryazino, Moscow District, Russia

(Submitted November 7, 1999; revised July 17, 2000)
Fiz. Nizk. Temp. **27**, 103–108 (January 2001)

The role of the geometric factor of a superconducting sample in magnetic measurements of the critical current densities J_c is investigated. It is shown that a small difference of the shape of the sample from cylindrical does not have much effect on the value of J_c. It is found that the error in evaluating J_c for single crystals with the use of the standard expression for determining J_c of a ceramic is due to the low trapped magnetic flux density B_{tr} in single crystals as compared to ceramics. A technique is proposed for determining J_c for single-crystal and ceramic samples from measurements of the spatial distribution of B_{tr} produced by the Bean shielding supercurrents upon the transition of the whole volume of the sample to the critical state. A formula is obtained for determining J_c for single-crystal and ceramic superconducting samples in the form of polygonal and cylindrical slabs. To increase the accuracy of determining J_c the difference $B_0^*-B_{c1}$ was used instead of $B_{tr}^{max}(0)$ (B_0^* is the field that induces $B_{tr}^{max}(0)$ at the geometric axis of the sample, and B_{c1} is the first critical magnetic field of the sample). The values of J_c and of the pinning force in YBCO and BSCCO single-crystal samples are estimated. It is established that the magnetic flux trapping mechanisms in these layered structures are different. [DOI: 10.1063/1.1344148]

One of the central problems of the diagnostics of superconducting materials during their synthesis and application is to determine the critical current densities J_c as accurately and expeditiously as possible.

In the conventional noncontact method, J_c is determined from measurements of the hysteresis curve of the magnetization with the use of SQUID magnetometers or inductive methods.[1–6] However, these methods are complicated and uneconomical. It is therefore very important to devise simpler and more economical methods of accurately determining J_c.

In this paper we propose a simpler alternative to the standard method of measuring J_c for superconducting single crystals and ceramics. This new method is based on investigation of the local spatial distribution of the trapped magnetic field density B_{tr} produced by the Bean shielding supercurrents around the sample.

METHOD

The spatial distribution of the trapped magnetic flux (TMF) near $YBa_2Cu_3O_{7-x}$ (YBCO) ceramic samples was investigated experimentally in Ref. 7 as a function of the temperature, external magnetic field, and transport current. As a result, the ''evolution'' of the critical state inside the sample was described, and the domain of applicability of the Bean model[8] for accurate evaluation of the critical currents of the investigated YBCO high-T_c superconducting (HTSC) ceramics was determined. The normalized axial distribution of the maximum trapped field $B_{tr}^{max}(z)/B_{tr}^{max}(0)$ outside the sample and the critical current density J_c upon establishment of the critical state in the entire intergranular space are described by the expressions

$$\frac{B_{tr}^{max}(z)}{B_{tr}^{max}(0)}=\frac{1}{h\sinh^{-1}(R/h)}\times\left[(h+z)\sinh^{-1}\left(\frac{R}{h+z}\right)-z\sinh^{-1}\left(\frac{R}{z}\right)\right], \tag{1}$$

$$J_c=\frac{c}{\pi}\frac{B_{tr}^{max}(0)}{h\sinh^{-1}(R/h)}, \tag{2}$$

where z is the coordinate along the axis of the cylindrical sample, R is the radius and h the thickness of the sample, $B_{tr}^{max}(0)$ is the value of the maximum trapped field near the surface of the sample, and c is the speed of light.

However, the use of formula (2) to evaluate J_c for single-crystal samples of the HTSCs YBCO and $Bi_2Sr_2CaCu_2O_x$ (BSCCO) underestimated the values. With the goal of using the technique proposed in Ref. 7 for single crystals also, we have explored the possible causes of the error in the estimates of J_c for single-crystal HTSC samples. To study the influence of the shape and geometric dimensions of the sample on the value of J_c, the normalized axial distribution $B_{tr}^{max}(z)/B_{tr}^{max}(0)$ outside the superconducting sample was modeled on a computer with the use of formula (1). It was found that the $B_{tr}^{max}(z)/B_{tr}^{max}(0)$ is rather insensitive to variations of h over a wide range (0.01–0.5 mm) but

depends strongly on R, which was varied over the range 0.25–10 mm. When the experimental data were approximated by a curve calculated according to formula (1), it was found that if the radius R of the sample was varied with h held fixed, satisfactory agreement could not be achieved for any reasonable values of R and h. It was also impossible to obtain good agreement of the curves with a simultaneous variation of R and h as adjustable parameters. The values obtained for the optimal curves, R^*, R^{**}, and h^{**}, turned out to be too large in comparison with the radius R and height h of the samples (R was determined from the transverse dimensions of the real sample, a polygonal slab approximated by a cylinder). The impossibility of approximating the experimental data by the theoretical curves and the fact that the values obtained, R^*, R^{**}, h^{**}, are very large compared to the actual values R and h for the sample shows that the distribution of trapped fields is rather insensitive to the particular form of the current streamlines. This suggests that the small difference of the shape of the sample from cylindrical cannot be responsible for the large error in the calculated values of J_c.

According to Refs. 7 and 9, the values of the fields B_0^* at which the dependence of $B_{tr}(0)$ on B_0 reaches the saturation region are comparable to the fields $B_{tr}^{max}(0)$, and this provides an opportunity for accurate evaluation of J_c. In single-crystal HTSC samples the level of trapped fields on average is more than an order of magnitude lower than in ceramic HTSCs, and this leads to a substantial difference between the values of B_0^* and $B_{tr}^{max}(0)$. This, in turn, can lead to an error of more than an order of magnitude in the determination of J_c.

It will be shown below that if the difference $B_0^*-B_{c1}$ is used in formula (2) instead of $B_{tr}^{max}(0)$ (B_{c1} is the first critical magnetic field of the sample), one obtains values of J_c for YBCO and BSCCO that are in good agreement with published data. Here the following semiempirical expression is proposed:

$$J_c=\frac{c}{\pi}\frac{B_0^*-B_{c1}}{h\sinh^{-1}(R/h)} \tag{3}$$

which is valid for ceramics as well. In short, the capabilities of the technique described in Ref. 7 are extended considerably.

SAMPLES AND EXPERIMENTAL PROCEDURES

The samples for study were $YBa_2Cu_3O_{7-x}$ single crystals with a critical temperature of the superconducting transition $T_c\approx 91$ K and dimensions of $\sim 1\times 1\times 0.05$ mm, $2\times 1\times 0.05$ mm, and $0.8\times 0.7\times 0.05$ mm and $Bi_2Sr_2CaCu_2O_x$ single crystals with dimensions of $\sim 1.2\times 1{,}1\times 0.15$ mm, $4\times 4\times 0.1$ mm, $4\times 10\times 0.6$ mm, and $T_c\approx 90$ K. The measurements of the trapped field were made at liquid nitrogen temperature in static magnetic fields of up to 1 kG by means of a Hall sensor with a working are of 0.15×0.45 mm and a sensitivity of 10 μV/G. The magnetometer was capable of detecting fields to an accuracy of 10^{-2} G or better. The measurements of the TMF were made in the zero-field cooling (ZFC) regime, i.e., the sample was cooled to a temperature $T=77.4$ K$<T_c$ in zero magnetic field. Then a pulse of external magnetic field B_0 with a duration of 0.5 min was applied in the direction perpendicular to the plane of the sample. After a 30-minute wait from the time the field was removed (this time was sufficient to eliminate the rapidly relaxing part of the TMF) the value of $B_{tr}^{max}(z)$ was measured at various distances z (along the axis of the sample) between the sample and the Hall sensor. Then the sample was heated to a temperature $T>T_c$ and the procedure was repeated for a different value of B_0. Since HTSC single crystals usually have the shape of thin polygonal slabs and are very brittle materials, it is practically impossible to bring them to the shape of a cylindrical disk. Therefore the geometric axis of the sample was chosen as follows: a cylindrical recess was drilled at the center of a copper disk to a depth precisely equal to the thickness of the single-crystal HTSC slab, with allowance for the thickness of a thin layer of glue. The diameter of the recess was chosen so as to provide a snug setting for the sample. A Hall sensor was mounted in a similar way at the center of another copper disk. Threads were cut on the other side of the disk holding the sample to permit mounting the disk on the end of a copper rod with a heater wound on it. This mounting made it possible to move the disk holding the sample in a precisely coaxial relationship to the rigidly fixed disk holding the Hall sensor. For a sample in the form of a parallelepiped with dimensions comparable to those of the working area of the Hall sensor, this mounting made it possible, without further effort, to fix the position of the sample relative to the Hall sensor in such a way that the corresponding faces were parallel.

EXPERIMENTAL RESULTS AND DISCUSSION

Figure 1 shows the axial distributions of the normalized TMF density $B_{tr}^{max}(z)/B_{tr}^{max}(0)$ for YBCO and BSCCO single-crystal samples with dimensions of $1\times 1\times 0.05$ mm and $4\times 4\times 0.1$ mm, respectively. Points *1* correspond to the experiment. Curves *2* are the results of a calculation according to formula (1) for the specified dimensions of the samples. As we see from Fig. 1, in neither case does curve *2* agree with the experimental data *1*. Curves *3* were obtained by approximating the experimental data *1* with a theoretical curve by varying R. The effective radius R^* for these curves was 6 mm for the YBCO and 5.5 mm for the BSCCO single crystals. Curves *4* in Fig. 1 correspond to an approximation of the experimental data by simultaneous variation of R and h. For curves *4* the values $R^{**}=2.8\pm 1.8$ mm, $h^{**}=0.8\pm 1.4$ mm were obtained for the YBCO single crystals and $R^{**}=3.4\pm 0.9$ mm, $h^{**}=0.9\pm 0.8$ mm for the BSCCO single crystals. The values of R^*, R^{**}, and h^{**} differ considerably from the reduced radius and h of the real samples. The reduced radii R for the YBCO and BSCCO single-crystal samples were 0.7 and 2.8 mm, respectively.

The value of B_0^* can be determined from the curve of $B_{tr}(0)$ versus B_0 at values of B_0 corresponding to the saturation region of the curve. The value of B_{c1} can also be determined from the curve of $B_{tr}(0)$ versus B_0 when the Hall sensor registers a nonzero signal $B_{tr}(0)$. Figure 2 shows the field dependence of $B_{tr}(0)$ for YBCO and BSCCO single-crystal HTSC samples. As we see from the figure, the values of the fields B_{c1}, B_0^*, and $B_{tr}^{max}(0)$ equalled 50, 95, and 0.29 G for YBCO and 4.5, 30, and 2.1 G for BSCCO. Because of

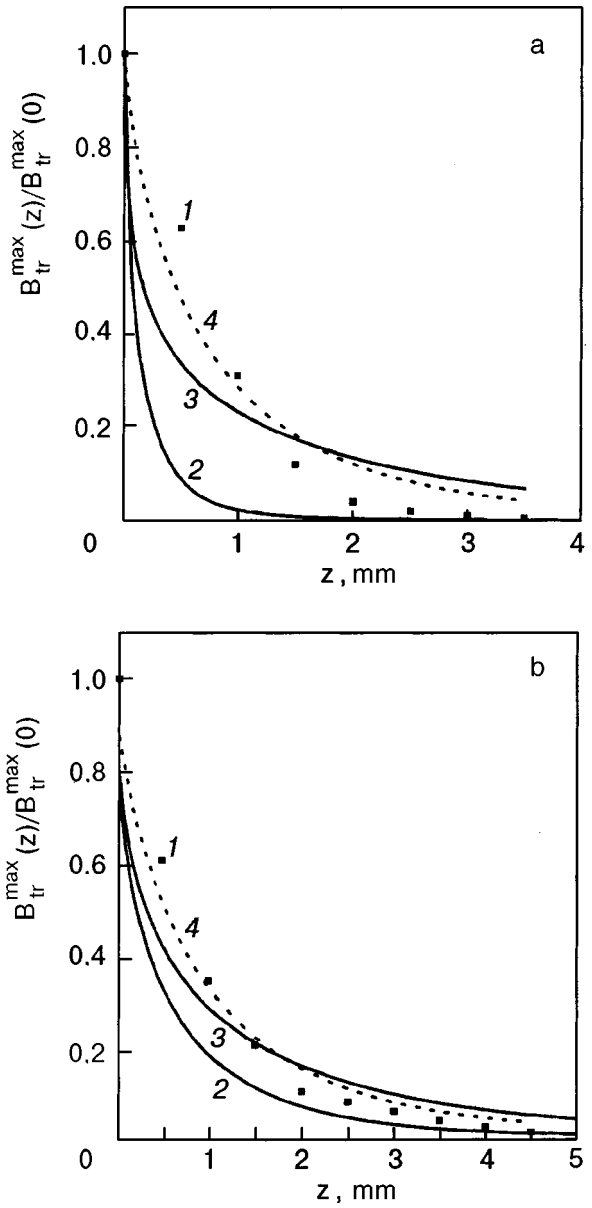

FIG. 1. Axial distributions of the normalized trapped magnetic flux density $B_{tr}^{max}(z)/B_{tr}^{max}(0)$: for a $YBa_2Cu_3O_{7-x}$ single-crystal sample with dimensions of $1\times1\times0.05$ mm (a) and for a $Bi_2Sr_2CaCu_2O_x$ single-crystal sample with dimensions of $4\times4\times0.1$ mm (b). Experiment (*1*), theory (*2*), approximation of the experimental by the theoretical dependence, with variation of the radius R of the sample (*3*), and the same but with simultaneous variation of R and the height h of the sample (*4*). $T=77.4$ K.

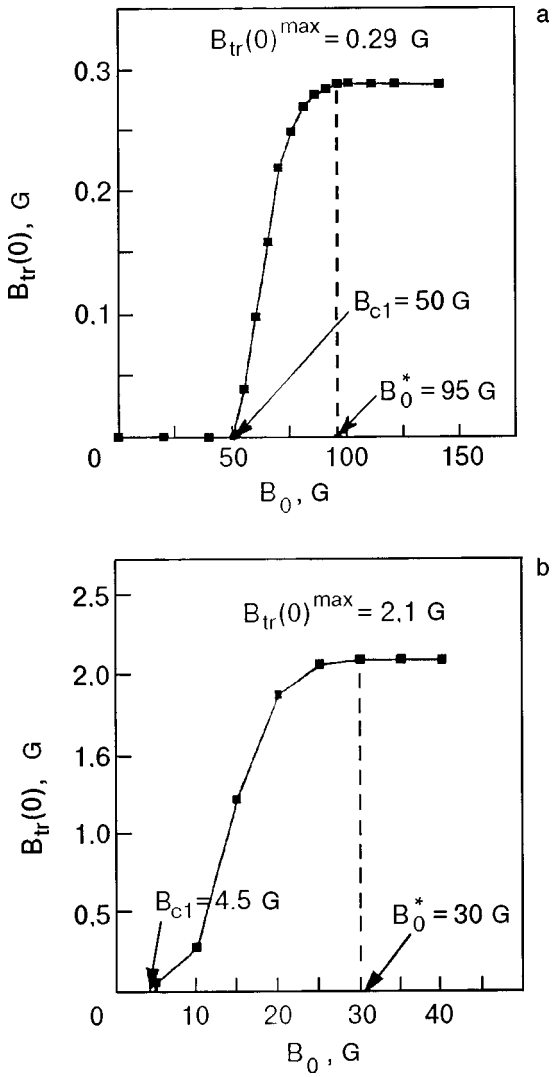

FIG. 2. Field dependence of the trapped magnetic field $B_{tr}(0)$ at $T=77.4$ K for the ZFC regime. For a YBCO single-crystal sample with dimensions of $1\times1\times0.05$ mm (a) and for a BSCCO single-crystal sample with dimensions of $4\times4\times0.1$ mm (b).

the current and potential contacts present on the surface of the Hall sensor, the minimum gap between the working surface of the Hall sensor and the surface of the sample was 200 μm. To establish the exact value of $B_{tr}^{max}(0)$ we constructed the unnormalized axial distributions $B_{tr}^{max}(z)$ for the YBCO and BSCCO single-crystal HTSC samples. Figure 3 shows a plot of $B_{tr}^{max}(z)$. Extrapolation of the curves to an ordinate axis shifted along z by -200 μm yields a more accurate value of $B_{tr}^{max}(0)$. For the YBCO and BSCCO samples the refined values of $B_{tr}^{max}(0)$ are 0.35 and 2.51 G. The values of the TMF determined from Figs. 2 and 3 could be used to determine J_c for the YBCO and BSCCO single-crystal samples according to formula (2). The volume density of the pinning force was determined according to the formula[1]

$$F_p=\frac{1}{c}J_cB_{tr}^{max}(0), \tag{4}$$

and the pinning force acting per unit length of vortex was found from the formula

$$f=(\Phi_0/c)J_c \tag{5}$$

(Φ_0 is the magnetic flux quantum). As we see from Table I, the values obtained for J_c are more than two orders of magnitude lower than the published data in the case of YBCO single crystals and more than one order of magnitude lower in the case of BSCCO single crystals. We now use formula (3) to recalculate the values of J_c for YBCO and BSCCO single crystals and, substituting the new values into formulas (4) and (5), again estimate the values of F_p and f. The results are given in Table II. It is seen from Table II that the corrected values of J_c are in good agreement with the published data.

By substituting $B_{c1}=0$ and $B_0^*=B_{tr}^{max}(0)$ into formula (3) we obtain formula (2). This substitution is justified because a magnetic field of 10^{-3} Oe will already penetrate into

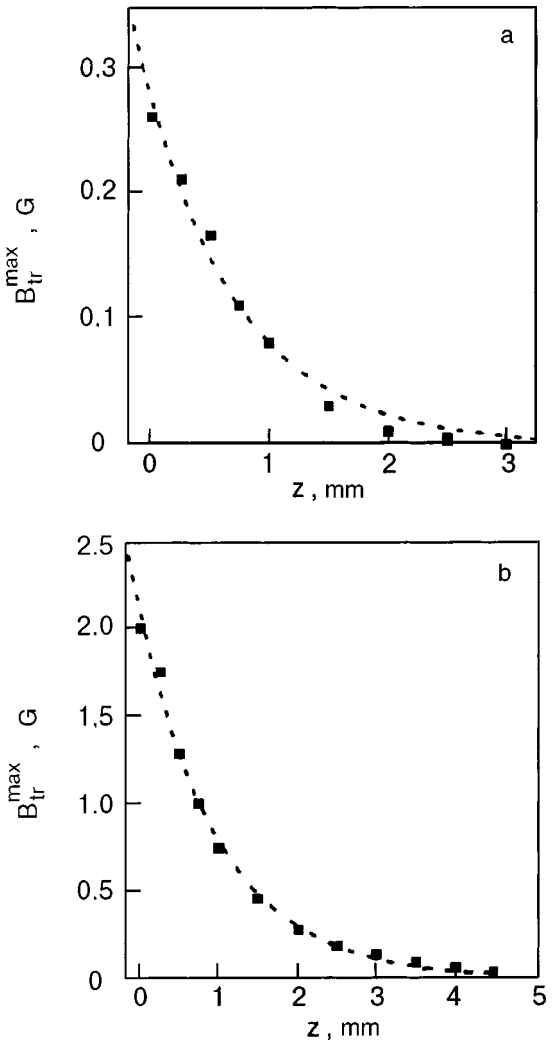

FIG. 3. Axial distribution of the unnormalized trapped field $B_{tr}^{max}(z)$ at $T=77.4$ K for the ZFC regime. For a YBCO single-crystal sample with dimensions of $1\times1\times0.05$ mm (a) and for a BSCCO single-crystal sample with dimensions of $4\times4\times0.1$ mm (b).

a HTSC ceramic,[10] and the value of the trapped field at which the critical state is established throughout the entire intergranular space is approximately equal to the value of its inducing field B_0^* (Refs. 7 and 9).

TABLE I. Critical current densities for YBCO and BSCCO single crystals. Calculation according to formula (2).

Single crystal	J_c, A/cm^{-2}	J_c, 10^3 A/cm^{-2} (Ref. 2)	F_p, dyn/cm^{-3}	f, 10^{-6} dyn/cm^{-1}
YBCO	66.7	5–50	2.34	1.38
BSCCO	198.4	1–10	49.8	4.1

TABLE II. Critical current densities for YBCO and BSCCO single crystals. Calculation according to formula (3).

Single crystal	J_c, 10^3 A/cm^{-2}	F_p, dyn/cm^{-3}	f, 10^{-6} dyn/cm^{-1}
YBCO	8.60	267	178
BSCCO	2.02	432	41.8

CONCLUSION

In summary, we have refined the method proposed in Ref. 7 by which one can determine J_c for single-crystal and ceramic superconducting samples in the shape of polygonal and cylindrical slabs. We have found that in comparison with YBCO, the difference between $B_{tr}^{max}(0)$ and B_0^* for BSCCO single-crystal samples is substantially smaller. BSCCO is characterized by a lower B_{c1}, a higher $B_{tr}^{max}(0)$, a stronger volume pinning, and a lower J_c, possibly because of the different mechanisms for magnetic flux trapping in these layered structures.

If the measurements are made using Hall or other types of sensors with a smaller size (the known Hall sensors have a working surface area of 20×20 μm), one can substantially increase the resolving power of the proposed method. According to Ref. 11, the threshold sensitivity of a Hall magnetometer can be improved to 6×10^{-5} G, which would make it possible to make express measurements of the $J_c\|C$ component of the critical current of single crystals and to perform a more detailed diagnostics of superconducting materials.

The author is extremely grateful to E. A. Bryun for supporting this study and to V. N. Gubankov for interest and helpful discussions.

*E-mail: vip197@ire216.msk.su

[1] A. M. Campbell and J. E. Evetts, *Critical Currents in Superconductors* [Taylor and Francis, London (1972); Mir, Moscow (1975)].
[2] A. A. Zhukov and V. V. Moshchalkov, Sverkhprovodimost' (KIAE) **4**, 850 (1991) [Superconductivity **4**, 759 (1991)].
[3] Yu. E. Kuzovlev, JETP Lett. **61**, 1000 (1995).
[4] J. R. Clem and A. Sanchez, Phys. Rev. B **50**, 9355 (1994).
[5] J. Zhu, J. Mester, J. Lockhart, and J. Turneaure, Physica C **212**, 216 (1993).
[6] P. N. Mikheenko and Yu. E. Kuzovlev, Physica C **204**, 229 (1993).
[7] Kh. R. Rostami, V. V. Mantorov, and V. I. Omel'chenko, Fiz. Nizk. Temp. **22**, 736 (1996) [Low Temp. Phys. **22**, 565 (1996)].
[8] C. P. Bean, Rev. Mod. Phys. **36**, 31 (1964).
[9] Kh. R. Rostami, A. A. Sukhanov, and V. V. Mantorov, Supercond. Sci. Technol. **9**, 736 (1996).
[10] B. Loegei, D. Bolmont, and A. Mahdaoui, Physica C **159**, 816 (1989).
[11] V. K. Ignat'ev and A. L. Yakimets, Prib. Tekh. Eksper., No. 5, 104 (1997).

Translated by Steve Torstveit